ABSTRACT

SIKDER, CHANDAN. Design and Controller Optimization of Switched Reluctance and Flux Switching PM Machines (Under the direction of Dr. Iqbal Husain).

This dissertation presents the design, modeling, control and implementation of two different radial flux electric machine topologies that use the same type of rotor with several specific objectives and requirements. Flux Switching PM (FSPM) machine is one of those machines which can be seen as an improved or modified version of the other which is the Switched Reluctance Machine (SRM) with better performance and higher power density.

A novel control technique for SRM is developed to maximize efficiency for a wide speed range. A geometry based analytical model was used to establish the concept and develop the control algorithm. Based on the simulation results, a correlation have been found between Switched Reluctance Generator (SRG) system efficiency and DC-link current ripple. A novel control algorithm has been developed that dynamically varies the commutation angles for the machine operation based on the required and commanded DC-link current along with continuously monitoring the ripple in DC-link current. The algorithm is implemented and successfully tested on a 1kW SRM drive. This control concept can generally be applied to any SRM for all speed ranges.

FSPM machine is one of the newer topologies that emerged as a potential alternative candidate to the existing popular topologies due to its ability to combine most of the features and advantages of SRM and conventional PM machines into one structure. This dissertation presents a methodology for designing low torque ripple FSPM by addressing the issue of cogging torque by rotor pole shaping. A generalized design rule on rotor pole shaping has been developed using permeance based model for cogging torque minimization. The proposed pole

shaping is shown to minimize the torque ripple to up to 97% with only 5.34% sacrifice on the average torque.

The issue of noise, vibration and stator deformation are also addressed from a design perspective. An analytical model has been proposed and verified with FEA to account for the natural mode frequencies of the segmented stator of FSPM. Based on the analytical model of natural mode frequencies, another design rule has been proposed to improve the noise and vibration characteristics of the machine. The proposed design modification reduces noise by 7-8 dB at all the operating speeds, whereas the stator deformation is within acceptable limits as found from structural FEA.

An accurate machine model incorporating saturation and mutual coupling has been developed using FEA based *d*- and *q*-axes flux linkage characteristics. The performance of the motor drive has been verified before fabrication using a coupled simulation of the FEA machine model and a dynamic simulation model of the controller and drive.

An experimental prototype of the designed 0.5kW, 12/10 FSPM machine was constructed with non-rare earth PM applying the design rules for reduction of cogging torque and acoustic noise. Based on the developed machine model and coupled simulation, stator field oriented vector controller has been implemented in the experimental setup. No-load back EMF, steady state torque and phase current waveforms have been collected from the experimental setup to evaluate and verify the motor drive system performance at different operating speeds and for up to 200% rated load. All the tests show excellent correlation to the FEA analysis and co-simulation results. In addition, a steady state heat run test was also performed to examine the temperature rise in different parts of the machine according to the losses.

© Copyright 2016 Chandan Sikder

All Rights Reserved

Design and Controller Optimization of Switched Reluctance and Flux Switching PM Machines

by
Chandan Sikder

A dissertation submitted to the Graduate Faculty of
North Carolina State University
in partial fulfillment of the
requirements for the Degree of
Doctor of Philosophy

Electrical Engineering

Raleigh, North Carolina

2016

APPROVED BY:

_____	_____
Dr. Iqbal Husain Committee Chair	Dr. Subhashish Bhattacharya
_____	_____
Dr. Srdjan Lukic	Dr. Gregory Buckner

DEDICATION

To my loving wife ***Sulagna Das***, who sacrificed a lot and together with whom we have gone through a lot at times of trouble.

To our first child ***Arniya Sikder***, who came as a blessing in these times of trouble and hard work. I am truly blessed to be your father.

To my loving mom (***Aloka Rani Kundu***) and dad (***Sikder Chatur Krishna***, *1947-1999*) without whose unconditional support, I would not have the chance to be who I am.

BIOGRAPHY

Chandan Sikder received his B.Sc. degree in Electrical and Electronic Engineering (EEE) from Bangladesh University of Engineering and Technology (BUET), Dhaka, Bangladesh, in 2006. He received his Ph.D. degree from the Department of Electrical and Computer Engineering at North Carolina State University, Raleigh, NC in 2016. He is currently working as a Senior Firmware Engineer in Rockwell Automation, Mequon, Wisconsin.

From 2010 to 2011, he was a Research Assistant at The University of Akron, Akron, OH, USA, working on control of Switched Reluctance Machines. During his time at NSF FREEDM Systems Center, NC State University (2012-2016), he worked in close collaboration with ABB US Corporate Research Center on design, modeling and control of new and innovative electric machine topologies for general purpose, industrial application. He also worked as a Research Intern at ABB USCRC during fall 2013 on design and modeling of Synchronous Machines. His research interests are in the areas of electromagnetics, electromechanical energy conversion systems, design, modeling and control of electric machines, motor drives, model based control of power electronics converter, and renewable or alternative energy systems in general.

ACKNOWLEDGMENTS

I wish to express my deepest gratitude goes to Dr. Iqbal Husain without whose ardent initiatives, compassionate advice and erudite guidance this research work would not have been materialized. I would like to thank all the committee members for their valuable suggestions and support for making this research a success. A very special thank you goes to Dr. Yilmaz Sozer for his mentorship towards my research during my time at the University of Akron.

I would like to acknowledge the financial support from ABB US Corporate Research Center during this research. The technical support from Dr. Wen Ouyang (ABB), Mr. Morihiro Saito (Motion System Tech) and Natsuki Watanabe (Komatsu Ltd) are highly appreciated.

A very special thanks goes to Dr. Rajib Mikal and Dr. Mehnaz Akhter Khan, who were my ex-colleagues here at FREEDM and happen to be good friends of mine since the first day of undergraduate studies. They provided critical support and encouragement since my first day here in the US. Dr. Mikail is an inspiring researcher and scientist who is always available with the right advice whenever required.

My sincere gratitude goes toward all the faculty, students and staffs working at the NSF FREEDM Systems Center, NC State University for providing a collaborative and state of the art research atmosphere. A special thanks goes to Adeeb Ahmed who helped me a lot in setting up the experimental test bench.

Finally, the support and inspiration from my wife Sulagna Das, my mom Aloka Rani Kundu and my daughter Arniya Sikder (born July 24, 2015) provided me moral strength and encouragement during all these years.

TABLE OF CONTENTS

LIST OF TABLES ix
LIST OF FIGURES x
CHAPTERS
Chapter 1 Introduction 1
1.1 Switched Reluctance Machine 3
1.1.1 Applications of SRM Drives 5
1.2 Stator PM Machine Technology 6
1.2.1 Prospect and Applications of FSPM drive 8
1.3 Research Motivation 9
1.4 Research Objective and Methodology 12
1.5 Dissertation Organization 14
Chapter 2 Switched Reluctance and Flux Switching Machines 17
2.1 Switched Reluctance Machine 18
2.1.1 Operating Principle of SRM 19
2.1.2 Motoring and Generating using SR Machines 20
2.1.3 SRM Drive System 21
2.1.4 SRM Power Converters 22
2.2 Flux Switching Machines 25
2.2.1 Background and Definition 25
2.2.2 Modes of Flux Switching 27
2.2.3 Evolution of Flux Switching Machines 28
2.2.3.1 Inductor Alternator 30
2.2.3.2 Flux Switching Alternator 33
2.2.3.3 Field assisted and PM assisted SRM 34
2.2.3.4 Flux Reversal Machine 36
2.2.3.5 Modern FSMs using Salient Rotor and Sandwiched Spoke magnet 39
2.3 Conclusion 44
Chapter 3 SRG Control for Optimal Power Generation 46
3.1 Generation with SRG from control perspective 46
3.2 Switched Reluctance Generator System 48

3.3	SRG System Electrical Losses ……	51
3.4	Data Collection and Analysis ……	56
3.5	SRG Controller ……	65
3.6	Controller Experimental Results ……	69
3.7	Conclusion ……	73
Chapter 4	**Comprehensive Design Methodology of FSPM** ……	74
4.1	Performance Requirements ……	75
4.2	Design Steps ……	75
4.3	Design Constraints ……	77
4.4	Selection of Parameters and Configuration ……	77
4.4.1	Number of Phases ……	77
4.4.2	Number of Stator and Rotor Poles ……	79
4.4.3	Pole Widths, Airgap and Split Ratio ……	81
4.5	Design Data ……	83
4.6	Design Specifications ……	85
4.7	Geometric Parameters ……	87
4.8	Winding Connections ……	89
4.9	Analytical Verification of Design Parameters ……	90
4.9.1	Calculation of Flux ……	90
4.9.2	Flux through Airgap ……	93
4.9.3	Number of Turns per Coil ……	94
4.9.4	Wire Size ……	96
4.9.5	Mean Length of Turn ……	96
4.9.6	Estimation of Back EMF, Current, Torque and Power ……	97
4.9.7	Number of Turns and Armature Current ……	98
4.10	Magnetic Saturation and Flux Density Distribution ……	99
4.11	Flux Linkages and Back EMF ……	100
4.12	Estimation of Core Loss Co-efficients ……	101
4.13	Input, Output and Losses from FEA ……	104
4.14	Electromagnetic Torque, Torque Ripple and Cogging Torque ……	107
4.15	Account of Temperature Effect for Continuous Operation ……	108

4.16	Power Factor Analysis ……..…...	112
4.17	Design and Comparison with SRM and Surface PM Machines …..……	115
4.17.1	Motor I – SRM …….……..	116
4.17.2	Motor II – Surface Mounted PM Brushless DC Machine…..…….	119
4.17.3	Comparison of Performances ……	123
4.18	Scalability and Design of a Larger FSPM ……..…….	124
4.18.1	No-load Results …….	127
4.18.2	Steady State Performance Under Load Condition …….……	130
4.19	Design of an FSPM with Rare earth Magnet ……..…….	131
4.19.1	No-load Results …….	131
4.19.2	Steady State Performance Under Load Condition …….……	134
4.20	Conclusion …….	135
Chapter 5	**Cogging Torque Reduction in FSPM** ……..	136
5.1	Existing Techniques of Cogging Torque Reduction in FSPM ……...….	136
5.2	Cogging Torque in FSPM ……..….	137
5.3	Selection of FSPM Topology …….……	140
5.4	Cogging Torque Reduction using Rotor Flange …….……	146
5.5	Flange Parameter Optimization with FEA ……..……	150
5.6	Rotor Pole Flange Effect on Back EMF and Torque ……...……	156
5.6.1	Torque Separation and effect on Reluctance Torque ……..…..……	158
5.6.2	Effect of Rotor Eccentricity ……..……..…	160
5.7	Rotor Pole Flange in E-Core and C-Core FSPM …….	163
5.8	Conclusion …….…	165
Chapter 6	**Design of a Low-Noise FSPM** …….....	167
6.1	Noise and Vibration in FSPM …….…..	167
6.2	Circumferential Mode Shapes Due to Stator Vibration ……...……..	169
6.3	Mode Frequencies for Segmented Stator ……...….....	171
6.4	Sources of Noise and Vibration in Electric Machine ……...…..	172
6.5	Design Parameters for a Low-Noise FSPM …….……..…...	175
6.5.1	Selection of α_s …….….	176
6.6	Final Design and Performance …….....	177

6.6.1 Improvement in Noise and Vibration with Structural FEA results……..... 178
6.6.2 Circumferential Deflection and Acoustic Noise Levels ……. 180
6.6.3 Effect on Electromagnetic Performance ……...……. 184
6.7 Stator Deformation from Static Structural FEA Model …….……..... 185
6.8 Conclusion ……..…….…. 188
Chapter 7 Modeling, Control and Performance Testing of FSPM Drive..... 189
7.1 Challenges and Possibilities of FSPM ……..…….… 189
7.2 Final Design of the Prototype FSPM ……. 191
7.3 Modeling of FSPM Including Saturation and Mutual Coupling ……..... 192
7.4 Field Oriented Control and Dynamic Co-simulation of FSPM Drive …..... 196
7.5 FSPM Drive Simulation Results ……..……..... 198
7.5.1 Generation using FSPM ……... 200
7.6 FSPM Prototype and Test Results …….…….... 205
7.6.1 No-Load Tests …….. 207
7.6.2 Steady State Phase Currents, Torque and Torque Ripple …….. 209
7.7 FSPM Performance at Different Load Conditions …….……... 211
7.8 Heat Run Test Results ……..…… 216
7.9 Conclusion …… 218
Chapter 8 Summary and Future Work …….. 219
8.1 Summary ……... 219
8.2 Future Work …….. 222

REFERENCES …….……. 226

LIST OF TABLES

Table 3.1: SRG parameters in the experimental setup 50

Table 3.2: $I_{ph(rms)}$ and $I_{dc\text{-}ripple(rms)}$ for different magnitude, duty and overlap situation 53

Table 3.3: DC-link current ripple and $I_{dc(avg)}/T_{avg}$ for different phase currents 56

Table 3.4: I_{ref} and θ_{cond} corresponding to $I_{dc(avg)}$ for 61

Table 3.5: Optimum I_{ref} and θ_{cond} for different $I_{dc(avg)}$ at 1000 rpm. 64

Table 3.6: Comparison of optimum values of I_{ref} and θ_{cond} from offline optimization with PI controller set values at 1000 rpm (experiment) 70

Table 4.1: Checklist on Application Requirements 75

Table 4.2: Design constraints of the FSPM 77

Table 4.3: Some possible stator/rotor pole combinations for 3-phase FSPM 81

Table 4.4: Design specifications of the FSPM 86

Table 4.5: Material Usage in the Designed Machine 86

Table 4.6: Geometric parameters of the FSPM 88

Table 4.7: Number of turns and current rating of the FSPM 98

Table 4.8: Available loss/kg data of steel at 200 Hz, 400 Hz and interpolated at 300 Hz 102

Table 4.9: Bertotti's coefficients determined based on the available loss data 103

Table 4.10: Comparison between cogging torque and ripple in average torque 108

Table 4.11: Coil resistance elevation due to increase in temperature at steady state 109

Table 4.12: Summary of the performance parameters of the designed FSPM 112

Table 4.13: Geometric parameters of SRM designed within the same volume as the FSPM 117

Table 4.14: Design data of surface mounted PM Brushless DC machine 120

Table 4.15: Comparison of SRM, SM PM BLDC and FSPM performances 123

Table 4.16: Design data of the 50kW FSPM 126

Table 4.17: Important performance parameters of the 50kW FSPM designed 131

Table 4.18: Important performance parameters of the rare earth FSPM designed 135

Table 5.1: Comparison among FSPMs 142

Table 5.2: 12/10 FSPM Design Parameters 144

Table 5.3: Preliminary design specifications of the 12/10 1kW FSPM 145

Table 5.4: Optimum flange width for machines of different sizes and stator tooth width. 155

Table 5.5: Reduction in cogging torque and average electromagnetic torque for various flange widths. 157

Table 5.6: Separation of Torque components by frozen permeability method 159

Table 5.7: Comparison of magnitudes of torque components 160

Table 5.8: Comparison of cogging torque amplitude (with and without flange) 162

Table 5.9: Cogging torque reduction in E-Core and C-Core machine using rotor flange 164

Table 5.10: Comparison among important geometrical parameters of the machine and optimum flange width among different topologies of FSPM 164

Table 6.1: Design parameters of the 0.5 kW FSPM 178

Table 6.2: Improvement in mode frequencies with α_s=1.7 179

Table 6.3: Comparison of noise levels at 1800 RPM 181

Table 6.4: Comparison of affected design and performance parameters between the base and Low-Noise design 185

Table 7.1: Geometric parameters of the final design 192

Table 7.2: FSPM motor co-efficients obtained using the advanced model 196

Table 7.3: FSPM Generator Performance at 1800 RPM and Rated Current 203

Table 7.4: Comparison of Torque ripple between simulation and experiment 210

LIST OF FIGURES

Figure 1.1: A three-phase, 12/8 SRM 4

Figure 1.2: Flux Switching PM Machines: Combining SRM and PMSM features 7

Figure 2.1: Operating Principle of SRM 19

Figure 2.2: Motoring and generating operation and their relation to inductance profile 21

Figure 2.3: Simplified basic SRM drive system 22

Figure 2.4: Classical bridge converter for a three-phase SRM 23

Figure 2.5: Operation of the classic bridge type converter 24

Figure 2.6: Converter switching sequence during motoring and generating 24

Figure 2.7: Unipolar and bipolar flux linkage with variation of permeance 28

Figure 2.8: Basic structure of the Homopolar Inductor Alternator (HIA) 31

Figure 2.9: Heteropolar machine topologies 32

Figure 2.10: Structure of a simplified flux switching alternator 34

Figure 2.11: Cross section of the basic field assisted SRM 35

Figure 2.12: Cross section of the proposed PM assisted SRM 35

Figure 2.13: Basic configuration of a 2/3 FRM 38

Figure 2.14: Operating principle of the FRM 38

Figure 2.15: Elementary cell of the modern flux switching structure 39

Figure 2.16: Various structures of modern flux switching machines 40

Figure 2.17: Basic principles with field coil excitation. 42

Figure 2.18: FSM topology using field winding excitation 42

Figure 2.19: Elementary cell structure for hybrid excitation 42

Figure 2.20: Graphical representation of the evolution of Flux Switching PM Machines 43

Figure 3.1: SRG drive system 49

Figure 3.2: Experimental setup for SRG operation 49

Figure 3.3: $I_{ph(rms)}$ and $I_{dc\text{-}ripple(rms)}$ variation with changing n. 54

Figure 3.4: (a) I_{ph} and I_{dc} for I_{ref} = 4.5 A and θ_{cond} = 18.5 mechanical degrees. (b) I_{ph} and I_{dc} for I_{ref} = 3.5 A and θ_{cond} = 19.5 mechanical degrees. (c) I_{ph} and I_{dc} for I_{ref} = 3 A and θ_{cond} = 20.5 mechanical degrees. 55

Figure 3.5: $I_{dc(avg)}/T_{avg}$ and nominal ripple variation with I_{ref} and θ_{cond} for (a) $I_{dc(avg)}$=0.7-0.8 Amp. (b) $I_{dc(avg)}$=0.4-0.5 Amp. 58

Figure 3.6: (a) $I_{dc}/Torque$ variation with θ_{off} angles, for different reference currents. (b) Nominal ripple variation with θ_{off} angles, for different reference currents 59

Figure 3.7: $I_{dc}/Torque$ variation with nominal ripple. 60

Figure 3.8: (a) Efficiency and nominal ripple variation with I_{ref} and θ_{cond} for $I_{dc(avg)}$=0.4 Amp (Experimental); (b) Efficiency and nominal ripple variation with I_{ref} and θ_{cond} for $I_{dc(avg)}$=0.24 Amp (Experimental). 62

Figure 3.9: (a) Efficiency variation with θ_{off} angles for different reference currents (Experimental); (b) Nominal ripple variation with θ_{off} angles for different reference currents (Experimental). 63

Figure 3.10: Efficiency variation with nominal ripple. 64

Figure 3.11: Block diagram of the two-loop controller. 65

Figure 3.12: Turn-off angle search controller algorithm. 66

Figure 3.13: (a) Change in $I_{dc(avg)}$, I_{ref} and θ_{cond} with time for $I_{dc(command)}$=0.5 A (simulation); (b) Change in nominal ripple and θ_{off} for $I_{dc(command)}$=0.5 A (simulation). 68

Figure 3.14: (a) The step response of $I_{dc(avg)}$ with change in $I_{dc(command)}$ from 0 to 0.4A at 0.2A/div and 1.00 sec/div. (b) Phase current and dc-link current when $I_{dc(command)}$=0.4A (at 0.2A/div and 4.00 msec/div). 69

Figure 3.15: (a) θ_{off} settling when $I_{dc(command)}$=0.4A. (b) Nominal ripple settling when $I_{dc(command)}$=0.4A. 70

Figure 3.16: Comparison of turn-off angles obtained from offline optimization with the closed-loop turn-off angle controller algorithm tested at 1000 r/min. 71

Figure 3.17: Comparison of turn-off angles obtained from offline optimization with the closed-loop turn-off angle controller algorithm tested at 700 rpm. 72

Figure 3.18: Comparison of turn-off angles obtained from offline optimization with the closed-loop turn-off angle controller algorithm tested at 1200 rpm. 72

Figure 4.1: Flowchart of the overall design methodology of FSPM. 76

Figure 4.2: Accommodating teeth, coil and magnet within one stator pole pitch. 82

Figure 4.3: Cross section view of the FSPM geometry in FEA..... 84

Figure 4.4: Geometry of the designed machine with FE Mesh 85

Figure 4.5: Geometric parameters of the FSPM designed (a) whole machine, (b) closer view of one stator and one rotor pole. 87

Figure 4.6: Coil connection of the 12/10 FSPM (a) Face region marked with associated coil. (b) Three-phase, Y-connected armature coils circuit..... 89

Figure 4.7: Typical Flux-MMF and B-H characteristics of a permanent magnet material. ... 90

Figure 4.8: Simplified magnetic equivalent circuit for one pole of PM machine..... 91

Figure 4.9: B/H Curve of Allen-Bradley/TDK magnet material FB4B [101]..... 93

Figure 4.10: Flux density distribution at no-load using color density plot (a) phase-A aligned, (b) phase-A unaligned..... 99

Figure 4.11: Flux density distribution at loaded condition using color density plot (a) phase-A aligned, (b) phase-A unaligned..... 99

Figure 4.12: Air gap flux density distribution of the designed FSPM..... 100

Figure 4.13: Phase-A flux linkage and back-EMF of the designed machine 101

Figure 4.14: Loss data of the core material at 200 Hz and 400 Hz..... 103

Figure 4.15: Different loss components using the co-efficients calculated..... 104

Figure 4.16: Phase current and terminal voltage of the FSPM from FEA simulation..... 105

Figure 4.17: Different power components of the designed FSPM from FEA: (a) Input, (b) Output torque (c) Output power, (d) Copper loss. 106

Figure 4.18: Output electromagnetic torque of the FSPM at rated (3.83 Amp) RMS current. 107

Figure 4.19: (a) A closer view of the output torque in 6 degree mechanical, (b) Cogging torque in one period 108

Figure 4.20: Demagnetization curve of TDK FB9 series Ferrite magnet used [102]..... 110

Figure 4.21: Flux density distribution in phase-A magnets at aligned and unaligned position 111

Figure 4.22: Vector Diagram of a FSPM when $i_d \neq 0$ 113

Figure 4.23: Vector diagram when $i_d = 0$..... 113

Figure 4.24: Vector diagram illustrating the effect of magnitude of negative *d*-axis current on power factor angle..... 114

Figure 4.25: Vector diagram illustrating the effect of magnet flux linkage on power factor angle..... 114

Figure 4.26: FEA Model of the designed SRM 116

Figure 4.27: Flux density map when the stator and rotor poles are (a) aligned and (b) unaligned at phase-A..... 117

Figure 4.28: Phase currents and torque from the designed SRM 118

Figure 4.29: FEA Model of the surface mounted PMSM..... 119

Figure 4.30: Flux density map of the PMSM at (a) no-load, and (b) rated load..... 120

Figure 4.31: Back EMF, rated phase currents and torque of the designed Surface Mount PMSM at 1800 RPM..... 122

Figure 4.32: Dimensions of NEMA 365T frame 124

Figure 4.33: 3D view of the base (0.5kW) design and scaled up (50kW) design of FSPM. 125

Figure 4.34: Winding connection of the 50kW FSPM 127

Figure 4.35: Flux density distribution of the 50 kW FSPM using color density plot (a) no-load, phase-A aligned, (b) no-load, phase-A unaligned, (c) loaded, phase-A aligned, (d) loaded, phase-A unaligned..... 128

Figure 4.36: No-load performance parameters of the 50kW FSPM (a) Airgap flux density, (b) Coil and phase-A flux linkage, (c) Phase A Back EMF, (d) Spectrum of Back EMF 129

Figure 4.37: Performance of the 50 kW FSPM under loaded condition, (a) Torque, (b) Torque vs. Current 130

Figure 4.38: Flux density distribution of the FSPM with NdFeB using color density plot (a) no-load, phase-A aligned, (b) no-load, phase-A unaligned, (c) loaded, phase-A aligned, (d) loaded, phase-A unaligned..... 132

Figure 4.39: No-load performance parameters of FSPM with NdFeB (a) Airgap flux density, (b) Coil and phase-A flux linkage, (c) Phase A Back EMF, (d) Spectrum of Back EMF.... 133

Figure 4.40: Performance of the FSPM with NdFeB under loaded condition, (a) Torque, (b) Torque vs. Current 134

Figure 5.1: Cross section of three different FSPM topologies (a) Conventional 12/10, (b) E-core 6/11, (c) C-core 6/13 138

Figure 5.2: Back-EMF of 1 kW FSPMs at 400 rpm 141

Figure 5.3: Back-EMF harmonics of the 1kW FSPM at 400 rpm. 141

Figure 5.4: Electromagnetic torque of different FSPMs with rms current density=6 A/mm^2 141

Figure 5.5: Dimensional design parameters for a stator and rotor pole. 143

Figure 5.6: Stator and rotor shapes with magnet. 144

Figure 5.7: FEM plot of flux density distribution for the 12/10 FSPM at rated condition... 145

Figure 5.8: Simplified flux paths between one stator tooth and rotor pole when they are not overlapping (a) without flange, (b) with flange. 146

Figure 5.9: Different rotor pole width scenario with respect to stator tooth width (a) Rotor pole width=Stator tooth width, (b) Rotor pole width = 1.4*Stator tooth width, (c) Rotor pole width=1.4*Stator tooth width with flange 149

Figure 5.10: FEA schematic of FSPM with rotor flange. 151

Figure 5.11: Topology of the FSPM with rotor flange. 151

Figure 5.12: Flow chart of cogging torque minimization method 152

Figure 5.13: Variation in cogging torque with flange width for the machine of outer radius=45 mm. 153

Figure 5.14: Cogging torque variation with rotor flange width for the machine with outer radius=67.5 mm and same L_{stk}. 153

Figure 5.15: Cogging torque variation with rotor flange width for the machine with outer radius=90 mm and same L_{stk}. 153

Figure 5.16: Cogging torque magnitude variation with rotor flange width for FSPM of three different sizes. 154

Figure 5.17: Variation of optimum flange width with stator tooth width. 155

Figure 5.18: Variation in back-EMF at 400 rpm with the width of rotor 156

Figure 5.19: Variation in average electromagnetic torque at 400 rpm and J=5A/mm2 with the width of rotor flange. 157

Figure 5.20: Torque separation in 1kW, 12/10 FSPM, (a) without flange, (b) with flange . 159

Figure 5.21: Eccentricity effect on cogging torque (a) without flange, (b) with flange 161

Figure 5.22: Rotor flange in minimizing cogging torque in healthy and eccentric FSPM ... 162

Figure 5.23: Cogging torque in E-core, 6/11 FSPM (a) Cogging torque as flange width is varied, (b) Variation in cogging torque magnitude with flange width. 163

Figure 5.24: Cogging torque in C-core, 6/13 FSPM (a) Cogging torque as flange width is varied, (b) Variation in cogging torque magnitude with flange width. 164

Figure 6.1: Different circumferential mode shapes 169

Figure 6.2: Cross-section of a 3-phase, 12/10 FSPM showing parameters 171

Figure 6.3: Graphical representation of source of noise and vibration in electric motor with preferred mitigation approach 174

Figure 6.4: Schematic of part of the FSPM showing design parameters affecting mode frequency, noise and vibration 176

Figure 6.5: Effect of varying α_s on second order mode frequency and available slot area .. 177

Figure 6.6: Circumferential Mode Shapes of the stator for (a) m=2, base design, (b) m=2, Low-Noise FSPM 179

Figure 6.7: Circumferential deflection and noise levels vs. f_{exc} for (a) base design, and (b) low-noise design at 1800 RPM 180

Figure 6.8: Peak circumferential deformation from static structural FEA simulation, (a) base design, (b) Low-Noise design 181

Figure 6.9: Circumferential deflection and noise levels vs. f_{exc} for (a) base design at 3276 rpm, and (b) low-noise design at 6588 RPM 182

Figure 6.10: Circumferential deflection and noise levels vs. f_{exc} for (a) base design at 1638 rpm, and (b) low-noise design at 3294 RPM 183

Figure 6.11: Circumferential deflection and noise levels vs. fexc for (a) base design at 1092 rpm, and (b) low-noise design at 2196 RPM 183

Figure 6.12: Effect of changing back iron thickness on cogging torque 184

Figure 6.13: Effect of increasing back iron thickness on output torque for the same slot current density 185

Figure 6.14: (a) The static structural simulation setup showing forces applied on the 24 stator tooth tips, (b) Force on one stator tooth obtained from electromagnetic FEA 186

Figure 6.15: Exaggerated stator deformation at one instance within one electric cycle 187

Figure 6.16: Magnitude of stator deformation, showing minimum and maximum 187

Figure 7.1: FEA Model of the final design of the prototype 192

Figure 7.2: *d*- and *q*-axis flux linkage with corresponding axis currents, with ϕ_m and I_0 194

Figure 7.3: Vector diagram of FSPM with non-zero i_q and i_d 195

Figure 7.4: Correlation between and current and magnetic flux linkage, from FEA model and using the co-efficients for curve-fitting 196

Figure 7.5: Block diagram representation of FSPM drive with stator field oriented control. 198

Figure 7.6: Controller response when the command current changes from 4.7 Amp (rated) to 2.35 Amp (50% rated) to 3.53 Amp (75% rated) 200

Figure 7.7: Timing of phase current excitation for motor and generator operation using FSPM machine based on rotor angular position. 201

Figure 7.8: Controller response when the command current changes from -4.7 Amp (rated) to -2.35 Amp (50% rated) to -3.53 Amp (75% rated) in generator mode (a) Iq, (b) Torque, (c) Phase Currents 202

Figure 7.9: FSPM Generator Performance at 1800 RPM (a)Mechanical Input Power, (b)Electrical Output Power, (c)DC-Link Current Generated..... 203

Figure 7.10: FSPM Generator Performance at 1800 RPM (a) DC-link current variation with input torque and power, (b) Efficiency variation with input power 204

Figure 7.11: FSPM Generator Performance at 1000 RPM (a) DC-link current variation with input torque and power, (b) Efficiency variation with input power 205

Figure 7.12: FSPM Generator Performance at 500 RPM (a) DC-link current variation with input torque and power, (b) Efficiency variation with input power 206

Figure 7.13: Photographs of the prototype built (a) different parts, (b) stator with winding, (c) rotor, (d) complete motor after assembling the stator and rotor into the frame, (e) TI High Voltage Motor Control Kit..... 207

Figure 7.14: Experimental dyno setup of the FSPM drive system (a) photograph, (b) block diagram 208

Figure 7.15: Measured and FEA calculated back-EMF magnitude against speed. 209

Figure 7.16: Spectrum analysis of the measured and FEA calculated back-EMF by FFT for different speeds, (a) 500 RPM, (b) 1000 RPM, (c) 1800 RPM 209

Figure 7.17: Phase current and torque from (a) experiment, and (b) simulation at 100 RPM for different current commands. 211

Figure 7.18: Experimental results from the prototype and their comparison with FEA at 1800 RPM (a) Torque vs. i_q, (b) Input power vs. i_q, (c) Output power vs. i_q, (d)Efficiency vs. i_q, and (e) Power factor vs. i_q, (f) Esimated torque and Iq*Torque Constant vs. i_q..... 213

Figure 7.19: Sample data from power analyzer for a command of 1.4 Amps at 1800 RPM 214

Figure 7.20: Experimental results from the prototype and their comparison with FEA at 1000 RPM (a) Torque vs. i_q, (b)Input power vs. i_q, (c)Efficiency vs. i_q, and (d) Power factor vs. i_q 215

Figure 7.21: Experimental results from the prototype and their comparison with FEA at 500 RPM (a) Torque vs. i_q, (b)Input power vs. i_q, (c)Efficiency vs. i_q, and (d) Power factor vs. i_q 216

Figure 7.22: Steady state heat run results from the prototype (a) Measured temperatures at three key locations during a heat run under 0.5kW, 1800 RPM continuous operation, (b) Steady state temperature, (c) Comparison of temperature rise in the three regions measured 218

Chapter 1

Introduction

The motivation behind the research and development of innovative types of electric machines in the recent years have primarily been driven by economic and environmental factors. While the AC machines, such as synchronous and induction machines have been widely accepted to work well for most of the renewable energy systems where electromechanical energy conversion is required, why is there continued research activities on electric machines in the recent past half century? The answer is the search for novel machine technologies to efficiently and effectively harness renewable energy [1]–[4] as well as to keep up with the new standardization and global regulations [5]–[8]. As the high-flux density permanent magnets based on rare earth elements such as neodymium (Nd) emerged in the 1980's [9]–[12], permanent magnet-based electric machines [13], [14] had a clear performance and cost advantage over induction machines and reluctance machines when weight and size factors are considered such as in hybrid electric vehicles and wind turbines. However, the supply and high price of rare earth permanent magnet (PM) materials may obscure the advantages of such machines. Between 2007-2012, there has been nearly a 10-fold increase [15] in price and the imposition of export limits of rare earth magnets by the major producing country China. During this period, an additional requirement or trend of reducing the use of rare earth magnet [16]–[18]; designing electrical machines that are 'rare earth free' or employ 'non-rare earth magnets' has come to practice. Although the price of rare earth PM material slumped to some extent past 2012, the need to remove dependency on these materials is of the utmost importance.

While recognizing the influence of these constraints and requirements, it must also be acknowledged that the notable developments shown in the appearance of innovative electrical machines during this period are due to the corresponding rapid developments in power semiconductor, integrated circuit devices [19]–[27], computer simulation capability including tools for Finite Element Analysis (FEA) and numerical analysis [28]–[30]. Before this period, the configurations that define the DC commutator machine, AC induction and AC synchronous machine were the dominant types. Now, the electric machines types have been augmented by the entry of the AC synchronous reluctance machine (SynRM), the switched reluctance machine (SRM) and various types of brushless AC and DC permanent magnet machines.

The SRM and permanent magnet synchronous machine (PMSM) are the traditional electric machines used in many industries and applications mainly due to their advantages in maintenance and cost. There is a recent trend to search for alternatives that are efficient both in terms of power and volume. In many applications, it is an important issue to keep balance between these two. Flux switching permanent magnet (FSPM) machine realizes many combined advantages of reluctance machines (i.e. SRM) and PM machines (i.e. PMSM, BLDC) into one topology. It displays the robustness and simplicity of SRM, power density of PMSM, as well as the advantage of using low-cost sensorless electronic controller and fault tolerance and robustness against output short-circuit and overload.

The emergence of the flux switching machine (FSM) is as recent as just over a decade ago, exploiting the advances in drives technology for feasibility of operation and exhibiting high specific output and economy of construction. Yet there are few drawbacks or issues where there are room for improvement in the conventional FSPM machine technology. This thesis contributes in many of those, namely cogging torque minimization, noise and vibration

reduction, and modeling of FSPM considering saturation and mutual coupling. It describes the modeling, analysis, and control of SRM and FSPM, with an emphasis on current ripple minimization in Switched Reluctance Generator (SRG), design of an FSPM for cogging torque minimization and low-noise performance. This chapter concludes with a brief introduction to SRM and FSPM, an outline of the thesis structure and original contributions.

1.1 Switched Reluctance Machine (SRM)

The SRM is comparatively new among the brushless machines family, although its concept was developed more than 150 years ago. The torque in a SRM is produced by the tendency of its rotor to move to a position where the inductance of the excited winding is maximized. SRM technology was not widely used until recently due to the absence of suitable semiconductor switches for controlling the machine. In the late 1960's, the control of the SRM became much easier creating a renewed interest in SRM drives due to:

1. The availability and improvement of cost-effective high power fast semiconductor switches;

2. Heavy computational power at an affordable price to use extremely convenient finite element method for machine design;

3. Extensive use of microcontrollers and integrated circuits that facilitated high speed signal processing and control of electric machines.

Exploiting these developments, the fundamental design, and operating principles of the machine was established in 1970s [31]. The cross section of a modern, three-phase SRM with 12 stator poles and 8 rotor poles is shown in Figure 1.1.

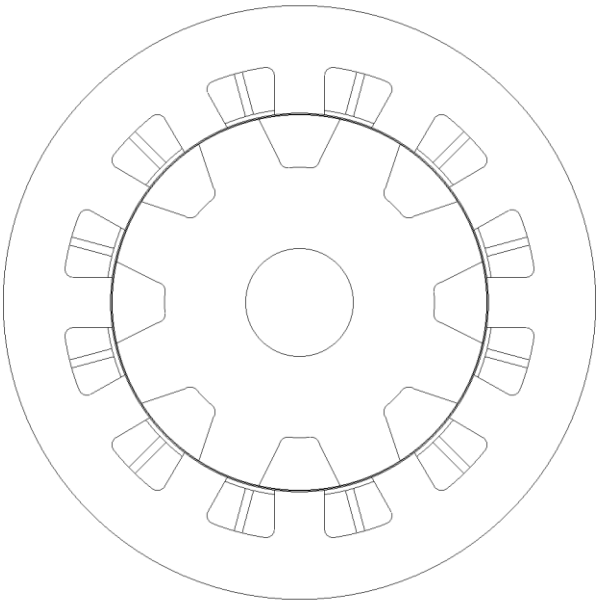

Figure 1.1: A three-phase, 12/8 SRM.

The reason behind the growing interest in SR machines technology is best understood from a summary of their numerous advantages and a few disadvantages:

Advantages of SRM drive

1. Simple, robust, and rugged structure which leads to its high reliability.
2. Concentrated stator winding which is easy to repair.
3. No winding in rotor; hence low inertia and quicker dynamic response.
4. Most losses occur in the stator which is easily cooled.
5. The rotor losses are very small; hence the rotor cooling problems vanish.
6. The motor and the converter are inherently fault tolerant.
7. High starting torque without the problem of inrush current.
8. Four-quadrant operation is possible.

9. No winding or PM in rotor; therefore, ideal for high speed operation.

10. The torque production is independent of the polarity of the phase current; therefore, a simplified power converter can be used with a reduced number of power semiconductor switches.

Disadvantages of SRM drive

1. Inherent torque ripple and acoustic noise due to doubly salient structure.

2. Converter requires high kVA.

3. Same excitation penalty as IM, and cannot equal the efficiency or power density of the PM motor in small sizes.

4. Position information and current control: incurs complexity, cost and size concern to SRM drive system.

In summary, SRM drives have the potential to be a less expensive alternative to other types of electrical motor drives. However, the requirement of rotor position sensor, greater torque pulsation [32]–[34] and acoustic noise [35]–[37] are the major drawbacks of SRM drive and could limit the use of SRM in some applications.

1.1.1 Applications of SRM Drives

Due to the ability of operation in high temperature, simple construction, absence of PM, rotor conductor or brushes, SRM drive applications include (but are not limited to):

1. Electric vehicles: ordinary cars and trucks, electrically powered bikes and scooters, industrial utility vehicles, station cars and wheel chairs [38];

2. Aerospace: where a smaller weight is essential [39], [40];

3. Household appliances: washing machines and vacuum cleaners [41];

4. Robotics: use as direct drive actuators [34];

5. Variable speed and servo-type applications: Starter/generator systems for gas turbine applications [31], [42].

1.2 Stator PM Machine Technology

In general, stator PM machines have all excitation sources on the stator, requiring simpler cooling method, leaving the rotor to carry neither windings nor magnets; and essentially getting rid of the brush gear and slip rings. There are several varieties of stator-PM machines, through which the Flux Switching technology evolved gradually, discussed in detail in Chapter 2.

FSPMs are gradually gaining increasing interest in high performance drives due to their numerous advantages over other brushless machines [43], [44]. However, there is room for improvement in cogging torque and noise/vibration performance through geometric modification in the design stage of the FSPM. So far most of the research have been conducted using rare earth magnet. Using non-rare earth magnet for FSPM is another interesting direction as the FSPM already shows promising torque density as compared to conventional PM machines. Overall, these are the obvious direction to reduce cost as well as improve electromagnetic and structural performance.

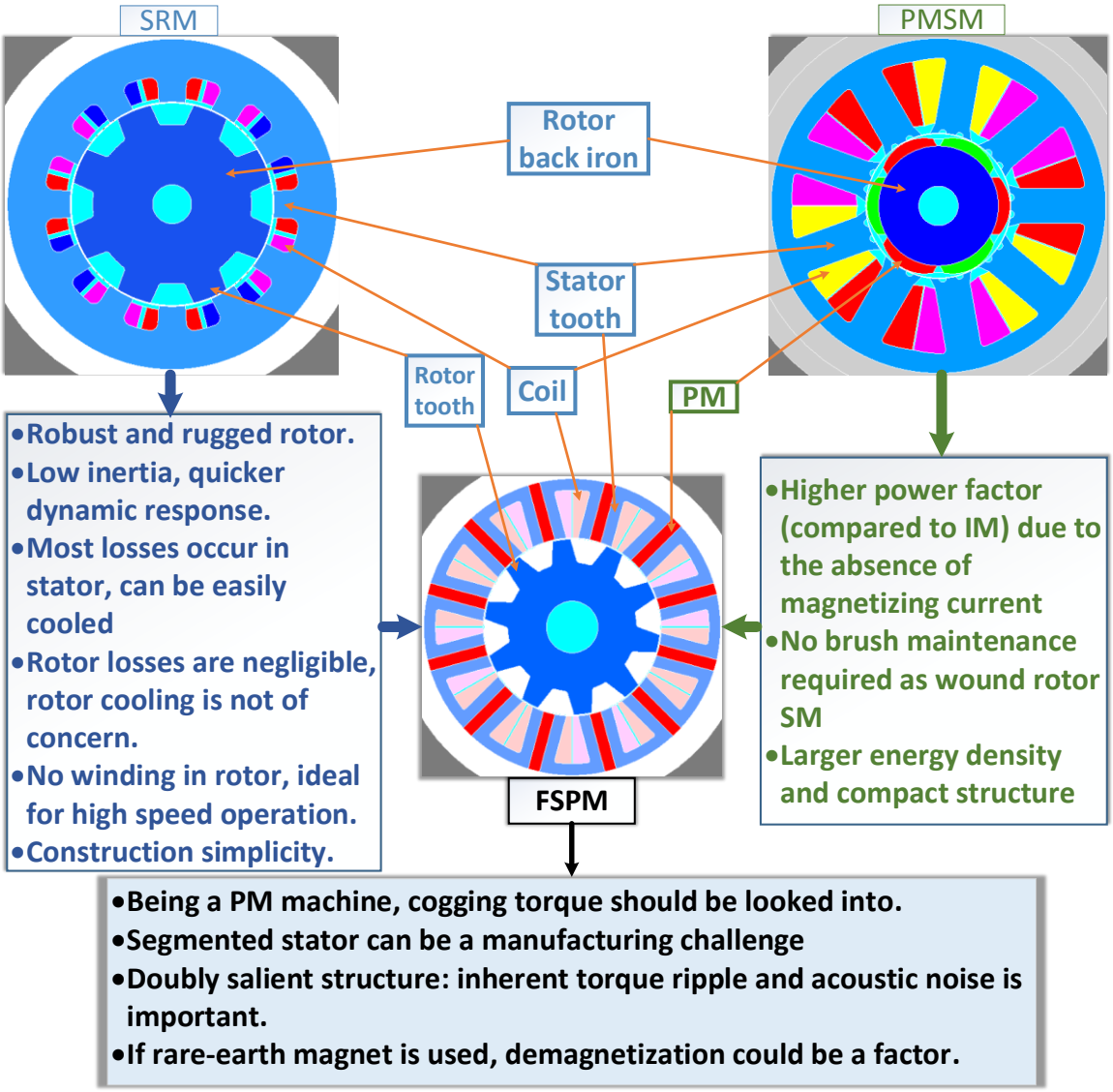

Figure 1.2: Flux Switching PM Machines: Combining SRM and PMSM features.

As an introductory overview, it can be said that the FSPM, employing segmental stators in three phase configuration, combines already well-known configurations of stator and rotor topologies to combine the positive attributes of SR and PM machines into one machine. A graphical representation of this phenomena is shown in Figure 1.2. The rotor structure is similar to that of SR machines inheriting the associated advantages in terms of robustness and construction simplicity. In terms of operation, FSPM is an AC machine having a sinusoidally varying permanent-magnet flux-linking each phase winding with rotor rotation. It can thus be

sinusoidally driven and have the associated advantages of sinusoidally excited machines including a smooth output torque and constant input power in steady-state balanced operation. The output torque can be dynamically controlled using vector-control algorithms. However, there are some forms of sacrifice or disadvantages, which were also taken into account and considered for performance improvement during the design stage.

1.2.1 Prospect and Applications of FSPM drive:

As the machine combines many well-known advantages and features from both SRM and PMSM, presumably, it can be used for a wide range of application traditionally suitable for both kind of machines. They include (but not limited to)

1. Electric and Plug-in hybrid vehicles (Can achieve competitive power density as rare earth PM machines).
2. Fault tolerant applications such as in aerospace. (Competitive with PMSM, higher power density than SRM).
3. Downhole applications where continuous operating temperature is as high as 150° C.
4. High speed applications (DC Alternator).
5. Variable speed and servo type applications (an alternative to BLDC motor).
6. Gearless drive applications.

Details on flux switching machines, including its history and operating principle are discussed in Chapter 2.

1.3 Research Motivation

With growing interest in SR machines, extensive research has been carried out on its design and control. Because of its feasibility in four quadrant operation, it is a very lucrative candidate for applications where both motoring and generating is required at various speed range. Torque ripple and current ripple are the key issues during SRM operations for motoring and generating, respectively. They can be addressed by both manipulating the design or innovative control algorithm and techniques.

Researchers have been trying to minimize these key demerits for both motoring and generating controls of SRM [45]–[47] . Several techniques have been proposed for maximizing the efficiency when SRM is used as a generator by controlling the commutation angles. The attractive advantages of SRM can be effectively utilized in many applications with improvements in the generated current ripple. This thesis presents a new control technique of SRM as a generator based on geometry based analytical model. The system operation has been verified experimentally using a 1kW SRM drive setup. A detailed analysis has been performed on the DC-link current ripples affecting the overall system performance, efficiency, and battery life during generation using SRM. It has also been shown that minimizing current ripple while generating indirectly maximizes the efficiency of the whole SRM drive system.

Efficient and optimum SRG control requires carefully fine-tuned commutation angles. The complexity increases at low speed as compared to high speed operation. At high speeds, phase currents go into single pulse mode where no hysteresis control is required. At low speeds, phase current is controlled by hysteresis. Therefore, to achieve ripple minimization or efficiency maximization for operation where wide speed range of operation is prerequisite, a two loop controller which controls all the commutation angles along with the reference current

is essential.

A control algorithm has been developed that dynamically varies the commutation angles for the machine operation based on the required and commanded DC-link current level along with continuously monitoring the ripple in DC-link current. The algorithm is implemented and tested at different operating speeds where hysteresis control is applicable. This control concept can generally be applied to any SRM for all speed ranges.

It is today's challenge to come up with new and innovative machine topologies by combining already existing knowledge in this field of research. Flux reversal or flux switching is another concept of energy conversion which was first proposed back in 1950's and emerged recently exploiting the advances in power electronics, microcontrollers, and high fidelity finite element analysis (FEA). Among the existing machine structures, PM machines, namely Permanent Magnet Synchronous Machine (PMSM), Interior PM (IPM) and surface mounted PM-BLDC machines offer the highest power density using rare earth magnets. However, Flux Switching machine topologies can achieve torque and power density very close to that of today's rare earth PM machine topologies with non-rare earth magnets because of their flux focusing structure.

Unlike any electric machine technology, there are areas that can be improved in terms of performance and efficiency. FSPMs have naturally low torque ripple and the main source of that is the cogging due to the presence of flux focusing magnets. FSPM can be controlled using standard *dq* control. Therefore, it would be helpful if the cogging torque can be minimized during the design stage. Among the existing techniques to achieve that, skewing the rotor poses difficulty in manufacturing. One of the motivations for this research is to develop a novel yet simple method of minimizing cogging torque from machine design perspective. Consequently,

if a design rule can be established that can be applied to FSPM design in general, that helps in further adopting such machine topologies in high performance applications where low torque ripple is a prerequisite.

Because of the structure, the most feasible three-phase topology is 12/10, but this poses another challenge of low second order mode frequency which will cause high noise and vibration. The segmented stator structure also needs to be looked into for analytically predicting the mode frequencies, and hence, noise and vibration. Unlike cogging torque, it is possible to minimize the noise and vibration by tweaking the geometrical design of the machine to verify it using FEA. Another motivation is to develop a geometric pole shaping and eventually to establish a design rule to minimize noise and vibration in FSPM machine. Eventually, a comprehensive design methodology is to be developed so as to facilitate FSPM design for high performance, low torque ripple, low noise applications.

Because of the nature of operation, FSPM can be controlled in a similar technique as done for IPM and Brushless DC machines. However, precise control requires fine modeling of the machine. Existing models do not consider the effects of saturation and mutual coupling. This research introduces a model of FSPM including the saturation and cross-coupling effect. The model is to be used to develop and implement control of FSPM machines. The motivation of this research is to address all the issues in FSPM operation and find solution from design and control perspective so that it can be applied to FSPM design for low torque ripple, low noise applications in general

1.4 Research Objective and Methodology

The primary objective of this dissertation is to evaluate the recent trends and goals in electric machines and drives industry to design and develop controllers and high performance doubly salient, radial flux machines without using rare earth PM materials. In this research, an understanding of cogging torque, noise, and vibrations in FSPM designs have been developed in order to facilitate the design of a low cogging torque, low noise FSPM with non-rare earth magnet. In addition, the issue of low efficiency for SRG operation is also addressed by developing a novel two loop controller for a wide speed range.

SRM's are attractive for many applications where energy conversion is required in both ways. However, there are two shortcomings in the existing literature, (i) maximizing efficiency is not obtained in real time operation because it was not correlated to any physical parameter, and (ii) methods for control parameter optimization for SRG have only been addressed at higher speed [45], [47], [48], [49]. Generally, SRG control is more complex at lower speed than at higher speed because at lower speed when current goes into hysteresis mode, there are more parameters to control than at higher speed, single pulse mode. This research intends to fill in these gaps for SRG operation. A correlation was established between SRG system efficiency and generated current ripple through theoretical analysis and results obtained from simulation. Extensive set of data for a wide range of speeds and currents were obtained and analyzed for this. Based on the collected data, a novel, two loop controller was developed and implemented that minimizes DC-link current ripple and maximizes efficiency at all speeds. The control algorithm was implemented and tested successfully on a 1kW SRG drive system.

The next research objective of this dissertation is to develop an understanding of torque ripple and vibrations in various FSPM designs in order to facilitate the design of a low torque

ripple, low noise FSPM. A comprehensive design methodology is to be developed that can be used to design FSPM of any size and power level. The mechanism of flux switching using PM to produce three phase configuration was characterized. All the possible geometric parameters were examined to design a geometrically optimized FSPM within a set of constraints. The design is made highly scalable so as to be applied to any size and power level.

For cogging torque minimization, several FSPM configurations were assessed and the factors and geometric parameters that affect cogging torque the most was identified. Based on this, a unique pole shaping design was developed to minimize the cogging torque. A design rule that can be applicable to any FSPM configuration has been developed through theoretical analysis founded on a permeance based model. A detailed analysis of cogging torque has been done in relation to reluctance torque, torque ripple and rotor eccentricity.

The existing methods of calculating stator mode frequencies do not consider segmented stator structure. One of the important design objectives is to address the issues of noise and vibration FSPM to develop a low noise design. An analytical model was developed to predict mode frequencies of a segmented structure like FSPM. Based on that, a pole shaping was proposed that would minimize the noise due to the vibration for second order mode frequency at all operating speeds. The contributors to acoustic noise and vibration have been analyzed to develop a low-noise machine. A static structural FEA model has been developed using magnetic radial forces obtained from electromagnetic FEA to predict the stator tooth deformation accurately. The techniques for minimization of cogging torque and acoustic noise are combined with the basic design to present a comprehensive methodology for FSPM design.

The next step is to materialize the design into a physical prototype to be tested. An FSPM prototype was built based on the design developed. Modeling the machine parameters are

extremely important to develop the motor control algorithm. A novel method of modeling the FSPM based on FEA results incorporating saturation and mutual coupling has been developed. Machine parameters obtained from this model have been used to control the machine operation. This is particularly helpful in analyzing the performance of the machine at different operating conditions with different control methods.

Stator field oriented vector control was implemented on the FSPM based on the machine parameters identified. A high fidelity, dynamic co-simulation model was used to accurately model and predict the response of the motor and the controller. Upon obtaining satisfactory performance, the controller was also implemented in the experimental hardware.

The final step of this research is to conduct the experiments to verify the performance of the motor designed and constructed. Standard laboratory testing at no-load and loaded conditions have been performed and verified with analytical and FEA based results. The motor was loaded to up to 200% rated current, and was tested at a range of operating speeds. A steady state heat-run test was also performed to examine the steady state thermal capabilities of the motor and losses and temperature rise at different parts at different operating conditions.

1.5 Dissertation Organization

Chapter 1 presents a general introduction to the two types of electric machines in consideration, their features followed by advantages and disadvantages and applications. It describes how FSPM can combine features and advantages from the existing popular technologies (SR and PM) into one machine. The main objective, motivation and approach of the dissertation are also presented.

Chapter 2 provides detailed background of SRM and FSPM technologies. The construction, operating principle, control and converter topologies of SRM is discussed. As FSPM is comparatively new, the evolution of FSPM has been presented.

Chapter 3 presents the design of an optimum, two loop controller for SR generators that maximizes the efficiency of the system for a wide speed range. At low speed, the reference current, along with turn on and turn off angles need to be controlled precisely to minimize the current ripple. A theoretical analysis has been provided to show the effect of current ripple on system efficiency. A geometry based model of SRM has been used to generate large set of data to validate the analysis. A two-loop controller has been developed in simulation, and then implemented experimentally. Finally a generalized theory is proposed to validate the functionality of the SRG controller for a wide speed range.

Chapter 4 covers the comprehensive design methodology of FSPM. The topological configurations for three-phase arrangements are discussed. A set of constraints have been set to facilitate manufacturing of a prototype and laboratory testing. Based on the constraints, a complete, exhaustive and comprehensive design is performed. Existing theory and techniques have been used in this design to start with. Towards the end, the performance of the machine is predicted through FE analysis and existing and adopted rules on the design of electromagnetic systems.

Chapter 5 presents a novel pole shaping method to minimize cogging torque in FSPM. The sources of cogging torque have been discussed and an analytical verification of this pole shaping is also covered. Detailed FEA based parametric sweep has been performed to develop a generalized design rule that can be applicable to any FSPM topology and structure. The effect of this poles shaping on reluctance torque and rotor eccentricity is also analyzed.

The discussions on the stator vibration, structural damping and circumferential mode shapes of stator vibrations are presented in Chapter 6. A method to predict the mode frequencies for such structures has been developed in this chapter. The key parameters that have affects the stator vibration and noise have been identified. Based on this, another pole shaping on the stator was proposed and applied for a low-noise design. The mode frequencies of the base design and the low-noise design have been verified using the proposed model and structural FEA. To the end, a static structural FEA simulation (including magnetic radial force calculated from electromagnetic FEA) has been performed to show that the stator deformation of the final design is within the acceptable limit.

Chapter 7 presents the description of the experimental setup with the prototype built. An advanced modeling technique was used to identify the motor parameters including the effect of saturation and mutual coupling. Vector control was implemented using the machine parameters identified, both in simulation and in the experimental hardware. The general performance parameters of the prototype was tested at rated speed and at other speeds, for up to 200% of rated current. In addition, a steady state heat run test was also performed to examine the temperature rise at different parts of the machine.

A relatively new and an older motor topology have been tested through this dissertation via extensive simulation and experimental work. In doing so, notable novel contributions have been made in the areas of design and control of SRM and FSPM. Yet, there still exist the scope for further research and improvement. A summary of the research accomplishments achieved through this dissertation and scope of future works are discussed in Chapter 8.

Chapter 2

Switched Reluctance and Flux Switching Machines

This chapter presents the basic operating principal of the two types of electric machines in consideration, along with the evolution and background of FSPM. The concept of SR machines has been around since the mid-18th century. The machine concept was established by Davidson as early as in 1838 and it was used to propel a locomotive on the Glasgow-Edinburgh railway [31] at that time. With the development of fast-acting power semiconductor switches in the 1970's, SR machines experienced growing interest and showed great potential for various applications and research. On the other hand, among the popular PM machine topologies where the magnets are located in the rotor, poor cooling and limitation in high speed operation are the issues which limit their performance in many applications. Researchers in the field of electric machine and motor drives are always striving to come up with new and unique topologies that offer advantages over various established topologies into one. To decrease total system cost, increasing power density of the electric machine is important. In the stator PM machine (where permanent magnets are located on the stator), the temperature rise in the PMs is less severe and can be controlled in a much easier way. The rotor of these machines is very simple and robust like SRM, and therefore, can be operated at a very high speed. With the idea of stator-PM and SRM like simple, salient rotor in mind, a few stator PM topologies have been proposed, and the FSPM topology evolved gradually.

2.1 Switched Reluctance Machines

Among all the existing machines, SRM arguably has the simplest structure. It is a doubly salient, singly excited machine with unequal number of stator and rotor poles. SRM uses reluctance torque production technique to convert electrical energy to mechanical energy. For a continuous torque production, as the stator poles are energized, the most adjacent rotor pole is attracted towards the stator pole carrying armature current to attain minimum reluctance of the corresponding magnetic path. Obviously, the unequal stator-rotor pole combination is to ensure a continuous torque production, so that the torque is never zero (i.e., all rotor poles are aligned with stator poles and stalled). The stator and rotor structures are made of magnetic steel laminations. Only the stator has windings, which are excited from an external DC source through a power converter. The windings are placed around the stator poles to configure the independent phases. Windings on diametrically opposite poles are connected either in series or in parallel to make one phase of the machine.

The SRMs can be of various numbers of stator and rotor pole combinations which gives rise to different phase configurations. For a 3-phase machine, the basic structure has 6 stator poles and 4 rotor poles. Based on this 6/4 structure, the pole count can be increased to 12/8, 18/12 structure, which is known as 2-repitition and 3-repitition version of the basic. Similarly, 8/6 (basic), 16/12 (2-repitition) and 24/16 (3-repitition) are some possible structures for four-phase SRM. The choice of the number of phases in SRM is a compromise between low torque ripple and cost of power electronic converter [31].

2.1.1 Operating Principle of SRM

The principle of operation of a SRM is based on the fact that in any electromagnetic system the stable equilibrium is the position where the reluctance of the magnetic path is minimum. Unlike any rotating electric machine, the stator pole and rotor pole are separated by an airgap in SRM. When a stator pole is excited, the closest rotor pole is attracted towards the stator pole so that the reluctance of the magnetic path between the stator and the rotor is minimum, resulting in torque production. When a pair of rotor poles become aligned with a pair of stator poles, an adjacent pair of stator poles is excited to bring a second pair of rotor poles into alignment. The successive movement of a 3-phase, 12/8 SRM is shown in Figure 2.1. The synchronization of the stator phase excitation is readily accomplished with rotor position feedback.

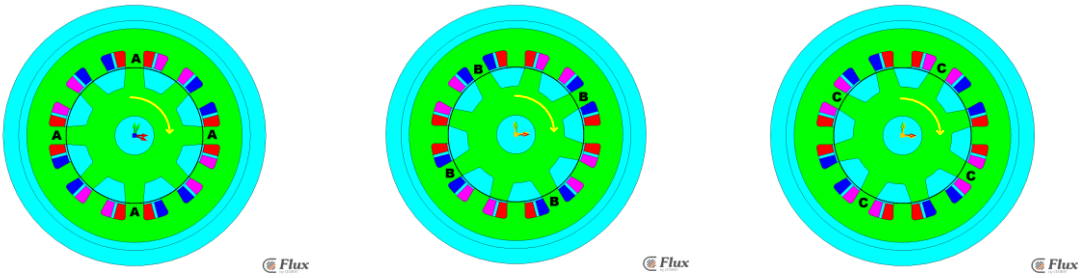

A: Aligned
B: Unaligned and about to align next for clockwise rotation
C: Unaligned

A: Unaligned
B: Aligned
C: Unaligned and about to align next for clockwise rotation

A: Unaligned and about to align next for clockwise rotation
B: Unaligned
C: Aligned

Figure 2.1: Operating Principle of SRM.

The aligned position of any phase is defined to be the situation when the stator and rotor poles of the phase are perfectly aligned with each other attaining the minimum reluctance position. The unsaturated phase inductance, L_a is maximum in this position. The phase

inductance decreases gradually as the rotor poles move away from the aligned position in either direction. When the rotor poles are symmetrically misaligned with the stator poles of a phase, the position is said to be unaligned position. The phase inductance is minimum in this position, and is called the unaligned inductance L_u.

2.1.2 Motoring and Generating using SRM

In this section, the operation of SRM will be explained with the help of the governing mathematical equations. The difference between motoring and generating operation and their relation to inductance profile will be explained and the importance of different control parameters will be elaborated.

The general expression for phase voltage of SRM is

$$V_{ph} = i_{ph}R_{ph} + \frac{d\lambda}{dt} \quad \ldots(2.1)$$

where V_{ph} is the DC-bus voltage, i_{ph} is the instantaneous phase current, R_{ph} is the winding resistance, and λ is the phase flux-linkage. The SRM is always driven into saturation to maximize the utilization of the magnetic circuit, and hence, the flux-linkage (λ) is a non-linear function of stator current and rotor position

$$\lambda_{ph} = \lambda(i_{ph}, \theta_{ph}) \quad \ldots(2.2)$$

The stator phase voltage in Eqn. (2.1) can be expressed as

$$V_{ph} = i_{ph}R_{ph} + \frac{d\lambda}{di}.\frac{di}{dt} + \frac{d\lambda}{d\theta}.\frac{d\theta}{dt} = i_{ph}R_{ph} + L(\theta)\frac{di}{dt} + i_{ph}\frac{dL(\theta)}{dt}\omega$$

where

$$\frac{di}{dt} = \frac{V_{ph} - i_{ph}R_{ph} - i_{ph}\frac{dL(\theta)}{dt}\omega}{L(\theta)} \quad \ldots(2.3)$$

From Eqn. (2.3), it is apparent that the left hand side is positive when $\frac{dL(\theta)}{dt}$ has a negative value, and vice versa. The required excitation region of phase current according to inductance variation can be elaborated easily using Figure 2.2. If phase current is applied at positive slope of inductance, the machine will convert electrical energy into mechanical. On the other hand, if switches are turned on in a particular sequence so that phase current is applied into the winding at negative slope of the inductance, then the machine will generate more energy than drawn and push it back to the source, hence converting mechanical energy into electrical.

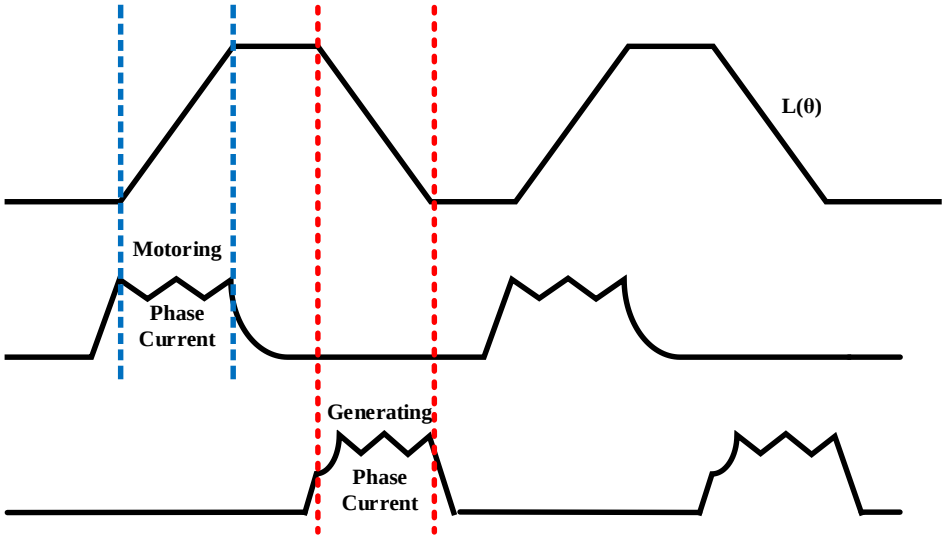

Figure 2.2: Motoring and generating operation and their relation to inductance profile.

2.1.3 SRM Drive System:

The SRM drive system is composed of (1) the controller module, (2) the power converter and (3) the machine itself. The simplest block diagram representation of an SRM drive is

shown in Figure 2.3. The control module determines a phase current command and corresponding commutation angles based on the rotor position and the phase current feedback. The phase current commands are configured for producing the phase torque at the output shaft to satisfy the load requirement. In the case of generating mode, phase current and commutation angles are determined by the controller module to produce the required current output. The output torque will have some torque ripple around the average torque output which should be within the predefined range by design. There will also be current ripple, and it is one of the control objectives to reduce this. The phase current commands are converted to gate switching signals in the controller for the power semiconductor devices in the inverter. The inverter then produces the phase voltages based on the commanded signals to drive the machine that delivers the desired torque at the appropriate speed. The research presented in this dissertation makes significant contributions on the control of SR generators, for optimal power generation and maximizing generator efficiency for a wide speed range.

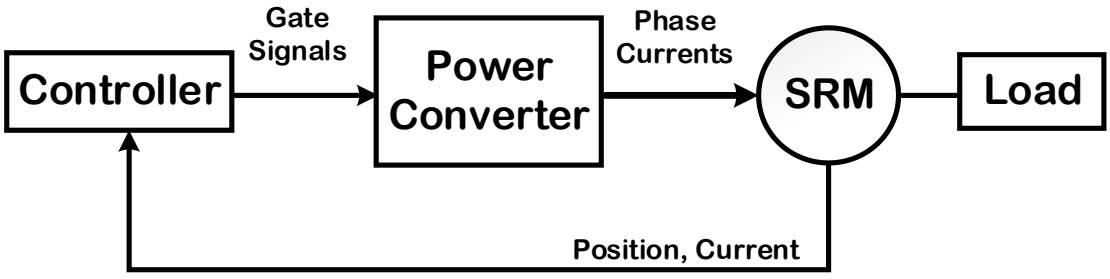

Figure 2.3: Simplified basic SRM drive system.

2.1.4 SRM Power Converters

SRM power inverter is significantly different from other multiphase machine technologies. Each phase is independently controlled by its own converter phase leg. Several converter topologies suitable for SRM drives have been proposed in the literature [31], [42],

[50]. The most commonly used, yet the most flexible and versatile converter is the classic bridge converter shown in Figure 2.4 [50]. It requires two switches and two diodes per phase.

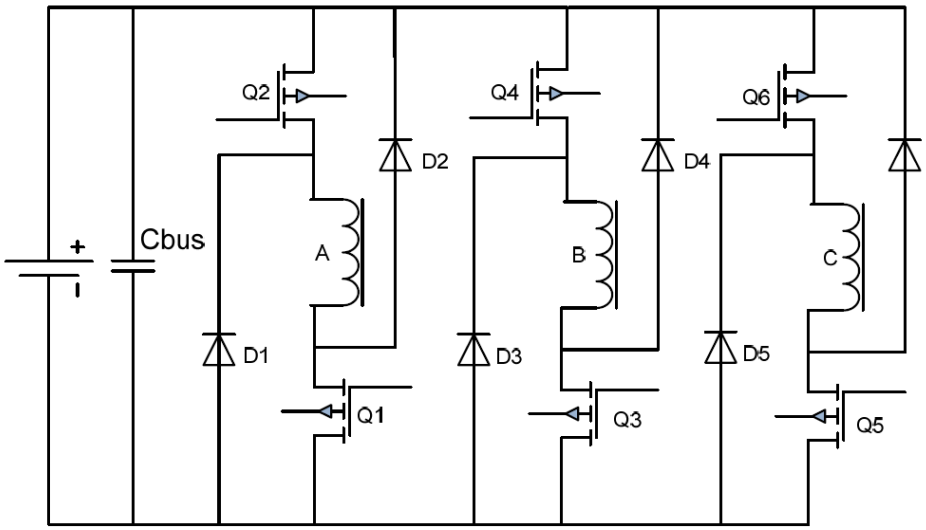

Figure 2.4: Classical bridge converter for a three-phase SRM.

The top and bottom switches along with the freewheeling diodes of the inverter circuit in Figure 2.4 are used for controlling the machine. To turn on any phase so that the armature winding can draw current from the supply, both the top and bottom switches of that phase are turned ON. This effectively applies the DC bus across the phase. Similarly, both the switches are turned off simultaneously to turn off the phase. During the turn off period, the phase current flows through the freewheeling diodes and return the trapped magnetic energy back into the DC link. Zero voltage can be applied across a phase by turning off either the top or the bottom switch; this conduction period is known as the natural commutation period or freewheeling period. Figure 2.5 shows the different conduction sequences of a phase using the classical bridge converter. Each phase is independently controlled by the controller and inverter.

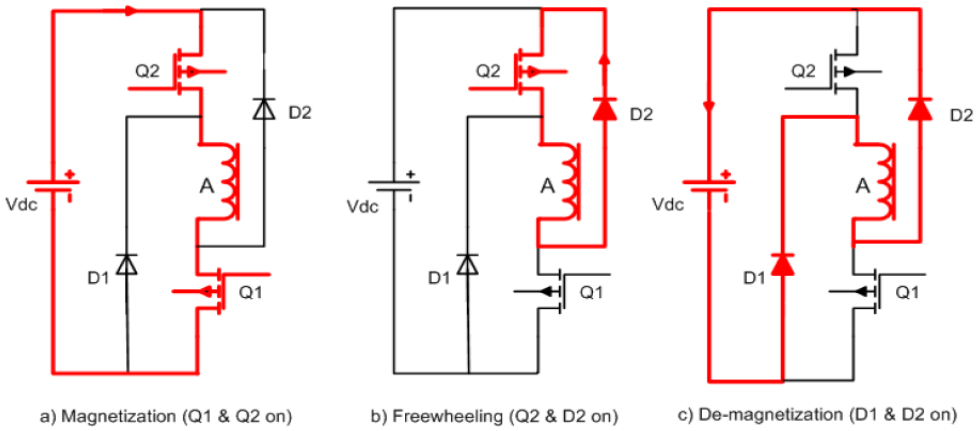

Figure 2.5: Operation of the classic bridge type converter.

For the generating mode of operation, the Switched Reluctance Generator (SRG) requires a source of excitation in order to generate electrical energy. The excitation is derived from the converter. When both switches are 'on,' current builds in the SRG phase winding. Once current is built up, the phase conduction is cycled between freewheeling (zero volts) and de-magnetization (-Vdc) during current hysteresis at low speeds. This way, more energy is returned to the source than was provided for excitation.

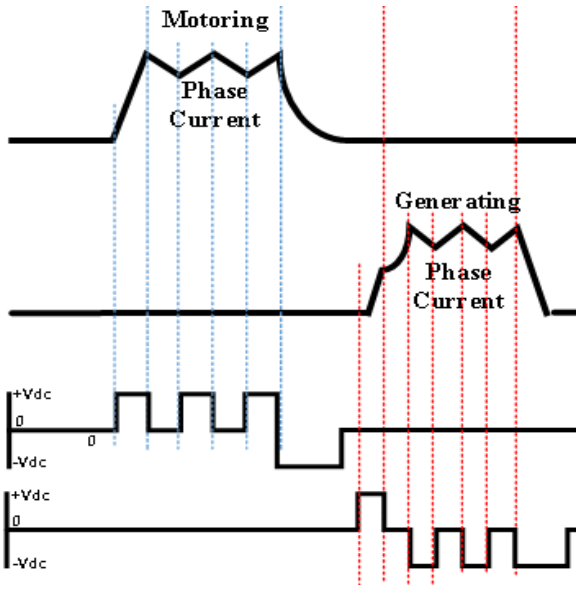

Figure 2.6: Converter switching sequence during motoring and generating.

The sequence of switching and corresponding voltage across the phase for motoring and generating is shown in Figure 2.6. For motoring, the sequence is (+Vdc ~ zero ~ +Vdc ~ zero ~ Vdc ~ -Vdc) in the increasing inductance region, and the sequence is (+Vdc ~ zero ~ -Vdc ~ zero ~ -Vdc ~ zero) for generating in the decreasing inductance region. The machine draws energy at the beginning only during magnetization; then, circulates within the converter during freewheeling and generates back to the source during demagnetization. The net energy pushed back to the DC-bus is more than drawn, hence the machine operates as a generator. It is very important to recognize and understand the difference between motoring and generating to develop and implement a target control algorithm that works successfully all four-quadrant operating region.

2.2 Flux Switching Machines

This section presents the background and literature review of the types of electric machines that operates based on the principle of flux switching. Firstly, the definition of the term 'flux switching' is presented with the principle of operation. Different types flux switching concepts are described from the early schemes to the later ones before introducing the modern flux switching topology using toothed rotor and spoke-shaped magnets in the stator. As the thesis is on modern flux switching permanent magnet (FSPM) machines with doubly salient structure, more detail and on this type of machines is presented towards the end of the chapter.

2.2.1 Background and Definition

In any electromechanical system, the induced voltage *e,* can be predicted by Faraday's

law at a specified mechanical angular speed ω_r as the change of flux linkages φ_a with position θ,

$$e = -\omega_r \frac{d\varphi_a}{d\theta} \quad \ldots(2.4)$$

This applies to any electric machine having coils in the armature linking flux from the field. As the rotor rotates, the flux linking the armature coil from the field changes with time. This change in flux linkage is periodic, which builds up to a maximum value and then gradually decreases to a minimum. In the conventional configuration of electric machines, the change of state of the armature flux between low and high is assisted by the relative motion of the polarized field system. Field excitation can either be a magnet consisting a pair of N and S poles or DC field using an electric circuit. The amount of armature flux linkage changes with the relative position between the field poles and the armature windings.

It is possible to establish a variation in flux linkage between low to high without using the change of the relative position of the N and S polarization of the field with the armature. One way to do this is to modulate the flux linking the armature using an external field with a fixed excitation by changing the permeance seen by the armature. The permeance seen by the armature is then controlled by the position of the rotor. For the rotor position to influence the permeance seen by the armature in an impactful way, the rotor must have saliency. Saliency can be introduced in the geometry mechanically using rotor slots or teeth. The change of the armature flux from maximum to minimum as caused by variation of the permeance seen by the armature is addressed as 'Flux Switching.' Electric machines that work on this principle are popularly addressed as 'Flux Switching Machines (FSM).' Therefore, the key requirements of flux switching machines are

(i) Presence of both the field and the armature coils in the stator,

(ii) Slotted/toothed structure to provide saliency for permeance variation.

By requirements, it is apparent that the rotor is very similar to the conventional SR machines, thus allowing many advantages of SRM such as simplicity of construction and robustness to be retained.

2.2.2 Modes of Flux Switching

The idea behind the principle of flux switching is that the armature flux linkage changes with position principally due to the change in the permeance seen by the armature coils with position. The variation of flux between maximum and minimum values can be distinguished by two modes: (i) unipolar and (ii) bipolar flux linkages. As the names suggest, unipolar mode is of one polarity, all positive flux; whereas bipolar is between positive maximum and negative maximum values. The two modes of flux linkages are depicted in Figure 2.7 assuming ideal permeance variation.

The unipolar flux switching is entirely influenced by the variation of the permeance. However, for bipolar flux switching, the armature coils need to link flux from both the N and S poles from the field in addition to the effect of permeance variation. The amount of flux linkages by each pole is governed by the position of the salient rotor.

As the field (either PM or DC) in the flux switching arrangement is of fixed polarity, the magnetic circuits associated with the armature coils are required to operate with unipolar or bipolar flux if the flux linkages are unipolar or bipolar, respectively. However, it is obvious that bipolar flux will provide better utilization of the armature magnetic circuit or less material usage, resulting in higher power densities and less copper loss [51]–[56].

In both the unipolar and bipolar mode if current i_a is applied in the armature coil, the electromagnetic torque T_e developed is

$$T_e = i_a \frac{d\varphi_a}{d\theta}.$$

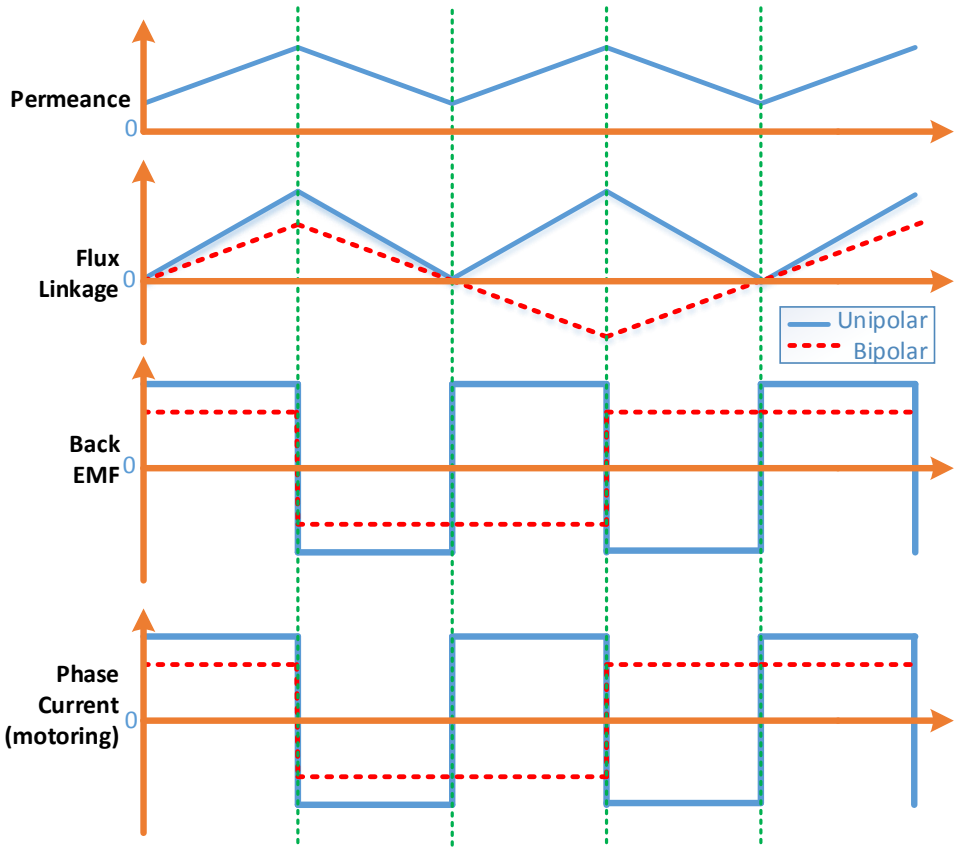

Figure 2.7: Unipolar and bipolar flux linkage with variation of permeance.

2.2.3 Evolution of Flux Switching Machines

From the definition of flux switching, the family of flux switching machines can be classified based on:

(a) Source of the field flux (DC field winding or PM);

(b) Orientation of the source of field;

(c) Operating mode of the armature flux, (unipolar or bipolar); and

(d) The form of the armature current.

The early implementation of flux switching machines employed wound-field excitation. As both the phase coils and the field are placed in the stator, the magnet demagnetization at high temperature was a concern for the low energy magnets. As material development advanced, the high-energy magnets became available which can operate at a temperature as high as 100 °C. The possibility of replacing the wound field with PM became obvious for high power applications. Few advantages of using PM instead of wound field for flux switching are: (i) Loss free excitation, (ii) Occupy less space, therefore, (iii) electric loading of the machine can be increased as more space is available for the armature in the stator.

Other than the source of field excitation, the orientation of the field is another factor which leads to few different types of Flux Switching topologies. The source of the field excitation can be (i) in the radial direction (i.e. across the width of stator tooth body), (ii) in the circumferential direction (along the back-iron body), or (iii) in the longitudinal (axial) direction. All of these have their pros and cons. Option (i) is subject to balance the stator slot space between the field and armature systems if the excitation is wound-field. Option (ii) is preferably deployed with a PM field, especially if the source is oriented across the width of stator tooth body. Option (iii) was used in the oldest types of flux switching machine, popularly known as homopolar inductor alternators. This configuration has the advantage of having the entire slot space on the stator for armature winding, and has also been exploited in the development of the Transverse Flux Machine (TFM).

A basis for classifying flux switching machines into different categories is whether the flux linkage is unipolar or bipolar. The early types of flux switching machines in the literature,

including heteropolar configurations, typically produced unipolar flux linkages; however, nearly all types of flux switching machines developed in the last two decades produce bipolar flux linkage. Bipolar flux linkage has clear advantage over unipolar as the magnetic circuit can actually undergo twice the flux change. Hence, the produced power density and torque density is also higher. In the following sections, the major types of flux switching machines based on the differences listed above are described briefly.

2.2.3.1 Inductor Alternator

The inductor alternator appears to be oldest in the class of flux switching machines. The theory of inductor alternator was first proposed and established by Walker in 1942 [57]. It had quite a bit of history of use as a high frequency generator at that time. However, in its most conventional application it has been replaced by wound-field or PM synchronous machine. It was an attractive choice in applications where generation of high frequency currents was required and thus proved suitable in wireless telegraphy and high frequency electric furnaces.

There are two types of Inductor Alternators based on the principal of operation: (i) Homopolar machine, and (ii) Heteropolar machine. In spite of such names, both of them operates under unipolar armature flux linkages. As well as operational differences, they also differ structurally.

The radial and axial cross section of the Homopolar Inductor Alternator (HIA) is shown in Figure 2.8. The most common electric machines popular in research are either radial flux or axial flux machines. The HIA is a combination of both. It consists of a slotted and laminated armature core in two parts, a1 and a2, joined on a common frame. A field coil F is wound concentric with the longitudinal axis of the machine. A slotted rotor core **r** completes the path for the flux, shown in the longitudinal view of the Figure 2.8.

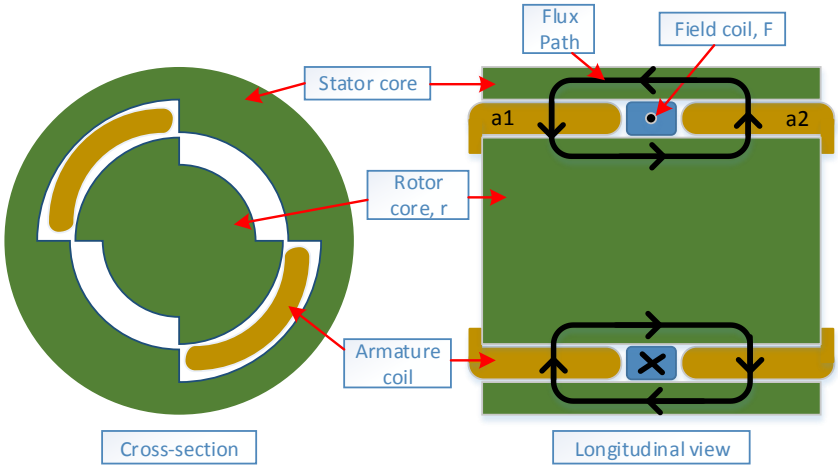

Figure 2.8: Basic structure of the Homopolar Inductor Alternator (HIA).

Rotary motion and torque is generated by the variation of the permeance seen by the armature coils due to changes in the airgap length and produces unidirectional flux linkage variation in the armature coils. As the armature coil links with unidirectional flux only, the flux linkage is characteristically unipolar.

Due to their complex 3D magnetic structure, analyzing HIA was not easy back in the 1950's and led to its demise until recent years where they have been proposed in very high power megawatt level naval [58] and generator [59] applications. It is not surprising that the prototypes report significantly lower flux linkages than expected when laminated steel is used, indicating substantial eddy currents due to cross flux in the laminations. A solution to this appears to employ powdered-iron cores, as in transverse flux machines, which minimizes eddy current effects in all directions.

The cross section of heteropolar inductor alternator is shown in Figure 2.9. It is relatively simpler than the homopolar machine, and the principal of operation can be explained by the radial cross section alone. The slotted stator core contains both the armature and field coils.

They can either be in the same slots, as in Figure 2.9(a), or they may be in alternate slots, as in Figure 2.9(b). The number of rotor slots may be designed to be an integer multiple of the number of stator slots.

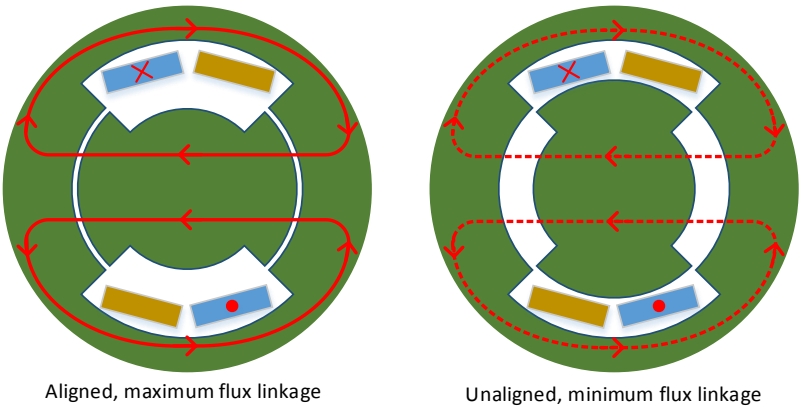

(a)

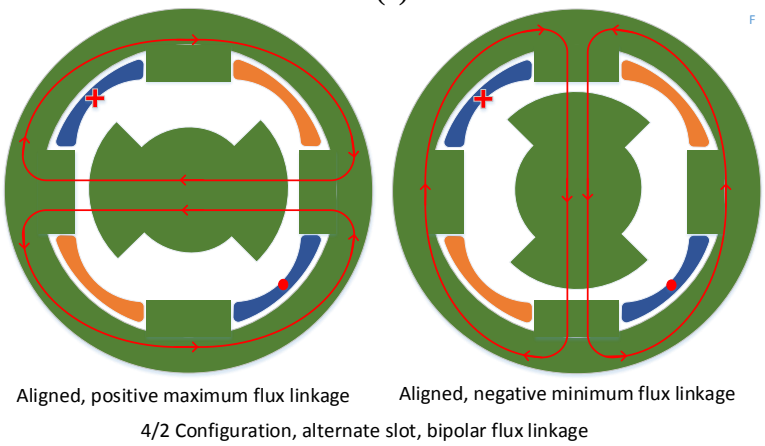

(b)

Figure 2.9: Heteropolar machine topologies.

There is no coil or winding in the toothed rotor. As the field is excited and the rotor rotates, the coil flux linkage varies with rotor position. As in the homopolar machine, the doubly salient stator and rotor causes change in permeance when the rotor moves that influences the flux linkages of the armature coil. The arrangement with alternate slots has been applied in modern

schemes to produce bipolar armature flux linkages by simply ensuring that the number of stator slots is less than the number of rotor teeth [60].

The heteropolar structure has a few advantages over the homopolar structure such as smaller time constant which makes it superior in applications requiring close and rapid control of alternator terminal voltage.

The application and dominance of inductor alternators reduced gradually because of lack of affordable power electronics and suitable tool to analyze such complex structures since it was first proposed in the 1940's. The concept has been revived in recent years with allusions to SRM control concepts, and an accompanying modern-day drive has been proposed.

2.2.3.2 The Flux Switching Alternator

Rauch and Johnson [51] first proposed the flux switching alternator in 1955. It can be seen as a variation of the heteropolar alternator mentioned in the previous section, where the field winding is replaced by permanent magnets. It can also be seen as one of the earliest attempt in using PMs in a variable reluctance machine. Nonetheless, it appears to be the earliest point in history that the term 'Flux Switching' is noticeably used to describe an inductor alternator with bipolar armature flux linkages. The cross section of the machine is presented in Figure 2.10. A pair of magnets with the orientation indicated is mounted on a stack of stator iron laminations which in turn are wound with armature coils. The rotor is a simple stack of laminations with two salient poles. As the rotor rotates, the flux paths switch to the stator poles having the least reluctance in the air gap. The flux shown in Figure 2.10(a) completely changes direction when the rotor has moved through half the electrical cycle in the position shown in part Figure 2.10(b). The rotor completes two electrical cycles in one revolution.

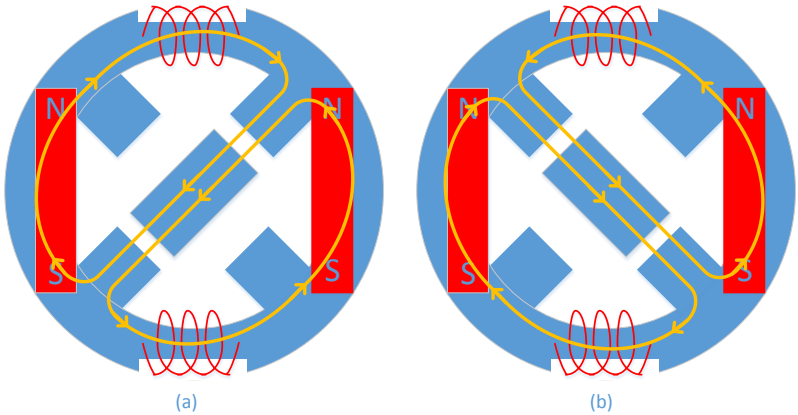

Figure 2.10: Structure of a simplified flux switching alternator.

The flux switching principle positively resulted in the rate of flux linkage to double as compared to the homopolar inductor alternator. This configuration of flux-switching alternator was claimed to have a higher power density that the HIA which was less efficient.

2.2.3.3 Field assisted and PM assisted SRM

In 1989, Phillips [61] proposed a new configuration based on the concept of pre-magnetization over the traditional SRM. A full pitched winding in the stator was added to the conventional SRM to act as a field winding to improve its torque capability. The machine was basically a single stack homopolar inductor machine fed from a unipolar converter, with the field excitation provided by the additional full-pitched winding. A cross section of the machine is shown in Figure 2.11. This machine configuration has also been explored by other researchers from a different perspective, where an auxiliary commutation winding was used to retain and utilize the field energy within the motor [62]. All these machines can be viewed as field-assisted SR machines with energy converted primarily through reluctance torque.

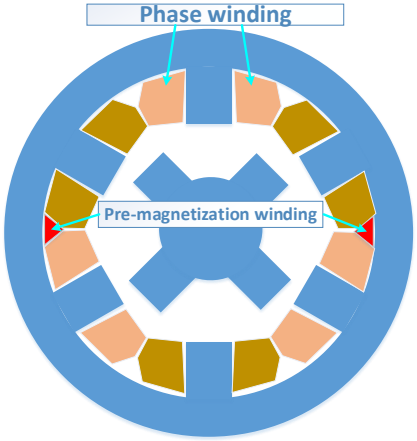

Figure 2.11: Cross section of the basic field assisted SRM.

In 1992, Liao, Liang and Lipo proposed a new topology called Doubly Salient Permanent Magnet (DSPM) machine, where the field excitation is supplied by permanent magnets in the stator [63]. It can either be seen as another improvement over field assisted SRM, or an improved FSM with PMs embedded in the stator back-iron providing the same benefits as the Flux Switching Alternator with even higher power density. Because of the unipolar nature of flux, it was a flux pulsation machine as compared to the bipolar, flux reversal machine. A three-phase, 6/4 DSPM with PMs in the stator yoke is shown in Figure 2.12.

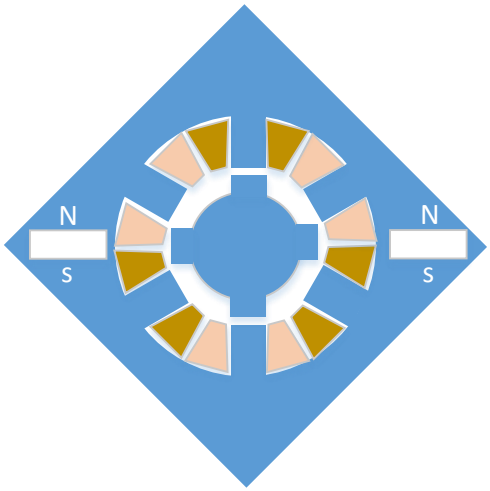

Figure 2.12: Cross section of the proposed PM assisted SRM.

A linear variation of PM flux-linkage with rotor position and consequently a trapezoidal back-EMF is induced in the stator windings on no-load. Because of the trapezoidal back EMF, DSPM machine is more suitable for brushless DC operation. Due to the existence of the PMs, a very high reluctance path for the armature reaction flux exists. Therefore, the inductance of phase winding is small at both aligned and unaligned positions. Consequently, unidirectional torque can be achieved by applying a positive current when the PM flux is increasing and a negative current when the PM flux is decreasing to the corresponding winding. The torque is dominated by the permanent magnet excited torque, and the resultant reluctance torque as well as cogging torque are negligible.

Other than the robust SRM-like rotor, this structure showed few advantages over SRM such as torque density, efficiency and converter VA rating. It was an attractive alternative because of torque production and structural simplicity. A high reluctance path in the rotor back iron due to the PM forces the phase flux to take a leakage path through adjacent stator poles where reluctance is minimum. The leakage path reduces the phase flux and may cause cancellation of winding MMF if the phases are excited simultaneously depending on the polarity of windings around the stator poles. Leakage flux along with self-inductance and torque capability are among the few concerns of this structure where there was room for improvement.

2.2.3.4 Flux Reversal Machine

The flux reversal machine (FRM) is another form of flux switching machine that appeared in literature [53] in 1997 for the first time. It is the first machine among those having stationary magnet that utilizes bipolar armature flux linkage and MMF variation for energy conversion. The rotor is similar to SRM having a simple, salient structure. The stator is also similar to SRM

except with a pair of high energy permanent magnets with opposing polarity attached under the stator teeth near the airgap. FRM possesses a naturally low inductance, hence low electrical time constant and low mechanical inertia. As a result it appears suitable in applications that require fast response, such as electric vehicle generators.

Figure 2.13 shows the basic configuration of the FRM, consisting two stator poles and three rotor poles. Magnets of opposite polarity are mounted on the stator pole faces at the airgap. Due to the rotor saliency, as it rotates, the armature coil 'sees' varying permeance with respect to rotor position.

The variation in permeance and coil flux linkage with respect to rotor position follow similar trend as shown in Figure 2.7. Figure 2.14 illustrates the operating principle of FRM with the help of the cross section at different rotor positions. At (a), no flux links the stator back iron and the coil, and hence, the permeance seen by the stator is zero. At (b), which is at 30 degree counter clock wise (CCW) position from (a), the phase flux linkage is maximum and so is the permeance. At (c), it is similar to (a), the flux linkage is zero and permeance is minimum again. At (d), phase flux is maximum again (in the direction opposite to (b)), and the permeance is maximum. As the rotor rotates one complete mechanical cycle, the armature flux linkages and the flux in the stator pole undergo complete 'flux reversal' by varying from zero to positive maximum, and back to zero before going to negative maximum. The linear bipolar variation of phase flux results in a square-wave EMF. Applying Faraday's law, it can be shown that the back EMF is maximum at (a), negative maximum at (c) and zero at (b) and (d).

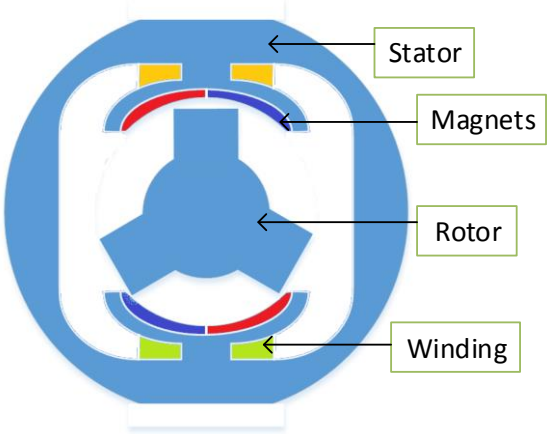

Figure 2.13: Basic configuration of a 2/3 FRM.

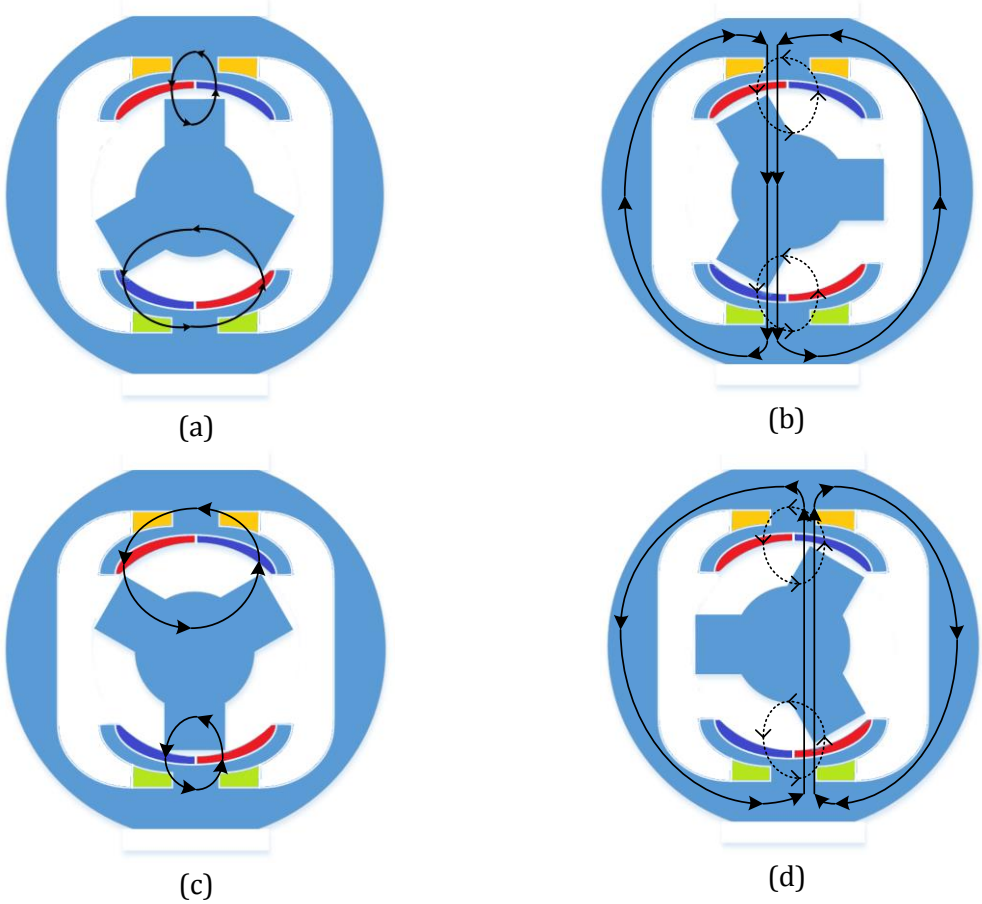

Figure 2.14: Operating principle of the FRM.

The basic concept is explained using simple 2/3 topology. Variation in number of stator/rotor poles can be applied to produce different multiphase configuration [64], [65].

2.2.3.5 Modern FSMs using salient rotor and sandwiched spoke magnet

In 1997, Hoang et al. [52] presented a new stator structure that supposedly allows an efficient and balanced accommodation of PM, armature coil, and magnetic steel core on the stator. The stator core was modular or segmented, U-shaped pieces. It is easier for a reader to realize the principle of operation of such structure if the circular co-ordinate is laid in a linear fashion as in Figure 2.15. It shows one elementary cell which contains a permanent magnet sandwiched between two U-shaped magnetic stator cores, an armature winding and a toothed-rotor. At (a), the rotor teeth are aligned with corresponding stator teeth and the flux path is clockwise. As the rotor rotates from (a), (b) is the next position where the rotor is again aligned with the stator. The polarity of flux linkage reverses from (a) to (b). Therefore, as the rotor rotates, bipolar variation of flux is occurs.

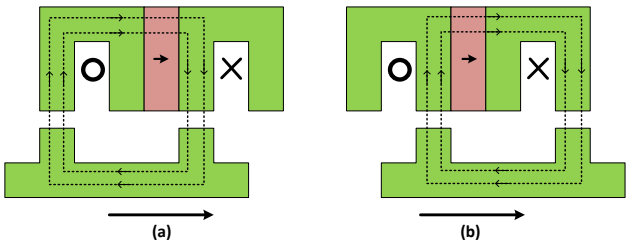

Figure 2.15: Elementary cell of the modern flux switching structure.

In practice, a concatenation of a series of the elementary cells in rotary arrangement is used to get an optimum circular design for a rotating machine based on this structure. Careful choice of the combination of the number of stator teeth and rotor poles can be used to create multiphase topologies. Based on this idea, an elementary single-phase structure has been discussed in [66], and a practical single phase concept containing four U-stator cores, four magnets and a 4-tooth rotor has been developed for an industrial application [67]. Further research and developments on these structures have been carried on for multiphase arrangements [52], [54], [68]–[75]. Some of the structures of these modern FSM topologies

are shown in Figure 2.16.

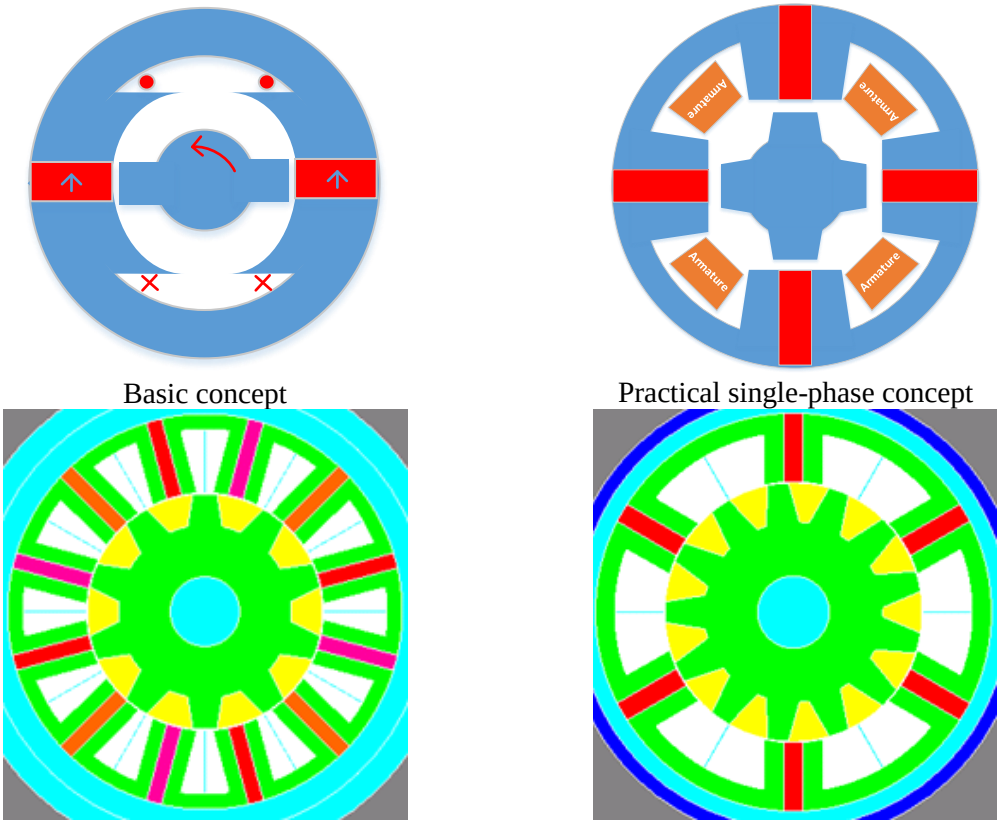

Basic concept | Practical single-phase concept

Three-phase, 12/10 structure | E-core, 6/13 FSPM

Figure 2.16: Various structures of modern flux switching machines.

The conventional FSPM topology containing U-shaped laminated segments and spoke type rare earth PM has shortcomings like low magnet utilization ratio and high cost. In an attempt to reduce the volume of magnet but retain other positive features of FSPM, multi-tooth and E-Core FSPM has been proposed [76]–[78]. Multi-tooth FSPM has a further split in the stator tooth near the airgap presenting two stator teeth on each side of the sandwiched permanent magnets. The configuration required increased number of rotor poles as well. Multi-tooth FSPM featured reduced magnet usage than the conventional FSPM for a three-phase machine at the cost of higher electric loading to maintain same torque capability [73]. A multi-

tooth structure is also reported to have lower torque ripple and higher torque density at low armature currents. However, at higher current, torque does not increase as compared to conventional single tooth structure. As the name suggests, E-core machine used E-shaped laminated segments instead of conventional U-shaped segments. This structure also reduced the magnet area by half and had increased slot area for armature coils. Unfortunately most optimal stator rotor pole combination requires an odd number of rotor poles (to have minimum back EMF harmonic and torque ripple) that results in unbalanced magnetic force and unwanted noise and vibration.

Pollock and Wallace [60] proposed another structure applying a field winding excitation on this concept in an electric motor for the first time. It can be seen as a form of DC motor without brushes or magnets. The scheme evolves from the basic concept of the inductor alternator with bipolar flux linkages shown in Figure 2.9, where the number of stator teeth is purposefully chosen to be twice the number of rotor teeth. Figure 2.17 explains the basic principle of FSM with field coil excitation. A practical topology for such a structure is shown in Figure 2.18. Similar configuration can also be formed as 4/2 and 12/6 topology. It has the advantages of reducing end winding conductor material. Such configurations have been demonstrated for industrial applications where high power density and durability is required [79], [80].

Based on the conventional U-core and E-core FSPM, hybrid excited Flux Switching machines have also appeared in literature. As the name suggests, hybrid excited machine would have both PM and controllable DC field in stator. A topology with hybrid excitation naturally raises concern in practical implementation than in concept. Hoang et al [81], [82] proposed an elementary presentation of hybrid excited FSM and an accompanying three-phase topology as

shown in Figure 2.19. In this concept, the permanent magnets provide the primary field flux as in conventional FSPM while a variable DC field winding acts as a provider for secondary field flux, which can be either additive or differential.

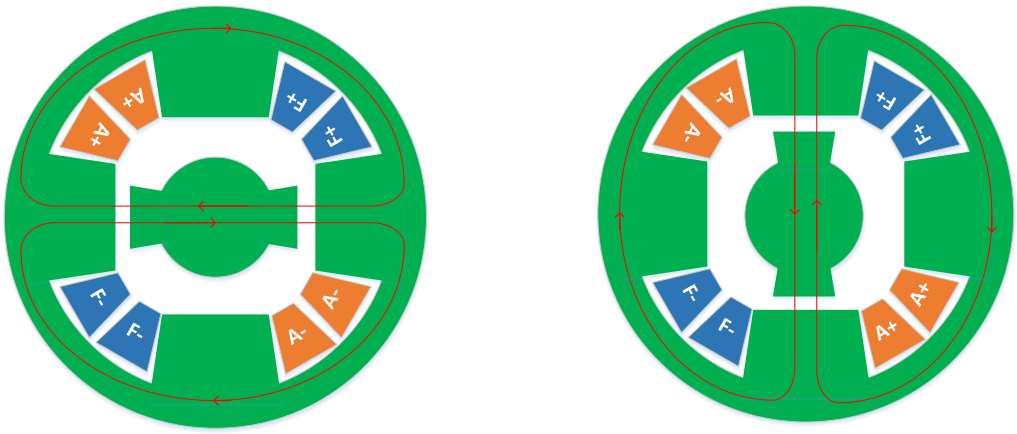

(a) Positive armature flux linkage (b) Negative armature flux linkage

Figure 2.17: Basic principles with field coil excitation.

Figure 2.18: FSM topology using field winding excitation.

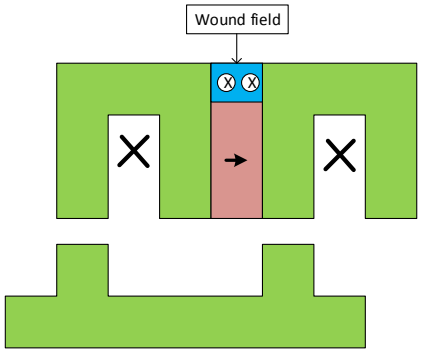

Figure 2.19: Elementary cell structure for hybrid excitation.

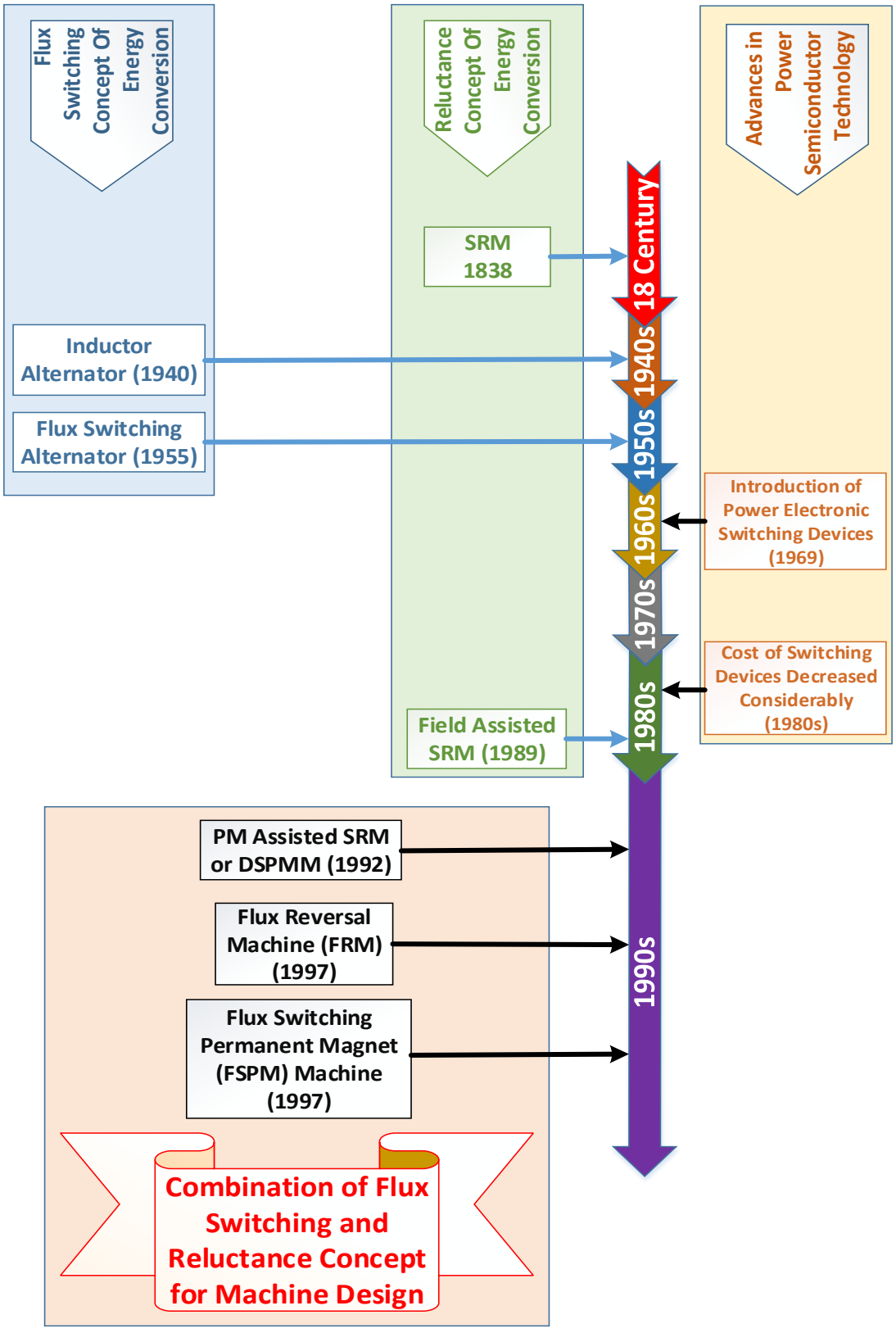

Figure 2.20: Graphical representation of the evolution of Flux Switching PM Machines.

Although the addition of DC source pose added complexity and cost, it can be useful for flux weakening operation and for manipulating the core losses by changing field current. Subsequently, promising useful applications can be gearless drive with a large operating speed range. Recently, the effect of flux bridges have been investigated [83] among the research using hybrid excited FSM.

Figure 2.20 shows a graphical representation of the evolution of modern Flux-Switching PM machines from SR and Flux switching machine technologies using a timeline. The timely advancement in power semiconductor technology aided in both technologies towards their acceptance and popularity in numerous commercial and industrial applications as well.

2.3 Conclusion

The background and operating principle of SRM and FSPM topologies are presented in this chapter. By embracing a clear yet broad definition of the term ‘flux switching,’ it has been shown how machines operating on the principle of flux switching have evolved through the last century, culminating in the modern configurations FSPM. Because of the flux focusing nature of the machine, FSPM promises high torque density within the same dimensions than brushless dc or other pm machines employing same magnetic material. Likewise, using non-rare earth magnet in FSPM is another interesting and promising idea to obtain close to rare earth like electromagnetic performance. Unlike all other PM machines, cogging torque is an important concern while designing an FSPM. Also, as FSPM employs a segmented stator, the noise and vibration due to magnetic force also requires attention. Improving major performance parameters like torque ripple, noise and vibration is the directions followed by

the work in this dissertation. They are accomplished by applying unique design strategy and pole shaping. Specific study of minimizing cogging torque, noise and vibration by design innovations have culminated in this thesis on three phase FSPM. A prototype was built and tested based on the design performed.

Chapter 3

SRG Control for Optimal Power Generation

This chapter presents a novel method of controlling switched reluctance generators (SRGs) for maximum efficiency with active current regulation. The effect of varying the input control parameters on the efficiency of the SRG is first analyzed through exhaustive data collection through simulation and experiments. The analysis of the collected data showed that the input control parameters that minimize the dc-link current ripple also maximize the generating efficiency. A novel control strategy based on the analysis is then developed to maximize the efficiency indirectly through the control parameters that minimize the dc-link current ripple in real time while delivering the commanded generation power. The controller algorithm has been implemented with a 1kW experimental three-phase SRG drive system charging a NiMH battery pack.

3.1 Generation with SRG from Control Perspective:

Because of the feasibility of four quadrant operation with a variable speed range, SR machines are attractive for many applications where energy conversion is required in both ways. The magnetic excitation in SR generators (SRGs) is established by three control parameters: the turn-on angle θ_{on}, the turn-off angle θ_{off} and the phase reference current I_{ref}. In the existing literature, methods for control parameter optimization for SRG have only been addressed at higher speeds when the machine operates in the single-pulse mode [45], [47]–[49], [84]–[88]. The controller development methodology has the following general procedure: (i) sweeping the control parameters through experiment or simulation, (ii) mapping of

experimental data, and (iii) developing a function or procedure based on the parameters for a desired performance optimization [84], [88]. This procedure optimizes one performance parameter at a time, and in all cases efficiency was chosen to be optimized. An automatic turn-on angle advancing algorithm including simultaneous adjustment of turn-off angle based on look-up table is presented for optimal efficiency operation in [89]. In [85], the optimal efficiency turn-off angles was characterized as a function of power level and speed; the turn-on angle was used to regulate the power produced by the SRG as necessary for closed loop control. When SRG is operated as a generator, the operating point is chosen in the constant power region which is why all the reported control methods in the generator mode are for high-speed single pulse mode of operation [49], [85], [86], [90]. More recently, switched relucatnce machines (SRMs) are being considered for traction applications where generation is required at lower speeds with phase current regulation through an active current control algorithm. Generation at lower speeds is also required for wind turbines where SRM is a candidate. Numerous control methods for operation in the motoring mode are reported in the literature, but these are not directly applicable in the low-speed generating mode [45], [48], [88]. The motoring mode controller optimizations focused on efficiency maximization, torque per ampere maximization or torque ripple minimization [91]. Concepts of controller optimization at lower speeds in motoring mode can be adapted to develop optimal control methods in the generting mode for such objectives as efficiency maximization or dc-link current ripple minimization.

Efficiency maximization through dc-link ripple minimization has been studied in the single pulse mode where the two control parameters of turn-on and turn-off angles were adjusted in a closed loop controller [90]. In the low speed region where current regulation is

essential, the reference phase current level also needs to be controlled along with excitation angles. The dc-link current ripple arises primarily from phase commutation, but also depends on the regulation level of the active phase currents. At lower speeds with active current regulation, the additional control command for reference phase current need to be generated. This chapter [92] presents a novel approach to control the SRG at lower speeds through current regulation while minimizing the dc-link current ripple and maximizing the generation efficiency. This will help maximize the system efficiency and minimize the impact of charging current ripple on the battery in traction applications. The chapter also presents a theoretical and experimental analysis for linking the dc-link ripple with efficiency.

3.2 Switched Reluctance Generator System

The SRG drive system considered in this research to collect extensive generating mode data consist of an SRG, a power converter, a controller, a battery pack, and a prime mover. Figure 3.1 gives the block diagram representation of the system. The SRG considered is a 1kW, three-phase, 12/8 machine. In the simulation set-up, the SRG has been modeled using a geometry-based analytical solution for the flux linked and the static torque produced by single SRG phase [93], [94].

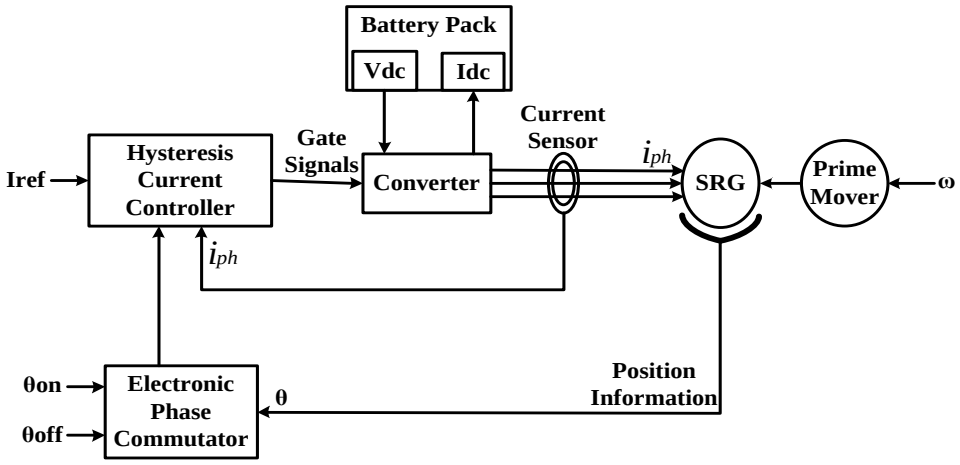

Figure 3.1: SRG drive system.

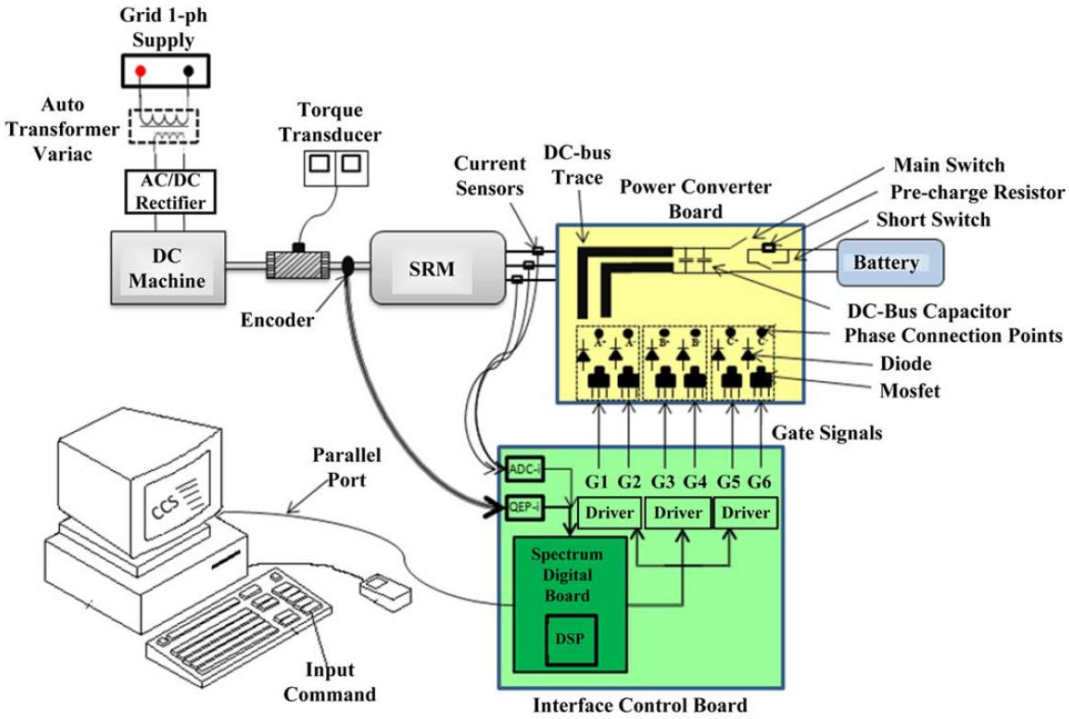

Figure 3.2: Experimental setup for SRG operation.

Figure 3.2 shows the experimental setup containing the controller card, the interface control board with the power MOSFET drivers, current sensing circuitry, quadrature encoder peripheral (QEP) unit, fault protection circuitry, and the power converter board with the dc-

link capacitor. In addition, there are current sensors for phase current measurements and the quadrature incremental encoder mounted on the shaft of the rotor of the SRM. The experimental set-up was used for both data collection and controller development. The SRG parameters for the experiments are given in Table 3.1.

Table 3.1: SRG parameters in the experimental setup

Parameter	Value
Rated battery voltage	165V
Rated SRG phase current	5.5A
Operating speed	1000 rpm
Rated Torque	1.5N-m
Rated Power	1kW
Phase Resistance	2.2Ohm

The input parameters that give the most efficient SRG operation at low speeds are identified through exhaustive data analysis using results from the dynamic simulation model and the experimental set-up. The objective of the data analysis is to identify the relationships among phase current $I_{ph(rms)}$, average dc current $I_{dc(avg)}$, dc-link current ripple $I_{dc\text{-}ripple(rms)}$ and efficiency, and then to test the controller developed through the research. The ripple on the dc bus current at the higher frequency is mainly the function of the switching frequency and can be filtered effectively through the bus capacitor. The ripple on the bus current due to the phase commutation is relatively at lower frequency and can be the function of the operating speed, number of phases and rotor poles and the control strategy. The ripple due to phase commutation can be used as a measure for the overall system efficiency and is the main consideration in this paper. The ripple in the phase or dc-link current due to the current regulation is negligible compared to the ripple due to commutation, and hence, the former is neglected in the analysis.

The data analysis showed that the excitation angles that produce the minimum ripple on the dc link current also deliver the maximum generating efficiency. Based on the observations, a multi-loop control algorithm has been developed to control the turn-on angle θ_{on}, turn-off angle θ_{off} and the peak value of the phase current for the SRG operation. The first control loop provides the reference current required to generate the commanded generating current. The second control loop continuously tracks and minimizes the nominal dc-link current ripple through adjusting the turn-off angle. The relationship between the conduction angle and the phase current command has been established and then tabulated for the closed loop operation. The conduction angle (θ_{cond}) is the difference between θ_{on} and θ_{off}. In the paper, the dc-link current is represented as I_{dc}, and the peak to peak ripple on I_{dc} is defined as $I_{dc(ripple)}$.

The developed controller was tested with the dynamic simulation model and then verified through the 1kW SRG experimental system.

3.3 SRG System Electrical Losses

The efficiency in an electric machine depends on the electrical, mechanical and iron losses. The drive efficiency depends on the conduction and switching losses of the power electronic converter and the parasitic resistances in the passive components such as the ESR in the DC-link capacitor. The SRG system efficiency maximization approach is based on the management of the DC-link current ripple. The same $I_{ph(avg)}$ and $I_{dc(avg)}$ can be obtained in the SRG drive system with phase currents of different peak amplitudes and pulse widths. The objective is to find the optimal peak phase current and conduction period which maximizes the efficiency. Minimizing the $I_{ph(rms)}$ will increase both SRG and the inverter efficiencies by reducing the

copper losses in the SRG and conduction losses in the power semiconductors. The losses directly linked with the DC-link current in the SRG drive system are the machine electrical loss (i.e., the copper loss) and the loss in the ESR. Hence, these two types of electrical losses for the SRG drive system are addressed in this research. The core losses does not have significant contribution on the SRG efficiency at low speeds and the changes in the core losses with different phase current options at the intended operating speeds are minimal. The rotational losses depend on the machine speed and are not significantly different for the different phase current options for the same operating point. Similarly, the conduction and switching losses also not significantly different for the different phase current options.

The electrical loss in the SRG is the copper loss which depends on the rms stator phase current. The loss is given by

$$P_{Cu} = mI_{ph(rms)}^2 R_{ph} \quad \ldots\ldots(3.1)$$

where m is the number of phases. The minimum rms phase current points will give the minimum copper loss and enhance the efficiency [95]. The electrical loss due to the dc-link current ripple is given by

$$P_{Cap} = I_{dc-ripple(RMS)}^2 R_{ESR} \quad \ldots\ldots(3.2)$$

where $I_{dc\text{-}ripple(RMS)}$ is the rms value of the dc-link current ripple and R_{ESR} is the equivalent series resistance of the dc-link capacitor [96].

A simplified analysis with rectangular phase current pulses shows that the minimum loss condition with a commanded average dc-link current occurs when the dc-link ripple is minimum. The $I_{ph(avg)}$ is $I_{Peak}D$ and the $I_{dc(avg)}$ is $3I_{Peak}D$ (here $m=3$) with the simple rectangular pulses. The same dc-link average current can be obtained if I_{Peak} is decreased by the same

factor by which the conduction period *D* is increased and vice versa. This factor is referred to as the multiplication factor *n*, which is given by $n = -\frac{I_{Peak}}{\Delta I_{Peak}}\frac{\Delta D}{D}$. The rms value of the phase current and the ripple on the dc bus current is affected with the change of *n*. Although the number *n* cannot be applied to practical phase currents as linearly as it is done with ideal rectangular currents, the analysis with the latter demonstrates that there is an optimum phase current peak and conduction width that give minimum dc-link ripple. As *n* changes (with $n_3 > n_2 > n_1$), the phase current amplitude $\frac{I_{Peak}}{n}$ and phase current conduction period $D{\times}n$ also changes keeping the average dc-link current the same ($= 3\frac{I_{Peak}}{n}Dn = 3I_{Peak}D$). Table 3.2 shows the effect of *n* on various currents for a three-phase machine for the same $I_{dc(avg)}$, and hence, the same output power.

Table 3.2: $I_{ph(rms)}$ and $I_{dc\text{-}ripple(rms)}$ for different magnitude, duty and overlap situation

Parameter	Expression
$I_{ph(avg)}$	$I_{Peak}D$
$I_{dc(avg)}$	$3I_{Peak}D$
$I_{ph(rms)}$	$\frac{I_{Peak}}{n}\sqrt{nD}$
$I_{dc-ripple(rms)}$ (No overlap)	$\frac{I_{Peak}}{n}\sqrt{3Dn \times (1-3Dn)}$
$I_{dc-ripple(rms)}$ (Overlap)	$\frac{I_{Peak}}{n}\sqrt{(3Dn-1) \times (2-3Dn)}$

For $n_3 > n_2 > n_1$,

$$I_{Peak1}\sqrt{D_1} > I_{Peak2}\sqrt{D_2} > I_{Peak3}\sqrt{D_3}$$

$$\frac{I_{Peak}}{n_1}\sqrt{n_1 D} > \frac{I_{Peak}}{n_2}\sqrt{n_2 D} > \frac{I_{Peak}}{n_3}\sqrt{n_3 D}$$

Also $I_{dc\text{-}ripple(rms)}$=0 when *3Dn*=1, non-zero for other cases.

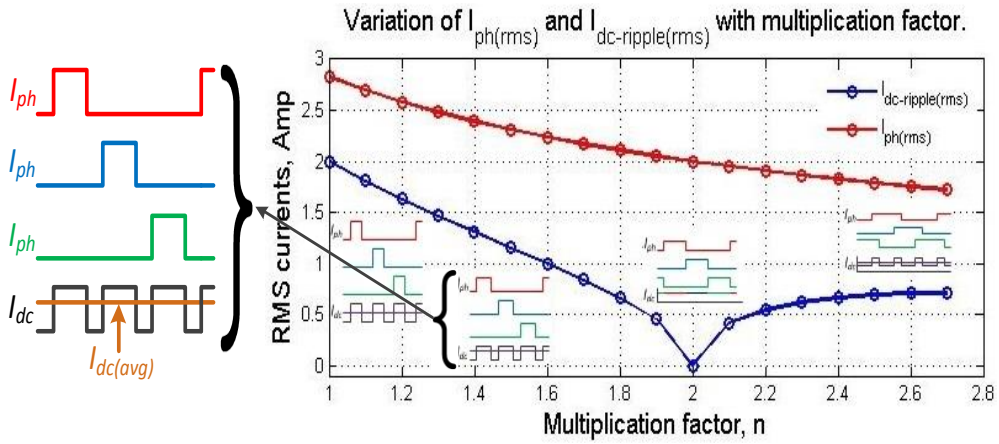

Figure 3.3: $I_{ph(rms)}$ and $I_{dc\text{-}ripple(rms)}$ variation with changing n.

The changes in $I_{ph(rms)}$ and $I_{dc\text{-}ripple(rms)}$ with the change in multiplication factor (n) are illustrated in Figure 3.3 where initial values of I_{Peak} and D are assumed to be 4 Amps and $\frac{1}{6}$, respectively. $I_{ph(rms)}$ keeps decreasing as D is increased and amplitude of phase current, I_{Peak} is decreased irrespective of the overlap between phases. If the conduction period is reduced, the reference current level required has to be increased to attain the same $I_{ph(avg)}$ and $I_{dc(avg)}$; this will result in higher dc-link current ripple due to phase commutation, and also result in higher copper loss due to the higher rms current. Again, if the conduction period is increased beyond a certain level where phase overlap is large, the current ripple will get increasingly larger due to sub-optimal large overlapping conduction. The analysis with the simple rectangular pulses shows that an optimal rms phase current value exists at the location of minimum dc-link current ripple; the loss due to $I_{dc\text{-}ripple(rms)}$ is at a minimum when the dc-link ripple is minimum since the losses start to increase again as phase overlap increases because of current conduction in two phases. The increase in $I_{dc\text{-}ripple(rms)}$ dominates over the small decrease in $I_{ph(rms)}$ in the phase current overlap region.

The above simplified analysis suggests that the total contribution to losses from $I_{ph(rms)}$ and $I_{dc\text{-}ripple(rms)}$ will be minimum if the phase excitation parameters of the SRG are continuously adjusted to minimize the dc-link current ripple. The phase current in the actual machine is far from simple rectangular pulses, but similar results are obtained from the nonlinear SRG system simulation model.

Figure *3.4* and Table 3.3 show the relationship between dc-link current ripple and efficiency for three different phase current overlap situations obtained from the simulation by changing I_{ref} and θ_{cond} while maintaining the same $I_{dc(avg)}$. The $I_{dc(avg)}$ per unit torque (T_{avg}) values are used to represent efficiency since speed is kept constant at the input and V_{dc} is kept constant at the output. The simulation results show that the efficiency increases as the dc-link current ripple decreases similar to the trend observed with ideal rectangular pulses. In the practical case, the SRG controller should target the optimum overlap angle where dc-link current ripple is minimum to maximize efficiency.

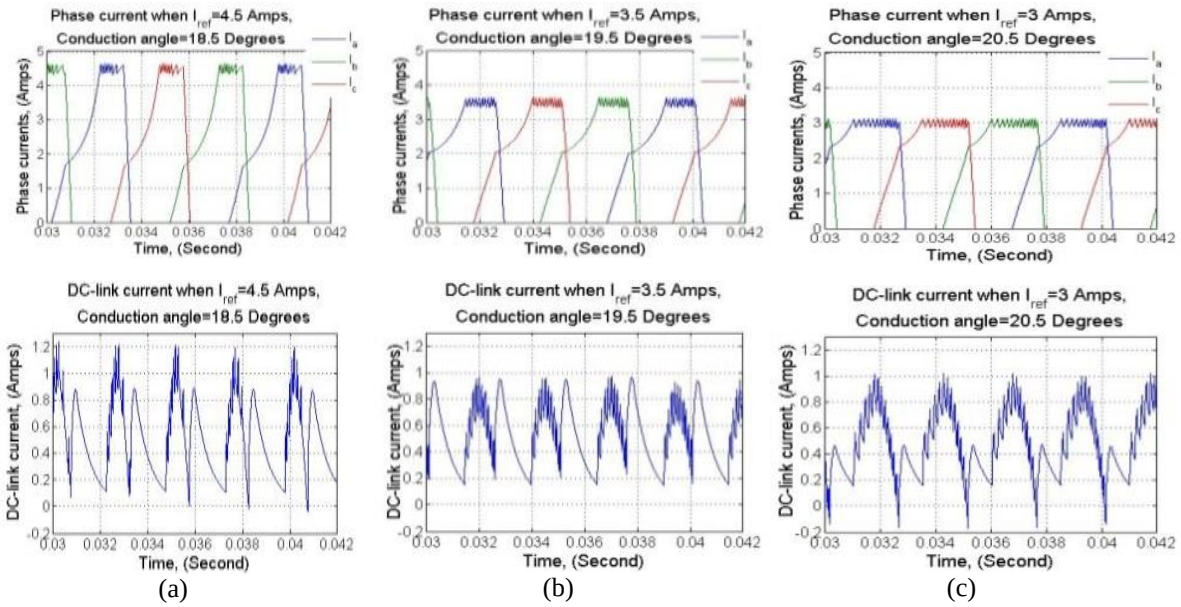

(a) (b) (c)

Figure 3.4: (a) I_{ph} and I_{dc} for I_{ref} = 4.5 A and θ_{cond} = 18.5 mechanical degrees. (b) I_{ph} and I_{dc} for I_{ref} = 3.5 A and θ_{cond} = 19.5 mechanical degrees. (c) I_{ph} and I_{dc} for I_{ref} = 3 A and θ_{cond} = 20.5 mechanical degrees.

Table 3.3: DC-link current ripple and $\frac{I_{dc(avg)}}{T_{avg}}$ for different phase currents with the same $I_{dc(avg)}$ of 0.49 Amps.

I_{ref} Amp.	θ_{cond} Mech degree	$I_{dc(ripple)}$ Amp.	$\frac{I_{dc(avg)}}{T_{avg}}$ Amp/N.m	$I_{ripple-nom}$
4	18.5	1.2	0.212	5.66
3.5	19.5	0.8	0.215	3.72
3	20.5	1.2	0.212	5.66

3.4 Data Collection and Analysis

The experimental SRG was run at 1000 rpm charging a 165 V battery and a set of data was collected by changing different input parameters. The objective of this data collection and analysis is to find the input parameters for which the SRG runs most efficiently at low speeds. For the SRG, the output power (and thus the average dc-link current, $I_{dc(avg)}$) depends on the reference phase current I_{ref} and the duration for which it is applied, i.e. the conduction angle θ_{cond}. On the other hand, proper selection of θ_{off} will ensure optimum overlap between phases so that the ripple due to phase-to-phase overlap is minimum. In the generator mode, I_{ref}, θ_{cond} and θ_{off} are the control parameters set by the controller. θ_{on} can be calculated from θ_{cond} and θ_{off}. The generator speed is set by the prime mover. The battery terminal voltage (V_{dc}) is the dc-link voltage set by the battery. The dc-link current (I_{dc}) is the generator output current which would dictate the charging rate of the battery in a traction application. All possible values of I_{ref}, θ_{on} and θ_{off} were swept at a particular speed to collect the output data for analysis.

The parameters observed through simulations and experiments are: average dc-link current $I_{dc(avg)}$, dc-link current ripple $I_{dc(ripple)}$, and average torque T_{avg}. The ratio $\frac{I_{dc(ripple)}}{I_{dc(avg)}}$ is considered as a critical parameter that need to be minimized and is designated henceforth as the nominal ripple $I_{ripple-nom}$. θ_{cond} and θ_{off} angles are swept over a range in the generating

region within one electrical period at constant speed and I_{ref}. One electrical cycle (360˚ electrical) is equal to a mechanical rotation of 45˚ for the 12/8 SRM, which gives 22.5˚ (mechanical) of motoring region and 22.5˚ (mechanical) of generating region. The range of conduction angles and turn-off angles swept are as follows:

- θ_{cond} angles are swept between 17˚ and 28˚ (mechanical) in 1˚ increments.
- θ_{off} angles are swept between 12˚ and 26˚ (mechanical) in 1˚ increments.

For the next set of data, I_{ref} is changed to a new set point, and θ_{cond} and θ_{off} angles are swept again for the same speed. I_{ref} currents are swept between 3.5 and 5 amperes in 0.5 Amp increments. The machine rated phase current is 5.5 Amps and the hysteresis band for current regulation is ±0.5 Amp. The data sets are collected for 1000 rpm operating speed for analysis. The simulation results are shown in

Figure *3.4* through Figure 3.6. Efficiency of the SRG drive system can be obtained from the ratio of the electrical power output and the mechanical power input. The power output is $V_{dc}\times I_{dc(avg)}$ while the input power is $T_{avg}\times \omega$, where T_{avg} is the torque and ω is the rotor angular speed. Efficiency is represented by $I_{dc(avg)}$ per unit torque (T_{avg}) in this paper since the prime mover speed on the mechanical input side and the dc-link voltage V_{dc} on the power output side have been maintained as constants in the different sets of experiments. Figure 3.5 shows the effect of applied I_{ref} and θ_{cond} on $\frac{I_{dc(avg)}}{T_{avg}}$ and the $I_{ripple-nom}$. The same amount of average generating current can be obtained with a higher I_{ref} (and corresponding lower θ_{cond}) or a lower I_{ref} (and corresponding higher θ_{cond}). Figure 3.5(a) shows that the lower I_{ref} gives higher efficiency and less $I_{ripple-nom}$ than the higher I_{ref}. Similar trend was obtained for other values of dc-link currents.

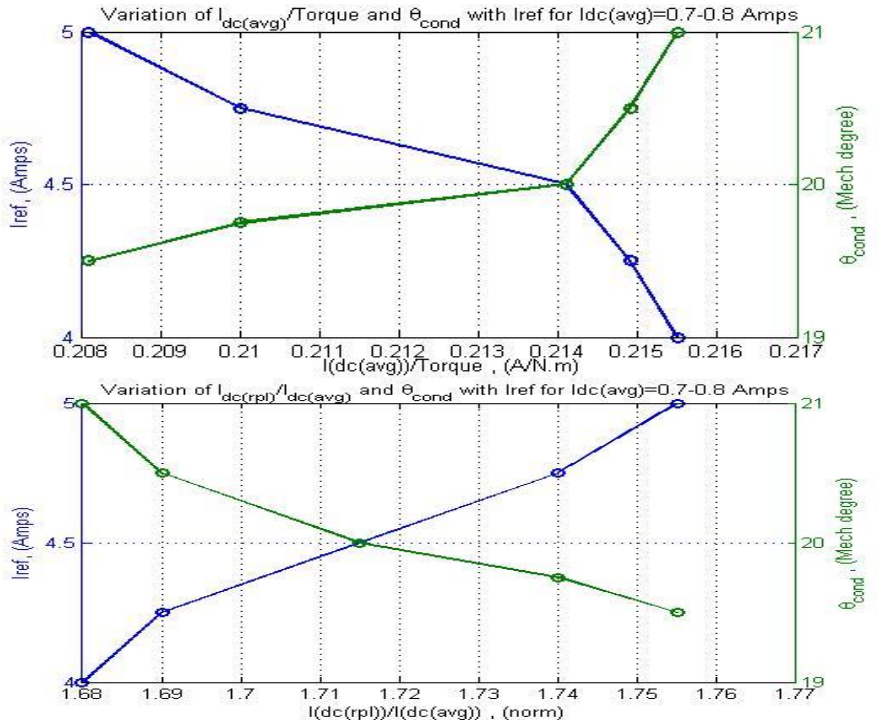

(a)

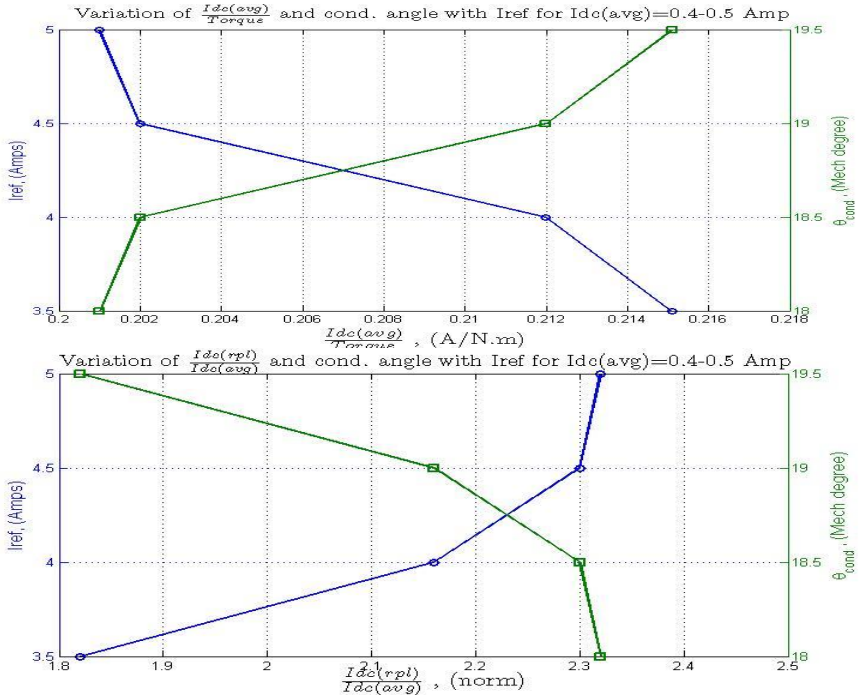

(b)

Figure 3.5: $I_{dc(avg)}/T_{avg}$ and nominal ripple variation with I_{ref} and θ_{cond} for (a) $I_{dc(avg)}$=0.7-0.8 Amp. (b) $I_{dc(avg)}$=0.4-0.5 Amp.

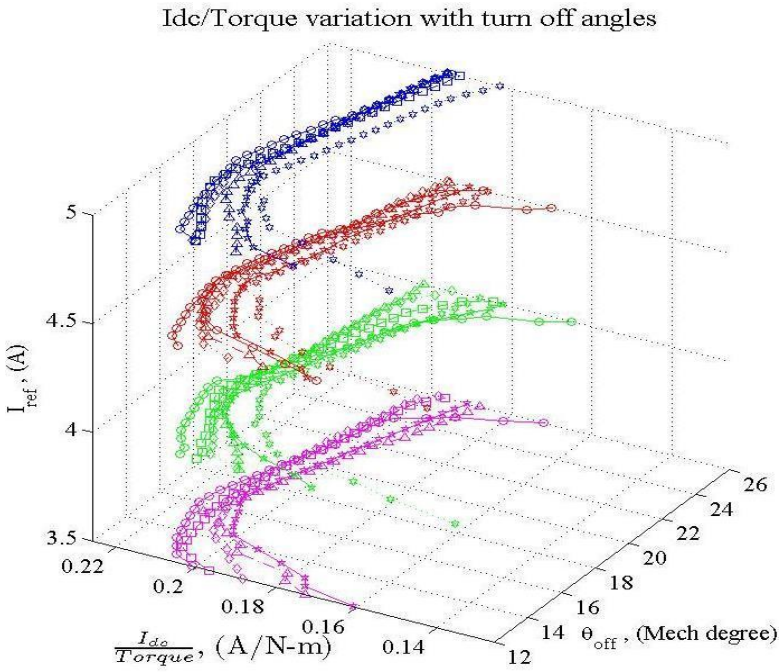

(a)

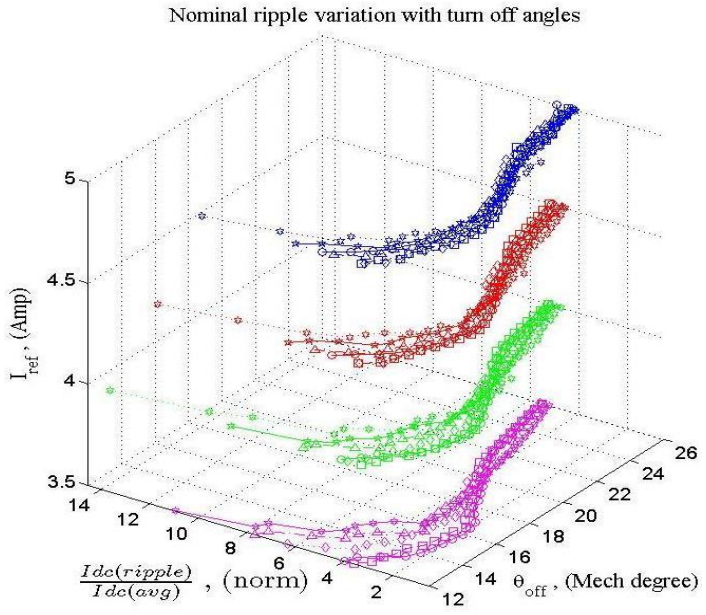

(b)

Figure 3.6: (a) $I_{dc}/Torque$ variation with θ_{off} angles, for different reference currents. (b) Nominal ripple variation with θ_{off} angles, for different reference currents.

Figure 3.6 shows the three-dimensional representations of $\frac{I_{dc(avg)}}{T_{avg}}$ and $I_{ripple-nom}$ variation with θ_{off} for different I_{ref}. As θ_{off} is varied, $\frac{I_{dc(avg)}}{T_{avg}}$ changes and is at its maximum for a particular θ_{off}. The different lines in the figure indicate different θ_{cond}. From this figure, it is observed that for any I_{ref} and θ_{cond}, the efficiency varies with change in θ_{off}. However, the efficiency is the maximum for a particular θ_{off} angle.

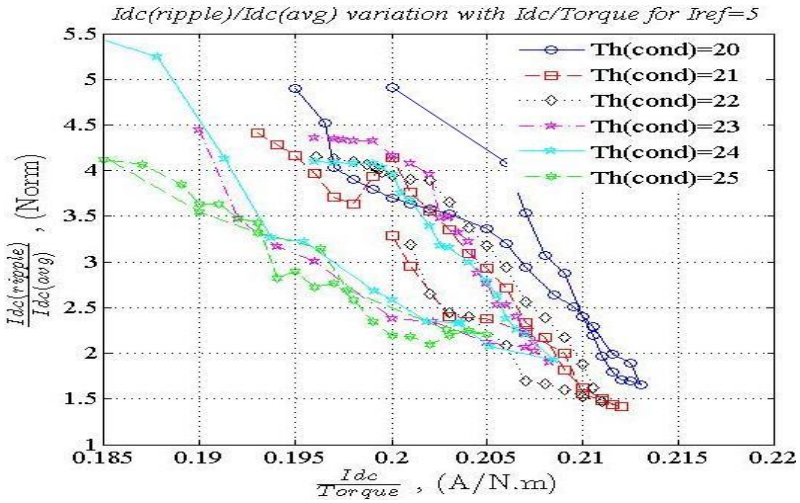

Figure 3.7: $I_{dc}/Torque$ variation with nominal ripple.

Figure 3.7 shows the effect of θ_{off} on $I_{ripple-nom}$ and efficiency more explicitly for I_{ref}=5 Amps. The different lines indicate different θ_{cond}. It is obvious from the figure that efficiency is maximum when $I_{ripple-nom}$ is minimum. The same trend is observed for other values of I_{ref}. This is the key observation that relates efficiency with the dc-link current ripple. It is difficult and costly to measure efficiency during operation as it requires torque information, but $I_{ripple-nom}$ can be measured; minimizing the ripple naturally maximizes the efficiency. Table 3.4 shows the values of I_{ref} and θ_{cond} corresponding to the values of $I_{dc(avg)}$ that gives the most efficient generating mode of operation with minimum dc-link ripple at 1000 rpm.

Table 3.4: I_{ref} and θ_{cond} corresponding to $I_{dc(avg)}$ for optimum generation (simulation) at 1000 rpm.

$I_{dc(avg)}$, Amps	I_{ref}, Amps	θ_{cond}, Mech. degree
0.4-0.5	3.5	19
0.7-0.8	4	19.5
0.9-1.0	4.5	20
1.0-1.1	5	20.5

Similar data was also collected from the experimental setup to corroborate with the simulation data analysis. The three-phase 12/8, 1kW SRM was used for the experiment. The SRG turn-on and turn-off sweep angle generators and current controller were implemented using a TI TMS320F2812 digital signal processor.

Figs. 3.8-3.10 shows the experimental data collected for a prime mover speed of 1000rpm. The efficiency numbers are fairly low in this experiment because of low speeds and low power levels. Low speed generation is expected to have lower efficiency due to the phase winding and switching loss. Figure 3.9 does show that the efficiency numbers improve as power levels are increased. However, the trend in output variation is the same as that obtained from simulation. The three important observations from the data analysis for a given operating condition are:

- Lower I_{ref} (and corresponding higher θ_{cond}) results in higher efficiency than higher I_{ref} (and corresponding lower θ_{cond}) (Figure 3.8, Table 3.4 and Table 3.5)
- Maximum efficiency can be obtained by changing θ_{off} (Figure 3.9), and
- Efficiency is the maximum when $I_{ripple-nom}$ is the minimum (Figure 3.10).

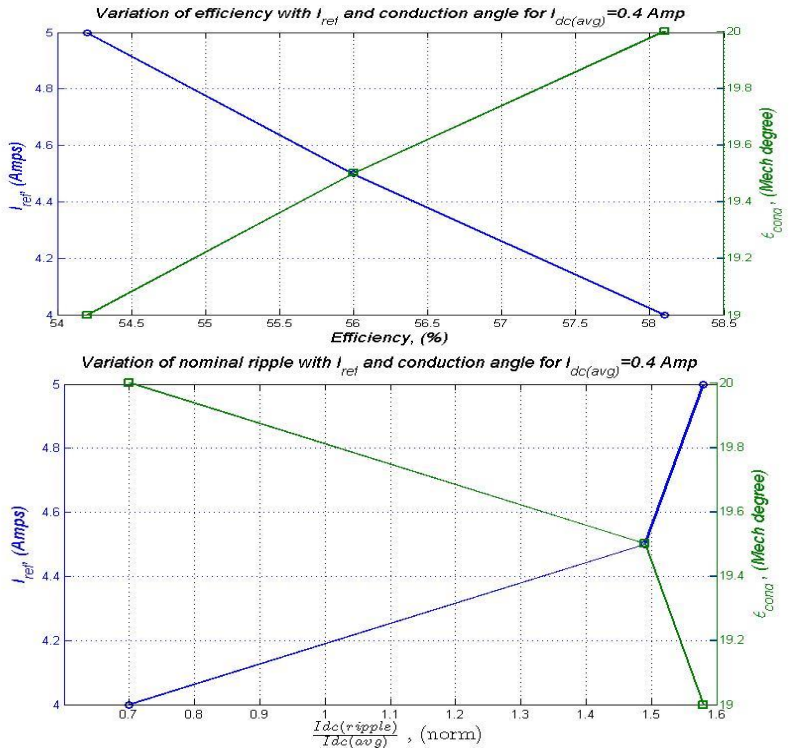

(a)

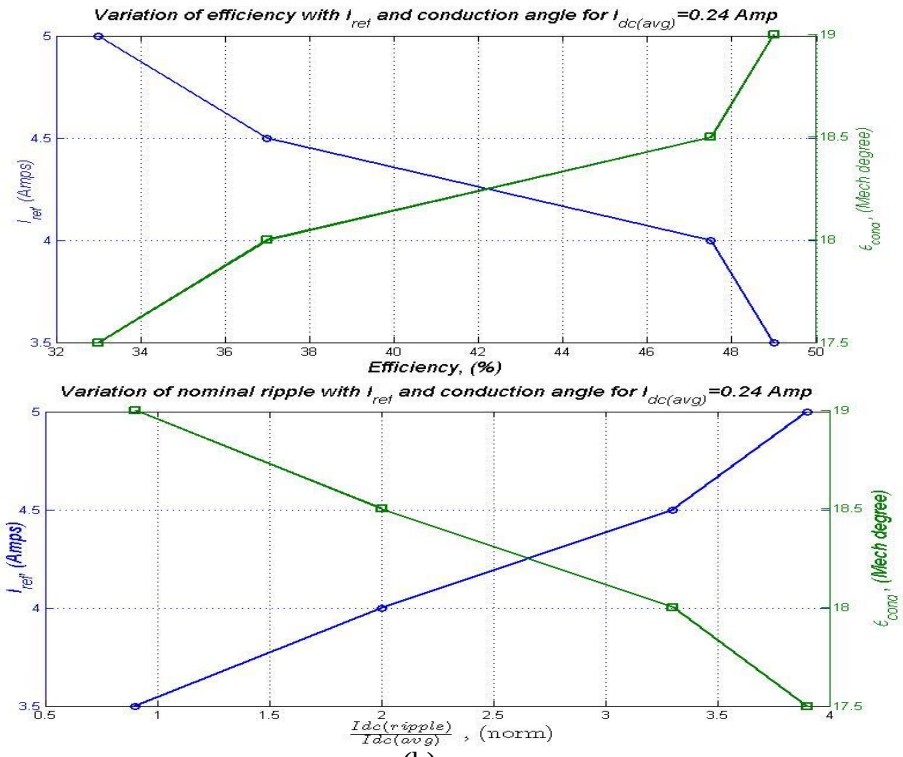

(b)

Figure 3.8: (a) Efficiency and nominal ripple variation with I_{ref} and θ_{cond} for $I_{dc(avg)}$=0.4 Amp (Experimental); (b) Efficiency and nominal ripple variation with I_{ref} and θ_{cond} for $I_{dc(avg)}$=0.24 Amp (Experimental).

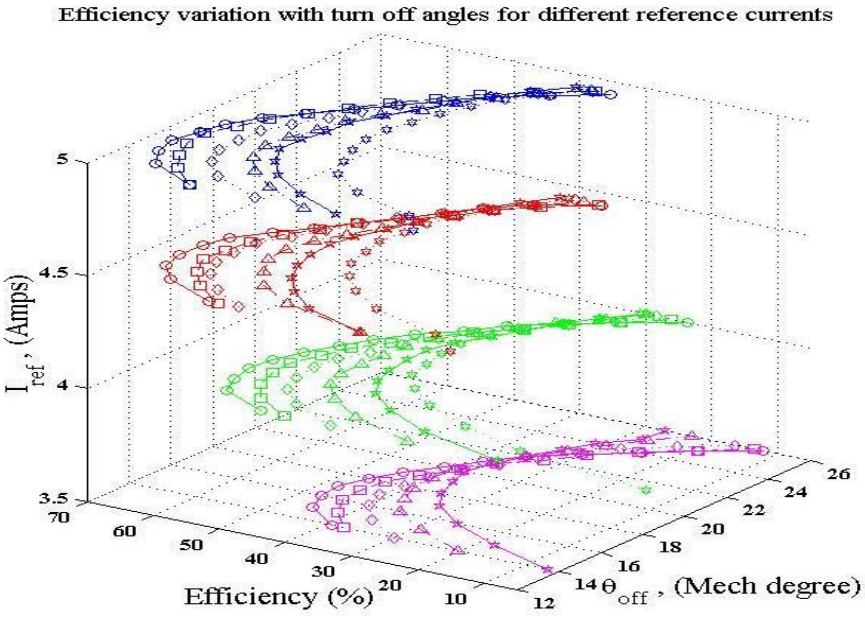

(a)

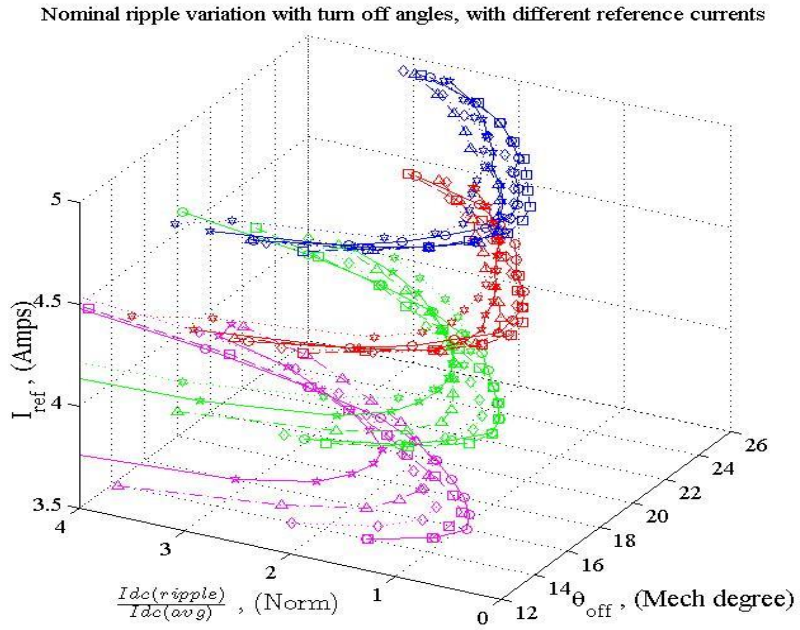

(b)

Figure 3.9: (a) Efficiency variation with θ_{off} angles for different reference currents (Experimental); (b) Nominal ripple variation with θ_{off} angles for different reference currents (Experimental).

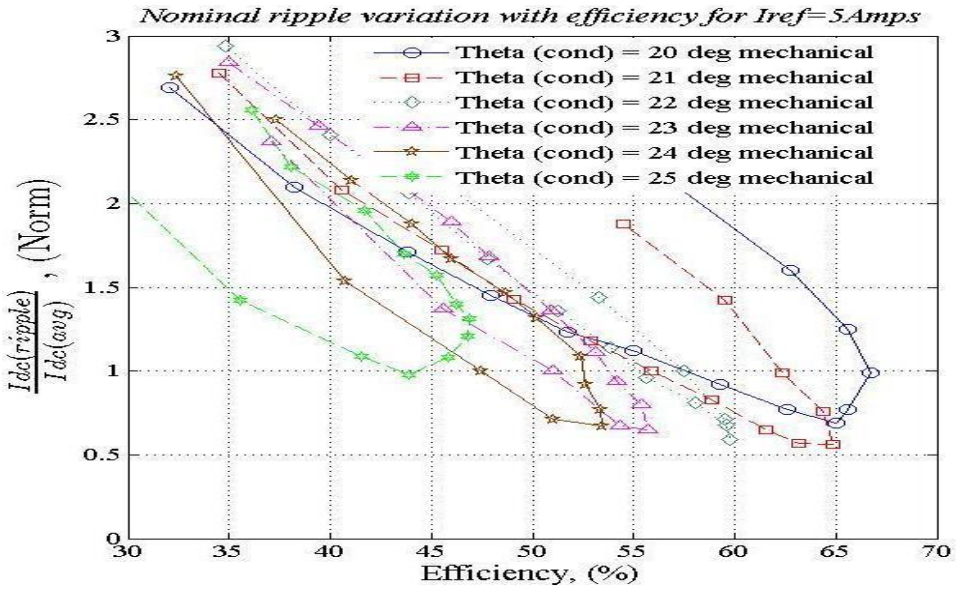

Figure 3.10: Efficiency variation with nominal ripple.

Table 3.5 shows the optimum values of I_{ref} and corresponding θ_{cond} obtained from experimental data for different required $I_{dc(avg)}$ at 1000 rpm. Experimental data shows less generation output than the simulation data since all the losses were not incorporated in the simulation model. However, both simulation and experimental data analysis show similar trends. The optimal controller for the SRG can now be designed and implemented based on the trends observed.

Table 3.5: Optimum I_{ref} and θ_{cond} for different $I_{dc(avg)}$ at 1000 rpm.

$I_{dc(avg)}$, Amps	I_{ref}, Amps	θ_{cond}, Mech. degree
0.24	3.5	19
0.4	4	20
0.58	4.5	21
0.65	5	22

3.5 SRG Controller

The SRG controller developed is based on a two-loop configuration. The average dc-link current output is controlled by adjusting I_{ref} through a PI controller. The conduction angle θ_{cond} is calculated from the reference phase current I_{ref} using a look-up table developed from the simulation and experimental data. The PI controller co-efficients were tuned to achieve zero steady state error with fast transient response. The PI controller output is limited using saturation block to prevent overflow of any parameter. The turn-off angle θ_{off} is controlled through a real-time search algorithm based on minimizing the dc-link current ripple. The two-loop controller block diagram is shown in Figure 3.11.

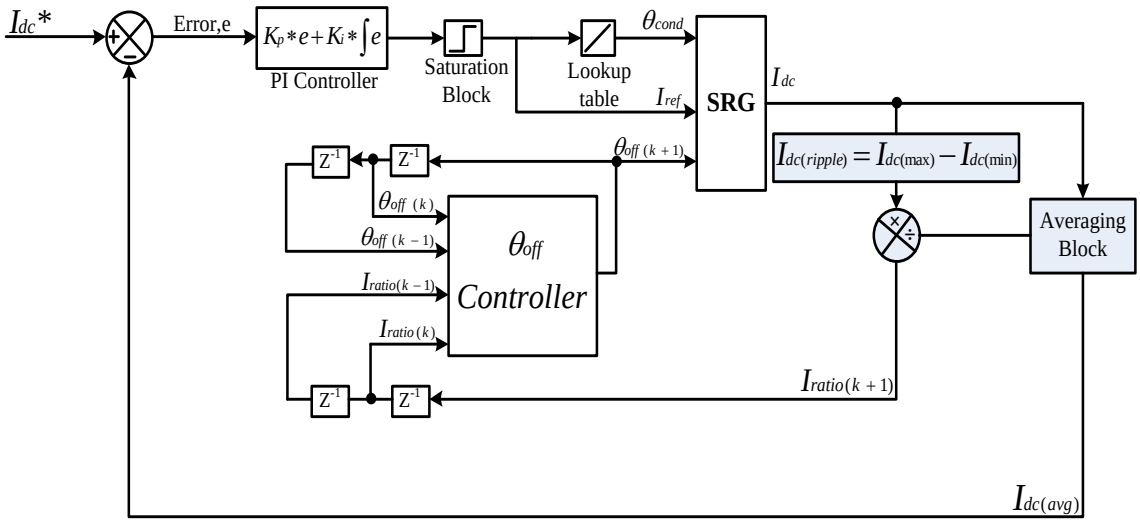

Figure 3.11: Block diagram of the two-loop controller.

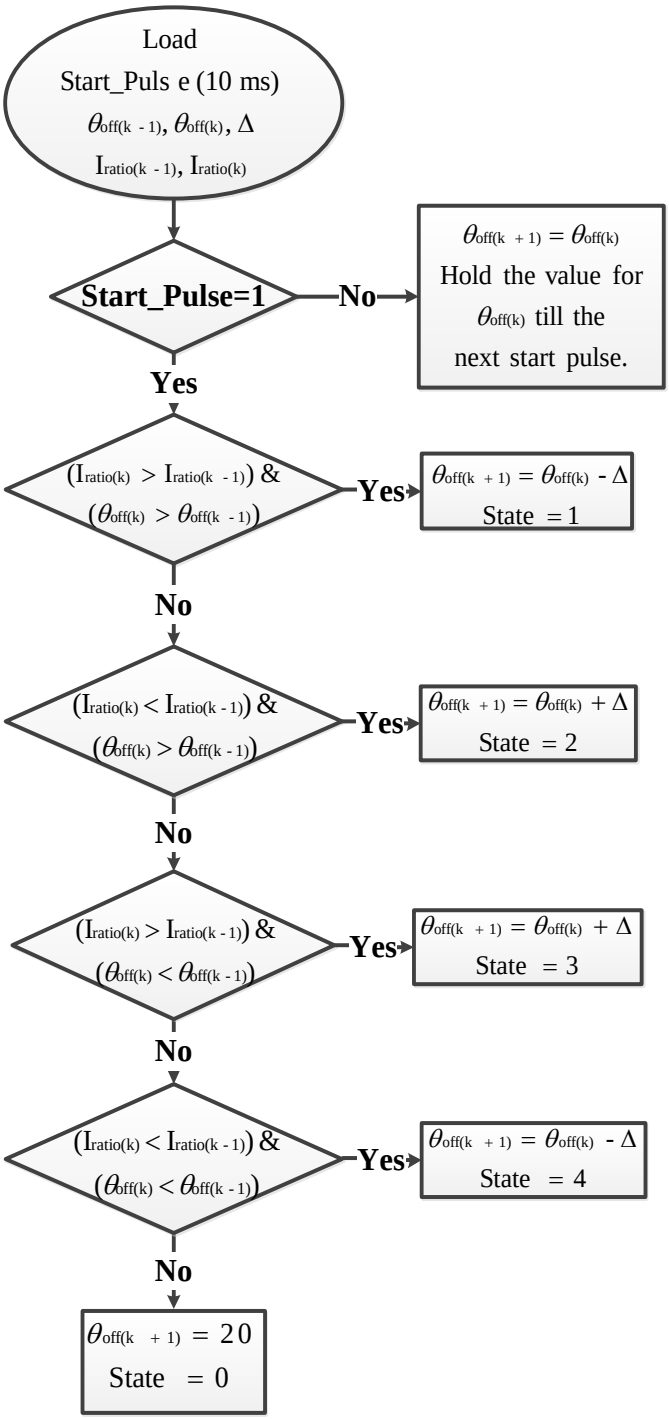

Figure 3.12: Turn-off angle search controller algorithm.

The search controller algorithm implemented to generate the θ_{off} is given in the flowchart of Figure 3.12. The principle of the controller is to perturb θ_{off} to find the direction for minimum $I_{ripple-nom}$ by comparing the latest $I_{ripple-nom}$ to that calculated in the previous step such that the ripple is less than that of the previous step.

The bandwidths of the two loops are partitioned such that the operation of one loop does not affect the functionality of the other loop. One electrical time period of the dc-link ripple current is given by $T_{elec} = \frac{60}{N \times N_r \times m}$ secs for an operating speed of N rpm, N_r number of rotor poles, and m number of phases. Therefore, the PI controller needs at least T_{elec} seconds to calculate $I_{dc(avg)}$ from the previous cycle. The turn off angle controller needs the values of $I_{dc(avg)}$ and $I_{dc(ripple)}$ of at least two previous cycles to calculate the value of θ_{off} for the next cycle; therefore, it should be at least two times slower than the PI controller for stable operation of the two-loop controller. In this research, the PI controller was updated every T_{elec} seconds, and the turn off angle controller was set to be 4 times slower updating every $4T_{elec}$ seconds.

The number of instantaneous current values read by the ADC in each control loop varies with the operating speed. Therefore, there is a loss in precision as the speed increases. This affects the values of DC-link ripple current, DC-link average current and the ratio of both the currents.

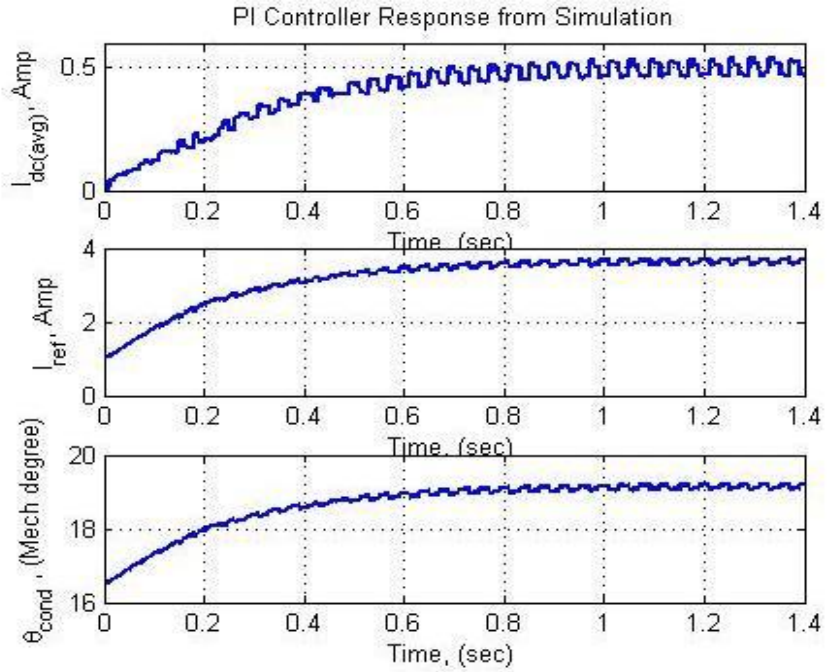

(a)

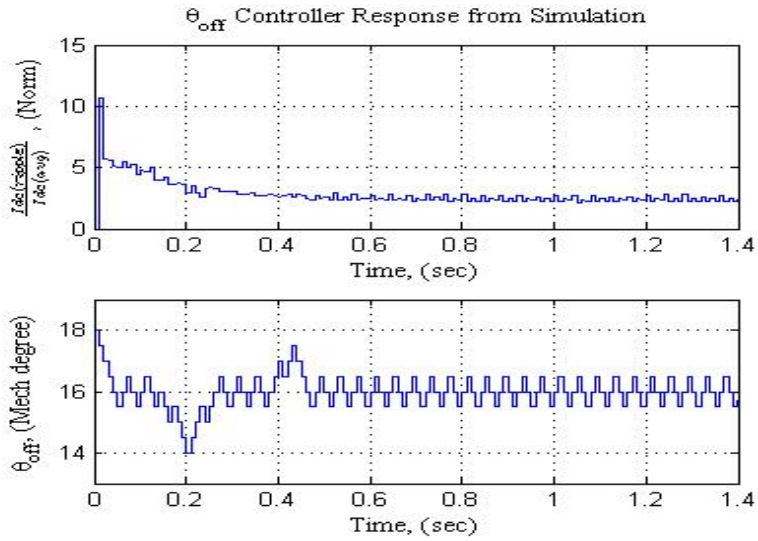

(b)

Figure 3.13: (a) Change in $I_{dc(avg)}$, I_{ref} and θ_{cond} with time for $I_{dc(command)}$=0.5 A (simulation); (b) Change in nominal ripple and θ_{off} for $I_{dc(command)}$=0.5 A (simulation).

The simulation step response with the two-loop controller is shown in Figure 3.13. For an $I_{dc(avg)}$ command of 0.5 A, the PI controller output settles to 3.5 A for I_{ref}. The θ_{off} controller output remains between 15.5 and 16.5 mechanical degrees for the minimum $I_{ripple-nom}$ at

steady state. These results are the same as those obtained from the open loop simulation and experiments.

3.6 Controller Experimental Results

The controller algorithm is implemented in a TI TMS320F2812 DSP processor which controls the SRG drive system. The control loop time in the controller algorithm implemented in the DSP is 33µsecs.

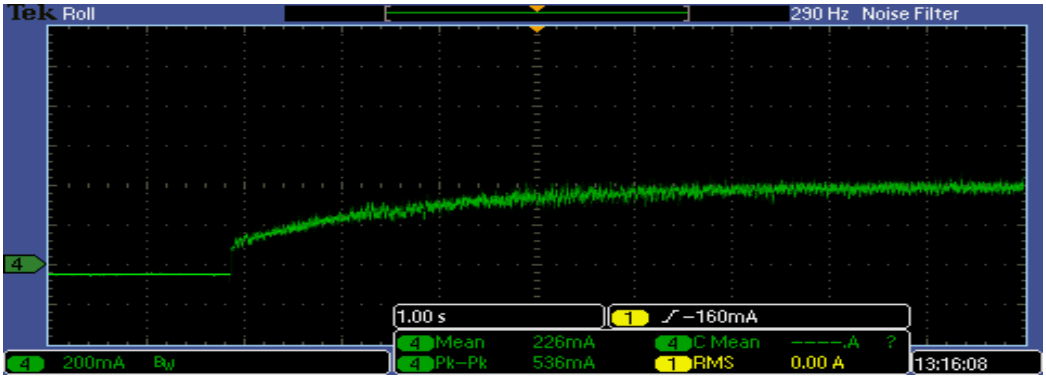

(a)

(b)

Figure 3.14: (a) The step response of $I_{dc(avg)}$ with change in $I_{dc(command)}$ from 0 to 0.4A at 0.2A/div and 1.00 sec/div. (b) Phase current and dc-link current when $I_{dc(command)}$=0.4A (at 0.2A/div and 4.00 msec/div).

Table 3.6: Comparison of optimum values of I_{ref} and θ_{cond} from offline optimization with PI controller set values at 1000 rpm (experiment)

$I_{dc(avg)}^{*}$, Amps	I_{ref}, Amps (Offline)	I_{ref}, Amps (Controller)	θ_{cond}, Mech. Degree, (Offline)	θ_{cond}, Mech. Degree, (Controller)
0.24	3.5	3.49	19	18.89
0.4	4	4.15	20	20.21
0.58	4.5	4.85	21	21.4
0.65	5	5.22	22	22.4

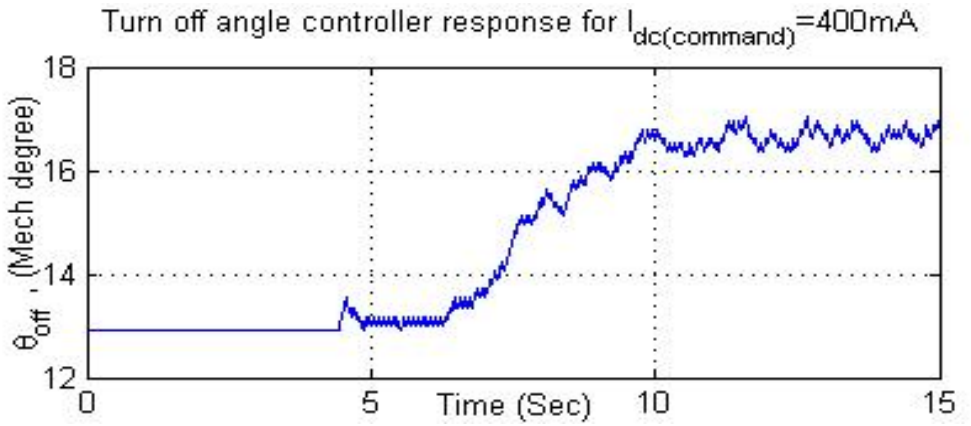

(a)

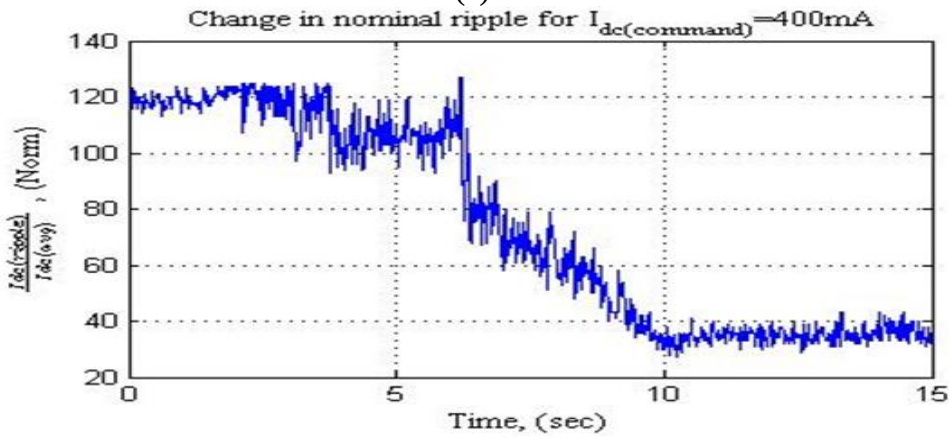

(b)

Figure 3.15: (a) θ_{off} settling when $I_{dc(command)}$=0.4A. (b) Nominal ripple settling when $I_{dc(command)}$=0.4A.

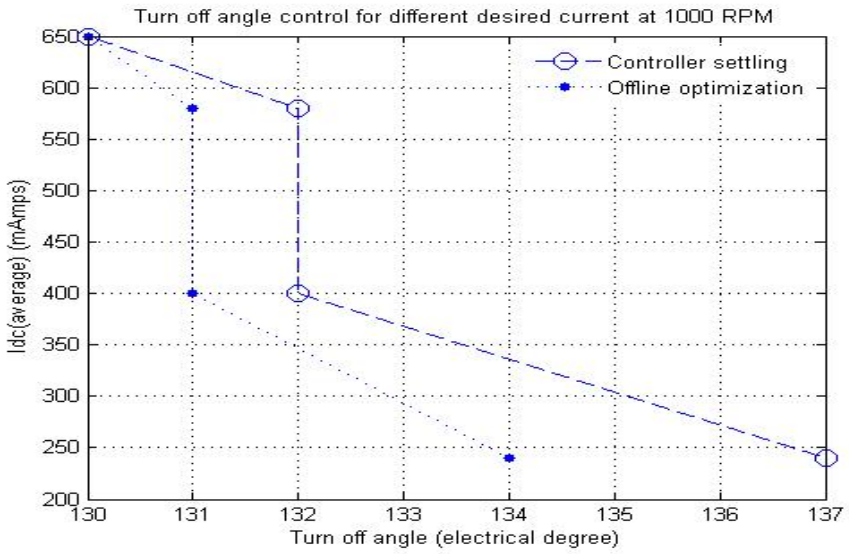

Figure 3.16: Comparison of turn-off angles obtained from offline optimization with the closed-loop turn-off angle controller algorithm tested at 1000 r/min.

The experimental results of I_{ref} and θ_{cond} settling and θ_{off} dynamic real time variation upon reaching the commanded dc-link current level are shown in Figure 3.14 and Figure 3.15(a), respectively at 1000 rpm. Figure 3.15(b) shows the reduction in dc-link ripple as the controller adjusts the θ_{off}, I_{ref} and θ_{cond} appropriately to achieve minimum dc-link ripple, and hence, maximum efficiency. The comparison of I_{ref} and θ_{cond} data from offline optimization and experiment is shown in Table 3.6.

The comparison of θ_{off} angles data from offline optimization and closed-loop experiments at 1000 rpm are shown in Figure 3.16. The speed is kept constant by the prime mover and the output dc-link current is regulated by the controller. The torque should be slightly varying as the efficiency of the system is being optimized through the control. For different $I_{dc(command)}$ set points, the closed loop controller settles down for a new θ_{off}. The difference between offline optimization and controller set value is larger at lower speeds and lower power generating region where the optimal θ_{off} angles are within 2 electrical degrees which is very close to the

resolution of the DSP program. The resolution for different angles (θ_{cond}, θ_{off}, θ_{on}) is 0.2 mechanical degree or 1.6 electrical degrees at 1000 rpm for the 12/8 SRM.

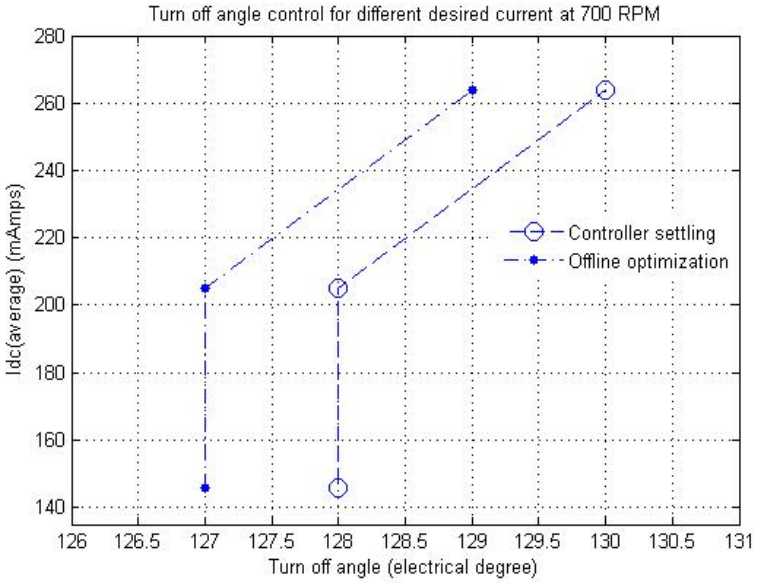

Figure 3.17: Comparison of turn-off angles obtained from offline optimization with the closed-loop turn-off angle controller algorithm tested at 700 rpm.

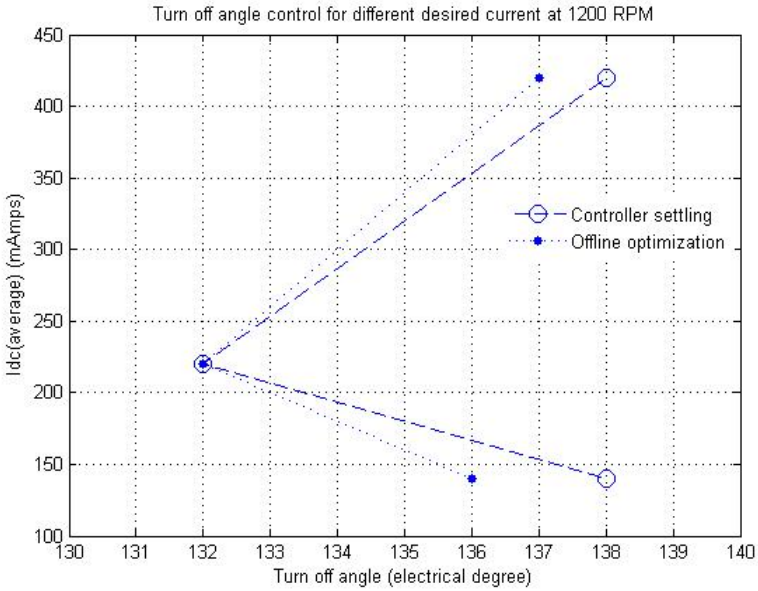

Figure 3.18: Comparison of turn-off angles obtained from offline optimization with the closed-loop turn-off angle controller algorithm tested at 1200 rpm.

To validate the operation of the θ_{off} controller at various speeds, the optimum angles were also determined at 700 rpm and 1200 rpm. Figure 3.17 and Figure 3.18 show the comparison data for θ_{off} angles data from offline optimization and closed-loop experiments. The experimental results obtained with the controllers correlate with the trends observed in Table 3.3 and Table 3.4. Figure 3.15-Figure *3.18* validate the functionality of the closed-loop controller for settling at the optimal commutation angles and I_{ref} for achieving maximum efficiency and minimum dc-link current ripple.

3.7 Conclusion

Offline analysis and optimization with open loop simulation and experimental data have shown that the maximum efficiency operating point in an SRG coincides with the minimum dc-link current ripple. A two-loop control algorithm can then be developed for dc-link current ripple minimization through real time control of the SRG excitation parameters. The developed controller adjusts the excitation parameters online using minimum offline data collection. The method developed is for low speed SRGs, which requires currents regulation on the phases. The controller developed facilitates the most efficient operation of SRG for a wide speed range. The two control loops need to be designed with sufficient bandwidth separation for stable operation. The system and the proposed control algorithm are applicable for traction application where the efficiency of the power conversion is the main concern.

Chapter 4

Comprehensive Design Methodology of FSPM

This chapter presents detailed design steps and procedure that can be applied to design an FSPM of any size. FSPM being a relatively new topology, a comprehensive design methodology is not available as of yet. Moreover, complete analytical model that can be used to estimate the sizing and electromagnetic design of FSPM is also not established as well. Such analytical models and software tools based on such models are traditionally used for an initial estimate about sizing and pole counts before starting to design an electrical machine like IM, PMSM or SR machines for which an established and tested model is available. However, because of the complex structure of the FSPM geometry, it is rather tedious and inefficient to perform a complete physics based modeling and analysis of such machines. In this chapter, existing models, design rules and techniques have been applied simultaneously along with FEA analysis to develop the final design of the machine so as to reflect the actual machine behavior. In doing so, a step by step design methodology have been developed that can be applied to design an FSPM of any size.

In this chapter a general but comprehensive design methodology is discussed with example, in terms of the basic principles of electromagnetics theory and practice. It is possible to include mutual coupling and saturation effects in the model with the help of FEA results of the flux linkage of the machine at different load conditions. Later sections cover more detail specifics about the design and other practical aspects.

4.1 Performance Requirements

Aside from the motor design, there are several other environmental and performance requirements that must be taken into account. A checklist of these are given in Table 4.1.

Table 4.1: Checklist on Application Requirements

1	Continuous power or torque requirement
2	Peak power or torque requirement
3	Maximum speed
4	Supply voltage
5	Supply frequency, AC or DC
6	Type of control required
7	Precision and bandwidth required in closed-loop control
8	Cooling method to be used (Naturally cooled, oil, water)
9	Cogging torque
10	Maximum level of acoustic noise
11	Vibration withstand levels
12	Fault protection

4.2 Design Steps

Design of any electric machine is an iterative process. Before a Flux Switching PM machine design can begin, several important decisions must be made. They include, but are not limited to the choice of number of phases, the number of poles, the number of stator slots, stator-rotor pole combinations and the winding configuration. The steps involved in designing an FSPM are summarized in the flowchart of Figure 4.1.

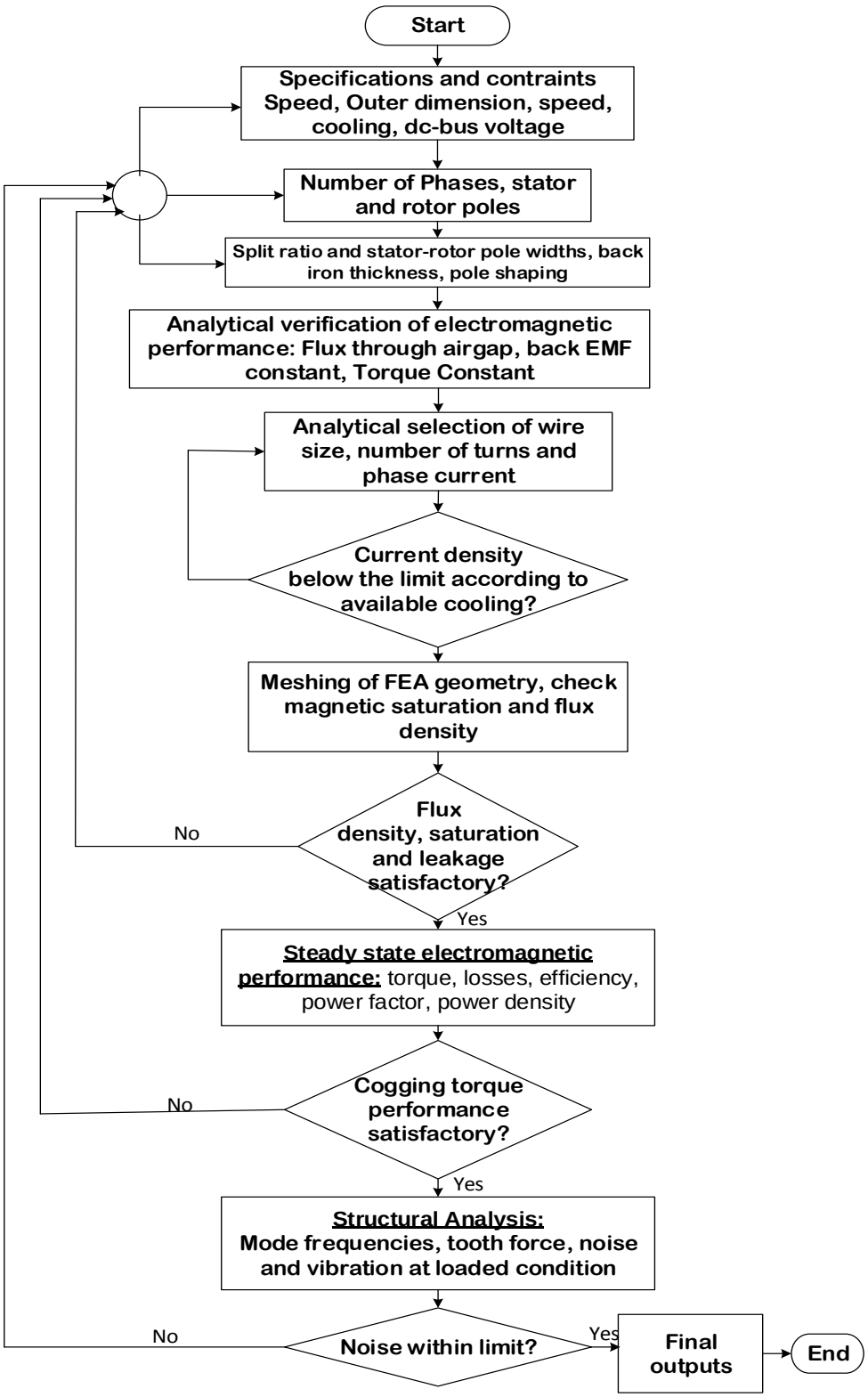

Figure 4.1: Flowchart of the overall design methodology of FSPM.

4.3 Design Constraints

One of the many advantages of FSPM machine is that it can be operated using standard six-switch inverter for a typical PM AC machine. The inverter is to be powered from 115 V AC single phase, full wave rectified to provide 160V DC bus. The machine outer diameter is constrained to 120 mm. The stack length of the machine is constrained to 40 mm. And for magnet materials, we use non-rare earth magnet, namely Hard Ferrite magnetic material. The current density in the coil areas must be below 6 Amps/mm^2 so that the machine will be naturally cooled with air, without any special cooling involved. And the rated speed is 1800 RPM. All these design constraints are summarized in Table 4.2.

Table 4.2: Design constraints of the FSPM

Lamination OD (outer diameter)	D_o	120mm = 4.7244 inch
Stack Length	L_{stk}	40mm = 1.575 inch
Magnet Type	Ferrite	B_m=0.405 T, Permeability=1.2
Voltage	Standard (115 V AC single phase, 160V DC Bus for the 6-switch inverter)	The inverter will be powered from 115V AC single phase, full wave rectified to provide 160V DC bus.

4.4 Selection of Parameters and Configuration

This section discusses the selection of the machine parameters and configuration of the FSPM to be designed. The relationship between the machine dimensions and these parameters are defined here with simplified equations.

4.4.1 Number of Phases

Typically permanent magnet AC machines are often assumed to have three phases but this

is not always the case. The flux reversal machine, which is a predecessor of the modern FSPM, was proposed as a single-phase machine in 1955. The single phase FRM suffered from disadvantages like (i) poor usage of rotor volume, (ii) stator vibration and (iii) difficulties in manufacturing the stator, and (iv) high cogging torque. To improve torque density, reduce stator vibration and simplify the manufacturing process, an improved single phase [53] was later proposed by increasing the number of rotor poles. It also increases the number of energy cycles per revolution. Phase inductance is drastically reduced and does not vary notably with rotor position. So the reluctance torque is small although the cogging torque was still rather high. To maintain the advantages of single phase FRM and reduce cogging torque, three-phase machine was proposed.

Three-phase machines are by far the most common choice for all but the lowest power levels. In common with AC machines generally, they have extremely good utilization of copper, iron, magnet, insulating materials and Silicon, in terms of quantity of these materials required for a given output power. Although the utilization can theoretically be argued to be higher in machines with higher phase counts, the gains would be offset by the increased number of leads and transistors, which increases cost, adds complexity in the control and may severely compromise reliability.

Three phase machines have the flexibility afforded by wye- or delta- connected windings, or even unipolar windings. They can operate with only three connecting leads with no loss of control flexibility. They have excellent starting characteristics, with smooth rotation in either direction, and low torque ripple. They can also work with a very wide range of magnet configurations and an enormous range of winding configurations. They can operate with either square-wave drive or sinewave drive, and are well adapted to the development of ‘sensorless’

control that require no position feedback.

4.4.2 Number of Stator and Rotor Poles

We choose to design a three-phase, fractional slot, non-overlapping winding machine. Choosing the number of stator and rotor poles is very important to obtain high torque density and high efficiency. In this topology the spoke type magnets in adjacent poles are directed opposite to each other. And in stator, a phase coil is wound around each magnet piece. Therefore, for the sake of symmetry, the number of stator poles must satisfy the following two criterion (i) Ns must be even, and (ii) Ns must be an integer multiple of 3. Satisfying these two criterion, for a three-phase FSPM, Ns must be a multiple of 6. Once the number of stator poles are fixed, any number of rotors can possibly be chosen except Ns=Nr for which it will generate no back EMF and thus no torque. Thus for a three phase machine, following two criterion must be satisfied:

$$N_s = 6k_1, k_1 = 1,2,3\ any\ integer\ number$$

$$N_r = N_s \pm k_2, k_2 = 1,2,3\ any\ integer\ number$$

A simple analysis using permeance method [74], [97] was performed to predict the torque constant as a function of Ns and Nr.

$$k_T \propto k_a = \sum_{i=0}^{1} (-1)^i \frac{1 + sin\left\{(-1)^i \frac{N_r \pi}{2N_s}\right\}}{2 + 2\,cos\frac{N_r \pi}{2N_s} sin\left\{(-1)^i \frac{N_r \pi}{N_s}\right\}} \qquad \ldots(4.1)$$

Where. $N_r k_a$ is proportional to the back EMF, and consequently the torque constant kT, it can be used to predict and compare the relative torque capability of alternate machine designs having different combinations of stator and rotor pole numbers. The magnitude variation of back EMF in one phase coil with the number of rotor poles in the 12-stator pole FSPM machine

is predicted by this formula and is compared with that predicted by FE analyses. It shows that the variation trend of the torque capability with number of rotor poles. The maximum torque is obtained when the rotor pole number is close to the stator pole numbers, similar to the conventional fractional slot PM machines.

Another concern is sinusoidal back EMF. In order to minimize torque ripple, a sinusoidal back EMF is desirable [98]. A three-phase, 12-stator pole FSPM contains 4 coils in each phase. In [99], authors showed that even if single coil back EMF is asymmetric, the resultant phase back EMF is symmetrical. The winding configuration of the studied topologies will be all poles wound. In order to obtain balanced symmetrical back EMF waveforms in three phase all poles wound FSPM machines, following equations has to be satisfied [74]

$$\frac{N_s}{GCD(N_s, N_r)} = 6k, k \in N \qquad \ldots(4.2)$$

In this Eq. (4.2), GCD refers to the greatest common divisor. For Ns=12, the only rotor poles possibilities that satisfy this relation, and that are close to 12, are $N_s \in \{10, 11, 13, 14\}$.

The required winding connection depends on the coil EMF vectors. However, it should be noted that the electrical degrees α_e between two vectors can be derived from the mechanical degrees α_m as [97]

$$\alpha_e = N_r \alpha_m \qquad \ldots(4.3)$$

It should be noted that the rotor pole numbers in an FSPM machine is equivalent to the number of pole pairs of rotor magnets in a conventional fractional slot PM machine. The electrical frequency, *f* in the FSPM machine is proportional to the number of rotor poles,

$$f = \frac{N_r n_r}{60} \qquad \ldots(4.4)$$

Table 4.3: Some possible stator/rotor pole combinations for 3-phase FSPM

No of stator poles	**6**					
No of rotor poles	4	5	6	7	8	9
Back EMF Magnitude	Good	Very Good	0	Very Good	Good	Okay
Winding type	Alternate poles wound, Concentrated	All poles wound, Concentrated	-	All poles wound, Concentrated	Alternate poles wound, Concentrated	
UMF	✓	✗	✗	✗	✓	✗
No of stator poles	**12**					
No of rotor poles	9	10	11	12	13	14
Back EMF Magnitude	Good	Very Good	Very Good	0	Very Good	Very Good
Winding type	All poles wound, Concentrated	All poles wound, Concentrated	All poles wound, Concentrated		All poles wound, Concentrated	All poles wound, Concentrated
UMF	✗	✓	✗	✗	✗	✓

Few possible combinations of stator/rotor poles and along with their back EMF, required winding type and UMF is summarized in Table 4.3.

4.4.3 Pole Widths, Airgap and Split Ratio

In [54] that described the basic operating principle of FSPM machines, the stator slot width, the stator tooth width and stator magnet thickness are assumed to be equal. Later in [100], It was shown that expanding stator tooth width above the original value (equal to the width of slot opening) would lead to a reduced electromagnetic torque for same copper losses. So the original design where the tooth width is equal to the slot opening offers the highest output torque. Reducing the stator tooth width also reduces phase flux linkage, and hence the

torque is reduced significantly. Similarly, increasing stator tooth width reduces the slot area, and hence the phase current has to be reduced for a fixed copper loss which also leads to a reduction in torque.

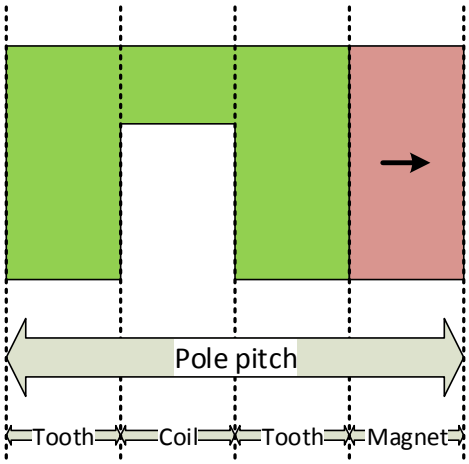

Figure 4.2: Accommodating teeth, coil and magnet within one stator pole pitch.

It is always desirable to minimize the magnet volume without sacrificing machine's electromagnetic performance. If the magnet thickness is reduced, the slot area increases. However, reducing magnet thickness have overall adverse effect on the machine output as it surpasses the little additional winding area that can be used have more electrical loading. Figure 4.2 shows the spread of stator tooth tips, coil and magnet within one stator pole pitch.

The stator back iron thickness of the each U-shaped segment is another design parameter which should also be looked into. From the flux distribution, it can be seen that the flux density in the stator back iron is much lower than that in the stator teeth due to leakage flux. So the back iron thickness can be reduced without sacrificing the machine output much. However, reducing the back iron thickness would reduce the stiffness of the structure, which might have adverse effect on the machine's structural performance, which is discussed in detail in a later chapter. For the initial design, the back-iron thickness is kept as the same as stator tooth width

so that the flux has uniform width through the path it travels.

Torque is also influenced by the stator inner to outer ratio or the split ratio. For many electric machines, torque is usually proportional to the square of the rotor diameter, while the stator slot area reduces as the rotor diameter is increased. In [100], it has been reported that 0.55~0.6 provides maximum output torque for a fixed copper loss.

Basically, the design objective of such PM AC machine is to achieve a sinusoidal back EMF, with minimum harmonics, balanced usage of magnet and iron, yielding a balanced electric and magnetic loading, maximizing the torque and power density of the machine. Again, this is an iterative process and achieving one objective can push a designer to sacrifice another. By extensive parameter sweeping in the FEA, the above goals have been achieved and the design rules have been verified and applied accordingly.

4.5 Design Data

Designing an electric machine is an iterative process. One has to go back and forth and recheck all the important parameters many times as shown in the flowchart before a design is finalized for manufacturing. At the same time, the required components of the motor-drive system are also designed around the machine design. However, once the stator rotor pole combination, airgap, stator-rotor pole width, magnet width and split ratio are determined, it is possible to build the whole machine in FEA, create mesh, check its performance and go back in case some modification is required.

The machine geometry was drawn in a parametrized way. Which means the design characteristics and analysis can be done with the variation of any geometric parameter. For

example, if the outer radius of the machine is changed, the other parameters affected by it will adjust themselves accordingly. However, it is always advisable to check with all the important parameters carefully if a design is modified or any of the small portions are resized.

Figure 4.3 shows the cross section of an FSPM with 12 stator poles and 10 rotor poles. As a design constraint, the OD (outer diameter of the stator), stack length and operating speed are known. Our objective is to design an FSPM within the constraints and estimate its number of turns, suitable current, and voltage rating (input) as well as possible output (torque, power) at rated speed. Once the estimates are obtained, we can implement the geometry, excitation current and number of turns to verify the estimates about output (torque, power) as well as fine tune the design. The cross section of the machine with FE generated mesh is shown in Figure 4.4.

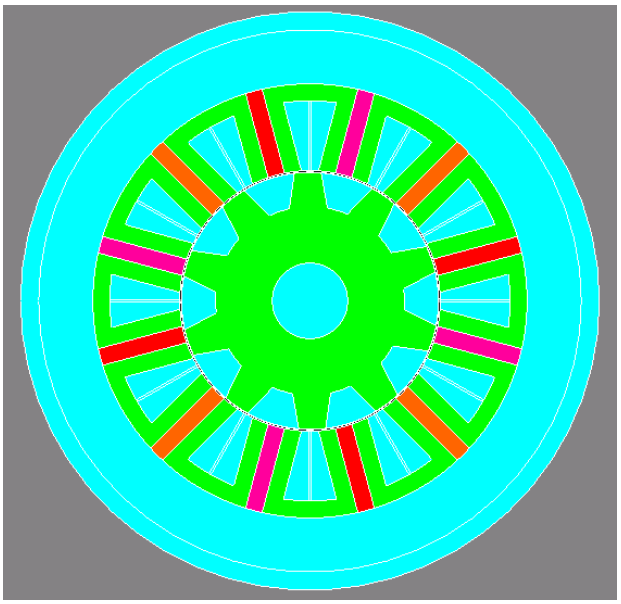

Figure 4.3: Cross section view of the FSPM geometry in FEA.

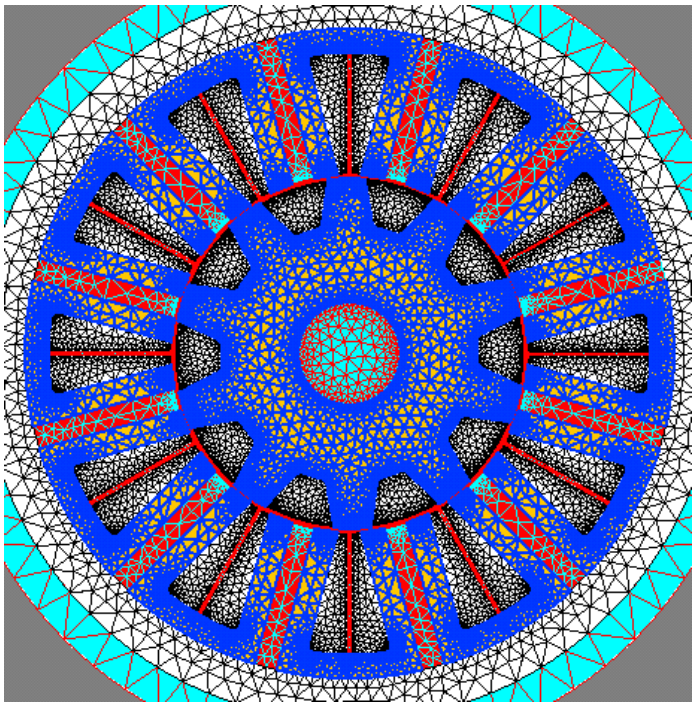

Figure 4.4: Geometry of the designed machine with FE Mesh.

4.6 Design Specifications

A 12/10, Ferrite magnet FSPM is designed within the frame size of OD=120mm, L_{stk}=40mm. A ferrite magnet FSPM machine can achieve very close power density of a PM-BLDC machine of same size with NdFeB magnet. Details analysis and performance of the machine will be provided in the following sections. Table 4.4 below provides the FSPM machine specifications.

Table 4.4: Design specifications of the FSPM

Parameter	**Value**
Stator Outer Radius	2.36 inch (60 mm)
Stack Length	1.575 inch (40 mm)
Rated Mechanical Power Output	520 W
Rated Torque	2.76 Nm.
Rated Speed	1800 RPM
Power Density Utilized	1.15 MW/m^3
Coil Turns	47
Winding Type	Fractional Slot, Non-overlapping, Concentrated
Maximum Ampere turns with natural air cooling	180 Amp-Turns per slot, 720 per phase
Rated Line Current	3.83 Amp
Volts	230V AC single phase, full wave rectified to provide 300V DC bus.
Power Input	558 W
Copper Loss	20 W
Core Loss	18 W
Magnet Loss	Negligible.
Total Losses	38 W
Power Output (Mechanical)	520 W
Efficiency	90 %
Power Factor	0.77

Table 4.5 below gives an overview about the material usage in the designed machine. The prototype (motor only) would weigh roughly about 2700 grams, with only 270 grams of magnet.

Table 4.5: Material Usage in the Designed Machine

	Volume	**Weight or Mass**
Steel in Stator	$1.45 \times 10^{-4}\ m^3$	1.1 kg
Steel in Rotor	$1.14 \times 10^{-4}\ m^3$	0.8 kg
Total Steel	$2.59 \times 10^{-4}\ m^3$	1.9 kg
Magnet	$5.44 \times 10^{-5}\ m^3$	0.27 kg
Copper	$8.4 \times 10^{-5}\ m^3$	0.75 kg
Total		2.673 kg

4.7 Geometric Parameters

Based on the U-core 12/10 FSPM topology, the geometric parameters of the FSPM with same outer dimensions as the aforementioned induction machine are listed in table. Figure 4.5 graphically shows the geometric parameters in the machine cross-section.

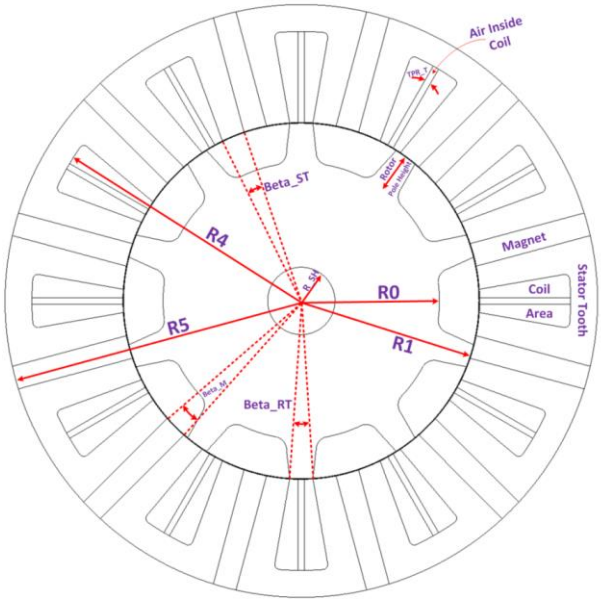

(a)

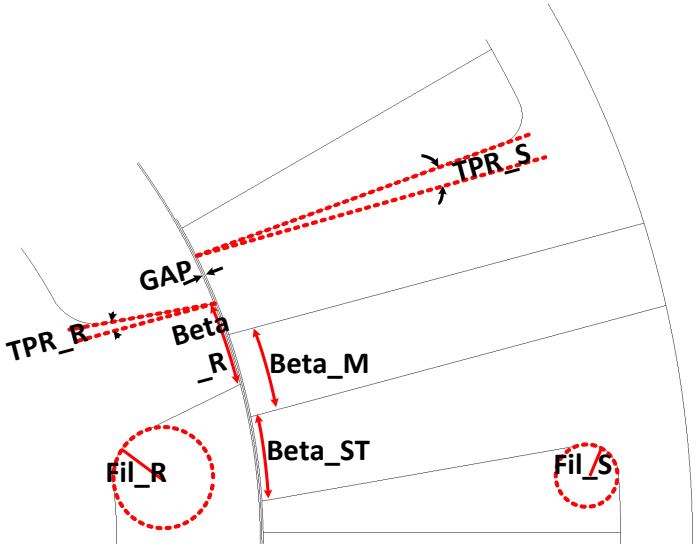

(b)

Figure 4.5: Geometric parameters of the FSPM designed (a) whole machine, (b) closer view of one stator and one rotor pole.

Table 4.6 presents the detailed geometric parameters used for the design of the machine and their values.

Table 4.6: Geometric parameters of the FSPM

Parameter	**Value**	**Formula/Relation with other Parameter**	**Value**
Given Basic Specs for machine size:			
R5	Machine Outer Radius		60 mm
LSTK	Length of Stack		40 mm
Optimum pole count			
Ns	No. of Stator Poles		12
Nr	No. of Rotor Poles		10
Calculation based lengths/radius			
R4	Stator Tooth Inner Radius	$R_5 - WST$	55.3 mm
R3	Stator PM and Tooth Inner Radius	$0.6(Split\ Ratio) \times R_5$	36 mm
R1	Rotor Outer Radius	$R_3 - GAP$	35.5 mm
R0	Rotor Inner Radius	$R_1 - HRP$	26.075 mm
RSH	Shaft Radius		10.43 mm
GAP	Air Gap Depth		0.5 mm
Pole, tooth, magnet and coil related parameters			
BETA_S	Angular Stator Pitch	$\frac{360}{N_S}$	30°
BETA_ST	Angular Stator Tooth Width	$Initial\ Value = \frac{\beta_S}{4}$	7.5°
BETA_C	Angular Coil Width	$Initial\ Value = \frac{\beta_S}{8} - \frac{TPRT}{2}$	3.25
BETA_M	Angular Magnet Width	$Initial\ Value = \frac{\beta_S}{4}$	7.5
BETA_R	Angular Rotor Pitch	$Initial\ Value = \frac{360}{N_R}$	36
BETA_RT	Angular Rotor Tooth Width	$Initial\ Value = \beta_{ST}$ $1.4\beta_{ST}$ (10.5)for sinusoidal BEMF, $1.6\beta_{ST}$ (12) for max torque	12°
WST	Stator Segment Tooth Width	$\frac{\beta_{ST} \times \pi \times R_3}{180}$	4.7 mm
TPM	PM Thickness	$\frac{\beta_M \times \pi \times R_3}{180}$	4.7 mm
WRP	Rotor Pole Width	$1.6 \times WST$	7.5 mm
HRP	Rotor Pole Height	$2 \times WST$	9.4 mm
Additional optimization and pole shaping			
TPRT	Air Depth Angle Inside Coil		1
TPR_S	Stator Pole Taper Angle		*0*
TPR_R	Rotor Pole Taper Angle		*10*
FIL_S	Stator Pole Fillet Radius		*2*
FIL_R	Rotor Pole Fillet Radius		*1*

4.8 Winding Connections

The stator is Y-connected, three phase, having a concentrated winding. For a 12/10, three phase machine, each phase contains four coils. These four coils can either be in series or in parallel. Arranging the coils in parallel have the risk of circulating current among the coils, giving rise to unbalanced flux linkage and large harmonic components. Therefore series connected coils are preferred and used in the design.

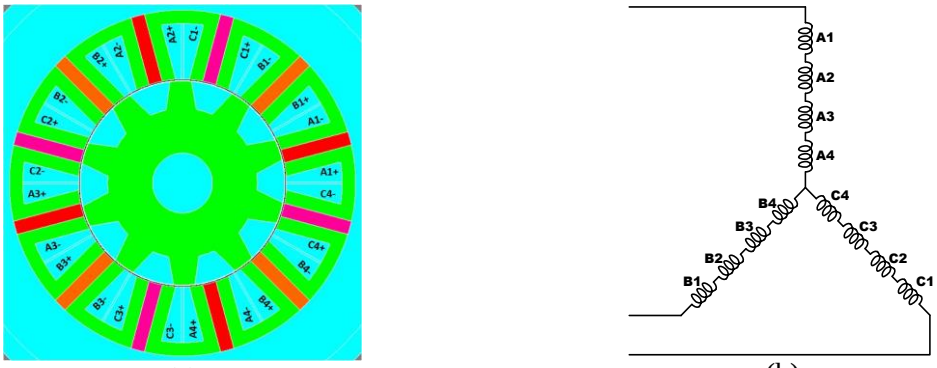

(a) (b)

Figure 4.6: Coil connection of the 12/10 FSPM (a) Face region marked with associated coil. (b) Three-phase, Y-connected armature coils circuit.

Figure 4.6 shows the coil connection of the three-phase, Y-connected winding of the designed FSPM. For a 12 pole, three-phase machine, each phase contains four coil pairs to be wound. The following section illustrates the selection of wire gauge, number of strands per turn of that wire gauge and calculation of appropriate winding resistance based on that.

The main goal in designing an FSPM is to provide the maximum number of flux lines per pole φ in such a configuration as to cost as little as possible (in terms of magnet cost), with the minimum amount of flux leakage. Before calculating the flux, however, it is recommended to understand the EMF and torque constants which link the electrical, magnetic and mechanical aspects of the design.

4.9 Analytical Verification of Design Parameters

4.9.1 Calculation of Flux

The airgap applies a static demagnetizing field to the magnet, causing it to operate below its remnant flux density. With no current in the phase windings, the operating point is typically at the point labeled open circuit in fig with magnet flux density Bm of the order of 0.7-0.95 times Br. The characteristics of a permanent magnet are shown graphically in Figure 4.7. It shows the relations between magnet flux and MMF, along with relating flux density with magnetizing force. The amount of flux that can be produced in an infinitely permeable material expresses the maximum available flux from the magnet is known as remnant flux Φr. The external demagnetizing MMF that must be applied to suppress all of the magnet flux is known as coercive MMF, F_c.

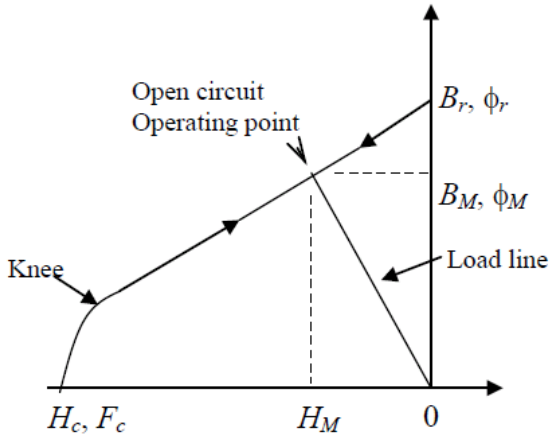

Figure 4.7: Typical Flux-MMF and B-H characteristics of a permanent magnet material.

The line from the origin through the open-circuit operating point is called the load-line. The slope of the load-line is the permeance co-efficient (PC). The permeance co-efficient is typically in the range of (5-15)

$$PC = \frac{B_M}{\mu_0 H_M} \qquad \ldots(4.5)$$

Figure 4.8 shows the magnetic equivalent circuit of one pole. The main flux or airgap flux φ_g crosses the airgap and lnks the coils of the phase windings. The magnet flux φ_M is the flux passing through the magnet and the leakage flux φ_L is the part of magnet flux that fails to link the phase windings. φ_g and φ_L are related to each other by a leakage co-efficient f_{lkg}

$$f_{lkg} = \frac{\varphi_g}{\varphi_M} = \frac{\varphi_g}{\varphi_g + \varphi_L} \qquad (4.6)$$

The leakage co-efficient is less that unity and its value depends on the configuration of the motor. Assuming very low leakage, typical 0.9 is used as a safely assumed value.

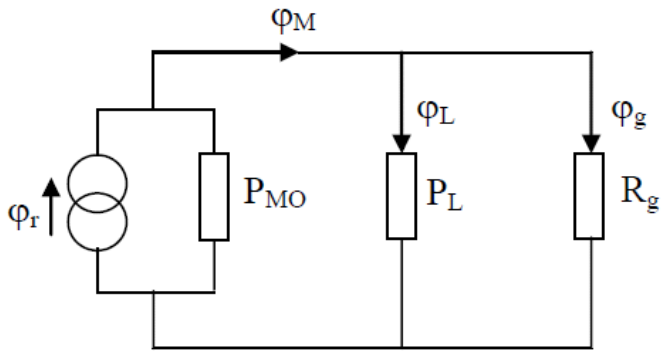

Figure 4.8: Simplified magnetic equivalent circuit for one pole of PM machine.

The airgap flux density B_g is related to B_M as

$$B_g = \mu_0 H_g = \frac{\varphi_g}{A_g} = \frac{f_{lkg}\varphi_M}{A_g} = \frac{f_{lkg} A_M B_M}{A_g} \qquad \ldots(4.7)$$

Where H_g the magnetic field in the airgap and A_g is the pole area at the airgap. Applying Ampere's law in the magnetic equivalent circuit,

$$2H_M l_m + 2H_g g = 0 => H_M l_m = -H_g g$$

The following relation can be derived from above equations

$$PC = \frac{B_M}{\mu_0 H_M} = \frac{1}{f_{lkg}} \times \frac{A_g}{A_M} \times \frac{l_m}{g} \quad \ldots(4.8)$$

P_{mo} in Figure 4.8 is the magnet internal permeance given by

$$P_{MO} = \mu_{rec}\mu_0 \frac{A_M}{l_m} \quad \ldots(4.9)$$

An example B-H curve of Allen-Bradley/TDK material known as FB4B Ferrite magnet is shown in Figure 4.9. If magnet pieces of uniform thickness and uniform magnetization are used, the resulting flux lines across the airgap should be uniform except where the stator slot openings are located.

Considering that only one magnet piece is contributing to the flux through each pole at the airgap, from the FEA drawing, L_m=4.717 mm, A_m=288.372 mm^2, A_g=221.48 mm^2, g=0.5 mm. Using these, PC becomes 7.24. From the demagnetization curve, it is obvious that for PC above 10, the flux density (B_m) does not change much and around the value of 3300 Gauss. So B_m=3300 Gauss is used for further calculation of flux.

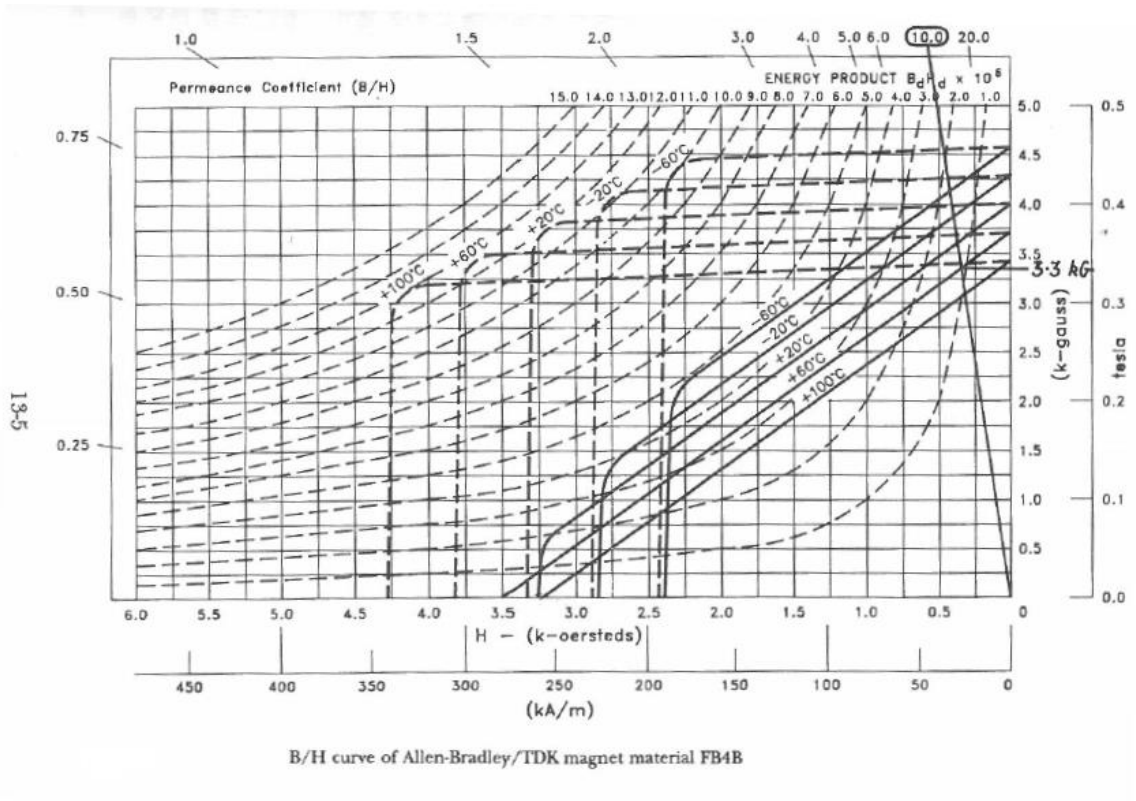

Figure 4.9: B/H Curve of Allen-Bradley/TDK magnet material FB4B [101].

4.9.2 Flux through Airgap (φ)

The intersection of load line with the B-H curve of the magnet at assumed temperature (60°C is a good choice for small machines) provides the operating flux density (B_m) of the magnet and field intensity. Therefore its Y-axis co-ordinate can be used as B_m. From the demagnetization curve of Figure 4.9, B_m=3300 Gauss (Assuming PC=10) and magnet area, A_m = 1.485 inch^2 from the FEA geometry. Then

$$\varphi = B_m A_m \times 2.54^2 (number\ of\ flux\ lines)$$

$$\varphi = B_m A_m \times 2.54^2 \times 10^{-7} Weber \qquad \ldots(4.10)$$

When A_m is in square inches, the factor 2.54 squared is multiplied. For our FSPM, φ =3.162×10^{-3} Webers.

4.9.3 Number of Turns per Coil

The next step is to estimate the number of turns per coil. The constraints that affect the number of turns, or the 'Ampere-Turns' of the machine are the applicable cooling method, no-load speed, rated speed and back EMF. In the iterative process, it is important to check all these important parameters that are being affected by the number of turns. One way to estimate the number of turns is via the EMF constant, k_E.

Since the rated operating speed is to be 1800 RPM, a conservative rule of thumb for Ferrite magnet machine is to begin with the rated speed as 80% of the no-load speed, giving

$$\omega_{NL} = \frac{\omega_{rated}}{0.8} \quad \ldots(4.11)$$

The operating or rated speed ω_{rated} is 1800 RPM (=188.5 rad/sec), using this, the no-load speed, $\omega_{NL}$is obtained to be 235 rad/sec.

The inverter will be powered from 115 V AC single phase, full-wave rectified to provide a 160V DC bus. A rough calculation of the EMF constant k_E and torque constant k_T can be determined by setting the back EMF at the no-load speed equal to the DC bus voltage, neglecting losses. Thus

$$k_E = \frac{V_{dc}}{\omega_{NL}}\ V - \frac{s}{rad} \quad \ldots(4.12)$$

$$k_T = 8.85 * k_E\ lbf - \frac{in}{Amp} \quad \ldots(4.13)$$

Using V_{dc}=160, ω_{NL}=235, we obtain k_E=0.68 and k_T=6.029.

As the PM rotor rotates, the flux linkage of a phase winding varies from a positive maximum φ to a negative maximum$-\varphi$. The transition takes place over π electrical radians. An electrical radian is equal to mechanical radians divided by the number of rotor poles Nr in one revolution. If the rotor is rotating at ω_m actual radians per second, the transition time from φ to $-\varphi$ is $\frac{\pi}{\omega_m N_r}$ seconds. If the complete machine has Z conductors, then there are $\frac{1}{3}\times \frac{Z}{2}\ turns/phase$, as one turn comprises of two conductors. Consequently by Faraday's law, with two phases in series at any time for squarewave motor, the average back EMF over half an electrical cycle (π electrical radians or 180 degrees electrical)

$$E = 2 \times \frac{\varphi - (-\varphi)}{\pi/\omega_m N_r} \times \frac{Z}{2 \times 3} \times \frac{1}{a} = \frac{2}{3}\frac{Z\varphi N_r}{a\pi}\omega_m = k_E \omega_m$$

Where a is number of parallel paths (1 for all series connected winding) and C depends on pole arc and winding distribution and connection (maximum value is 1).

However, the effective number of conductors Z must be determined for each situation. Because of the winding distribution, not all of the turns link the maximum flux φ at the same time, and their contributions to the total winding EMF are generally not in phase with each other and should be summed vectorially. The back EMF constant then can be modified to taking these practical factors into account by

$$k_E = \frac{2}{3}\frac{Z\varphi N_r}{a\pi}C$$

Therefore,

$$Z = \frac{3}{2}\frac{1}{C}\frac{\pi k_E}{\varphi N_r} \quad \ldots(4.14)$$

The value of the co-efficient C depends on the pole arc and the winding distribution and connection. To account for these non-idealities, C=0.9 can be assumed for winding and flux distribution effects. Using the values of k_E, C, φ and N_r, we obtain Z=1126. For 12/10 structure, we have 12 coils each with 2 sides. So, number of turns per coil=1126/24=47. This is the initial guess for number of turns.

4.9.4 Wire Size

The maximum wire diameter which will fit is determined by assuming the wire is square and solving for wire diameter D_w using the following equation:

$$D_w = \sqrt{\frac{A_{slot} F_{slot}}{N}} \quad \ldots(4.15)$$

Once D_w is achieved, we have an idea of which wire (from the AWG table) should be used.

From the FEA geometry, slot area is 87.5 mm^2 = 0.1356 $inch^2$. Applying the formulae above, bare wire diameter becomes 0.0416 inch. Nearest smaller wire is AWG 18 whose bare wire diameter is 0.0403 inch (without insulation). So we can chose AWG 18, 47 turns.

4.9.5 Mean Length of Turn

The winding resistance can be calculated after the mean length of turn (MLT) is determined as twice the slot pitch to the average center of the slot opening, plus twice the stack length plus two times the allowance for end turn on the automatic insertion machines.

$$MLT = 2 \times (slot\ pitch\ to\ the\ average\ center\ of\ the\ slot\ opening + Stack\ Length) + 2 \times allowance\ for\ end\ turn\ height\ on\ automatic\ insertion\ machine \quad \ldots(4.16)$$

After calculating MLT, coil resistance can be estimated using AWG table, number of turns per coil and MLT.

$$R_{coil} = \frac{N \times MLT}{12000} \times \frac{Ohm}{kilofeet} from\ AWG\ table \quad \ldots(4.17)$$

Line to line resistance with 2-phases on and wye connection is 2×Rcoil. For AWG 18, 47 turns, MLT becomes 4.56 inch. R_{coil}=0.11 Ohm. 4 wires per phase gives 0.456 Ohm, Line to line on 2-phase Y connection gives 0.912 Ohm.

4.9.6 Estimation of Back EMF, Current, Torque and Power

It is possible to estimate back EMF from $k_E\omega_{operating}$. We already know the bus voltage.

$$Estimated\ peak\ current = \frac{V_{dcbus} - k_E\omega_{operating} - Transistor\ Voltage\ Drop}{2R_{coil} + Effective\ Resistance\ of\ the\ source} \quad \ldots(4.18)$$

Torque and power can be estimated from

$$T = Estimated\ peak\ current \times k_T \quad \ldots(4.19)$$

$$P = T \times \omega_{operating} \quad \ldots(4.20)$$

For the designed FSPM, estimated back EMF at 1800 rpm is $k_E\omega_{operating}$=127 V. So estimated current becomes *(160-126-2)/(0.912+1)=16.7* Amps. Torque with 16.7 Amps=16.7×k_T=100.9 lb-f-in or 11 N.m.

4.9.7 Number of Turns and Armature Current

The current density at maximum power should be checked to determine approximate continuous rating. For sinusoidal currents of peak value of 16.7 Amps, the RMS current in each phase is 11.8 Amps. Dividing this by the cross section area of the copper conductor

$$J = \frac{I_{RMS}}{Bare\ Wire\ Area} \qquad \ldots(4.21)$$

$$J = \frac{11.8}{\frac{\pi}{4} \times 0.0403^2} = 9250\ Amp/inch^2$$

Because of the thermal constraint and the cooling method used, the current density cannot be more than 3000 Amp/inch^2. In the above equation, setting J=3000, the actual RMS current for continuous operation can be determined. So, using J=3000, maximum allowable rms current becomes 3.827 Amps. Torque=3.827×6.029=2.6 N.m and power at 1800 rpm=488 W.

It is important to note that there are other ways to estimate the number turns, wire size and RMS phase current. As it is an iterative process, a machine designer would have to go back and forth and check the slot current density after each estimate. As the slot area and allowable rated rms current density are fixed by the available cooling method, it will all come down to the same number of Ampere-turns (NI) at the end. The ampere-turns data that governs the electric loading and is actually constrained by the cooling is summarized in Table 4.7.

Table 4.7: Number of turns and current rating of the FSPM

Number of turns	47
Wire size	AWG 18
RMS phase current	3.83 Amp

4.10 Magnetic Saturation and Flux Density Distribution

Figure 4.10 show the no load flux density of the 12/10 FSPM when the *d*-axis is (a) aligned and (b) unaligned with phase A. Figure 4.11 shows the flux density distribution with rated load. Because of using the spoke shaped magnet and flux focusing in the stator, some pointy edges may tend to saturation when rare earth magnets are used. This machine is designed with non-rare earth Ferrite magnet. Therefore, the risk of saturation is even lower in this machine. From Figure 4.10 and 4.11, it is observed that the flux density may tend to be close to 2 Tesla near the edges depending on the rotor position, but generally remains below 1.6 Tesla in more than 90% of the iron region.

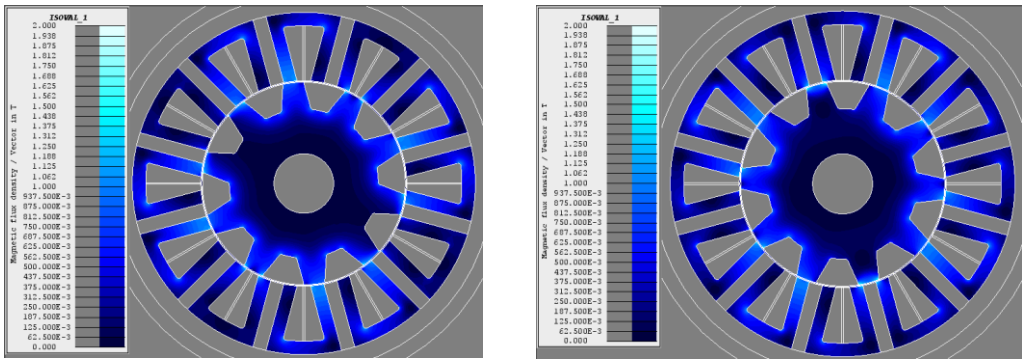

(a) (b)

Figure 4.10: Flux density distribution at no-load using color density plot (a) phase-A aligned, (b) phase-A unaligned.

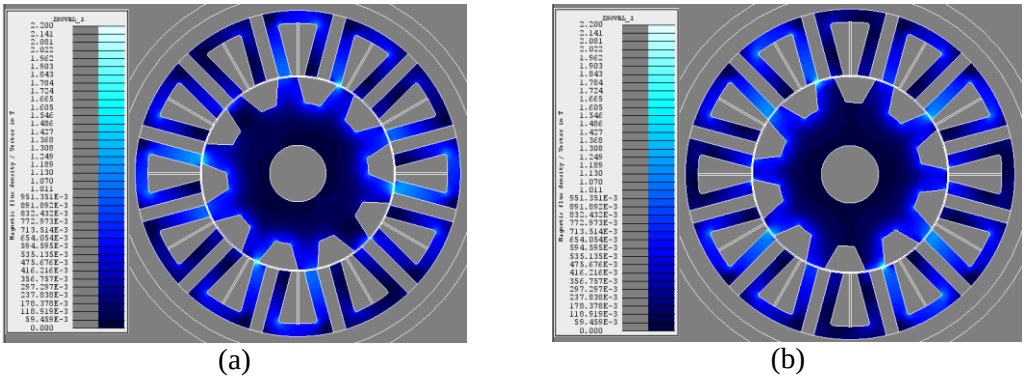

(a) (b)

Figure 4.11: Flux density distribution at loaded condition using color density plot (a) phase-A aligned, (b) phase-A unaligned.

The FEA calculated normal component of the air gap flux density is shown in Figure 4.12. With ferrite magnet, the maximum flux density is about 0.9 Tesla in the airgap region. Because of the stator-rotor pole combination, the machine is symmetric around 180 mechanical degrees. Therefore, the air gap flux density has a period of 180 degree mechanical as well. It should be noted that although the air gap flux density distribution is not sinusoidal, the phase flux linkage is sinusoidal in this topology, and so is the back EMF.

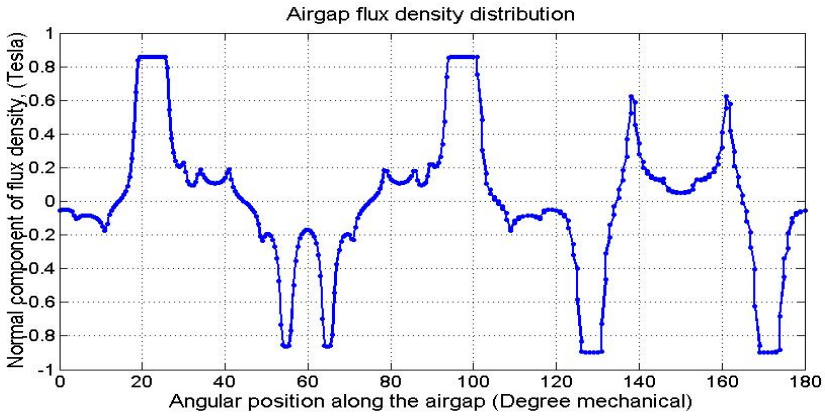

Figure 4.12: Air gap flux density distribution of the designed FSPM.

4.11 Flux Linkages and Back EMF

Phase-A individual coil flux linkage, total phase A flux linkage and the back EMF is shown in Figure 4.13. Geometrically symmetric coils A1-A3 and A2-A4 links the same amount of flux. As the coils are connected in series, there is no circulating current. Although individual coil flux linkages are not exactly sinusoidal and contains some harmonic components, when they are added up, the total phase flux linkage is closer to perfect sinusoid with very small harmonic components. Consequently phase-A back EMF is also sinusoidal with peak of 63.35 V (45.34 V rms) at 1800 rpm with negligible harmonics.

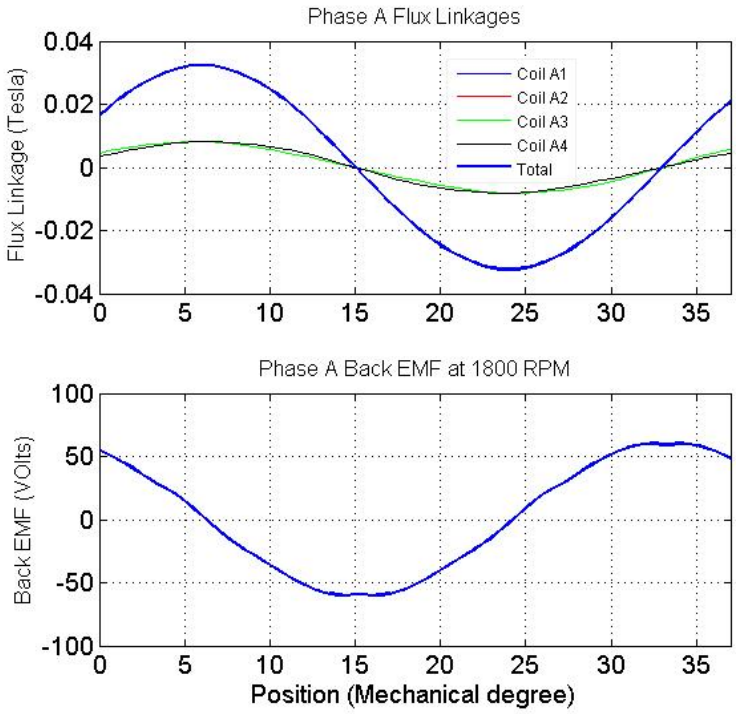

Figure 4.13: Phase-A flux linkage and back-EMF of the designed machine.

4.12 Estimation of Core Loss Co-efficients

The equation which is used to determine the co-efficients (K_h, K_e) to match with the experimental iron loss data is:

$$P = \left[K_h {B_m}^2 f + \frac{\pi^2 \sigma d^2}{6}(B_m f)^2 + 8.67 K_e (B_m f)^{1.5}\right] k_f \frac{1}{Mass\ Density} \qquad \ldots(4.22)$$

It is possible to obtain the core loss co-efficients for any particular lamination material at any frequency if the loss data are available at that frequency. We have loss data as in Table 4.8 for the lamination material at 200 Hz and at 400 Hz. The FSPM machine operating frequency is $\frac{Speed \times N_r}{60}$ Hz. In our case, the operating frequency becomes 300 Hz when the machine is running at 1800 RPM. The loss data (Watt/kg vs Flux Density curve) is interpolated to have 300 Hz curve as shown in Table 4.8. Figure 4.14 shows the Loss/kg variation with flux density at 200 Hz, 400 Hz and the interpolated Loss/kg at 300 Hz.

Table 4.8: Available loss/kg data of steel at 200 Hz, 400 Hz and interpolated at 300 Hz

Flux Density	Loss at 200 Hz	**Loss at 300 Hz (interpolated)**	Loss at 400 Hz
0.01		**0**	
0.02		**0**	
0.03		**0.005**	0.01
0.04	0.01	**0.02**	0.03
0.05	0.02	**0.03**	0.04
0.06	0.02	**0.04**	0.06
0.07	0.03	**0.055**	0.08
0.08	0.04	**0.075**	0.11
0.09	0.06	**0.1**	0.14
0.10	0.07	**0.125**	0.18
0.15	0.16	**0.285**	0.41
0.20	0.28	**0.505**	0.73
0.25	0.43	**0.775**	1.12
0.30	0.61	**1.09**	1.57
0.35	0.81	**1.45**	2.09
0.40	1.03	**1.845**	2.66
0.45	1.27	**2.28**	3.29
0.50	1.53	**2.745**	3.96
0.55	1.8	**3.245**	4.69
0.60	2.09	**3.79**	5.49
0.65	2.4	**4.36**	6.32
0.70	2.72	**4.97**	7.22
0.75	3.07	**5.595**	8.12
0.80	3.42	**6.27**	9.12
0.85	3.8	**6.99**	10.18
0.90	4.2	**7.75**	11.3
0.95	4.62	**8.555**	12.49
1.00	5.06	**9.405**	13.75
1.10	6.01	**11.255**	16.5
1.20	7.12	**13.4**	19.68
1.30	8.37	**15.82**	23.27
1.40	9.92	**18.765**	27.61
1.50	11.65	**22.115**	32.58
1.60	13.38	**25.465**	37.55
1.71	15.11	**28.815**	42.52

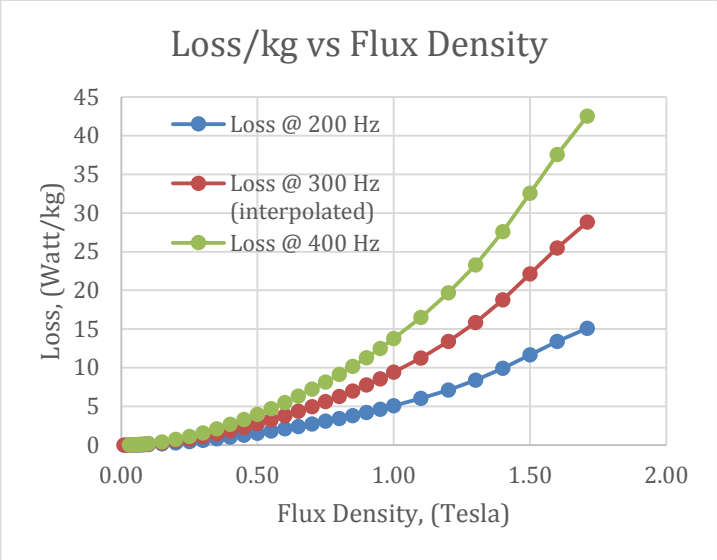

Figure 4.14: Loss data of the core material at 200 Hz and 400 Hz.

Based on these experimental values, the exact values of the co-efficients for core loss calculation can be obtained by numerical iteration, so that the core loss from Bertotti's formula matches exactly with the experimental loss data available. The value of the co-efficients obtained are summarized in Table 4.9.

Table 4.9: Bertotti's coefficients determined based on the available loss data

Electrical conductivity $1/(Ohm \cdot m)$:	2.00E+06
Density (kg/m^3):	7650
Thickness (m):	3.00E-04
Frequency (Hz):	200.0
K_e	**0.000**
K_h	**313.389**
Volume (kg)	1.31E-04

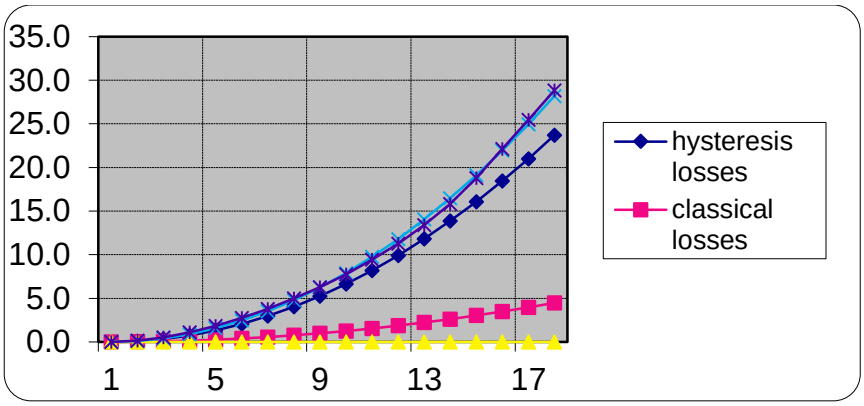

Figure 4.15: Different loss components using the co-efficients calculated.

An excel program is used to find the best values of K_h and K_e that gives exact match of Bertotti's loss with experimental core loss data. K_h=313.389, K_e=0. Lamination thickness=0.3 mm used core loss calculation. Figure 4.15 shows the different components of the core loss, namely, hysteresis loss, classical loss and excess loss using the co-efficients calculated and formula in equation.

4.13 Input, Output and Losses from FEA

The important electromagnetic performance parameters. Figure 4.16 shows the current per phase and terminal voltage from FEA simulations of the machine at 1800 r/min. Input power, output torque, output power at 1800 r/min and copper loss is shown in Figure 4.17. All the results are obtained using FEA, which will be verified later with the experiments.

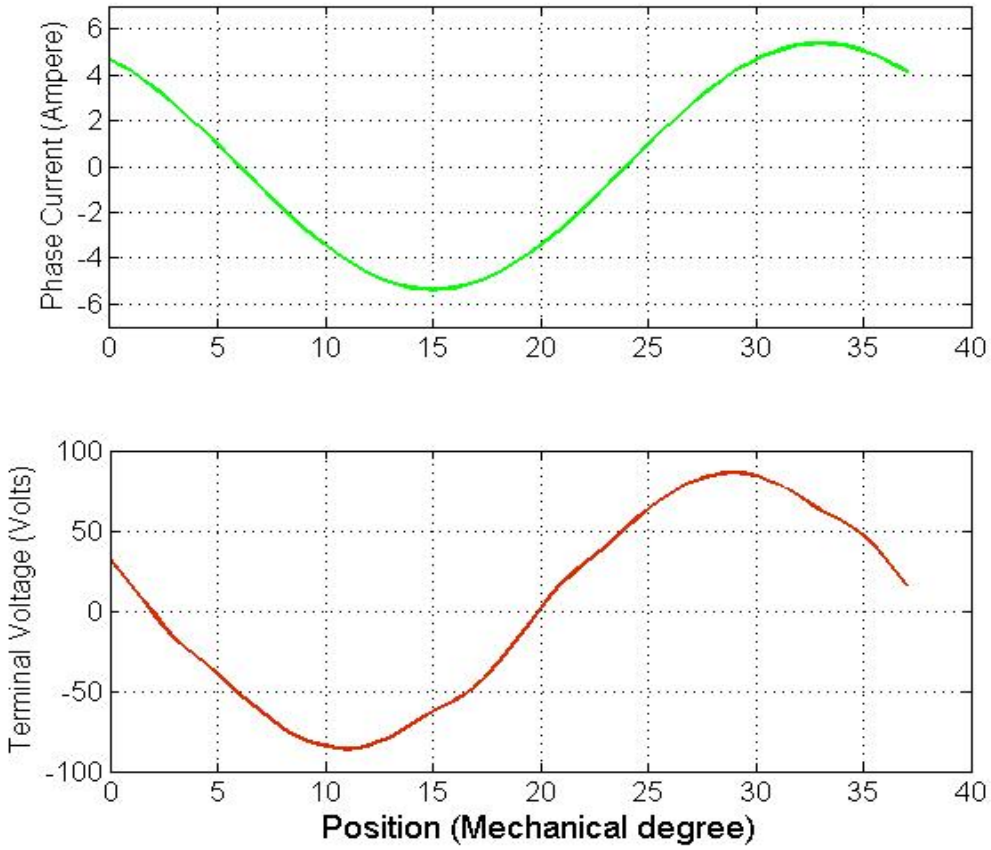

Figure 4.16: Phase current and terminal voltage of the FSPM from FEA simulation.

Power factor can also be calculated from phase difference between the phase current and terminal voltage as in Figure 4.16. From the plot, the difference is 4 degree mechanical, which results in 40 degree electrical, hence a P.F. of cos(40)=0.77.

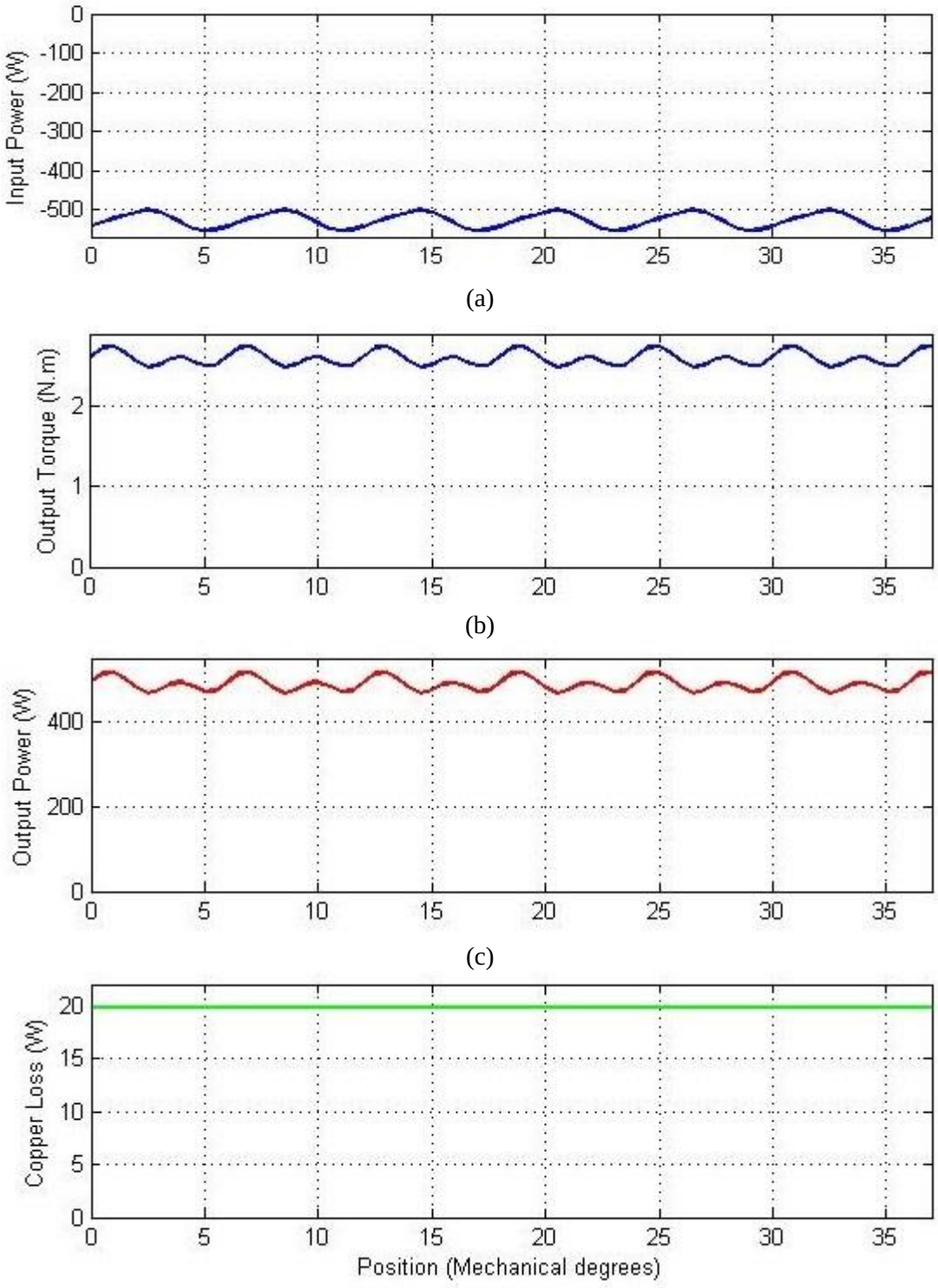

Figure 4.17: Different power components of the designed FSPM from FEA: (a) Input, (b) Output torque (c) Output power, (d) Copper loss.

4.14 Electromagnetic Torque, Torque Ripple and Cogging Torque

Figure 4.18 shows the output electromagnetic torque of the FSPM in one electric cycle, and a zoomed in version of it in one cycle of the cogging torque. The period of cogging torque is 6 degrees (mechanical) according to equation. On the other hand, one electric cycle of the designed 12/10 FSPM is 36 degree (mechanical). This figure shows that cogging torque is a major and probably most dominant source of ripple in this kind of machine. As the back EMF harmonics is made negligible and considerably very low by carefully choosing the design parameters, it is obvious that the ripple in output torque can be minimized by reducing the cogging torque.

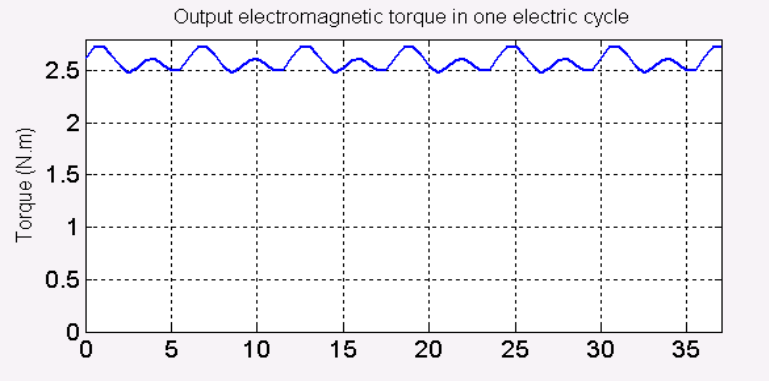

Figure 4.18: Output electromagnetic torque of the FSPM at rated (3.83 Amp) RMS current.

Figure 4.19 shows one period of cogging torque, and the variation of electromagnetic torque within that period of the designed machine. Table 4.10 shows a summary of the data and comparison among the ripple and average of electromagnetic torque and the cogging torque. It appears that the ripple magnitude in the output torque is 76% of that consisted in the cogging torque. Also, if the output torque and the cogging torque is observed closely within

the same X-axis value of mechanical position, the effect of cogging torque in the output electromagnetic torque is clearly visible.

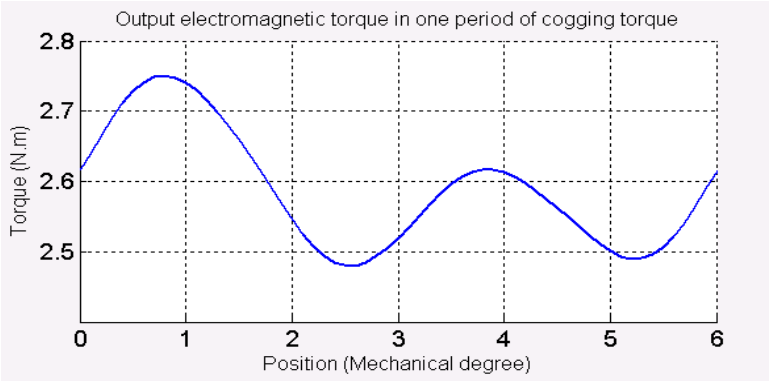

(a)

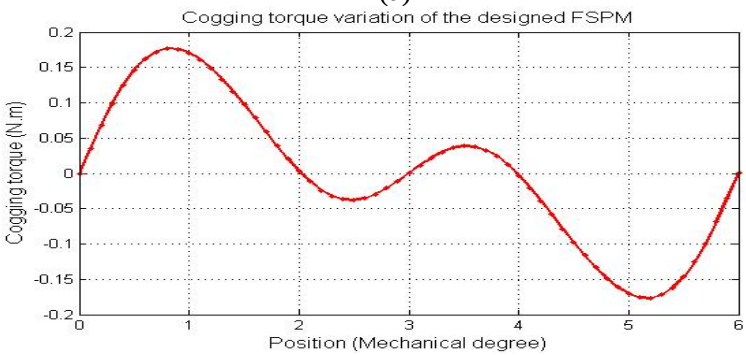

(b)

Figure 4.19: (a) A closer view of the output torque in 6 degree mechanical, (b) Cogging torque in one period.

Table 4.10: Comparison between cogging torque and ripple in average torque

	Average	Ripple	Ripple/Average
T_e	2.6	0.27	10%
$T_{cogging}$	0	0.354	-

4.15 Account for Temperature Effect for Continuous Operation

To account for the effect of temperature rise in the machine, a complete thermal-electromagnetic coupled simulation can be performed. However, the adverse effect of temperature rise in the machine can be simplified. At higher temperature, (i) Copper loss

increases due the increase in coil resistance, and (ii) The remnant flux density of the magnet decreases. These two phenomenon can be easily implemented in electromagnetic FEA by (i) increasing the coil resistance according to the temperature, (ii) derating the magnet by decreasing the remnant flux density.

The temperature co-efficient for copper is $\frac{1}{234}$ Ohm per degree Celsius. Using this, the increase in coil resistance can be adjusted as the values in the Table 4.11.

Table 4.11: Coil resistance elevation due to increase in temperature at steady state

	N_{turns}=47, AWG 18
Room Temperature	0.456 Ohm
80 C	0.554 Ohm
120 C	0.625 Ohm

Figure 4.20 shows the demagnetization curves of Ferrite magnets at different temperatures. As temperature increases, the strength of the magnet decreases. But at the same time, the knee point at the JH curve for Ferrite magnet also goes down. This means that the ferrite magnet is not very vulnerable for demagnetization at higher temperature. This is an important and notable advantage of using Ferrite magnet instead of using rare earth, NdFeB magnets. At higher temperature, the knee point of the NdFeB magnets goes up in the second quadrant in the demagnetization curves. As a result, the corners and edges of the magnet possess the risk of being irreversibly demagnetized where the flux density may decrease beyond the value of the knee point.

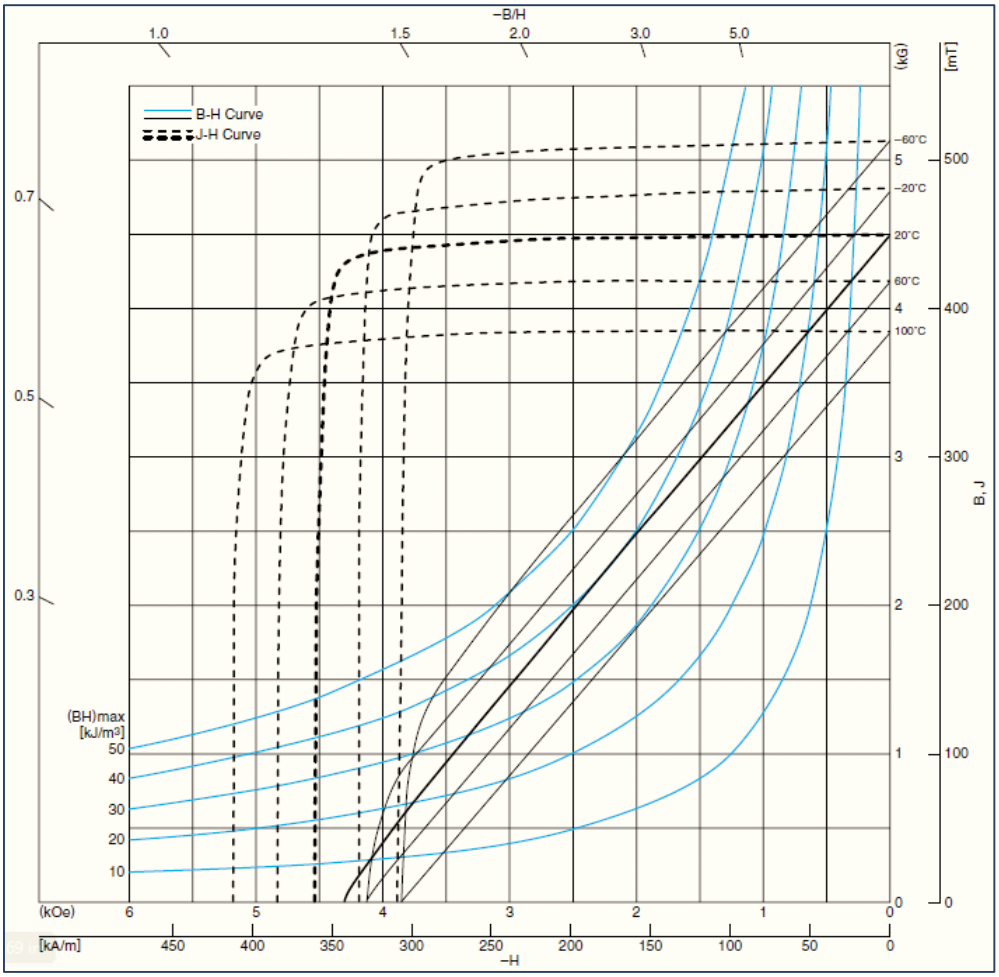

Figure 4.20: Demagnetization curve of TDK FB9 series Ferrite magnet used [102].

Figure 4.21 shows the flux density distribution in phase-A magnets at aligned and unaligned position. Using Ferrite magnets, to obtain machine performance at running condition, the remnant flux density of the magnets in FE analysis can be adjusted to lower value (0.35 T at 80 C and 0.325 T at 120 C) to account for temperature effect on magnet.

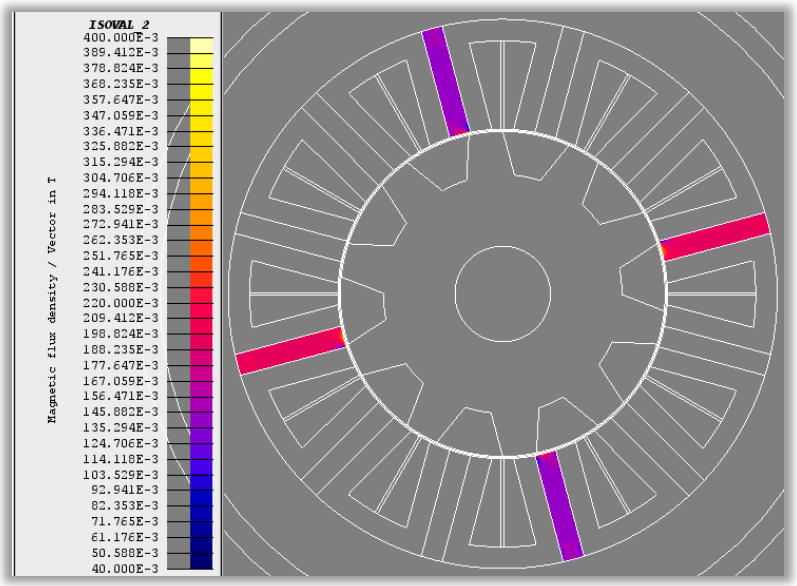

(a)

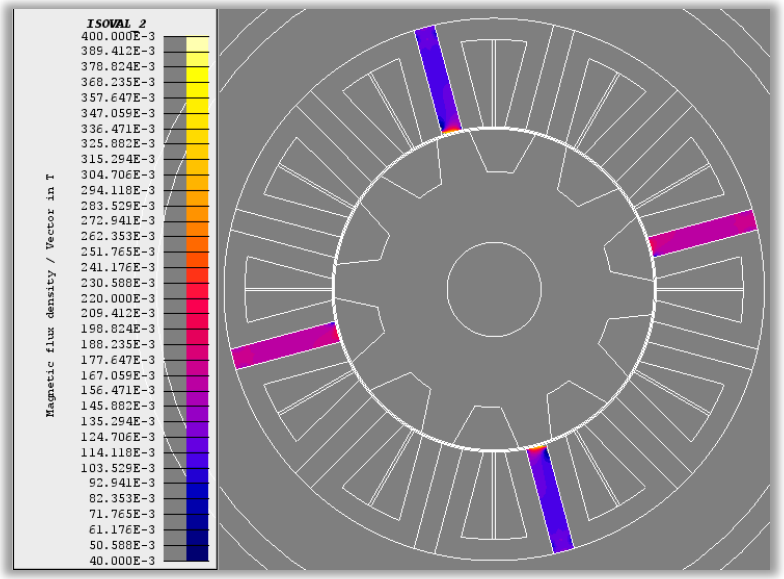

(b)

Figure 4.21: Flux density distribution in phase-A magnets at aligned and unaligned position.

Table 4.12 summarizes all the important electromagnetic performance data of the designed FSPM, at room temperature and at an elevated temperature assuming 80 C and 120 C for normal operation.

Table 4.12: Summary of the performance parameters of the designed FSPM

	N=47, I_{rms}=3.83	N=47, I_{rms}=3.83 Derated Magnet & increased R_{coil} at 80C	N=47, I_{rms}=3.83 Derated Magnet & increased R_{coil} at 120C
Remnant Flux Density of Magnet, Bm	0.405	0.35	0.325
Coil Resistance	0.456 Ohm	0.552	0.624
Terminal Voltage (RMS)	62.7 V	57.84	56.1
Terminal Voltage (Peak)	90.46 V	84.63	82.1
P_{in} (W)	558 W	492.4	463.9
P_{mech} (W)	520 kW	451	419.1
P_{Copper} (W)	20 W	24.3	27.5
P_{Core} (W)	18 W	15.4	14.2
Total Loss (W)	38 W	39.7	41.7
Efficiency	90%	88%	87%
PF	0.77	0.71	0.71

4.16 Power Factor Analysis

The *d*- and *q*-axes inductances and the permanent magnet flux linkage plays very important role in the power factor of any PM machine. This section will present the influence of all these on the power factor of the designed machine, as well as scope of improving power factor from a design perspective.

For the 3-phase FSPM operated by vector-control method, the average electromagnetic torque T_{em} can be expressed in the *dq* reference frame as

$$T_{em} = \frac{3}{2} N_r [\varphi_m I_q + (L_d - L_q) i_d i_q] \ldots \qquad \ldots(4.23)$$

where N_r is the number of rotor poles, φ_m is the PM flux linkage, i_d, i_q are *d* and *q*-axes currents respectively, as well as L_d, L_q are *d* and *q* axis inductances, respectively. The vector diagram at this operating points shown in Figure 4.22

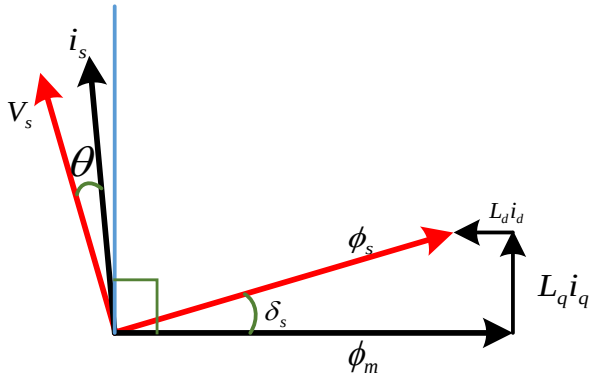

Figure 4.22: Vector Diagram of a FSPM when $i_d \neq 0$.

The equation indicates that the FSPM torque is composed of two components, the PM torque T_{PM} and the reluctance torque T_r caused by the difference of L_d and L_q. For FSPM motor T_r is negligible compared with the T_{PM} components since the *d*- and *q*-axes inductances are almost the same [15], [16]. The electromagnetic torque is dominated by the PM torque and can be simplified as

$$T_{em} \cong T_{PM} = \frac{3}{2} N_r \varphi_m I_q \qquad \ldots(4.24)$$

A negative *d*-axis current will increase the speed range, but the applicable torque is reduced because of stator current limit. The operating point where id=0 (gamma=0) is found to be the maximum torque-per-ampere point of the machine.

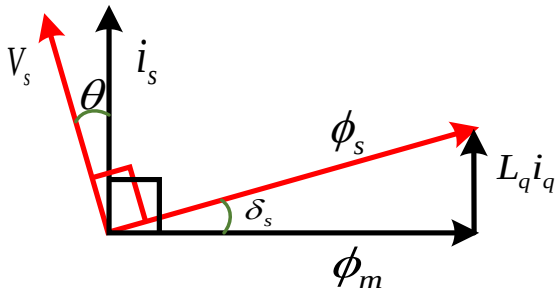

Figure 4.23: Vector diagram when i_d=0.

Figure 4.23 illustrates the motor operation with id=0 control. It is clear from the vector diagram that this method possess the risk of significantly lower power factor. The power factor angle depends on the relative magnitude of PM flux linkage and *q*-axis current. This figure also clearly indicates that the flux linkage produced by the permanent magnets of the motor should be higher in order to obtain an appropriate stator current at the rated torque.

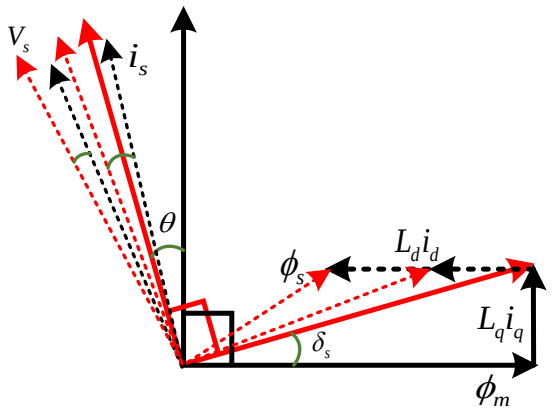

Figure 4.24: Vector diagram illustrating the effect of magnitude of negative *d*-axis current on power factor angle.

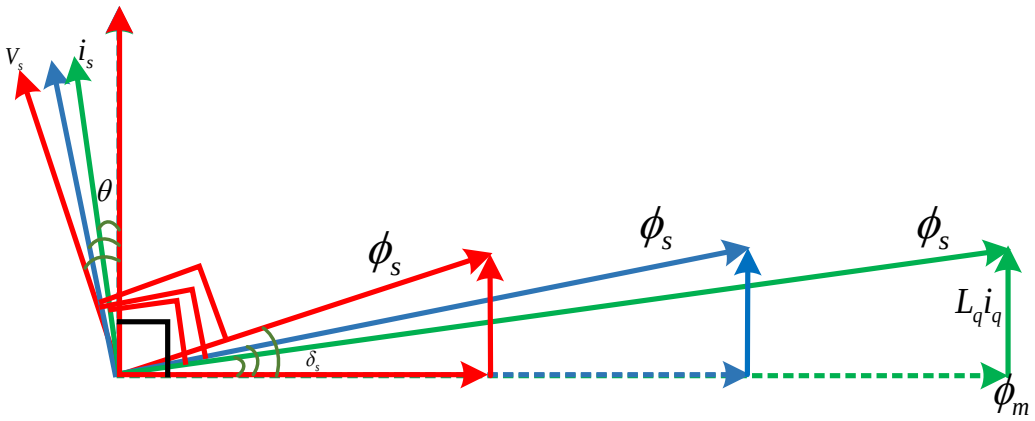

Figure 4.25: Vector diagram illustrating the effect of magnet flux linkage on power factor angle.

Figure 4.24 and Figure *4.25* show the effect of applying a negative i_d and using stronger magnet (higher magnet flux density) on power factor. It is to be noted that one is completely a design choice (PM material), whereas the other one is from control perspective. Applying negative i_d adds voltage reserve and the motor drive responds well to the increases in load in dynamic status, but the current increases considerably higher than intended. On the other hand, using stronger permanent magnets like rare earth NdFeB, the power factor improves significantly, but as it will also increase the back-EMF, the required supply voltage at the rated operating point also needs to be chosen carefully.

In practice, for any PM machine, magnets with higher coercive force would yield in better power factor. Applying negative id is particularly useful when stator flux-weakening is required to extend the speed range of the machine. Applications where field weakening will not be required, a design of this kind is used, such as high power high efficiency blower.

4.17 Design and Comparison with SRM and Surface PM Machines

This section aims to compare the FSPM designed with SRM and IPM. For a fare comparison, the motors are designed to have the same overall dimensions and operating conditions. The detailed design parameters are listed in. For comparison of the power density, electromagnetic performance, efficiency, and cost of the motors, some rules are listed as follows:

- All three motors have the same outside diameter and stack length.
- The RMS value of phase current of the motors are the same.

- The material properties of magnet, stator and rotor iron and the armature winding of the motors are all the same.

- The current density of the motors are the same.

4.17.1 Motor I – SRM within Same Volume

Figure 4.26 shows the structure of an SRM with 12 stator poled and 8 rotor poles. Each phase winding has four concentrated coils connected in series. In this section, the SRM is optimally designed based on the same parameters with the FSPM designed i.e. outer stator diameter, stack length, phase current, slot current density and same type of material. The detailed dimensions and materials are listed in Table 4.13.

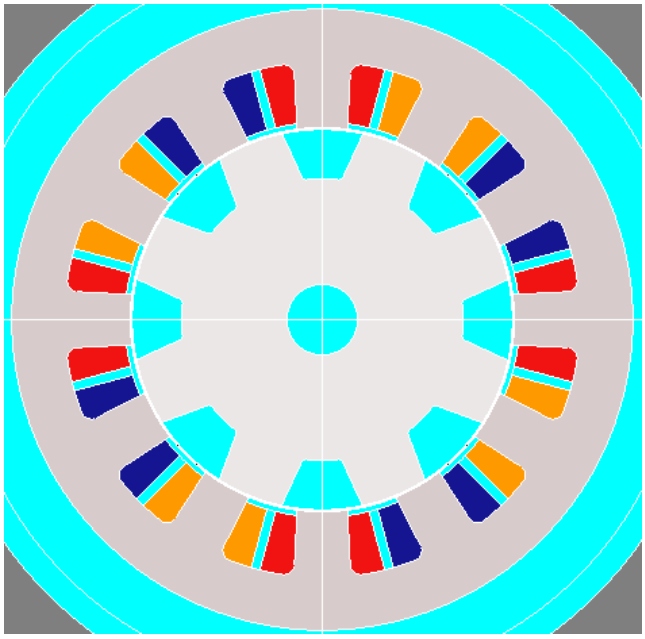

Figure 4.26: FEA Model of the designed SRM.

Table 4.13: Geometric parameters of SRM designed within the same volume as the FSPM

Parameter	**Description**	**Description**
R3	Machine Outer Radius	60 mm
LSTK	Length of Stack	40 mm
Ns	No. of Stator Poles	12
Nr	No. of Rotor Poles	8
R2	Stator Yolk Inner Radius	49.8 mm
R1	Rotor Outer Radius	36.72 mm
R0	Rotor Inner Radius	21.2 mm
RSH	Shaft Radius	6.8 mm
GAP	Air Gap Depth	0.4 mm
BETA_ST	Angular Stator Tooth Width	15^{o}
BETA_RT	Angular Rotor Tooth Width	20.5^{o}
N	Number of turns per coil	*75*

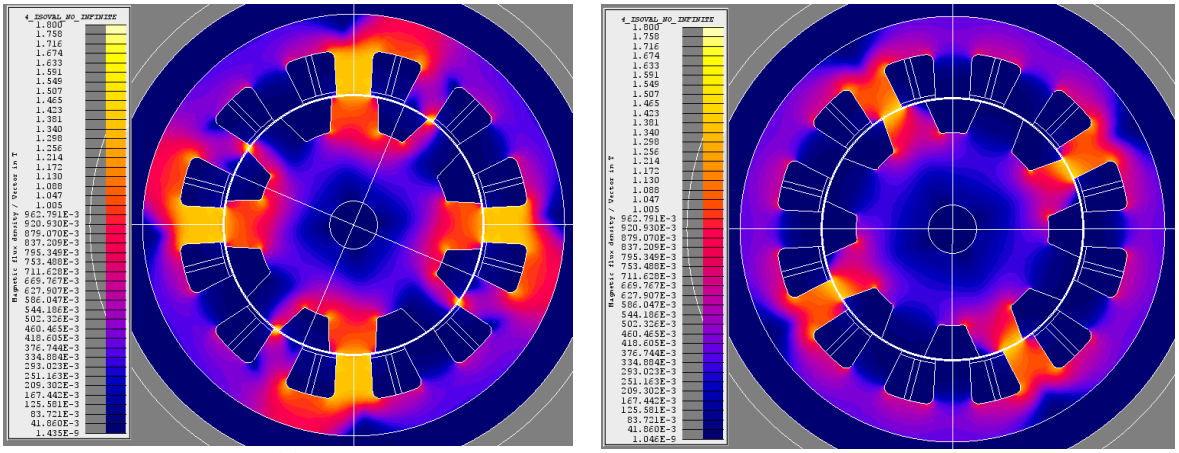

(a) (b)

Figure 4.27: Flux density map when the stator and rotor poles are (a) aligned and (b) unaligned at phase-A.

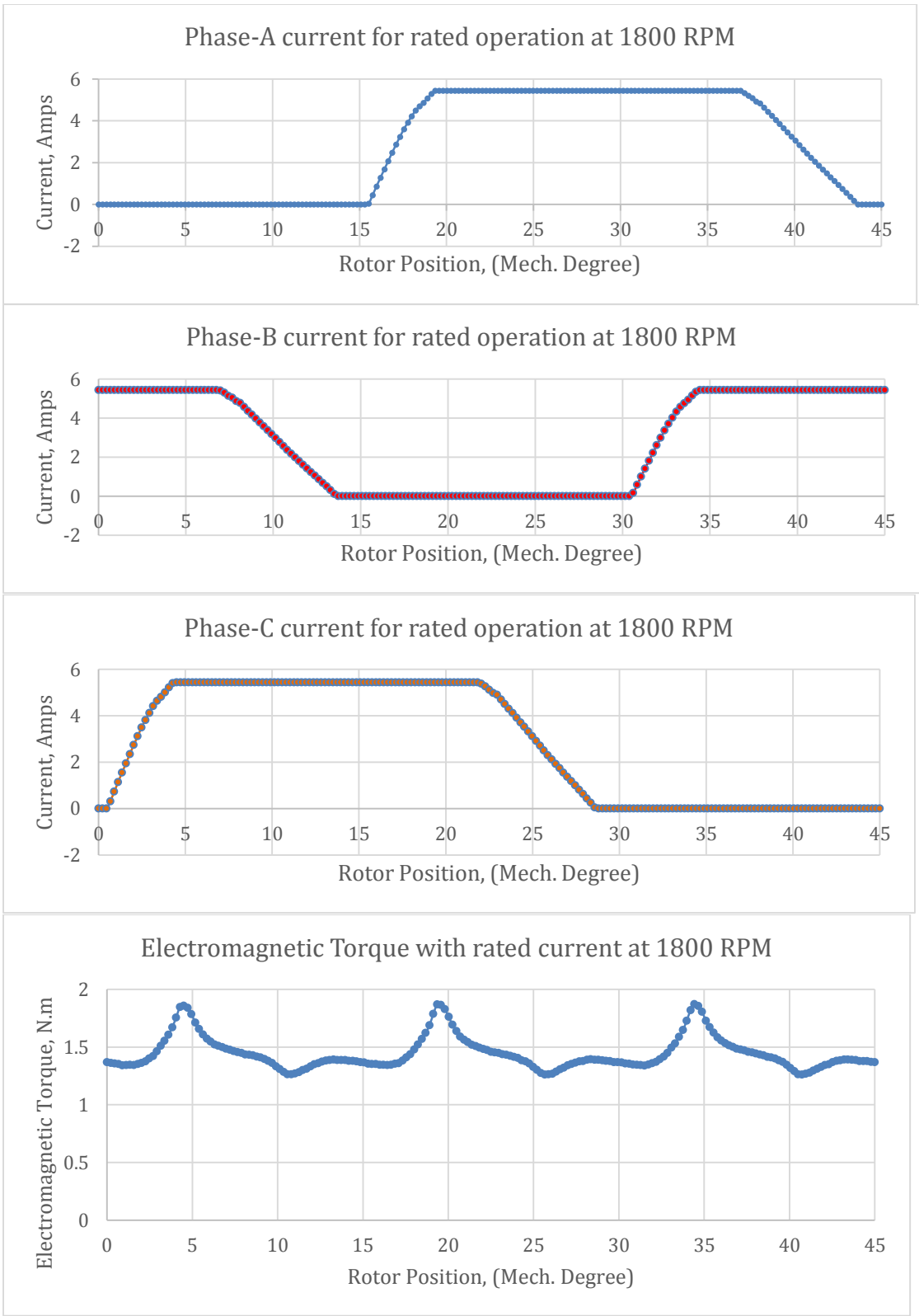

Figure 4.28: Phase currents and torque from the designed SRM.

Figure 4.27 shows the flux density map of the 12/8 SRM at rated current, when phase A is (a) aligned, and (b) unaligned with the nearest rotor pole. The slot area of the designed SRM is 62.2 mm^2. 75 turns of AWG 19 is chosen to be able to apply 3.73 Amps (RMS) during rated operation at 1800 RPM. Using this wire size and number of turns, the per-phase resistance becomes 0.3 Ohm. Figure 4.28 presents the phase current and output electromagnetic torque under rated load at 1800 rpm. Detailed comparison of the SRM performance with other designed machines within the same volume is presented at a later section.

4.17.2 Motor II – Surface Mounted PM Brushless DC Machine

Figure 4.29 and Table 4.14 contain the structure and parameters of a surface mounted PMSM with 9 stator poles and 6 rotor poles. Each phase winding has three concentrated coils connected in series. In this section, the PMSM is optimally designed based on the defining parameters of FSPM as in the previous section.

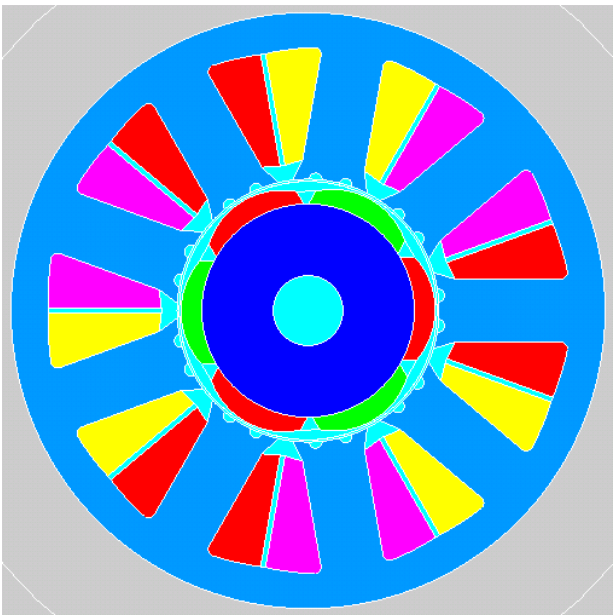

Figure 4.29: FEA Model of the surface mounted PMSM.

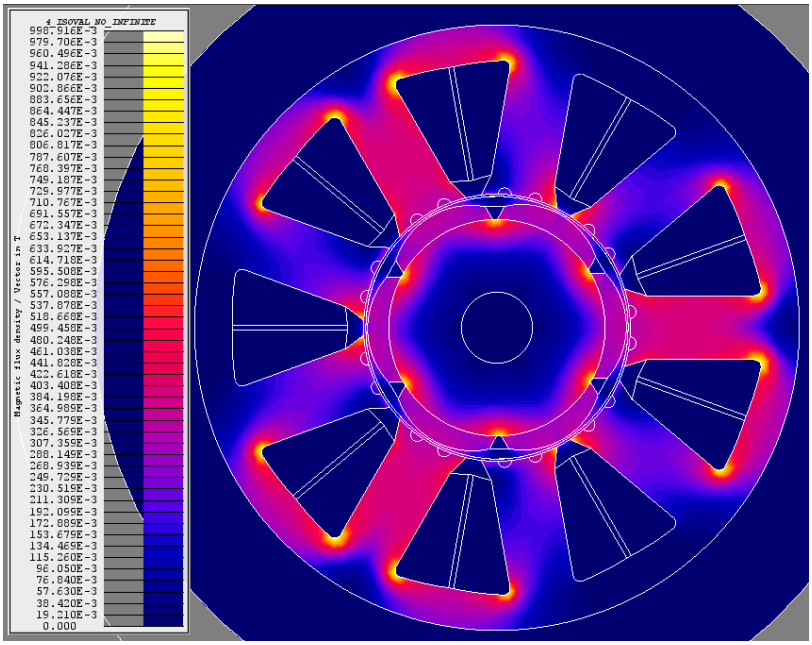

(a) No load

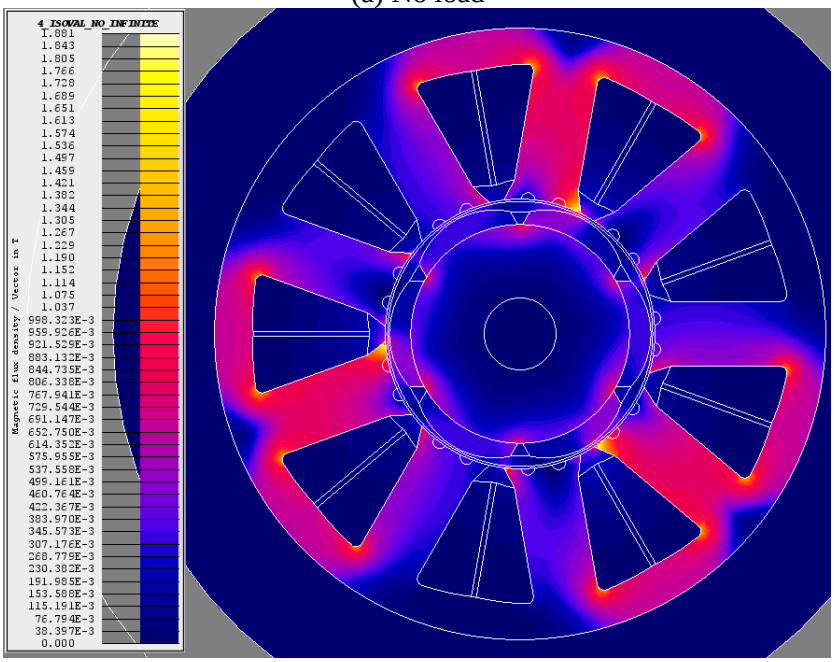

(b) Rated load

Figure 4.30: Flux density map of the PMSM at (a) no-load, and (b) rated load.

Table 4.14: Design data of surface mounted PM Brushless DC machine within same volume of the FSPM

Parameter	**Description**	**Description**
R5	Machine Outer Radius	60 mm
LSTK	Length of Stack	40 mm
Ns	No. of Stator Poles	9
Nr	No. of Rotor Poles	6
R4	Stator Tooth Inner Radius	55.3 mm
R3	Stator PM and Tooth Inner Radius	36 mm
R1	Rotor Outer Radius	35.5 mm
R0	Rotor Inner Radius	26.075 mm
RSH	Shaft Radius	10.43 mm
GAP	Air Gap Depth	0.5 mm
BETA_S	Angular Stator Pitch	30^o
BETA_ST	Angular Stator Tooth Width	7.5^o
BETA_C	Angular Coil Width	3.25
BETA_M	Angular Magnet Width	7.5
BETA_R	Angular Rotor Pitch	36
BETA_RT	Angular Rotor Tooth Width	12^o
WST	Stator Segment Tooth Width	4.7 mm
TPM	PM Thickness	4.7 mm
WRP	Rotor Pole Width	7.5 mm
HRP	Rotor Pole Height	9.4 mm
N	Number of Turns Per Coil	100

Figure 4.30 shows the flux density map at no-load and rated load conditions. In general, flux density in surface mounted PMSM is lower than that in FSPM in all the regions as there is no flux focusing here. Even at rated load, the peak flux density is 1.8 Tesla which covers less than 5% of the entire region. Flux density generally remains less than 1 Tesla in more than 90% of the region.

The slot area of the designed PMSM is 171 mm^2. 100 turns of AWG 18 is chosen to be able to apply 5.1 Amps (rms) during rated operation at 1800 rpm. Using the wire size and number of turns accordingly, per phase resistance becomes 0.75 Ohm.

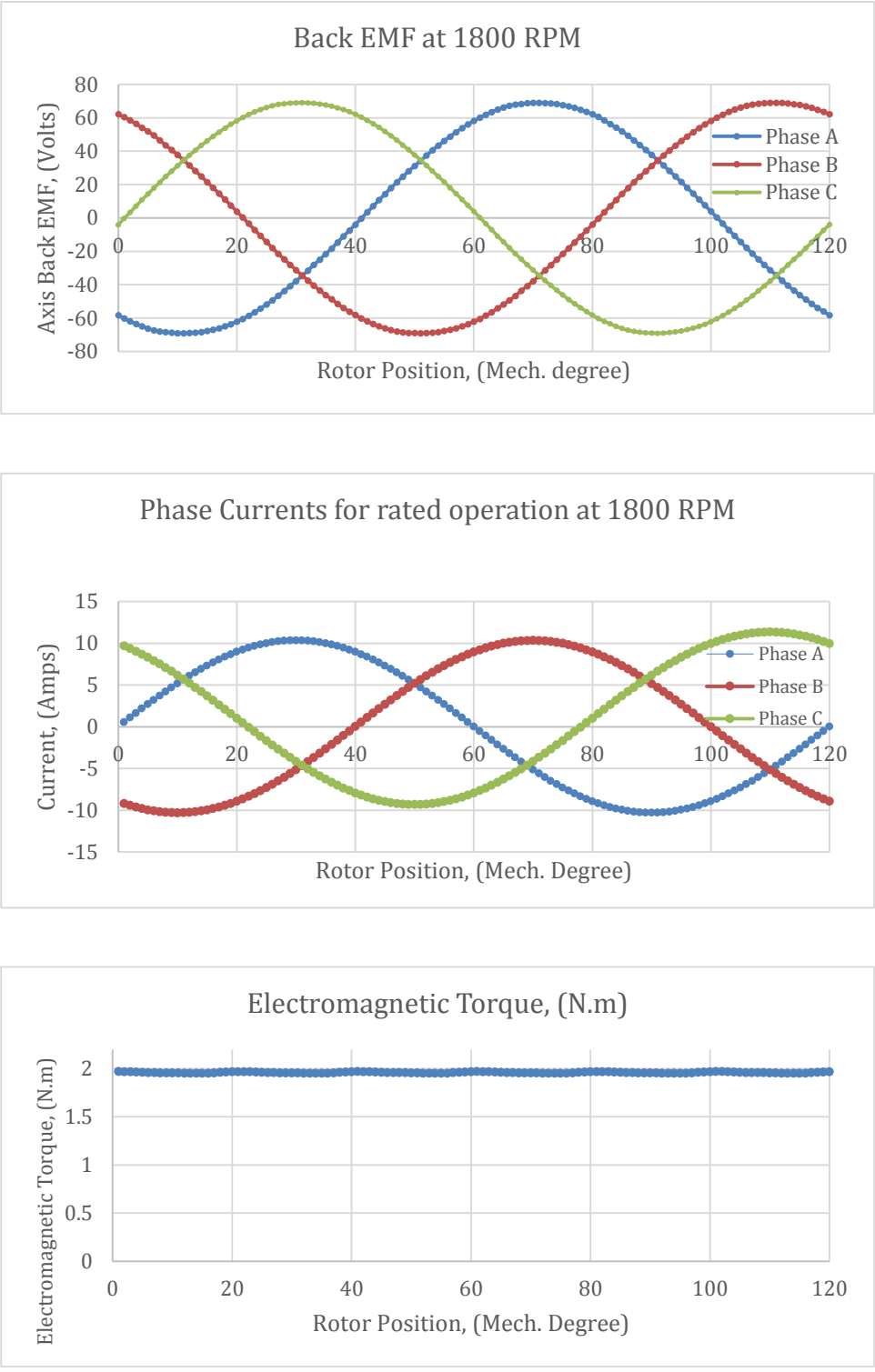

Figure 4.31: Back EMF, rated phase currents and torque of the designed Surface Mount PMSM at 1800 RPM.

Phase back EMF, applied phase current at rated operation and output electromagnetic torque is shown in Figure 4.31. More detailed comparison of the motor performance with SRM and FSPM is presented in the next section.

4.17.3 Comparison of Performances

Table 4.15 shows side by side comparison of the non-rare earth FSPM, rare earth FSPM, SRM and Surface mounted PMSM performances at a glance. FSPM shows clear advantage in terms of torque density and power density within the same volume and cooling constraints. Also, because of higher magnetic loading than PMSM, power factor is also better in FSPM. To compensate for the smaller magnetic loading, PMSM has more winding area and thus more ampere turns can be applied. It also results in higher copper loss as compared to FSPM. However, one drawback of FSPM is the smaller PM utilization ratio. Among the designed machines, it uses 2.8 times more magnet material than in the designed PMSM. Therefore, the output torque per kg PM of the PMSM is 2 times that of FSPM.

Table 4.15: Comparison of SRM, SM PM BLDC and FSPM performances

	SRM	**SM-PMSM**	**FSPM**
Slot Current Density (RMS)	Below 6 Amps/mm^2		
Machine Outer Radius (mm)	60		
Machine Stack Length (mm)	40		
Mass of Magnet (grams)	-	95	270
Pin (W)	291 W	440	558
Torque (N.m)	1.4	1.95	2.76
Pmech (W)	266 W	367.6	520
PCopper (W)	13.66 W	58	20
PCore (W)	6 W	4	18
Total Loss (W)	19.66	62	38
Efficiency	91%	84%	90%
PF	0.3	0.6	0.77

4.18 Scalability and Design of a Larger FSPM

The proposed design method is highly scalable and can easily be adopted to design a machine of larger size. All the geometric parameters are designed as a function of the outer radius and most of the design rules and ratios hold for any size. However, the machine performance depends highly on two things that actually defines the magnetic and electrical loading of the machine (i) Number of turns and current, and (ii) Strength of magnet. Last not but the least, the required voltage depends on the operating speed, and should be set based on the corner speed required by the application. Considering all these, a larger machine with the same Ferrite magnetic material is designed within same electrical loading for general purpose applications at 1800 RPM. The geometric parameters are scaled up accordingly.

The design technique developed and applied here is highly parameterized and scalable. The design guidelines and rules can be applied to an FSPM of any size and power level with a very few number of adjustments based on the available supply. A 50 kW (75 HP) FSPM is designed in this section following the same technique and design guidelines. A commercial, general purpose 75 HP Induction Motor has been used as a benchmark or starting point.

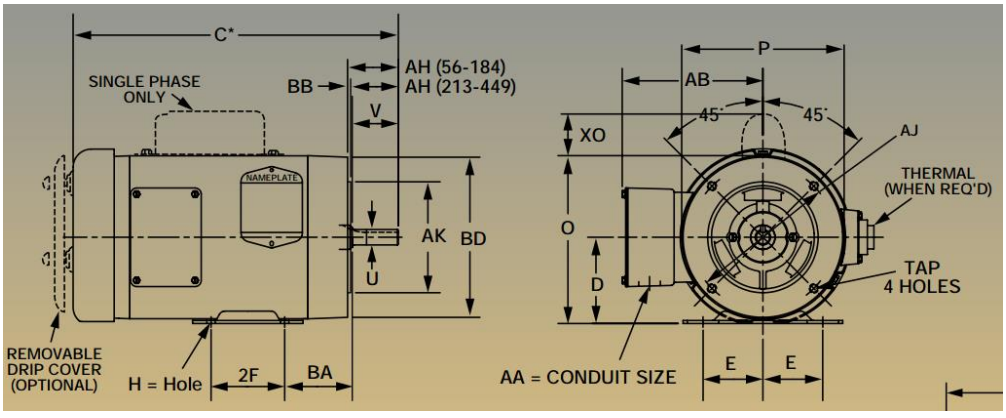

Figure 4.32: Dimensions of NEMA 365T frame.

Electric motors of this power range (75 HP) is usually equipped in a frame of NEMA 365T. For a frame of this size, E=7 inch (177.8 mm) and 2F=12.25 inch (311.15 mm) as shown in Figure 4.32. The outer dimensions of FSPM has been chosen accordingly so that it fits in this frame if required.

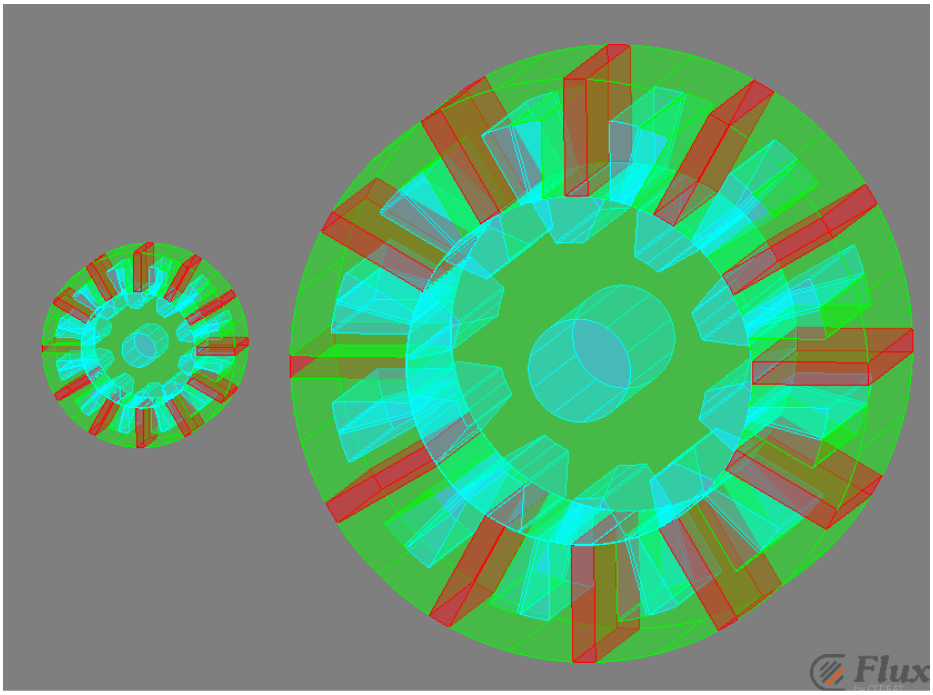

Figure 4.33: 3D view of the base (0.5kW) design and scaled up (50kW) design of FSPM.

Table 4.16 contains the detailed design with the important geometric parameters of the designed motor. All the geometric parameters are scaled up accordingly. Figure 4.33 shows 3D view of the base design and the scaled up design. However, it is very important to design the winding connection, number of turns, specify the current rating based on available supply voltage and cooling method. When all the phase coils are connected in series, the individual coil flux linkage and back EMF adds up. When the coils are connected in parallel, the phase current splits up in each coil. Considering the entire phase, it is up to the motor designer to design it as a high voltage, low current motor or a low voltage, high current motor. Also, the

available DC supply voltage plays an important role here. The specifications of the designed motor must be practical and realizable using commonly used and available resources.

Table 4.16: Design data of the 50kW FSPM

Parameter	**Value**
Stator outer radius	177 mm
Active stack length	140 mm
Number of stator poles, N_s	12
Number of rotor poles, N_r	10
Airgap length	0.7 mm
Rotor outer diameter	107.3 mm
Split ratio	0.6
Stator tooth width, β_{st}	$\mathbf{7.5}°$
Slot opening, β_{so}	$\mathbf{7.5}°$
Magnet thickness, β_m	$\mathbf{7.5}°$
Stator yoke thickness	$\mathbf{7.5}°$
Rotor pole width, β_{rt}	$\mathbf{12}°$
Stator Tooth Width	14.14 mm
Stator Back Iron Thickness	24.04 mm
RMS current density, J (A/mm^2)	6 A/mm^2
Rated Speed	1800 RPM
Rated Voltage	400 V
Rated rms phase current	440 Amps
Power	50 kW
Number of turns	12
Wire size	AWG 00
Winding connection	All 4 coils are in parallel
Per phase resistance	0.00021 Ohm
Magnet type	Ferrite

To be able to realize and implement the 50kW FSPM drive, the winding connections have been chosen to be parallel as shown in Figure 4.34. The winding connection, along with the number of turns and current have been determined using an iterative procedure, so that they satisfy the thermal limit, cooling and available DC-supply at rated speed.

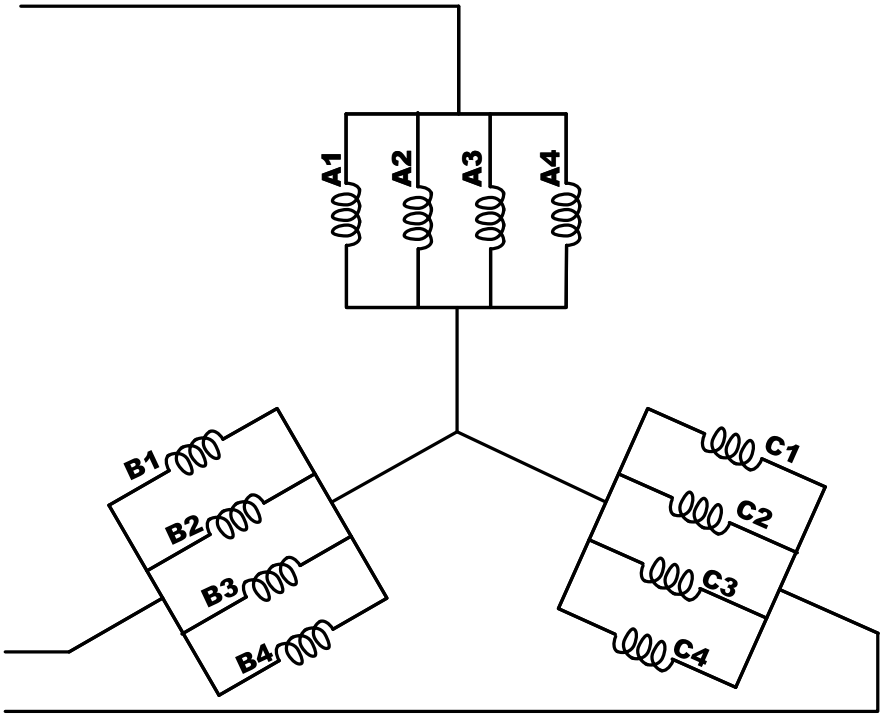

Figure 4.34: Winding connection of the 50kW FSPM.

4.18.1 No-load Results

Figure 4.35 shows the flux density color map in the 50kW FSPM when the *d*-axis is aligned and unaligned with phase-A, both for no-load and loaded condition. The flux density generally stays below 2 Tesla at no-load and 2.4 Tesla when under rated load. In a later part, it is shown that under rated load current, the machine has not undergone into saturation.

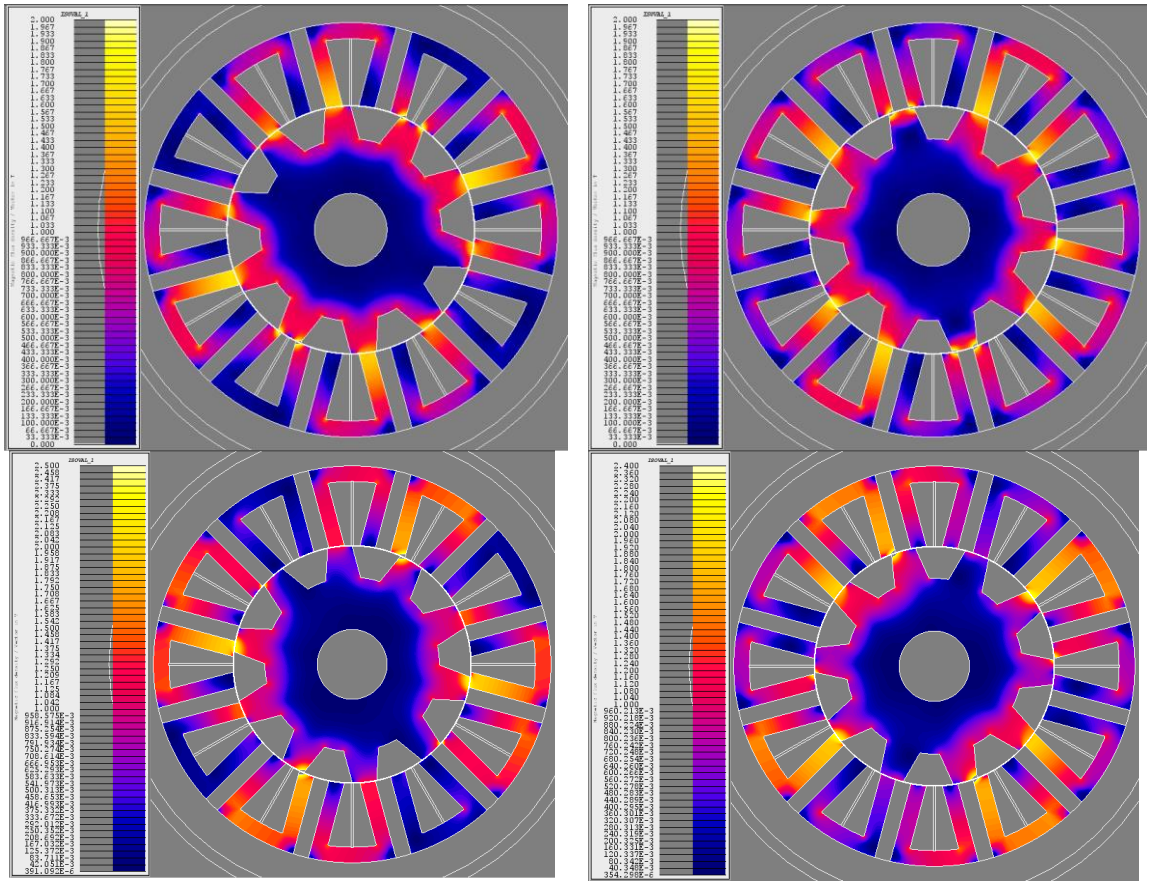

Figure 4.35: Flux density distribution of the 50 kW FSPM using color density plot (a) no-load, phase-A aligned, (b) no-load, phase-A unaligned, (c) loaded, phase-A aligned, (d) loaded, phase-A unaligned.

The FEA calculated normal component of airgap flux density, coil and phase-A flux linkage and back EMF of the 50kW FSPM are shown in Figure 4.36. The flux linkage and phase back EMF is sinusoidal for the scaled up machine and contains very negligible higher order harmonics, which is one of the most attractive feature of this machine. The FFT of the back EMF is also shown in Figure 4.36(d).

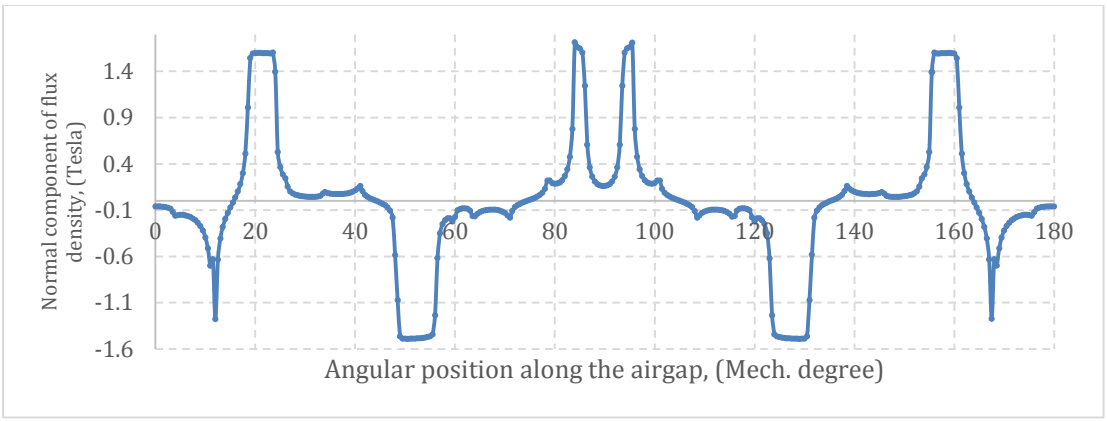

(a)

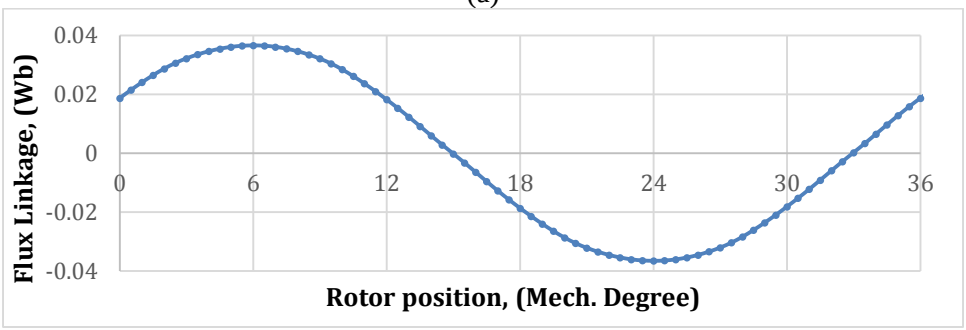

(b)

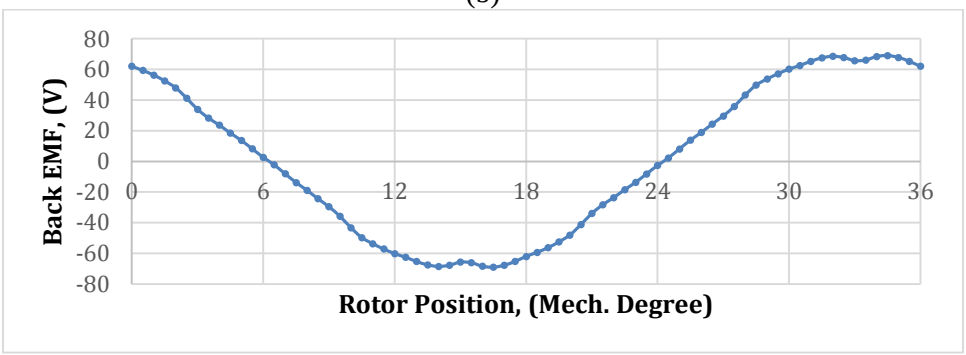

(c)

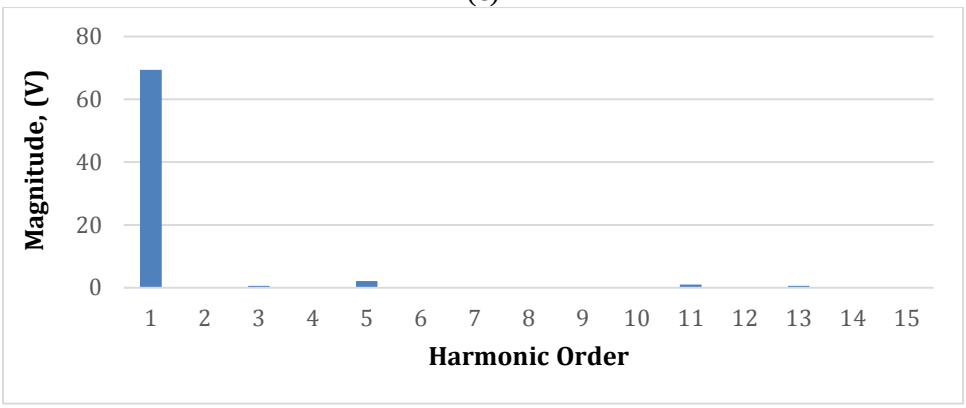

(d)

Figure 4.36: No-load performance parameters of the 50kW FSPM (a) Airgap flux density, (b) Coil and phase-A flux linkage, (c) Phase A Back EMF, (d) Spectrum of Back EMF.

4.18.1 Steady State Performance under Load Conditions

The important electromagnetic performance parameters of the designed machine are summarized in this section. Figure 4.37 (a) shows output electromagnetic torque when the machine is running under rated load of 440 Amps at 1800 RPM. Figure 4.37(b) shows the variation of average torque for different load conditions at 1800 RPM. The rated load is 440 Amps, and the machine starts going into saturation gradually for over 600 Amps. The most important performance and operation parameters of the machine are summarized in Table 4.17.

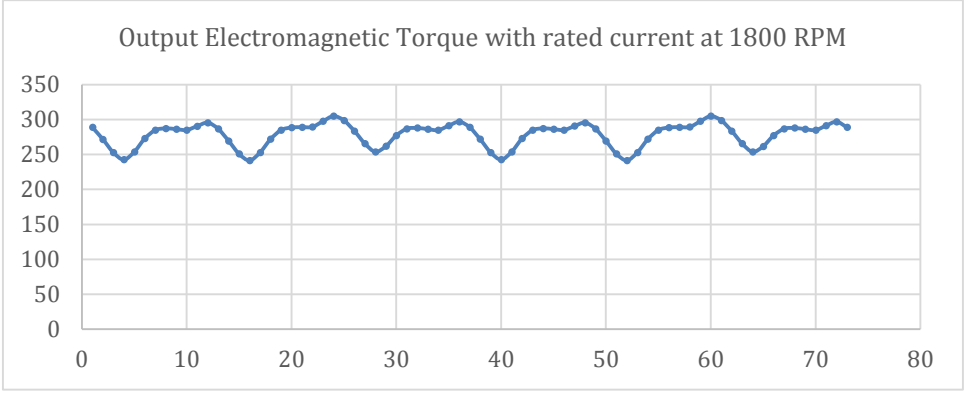

(a)

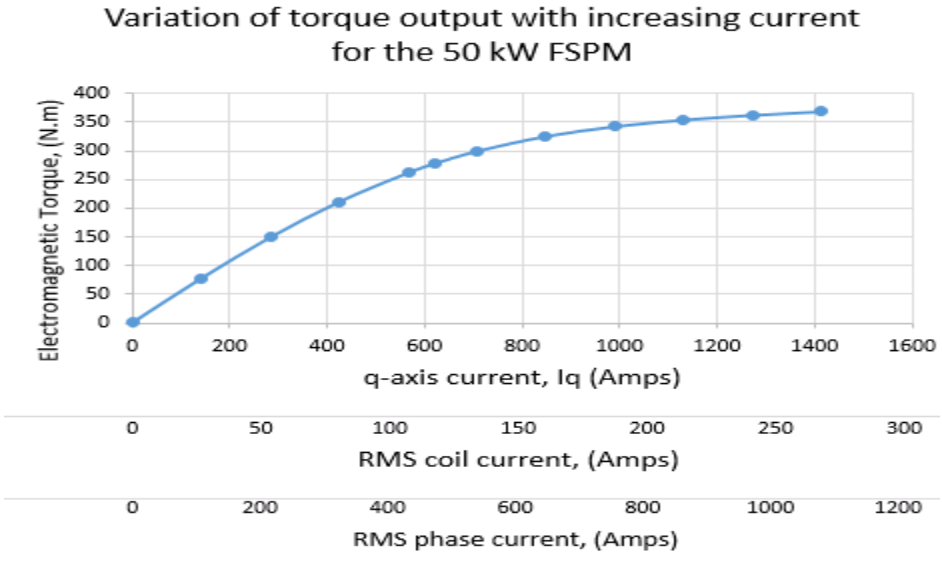

(b)

Figure 4.37: Performance of the 50 kW FSPM under loaded condition, (a) Torque, (b) Torque vs. Current.

Table 4.17: Important performance parameters of the 50kW FSPM designed

Ampere-turns	N=12, I_{rms}=110 Amps
Remnant Flux Density of Magnet, Bm	0.405
Coil Resistance	0.00084 Ohm
Phase Resistance	0.00021 Ohm
Terminal Voltage (RMS)	76.83 V
Terminal Voltage(Peak)	107.4 V
Rated phase current (rms)	440 Amps
Rated coil current (rms)	110 Amps
Pin (W)	56.3 kW
Rated Torque	278.3 N.m
Pmech (W)	52.5 kW
PCopper (W)	2 kW
PCore (W)	1.6 kW
Efficiency	90.4%
PF	0.6

4.19 Design of an FSPM with Rare Earth Magnet

Using rare earth, NdFeB magnet instead of Ferrite magnet subsequently increases the coil flux linkage, back EMF, air-gap flux density of motor for any operating condition, if all the rest of the design parameters are kept the same. It also improves the power factor for all operating condition and any electrical loading.

4.19.1 No-load Results

Figure 4.38 shows the flux density color map of the FSPM designed with rare earth, NdFeB magnet. Flux densities are higher in all parts of the iron core at all the situations as expected. At no-load, they are generally below 2.4 Tesla whereas when loaded, some pointy edges go as high as 2.55 Tesla.

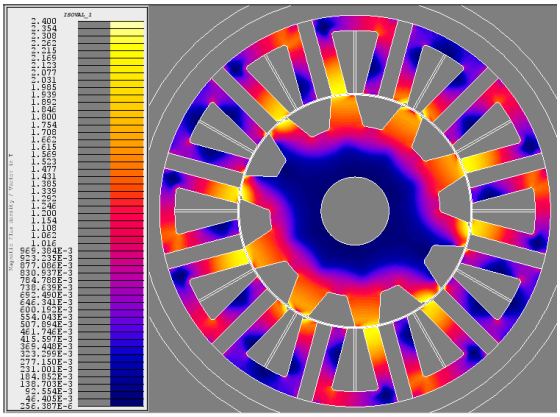

No load – phase A aligned

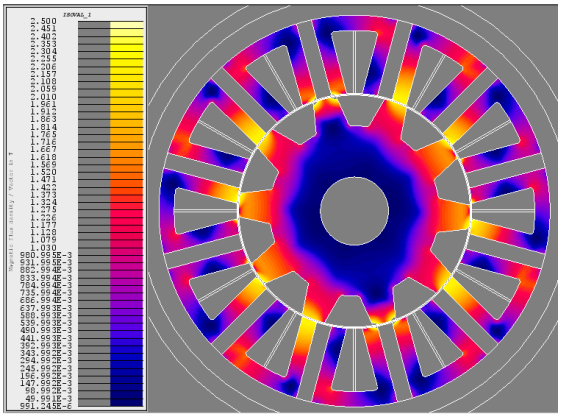

No load – phase A unaligned

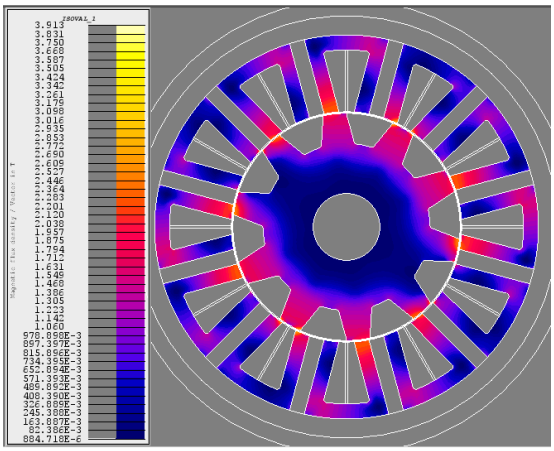

Loaded – phase A aligned

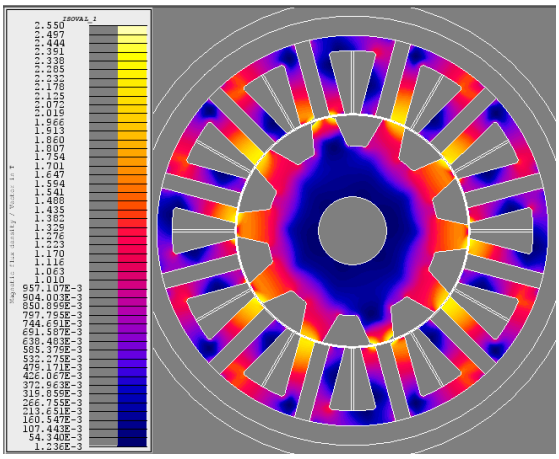

Loaded – phase A unaligned

Figure 4.38: Flux density distribution of the FSPM with NdFeB using color density plot (a) no-load, phase-A aligned, (b) no-load, phase-A unaligned, (c) loaded, phase-A aligned, (d) loaded, phase-A unaligned.

The FEA calculated normal component of airgap flux density, coil and phase flux linkage and back-EMF of the designed FSPM with NdFeB are shown in Figure 4.39. The maximum airgap flux linkage is 30% higher than non-rare earth machine. The phase flux linkage and back EMF is twice that of ferrite magnet machine, yielding in a smoother sinusoid with even more negligible harmonic components.

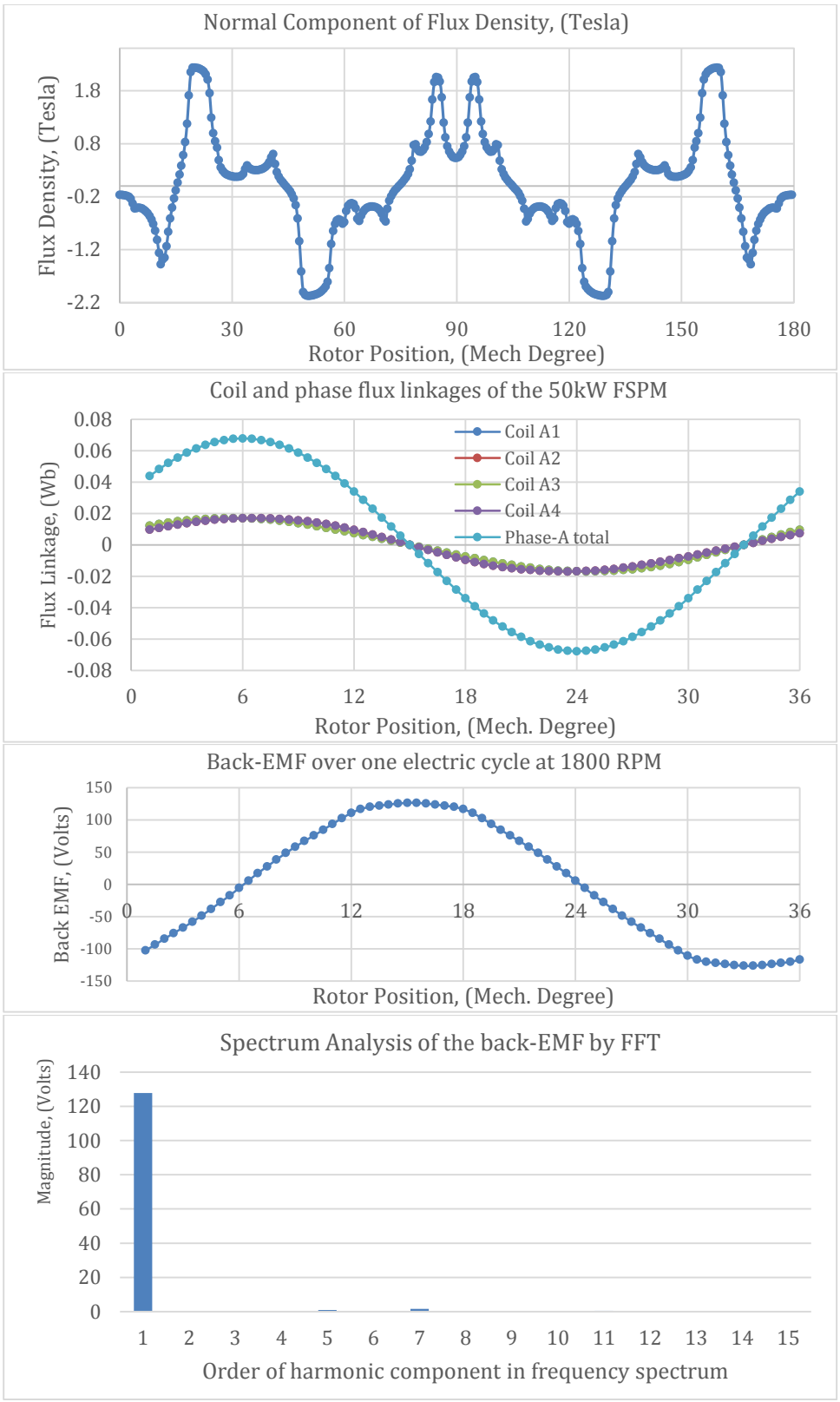

Figure 4.39: No-load performance parameters of FSPM with NdFeB (a) Airgap flux density, (b) Coil and phase-A flux linkage, (c) Phase-A Back EMF, (d) Spectrum of Back EMF.

4.19.2 Steady State Performance under Load Conditions

The key performance parameters of the designed FSPM with NdFeB magnet are shown in Figure 4.40. As no-load back EMF is twice that of non-rare earth machine, the input-output power and electromagnetic torque are also about twice that of non-rare earth machine for the same current as expected. For higher magnetic loading, power factor is also improved. As copper loss solely depends on the winding and armature current, for the same winding resistance and armature current, it remains the same as non-rare earth design. Therefore, efficiency is also higher as other losses are less influential than copper loss at this power and frequency level. The important performance measures of the machine is summarized in Table 4.18.

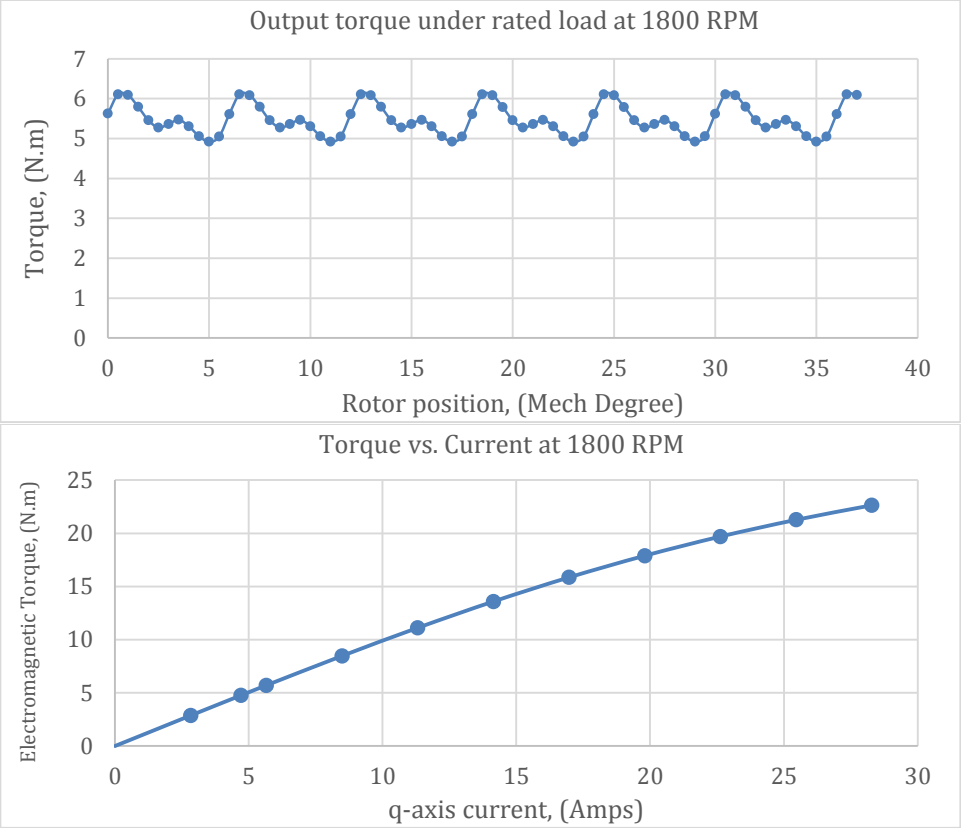

Figure 4.40: Performance of the FSPM with NdFeB under loaded condition, (a) Torque, (b) Torque vs. Current.

Table 4.18: Important performance parameters of the rare earth FSPM designed

Ampere-turns	N=47, I_{rms}=3.83 Amps
Remnant Flux Density of Magnet, B_m	1.22
Coil Resistance	0.456 Ohm
Terminal Voltage (RMS)	95.2 V
Terminal Voltage(Peak)	133 V
Pin (W)	1108 W
Rated Torque	5.48 N.m
P_{mech} (W)	1032 W
P_{Copper} (W)	20.1 W
P_{Core} (W)	44.9 W
P_{magnet} (W)	12.84
Efficiency	93%
Power Factor Angle	15 degree
PF	0.97

4.20 Conclusion

A comprehensive design methodology for Flux Switching PM machines that include FE computations has been presented in this chapter. The base machine, as well as a scaled up, higher power machine and an FSPM with rare earth PM is also designed and their performances was compared. Also, an SRM and a surface-mounted PMSM is also designed and compared with FSPM within the same volume. From the next chapter, improvement over the base design in terms of cogging torque and noise and vibration due to structural and mechanical issues will be presented. The next chapter will present novel FSPM design techniques to minimize cogging torque. One of the contributions of this research is the rotor pole shaping techniques to reduce cogging torque and hence torque ripple. Several design techniques will be applied to manage the cogging torque issue; which is discussed in detail in the next chapter. Also, the noise and vibration analysis will be presented in detail in Chapter 7. A novel analytical model to predict the radial vibration and acoustic noise from the radial pressure will be presented.

Chapter 5

Cogging Torque Reduction in FSPM

Cogging torque in FSPM is relatively high compared to the conventional rotor PM machines because of its doubly salient nature and high flux density resulting from the flux concentration effects of the circumferentially housed magnets. Reducing the cogging torque in the FSPM machine is of particular importance to make it a viable alternative to conventional rotor-PM machines. A new pole shaping method has been proposed in this chapter to reduce the cogging torque. The validity of the proposed method has been confirmed by analytical methods and finite element analysis based simulation. The influence of the proposed pole shaping method on the back-EMF and average electromagnetic torque has also been investigated.

5.1 Existing Techniques of Cogging Torque Reduction in FSPM

Prior research have demonstrated that FSPM has significant torque ripple compared to the rotor PM machines which is mainly caused by the cogging torque [103], [104]. Therefore, cogging torque minimization is important in designing an FSPM for high performance applications. Several methods have been published in the literature for cogging torque reduction on both radial [105]–[107] and axial type PM machines [98]. All of these methods cannot be directly applied to FSPM. Recently, a rotor axis teeth pairing method is presented in [108] which can only be used for machines with odd number of rotor poles; however, these machine have the disadvantage of unbalanced magnetic force compared to the machines with even number of rotor poles. In [105], harmonic current is injected into the excited winding to compensate the torque ripple resulting from cogging torque, which adds complexity in the

control system and causes additional loss. In [109] and [110], teeth notching scheme has been used to reduce the cogging torque which has manufacturing difficulty.

In this chapter [111], rotor pole shaping by introducing flange in the rotor teeth has been used as an effective cogging torque reduction method. Since the magnets are located in stator resulting in simple and robust rotor construction without any magnets or windings, it is convenient to reduce the cogging torque by modifying or manipulating the rotor dimensions with the stator unchanged. The flange geometry parameters that have influence on cogging torque are considered as design variables. Their impact on cogging torque has been examined and the required values of those parameters have been determined using finite element analysis (FEA). Based on the available FEA results on a few topologies of FSPM, a generalized design rule has been developed that can be applied to any FSPM regardless of the topology or machine size. Rotor flange can be applied with the available notching scheme to reduce cogging torque in FSPM. The effect of rotor flange on back-EMF, average electromagnetic torque and torque ripple have also been examined.

5.2 Cogging Torque in FSPM

Cogging torque is a periodic torque oscillation which occurs due to energy variation within a motor as the rotor rotates, even if there is no current in the windings with the tendency of the rotor field to align with the stator poles without currents in the windings [98], [106]–[108]. Figure 5.1 shows the cross section of the three different FSPM topologies, namely conventional 12/10, E-core 6/11 and C-core 6/13 FSPMs.

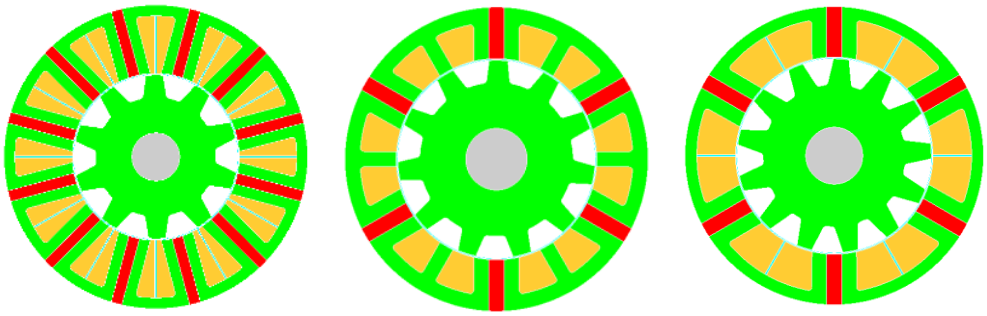

(a) (b) (c)

Figure 5.1: Cross section of three different FSPM topologies (a) Conventional 12/10, (b) E-core 6/11, (c) C-core 6/13.

Unlike PMSM, an FSPM can be modeled by a permanent magnet and an exciting coil. In a magnetic circuit composed of a permanent magnet and an exciting coil, the co-energy is given by

$$W_c = \frac{1}{2}Li^2 + \frac{1}{2}(\mathcal{R} + \mathcal{R}_m){\varphi_m}^2 + Ni\varphi_m \qquad \ldots\ldots(5.1)$$

where the first to third terms correspond to the co-energies of the self-inductance, the permanent magnet and that due to mutual flux, respectively. Here, $\mathcal{R}$ and $\mathcal{R}_m$ are the reluctances seen by the magneto-motive force source and the magnetic field, respectively, while φ_m is the magnetic flux of the magnet linking the exciting coil. The electromagnetic torque T_e can then be derived by differentiating the magnetic field energy W or total co-energy W_c with respect to mechanical angle as shown below:

$$T_e = \frac{\partial W_c}{\partial \theta} \; with \; i = constant \qquad \ldots\ldots(5.2)$$

where θ is the rotor movement angle. By substituting (5.1) into (5.2), the electromagnetic torque without any exciting current (i=0), can be calculated as

$$T_e = \frac{1}{2}i^2\frac{dL}{d\theta} - \frac{1}{2}{\varphi_m}^2\frac{d\mathcal{R}}{d\theta} + Ni\frac{d\varphi_m}{d\theta} \qquad \ldots\ldots(5.3)$$

Only the second term exists in (5.3) for cogging torque. Therefore, cogging torque can be evaluated by focusing on the magnetic interaction as well as the reluctance change between the coil and magnet which yields

$$T_{cog} = -\frac{1}{2}{\varphi_g}^2 \frac{d\mathcal{R}}{d\theta} \quad \ldots\ldots(5.4)$$

It is seen from Eq. (5.4) that the cogging torque is determined by the airgap flux, φ_g and the variation of reluctance in the magnetic circuit with the rotating displacement.

The magnetic co-energy W_c can be replaced by that stored in the airgap, W_{gap}, since the permeability of iron core is much larger than that of the airgap and PMs, ignoring the energy variation in the iron core

$$W_c \approx W_{gap} = \frac{1}{2\mu_0}\int_V B^2(\alpha)dV = \frac{1}{2\mu_0}\int_V {B_r}^2(\alpha)G^2(\alpha,\theta)dV \quad \ldots\ldots(5.5)$$

where α is the angle along the circumference of airgap, $B(\alpha)$ the flux density distribution generated by PMs in stator, $G^2(\alpha,\theta)$ the influence of salient rotor on stator flux density. The Fourier expansion of ${B_r}^2(\alpha)$ and $G^2(\alpha,\theta)$ are:

$${B_r}^2(\alpha) = B_{r0} + \sum_{m=1}^{\infty} B_{rm} cosmN_s\alpha \quad \ldots\ldots(5.6)$$

$$G^2(\alpha,\theta) = G_0 + \sum_{n=1}^{\infty} G_n cosnN_r(\alpha+\theta) \quad \ldots\ldots(5.7)$$

where N_s is the number of stator poles, N_r the number of rotor poles. The cogging torque expression in FSPM can be obtained by substituting Eqs. (5.5)-(5.7) into Eq. (5.2)

$$T_{cog}(\theta) = \frac{\pi L_{stk}}{4\mu_0}({R_2}^2 - {R_1}^2)\sum_{n=1}^{\infty} nN_L G_{nN_L} B_{nN_L} sinnN_L\alpha \quad \ldots\ldots(5.8)$$

where L_{stk} is the axial stack length, R_1 is the outer radius of the rotor, R_2 is the inner radius of the stator, G_{nN_L} and B_{nN_L} are the corresponding Fourier co-efficients of relative airgap permeance function and flux density function, and N_L is the least common multiple of the number of magnets and the number of rotor poles. The fundamental cycle of cogging torque is $\frac{2\pi}{N_L}$. Eq. (5.8) reveals that the cogging torque can be reduced by controlling N_L, G_{nN_L} and B_{nN_L}. The various design techniques can be applied to reduce cogging torque based on the expression for cogging torque.

5.3 Selection of FSPM Topology

In FSPM machines, flux focusing is utilized and high electromagnetic performance can be achieved. However, to obtain the most symmetrical back-EMF and maximum average electromagnetic torque with minimum torque ripple, certain combination of stator and rotor pole numbers are required [74]. Analytical optimization has shown that for three-phase FSPM the most feasible pole counts are 12/10 and 12/14 combinations. If the number of stator poles is 12, then 12/11 and 12/13 machines exhibit potential unbalanced magnetic force, although these have symmetric back-EMF and competitive torque density.

In an attempt to reduce magnet usage in the FSPM machines, E-core (6 E-shaped stator segments instead of 12 U-shaped segments) and C-core (6 stator pole FSPM) machines were developed [77], [78]. These topologies were optimized in terms of back-EMF and average electromagnetic torque and it was found that the 6/11 E-core and 6/13 C-core FSPMs exhibit the most symmetric back-EMF with minimum harmonics, higher torque density and efficiency.

However, due to odd number of rotor poles, these will also exhibit potential unbalanced magnetic forces.

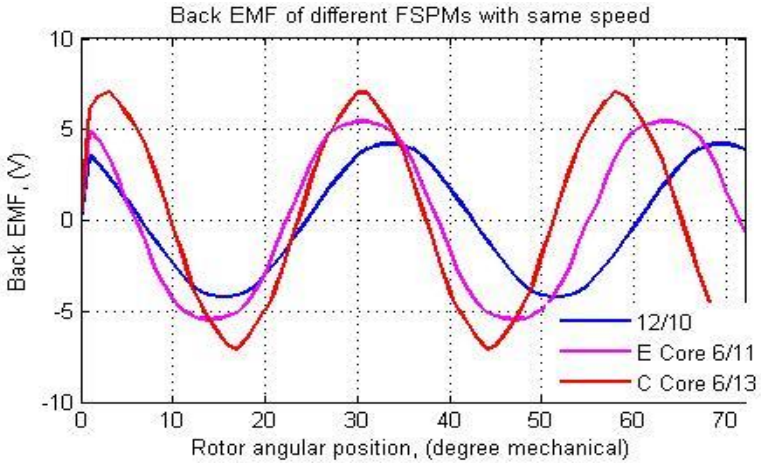

Figure 5.2: Back-EMF of 1 kW FSPMs at 400 rpm.

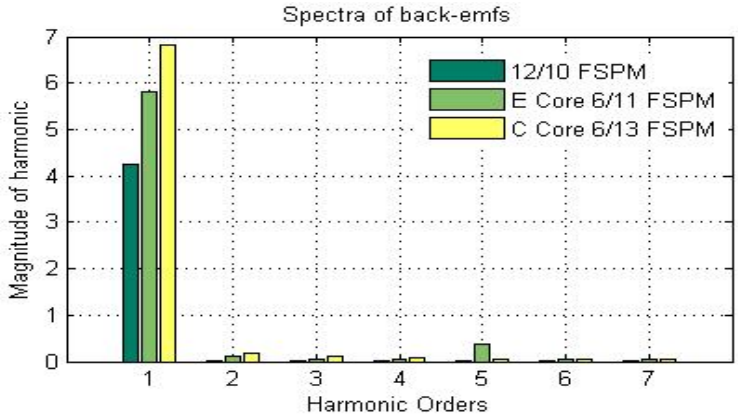

Figure 5.3: Back-EMF harmonics of the 1kW FSPM at 400 rpm.

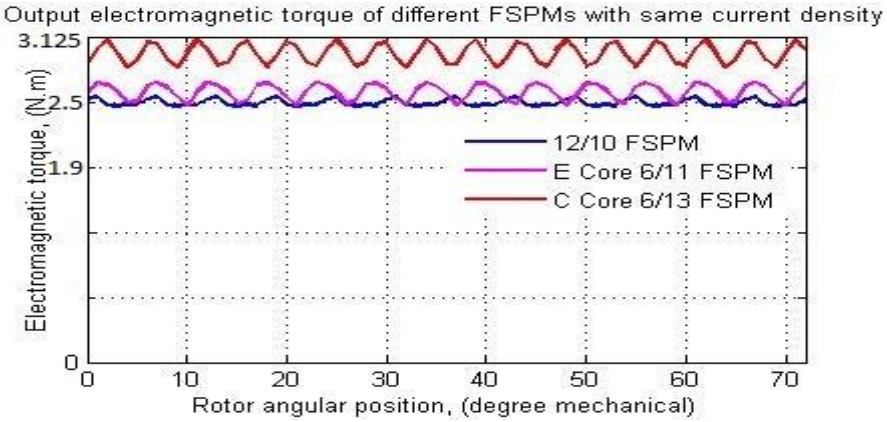

Figure 5.4: Electromagnetic torque of different FSPMs with rms current density=6 A/mm^2.

Table 5.1: Comparison among FSPMs

	$T_{e(avg)}$ (N.m)	$T_{e(ripple)}$ (N.m)	$\frac{T_{e(ripple)}}{T_{e(avg)}}$
12/10 FSPM	2.51	0.09	0.036
E-core 6/11 FSPM	2.575	0.225	0.087
C-core 6/13 FSPM	2.96	0.26	0.089

RMS current density = 6 A/mm^2, Stator outer radius=45 mm, Stack length=25 mm in all cases.

A 12/10 FSPM, a 6/11 E-core FSPM and a 6/13 C-core FSPM were designed with the constraints of 45mm stator outer radius and stack length of 25mm for finite element analysis. Regarding design of an FSPM, the general objective is to achieve symmetric, sinusoidal back EMF with minimum harmonic components to maximize the torque and power density. To achieve this, certain design rules are developed and applied accordingly. Figs. 5.2-5.4 and Table 5.1 illustrate the key performance attributes of these machines. Although E-core and C-core FSPMs offer slightly higher average torque, they exhibit significantly higher torque ripple due to the asymmetry and harmonics in back-EMF. The 12/10 FSPM exhibits the minimum per unit torque ripple.

Figure 5.6 shows the design variables using one stator pole and one rotor pole. Table 5.2 gives the values of the geometric parameters of the 12/10 FSPM machine designed based on the optimization methods available to maximize average output electromagnetic torque and to minimize cogging torque [100], [112]. Table 5.3 contains the preliminary electromagnetic design specs of the machine. Figure 5.5 shows the dimensions obtained with additional optimizations such as fillets and tapering of stator and rotor poles. The stator tooth arc β_{st}, the magnet width in magnetization direction β_m, and the slot opening, β_{so} are kept identical based on the optimization method;

$$\beta_{st} = \beta_m = \beta_{so} = \frac{360/12}{4} = 7.5° .$$

$\beta_{rt} = 1.6\beta_{st} = 12°$.

The period of cogging torque during a slot pitch rotation, N_p is given by [105]

$$N_p = \frac{360}{LCM(N_s, N_r)}$$

where $LCM(N_s, N_r)$is the least common multiple between N_s and N_r. For the 12/10 machine, N_p is 6°.

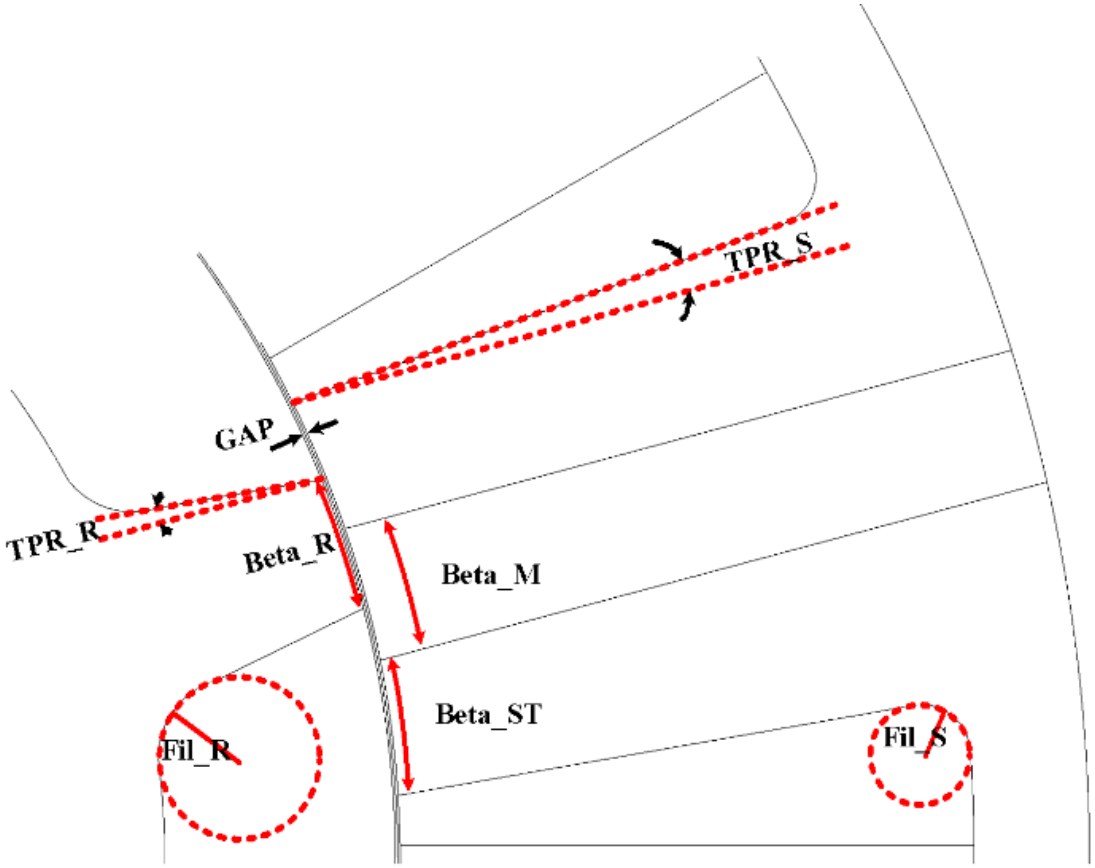

Figure 5.5: Dimensional design parameters for a stator and rotor pole.

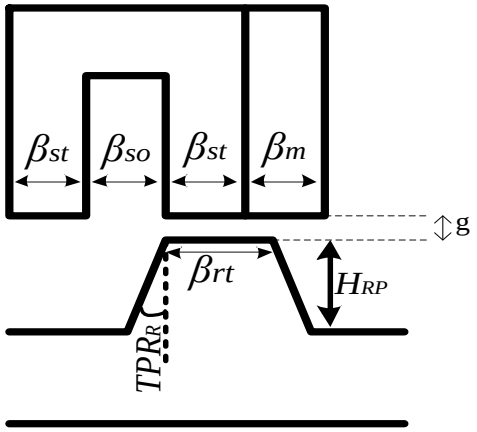

Figure 5.6: Stator and rotor shapes with magnet.

Table 5.2: 12/10 FSPM Design Parameters

Parameter	Value
Stator outer radius	45 mm
Active stack length	25 mm
Number of stator poles, N_s	12
Number of rotor poles, N_r	10
Airgap length	0.5 mm
Rotor outer diameter	24.75 mm
Split ratio	0.55
Stator tooth width, β_{st}	7.5°
Slot opening, β_{so}	7.5°
Magnet thickness, β_m	7.5°
Stator yoke thickness, W_s	3.24 mm
Angular stator tooth pitch, β_{st}	7.5°
Rotor pole width, β_{rt}	12°
Stator pole tapering, TPR_s	0°
Rotor pole tapering, TPR_r	10°
Stator pole fillet radius, FIL_s	2 mm
Rotor pole fillet radius, FIL_r	1 mm
RMS current density, J (A/mm^2)	6 A/mm^2
Speed	4000 RPM
Power	1 kW

Table 5.3: Preliminary design specifications of the 12/10 1kW FSPM

Parameter	Value
Rated speed	4000 RPM
Back EMF (RMS)	30 V
Phase Resistance	0.3 Ohm
Phase Inductance	0.073 mH
Power Factor	0.9
Core loss at 300 Hz	44 W
Copper Loss	107 W
Efficiency	85%

Figure 5.7 shows the flux density of the 12/10 machine at rated load when phase-A is completely unaligned with the rotor pole. The flux densities reach close to 2.5 Teslas in regions with sharp edges, but generally do not exceed 2 Teslas in most of the iron regions. [113], [114]

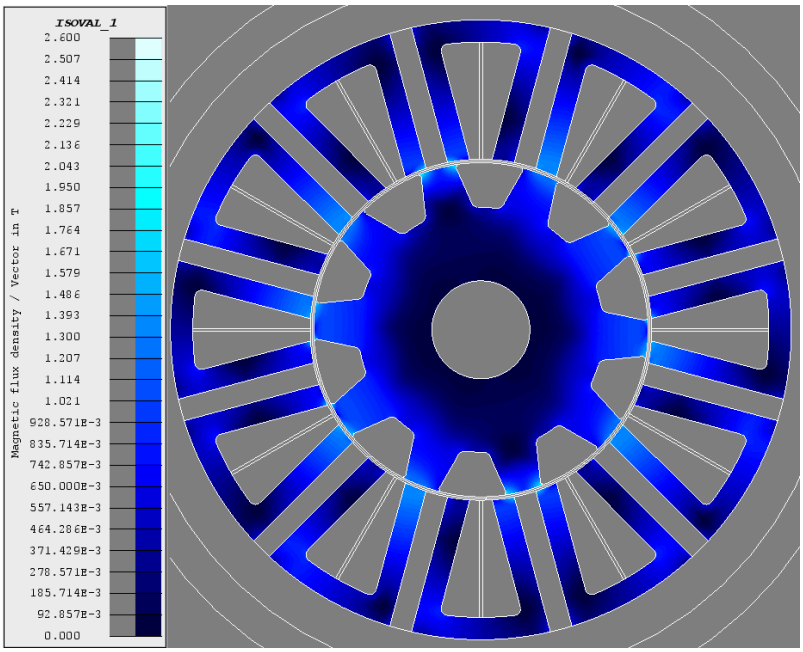

Figure 5.7: FEM plot of flux density distribution for the 12/10 FSPM at rated condition.

5.4 Cogging Torque Reduction Using Rotor Flange

Eqs. (5.4) and (5.8) clearly show that the variation of airgap permeance is one key parameter that affects the cogging torque apart from the airgap flux. The cogging torque can be reduced if the variation of airgap reluctance can be minimized as the rotor rotates. The permeances of the ferromagnetic regions and the permanent magnets can be obtained in a straightforward manner. However, the permeances of the airgap region are much more complicated, which is also the key airgap flux density prediction. The flux paths in the airgap region around each U-shaped stator segments are simplified, and the stator and rotor surfaces are assumed to be equipotentials to estimate the permeance [54].

The equivalent reluctance of the airgap is a function of the rotor position. The flux goes through air taking a circular path facing higher reluctance when there is no overlap between stator and rotor poles compared to the case when the poles overlap. Therefore, cogging torque can be minimized if this change can be made smoother, or less steep. This can be achieved by introducing more iron in the corner of the rotor poles towards the circumference structured like a flange or pole shoe.

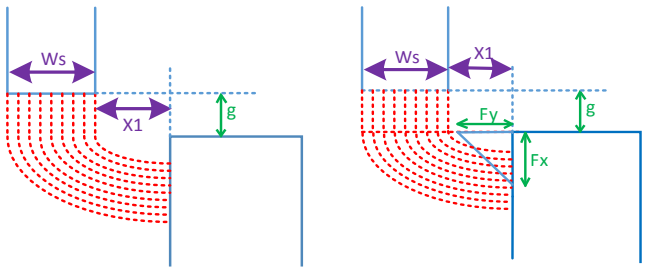

(a) (b)

Figure 5.8: Simplified flux paths between one stator tooth and rotor pole when they are not overlapping (a) without flange, (b) with flange.

Figure 5.8(a) shows the simplified flux paths between one stator tooth and one rotor pole before the rotor pole shaping. Flux lines are assumed to be straight lines in the airgap region and circular beyond the airgap region in between the rotor poles. The equation for permeance then becomes:

$$P = \frac{2\mu_0 L_{stk}}{\pi} ln\left(\frac{\pi X_1 + 2g + \pi W_s}{\pi X_1 + 2g}\right) \quad \ldots (5.9)$$

$$\mathcal{R} = \frac{1}{P} = \frac{\pi}{2\mu_0 L_{stk}} \frac{1}{ln\left(\frac{\pi X_1 + 2g + \pi W_s}{\pi X_1 + 2g}\right)} \quad \ldots (5.10)$$

The cylindrical co-ordinate is laid out in a linear fashion in Figure 5.8 for simplicity. As the rotor rotates, the angle θ changes in the cylindrical co-ordinate, which can be represented as X_1 in the linear co-ordinate. Therefore, in an attempt to minimize cogging torque, the reluctance can be differentiated with respect to rotor position X1 and set to zero to obtain the necessary condition. Setting $\frac{d\mathcal{R}}{dX_1} = 0$, it can be shown that $W_s = 0$. This shows that it is not possible to obtain zero cogging torque from this 2-D model without modifying the geometry. However, if pole shoe or flange is added to the periphery of the rotor teeth as shown in Figure 5.8(b), more iron is introduced instead of air. The flange offers a flux path for any stator-rotor pole position in which the variation of reluctance with respect to rotor position is also minimized. For simplicity, the width of flange F_y is assumed to be the same as its depth F_x. The equation for airgap permeance with this structure becomes:

$$P = \frac{\mu_0 L_{stk}}{\pi} ln\left(\frac{\pi X_1 + 2g + \pi F_y}{\pi X_1 + 2g - \pi F_y}\right) + \frac{2\mu_0 L_{stk}}{\pi} ln\left(\frac{\pi X_1 + 2g + \pi W_s + \pi F_y}{\pi X_1 + 2g + 2\pi F_y}\right) \quad \ldots (5.9)$$

The corresponding reluctance is given by

$$\mathcal{R} = \frac{1}{P} = \frac{\pi}{\mu_0 L_{stk}} \frac{1}{ln\left[\left(\frac{\pi X_1 + 2g + \pi F_y}{\pi X_1 + 2g - \pi F_y}\right) \times \left(\frac{\pi X_1 + 2g + \pi W_s + \pi F_y}{\pi X_1 + 2g + 2\pi F_y}\right)^2\right]} \quad \ldots (5.10)$$

Setting $\frac{d\mathcal{R}}{dX_1} = 0$, the following third order equation is obtained:

$$\pi^2 {F_y}^3 + {F_y}^2(3\pi A + 3\pi^2 W_s) + F_y(2A^2 + 2\pi W_s A) - W_s A^2 = 0 \quad \ldots (5.11)$$

where $A = \pi X_1 + 2g$ is used for convenience. Solving this equation using the solution for cubic polynomial, it is possible to obtain a condition for F_y in terms of g and W_s for any position X_1 that gives theoretically zero cogging torque.

$$x = \sqrt[3]{\left(\frac{-b^3}{27a^3} + \frac{bc}{6a^2} - \frac{d}{2a}\right) + \sqrt{\left(\frac{-b^3}{27a^3} + \frac{bc}{6a^2} - \frac{d}{2a}\right)^2 + \left(\frac{c}{3a} - \frac{b^2}{9a^2}\right)^3}} + \sqrt[3]{\left(\frac{-b^3}{27a^3} + \frac{bc}{6a^2} - \frac{d}{2a}\right) - \sqrt{\left(\frac{-b^3}{27a^3} + \frac{bc}{6a^2} - \frac{d}{2a}\right)^2 + \left(\frac{c}{3a} - \frac{b^2}{9a^2}\right)^3}} - \frac{b}{3a}$$

For a certain value of airgap g and stator tooth width, W_s, a value of F_y can be obtained by solving Eq. (5.14) that yields zero reluctance variation, and therefore, zero cogging torque. The value obtained may not match with the actual flange width required to achieve zero cogging torque since the influence of magnetic saturation and flux leakage were not considered, but does provide a theoretical basis for pole shaping to minimize the cogging torque. In a practical machine, the cogging torque results from the mutual torque produced by all the 12 magnets. In the simplified analysis presented, one magnet, one stator tooth and one rotor pole is considered. Also, localized saturation effect and flux leakage are not considered and simplified pole shape is assumed for the sake of simplifying the analysis. This analysis shows that adding flange to conventional rotor pole is helpful in minimizing the cogging torque. The required flange width

to minimize cogging torque in the final design is obtained from finite element analysis, but the initial estimate can be obtained from the analytical model.

The reason for cogging torque improvement with flange can further be explained with the help of Figure 5.9. It was observed that for a 12/10, 3-phase FSPM machine, the maximum phase flux linkage occurs when the center of a rotor tooth is 9° (mech.) apart from the axis of phase-A coil. In this situation, the stator tooth and rotor pole are completely unaligned with each other. Now, phase-A flux-linkage can be maximized if additional iron in the rotor pole periphery is aligned with the stator tooth surface while maintaining the 9° mechanical displacement from the phase-A coil axis. This means the flux linkage can be maximized if a wider rotor pole is used so that its left edge is aligned with the left edge of the corresponding stator tooth. The required rotor pole arc can then be calculated as 10.5° (mech.) which is 1.4 times that of the original stator tooth arc. The actual required rotor pole arc was found to be 1.6 times that of stator tooth arc using finite element analysis where the influence of magnetic saturation and leakage flux are considered [100].

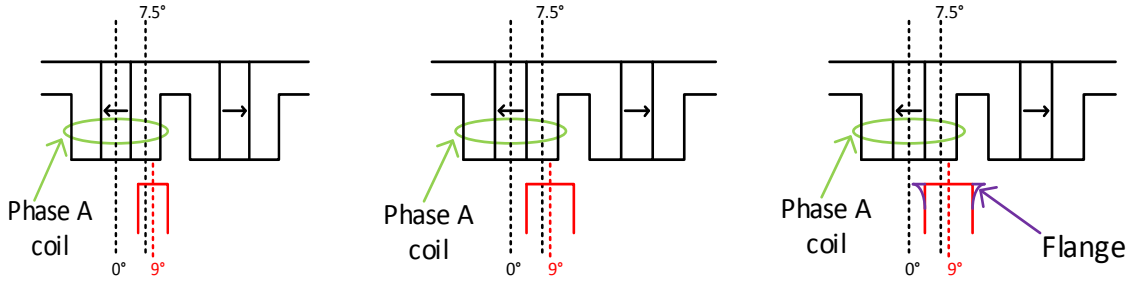

Figure 5.9: Different rotor pole width scenario with respect to stator tooth width (a) Rotor pole width=Stator tooth width, (b) Rotor pole width = 1.4*Stator tooth width, (c) Rotor pole width=1.4*Stator tooth width with flange.

Now, cogging torque occurs as the magnetic flux established by the magnets goes through a varying reluctance path as the rotor rotates. This variation can be minimized by introducing

small flange-like structure at the corners of the rotor pole periphery while maintaining the rotor pole arc at 1.6 times larger than the stator tooth so that the condition for maximum phase flux linkage is still satisfied. This structure of the rotor pole allows a more gradual change in reluctance for the flux path with rotor rotation, and consequently, reduces the cogging torque. The process above shows an analytical method for determining the rotor flange width that yields the minimum reluctance variation. The actual required rotor flange width for minimum cogging torque may not be the solution of the equation due to saturation and leakage fluxes, but should be close. The determination of the optimum flange width for different topologies of FSPM machines using FEA is described in the following section.

5.5 Flange Parameter Optimization with FEA

Cogging torque reduction can be achieved by shaping the rotor poles to provide a greater circumferential width in the region near the airgap to increase the amount of magnetic material where the flux density is the highest. This will also affect the reluctance torque produced by the machine. Figure 5.10 shows the rotor pole flange in the developed geometry in finite element analysis, and Figure 5.11 shows the topology. The optimum amount of spread of this rotor pole flange can be determined by finite element analysis. The procedure to determine the required flange width to minimize cogging torque, and hence, to come up with a design rule that can be applied to all flux switching machines is given in the flow chart shown in Figure 5.12. Rotor flange thickness t is kept constant and flange width (F_y) is the same as Flange height (F_x). F_y was swept from zero to 2 mm for the 1kW machine. Figure 5.13-Figure *5.16* show the effect of varying F_y on cogging torque for three different sized machine.

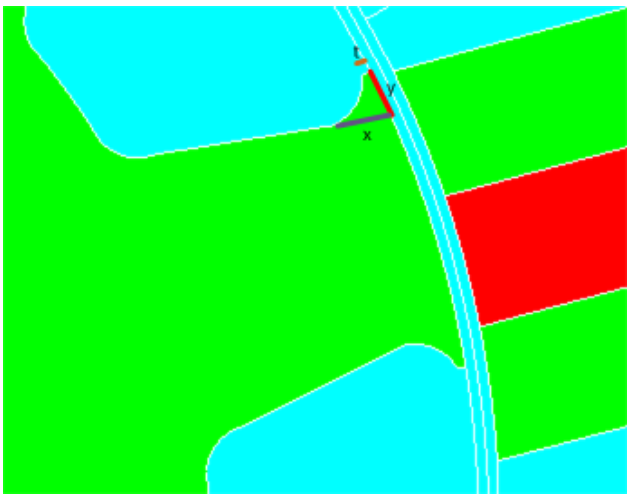

Figure 5.10: FEA schematic of FSPM with rotor flange.

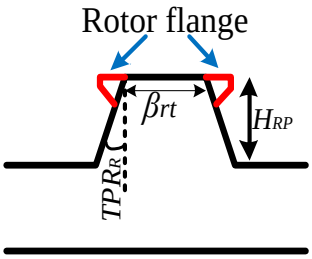

Figure 5.11: Topology of the FSPM with rotor flange.

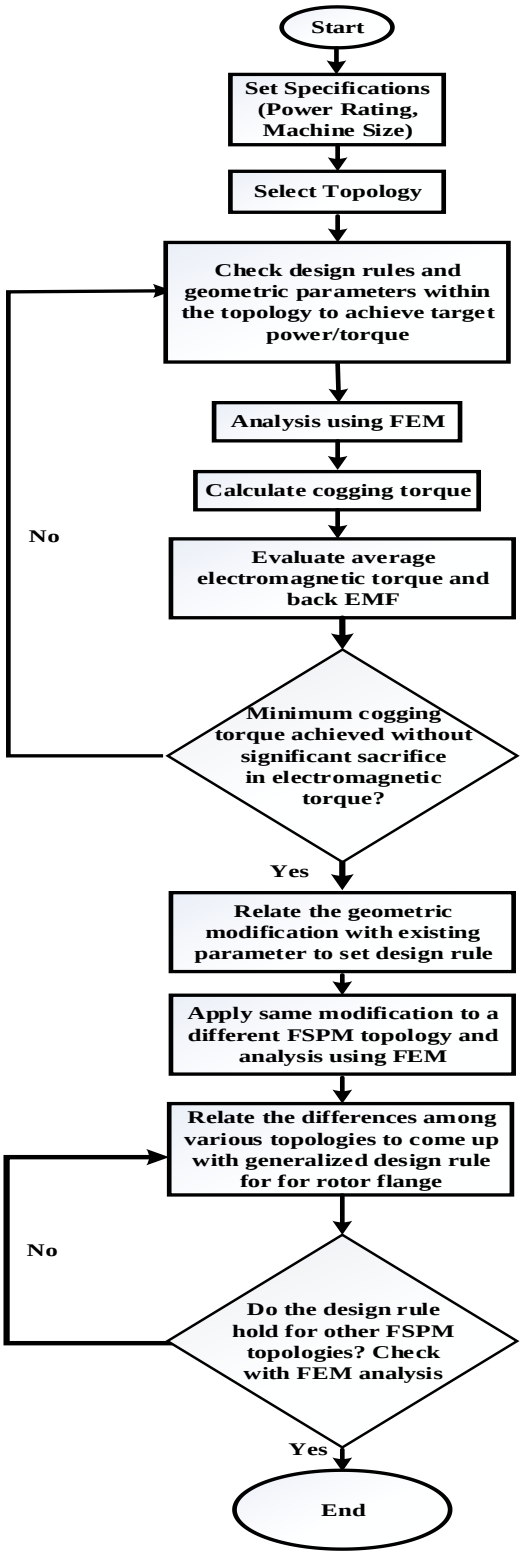

Figure 5.12: Flow chart of cogging torque minimization method.

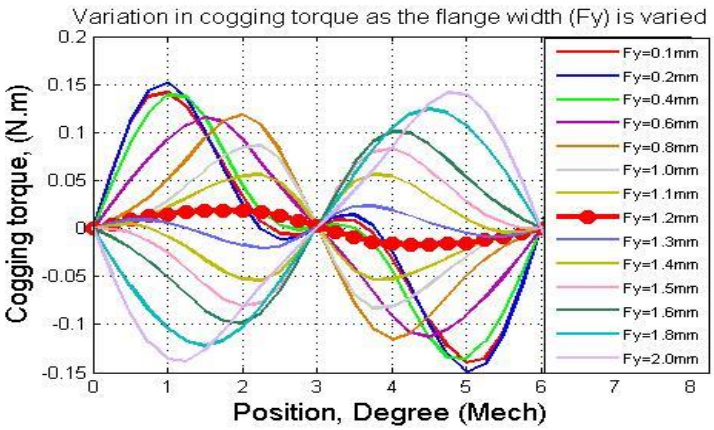

Figure 5.13: Variation in cogging torque with flange width for the machine of outer radius=45 mm.

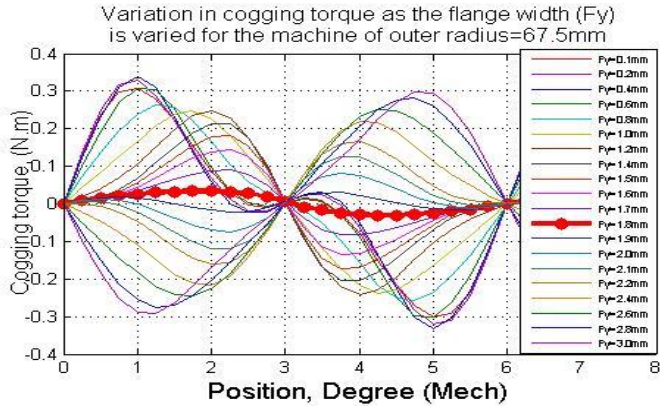

Figure 5.14: Cogging torque variation with rotor flange width for the machine with outer radius=67.5 mm and same L_{stk}.

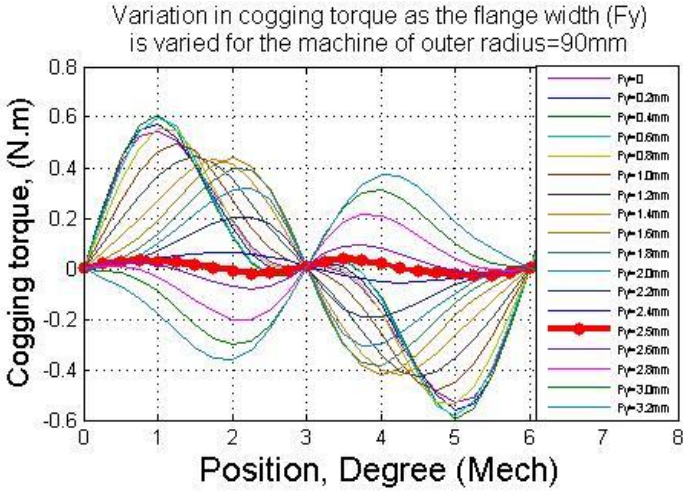

Figure 5.15: Cogging torque variation with rotor flange width for the machine with outer radius=90 mm and L_{stk}.

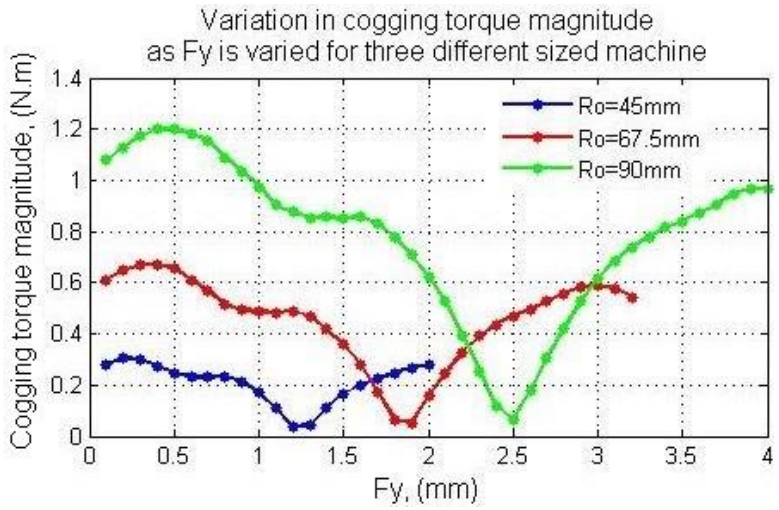

Figure 5.16: Cogging torque magnitude variation with rotor flange width for FSPM of three different sizes.

The simulation results with flange are summarized in Figure 5.13-5.16 and Table 5.4. The cogging torque waveform undergoes a phase reversal when passing through the optimal flange width, as shown in Figs. 5.13-5.15. Without the flange, smaller (low power) machine exhibits smaller cogging torque whereas larger (higher power) machine exhibits higher cogging torque. The magnitude of cogging torque varies similarly with flange width variation for any sized machine for the same topology. However, there exists a value of the flange width for which the cogging torque magnitude is the minimum and negligible. Figure 5.13 shows that cogging torque is minimum when F_y is 1.2 mm for the 1kW FSPM machine. As the flange width is increased, the magnitude of cogging torque decreases up to a certain width. After that, increasing the width further results in an increase in cogging torque. The scenario is the same for FSPMs of other sizes. Figs. 5.14-5.15 shows the cogging torque variation with flange width for a machine whose radius is 1.5 and 2 times that of the original 1kW machine, respectively. Other geometric parameters of the machine were scaled up accordingly.

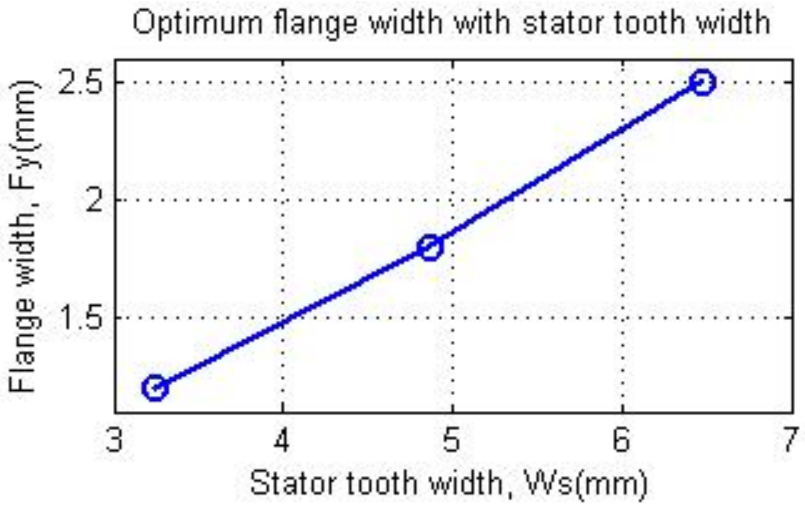

Figure 5.17: Variation of optimum flange width with stator tooth width.

Table 5.4: Optimum flange width for machines of different sizes and stator tooth width.

Machine outer radius, (mm)	Power, (kW)	Stator tooth width, Ws (mm)	Optimum flange width for minimum cogging torque	Fy for minimum reluctance variation (Eq. 5.13)
45 mm	1 kW	3.237 mm	1.2 mm	0.4 mm
67.5 mm	2.25 kW	4.86 mm	1.8 mm	0.6 mm
90 mm	4 kW	6.474 mm	2.5 mm	0.8 mm

The cogging torque peaks occur when the rotor poles are aligned with the stator teeth. Referring to Figure 5.9(c) and from Table 5.4, the following condition for flange to minimize cogging torque amplitude can be defined:

$$1.4W_s + 2F_y > 2W_s, or\ F_y > 0.3W_s$$

This allows flux linked with adjacent stator tooth to compensate for the cogging torque due to its alignment with one tooth at the peak condition. This holds for any FSPM with slot opening/pole pitch ratio of 0.5.

Figure 5.17 shows the change of optimum flange width for FSPMs of different sizes. The flange width is related to the stator tooth width and both of them increase as the machine size is increased. The trend is similar to that obtained from the analytical approach as given in column 5 of Table 5.4, but the values are different; this is due to the effect of magnetic saturation and leakage flux that was neglected in the theoretical analysis. Also, a single magnet piece with single stator tooth and rotor pole was considered for the analysis. The net cogging torque is the combined mutual effect of all 12 magnets in the machine.

5.6 Rotor Pole Flange Effect on Back EMF and Torque

Cogging torque reduction is often achieved at the cost of electromagnetic performance. It is important to observe the effect of rotor flange on back-EMF and electromagnetic torque.

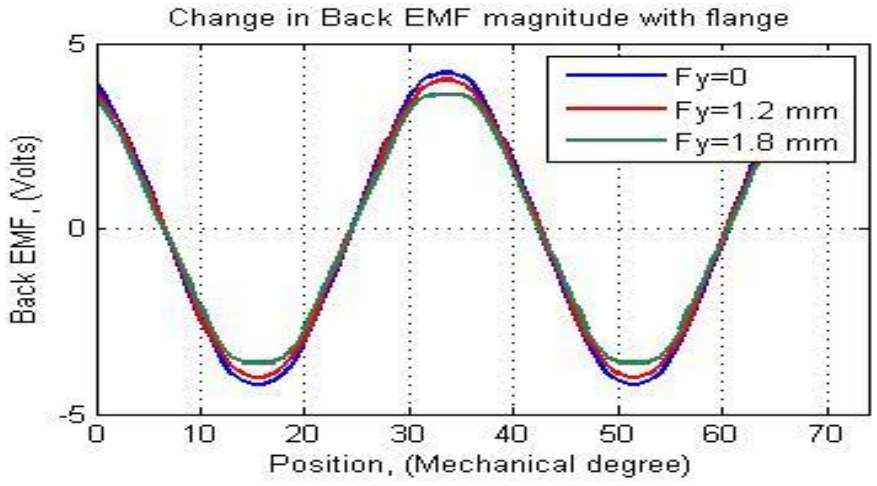

Figure 5.18: Variation in back-EMF at 400 rpm with the width of rotor.

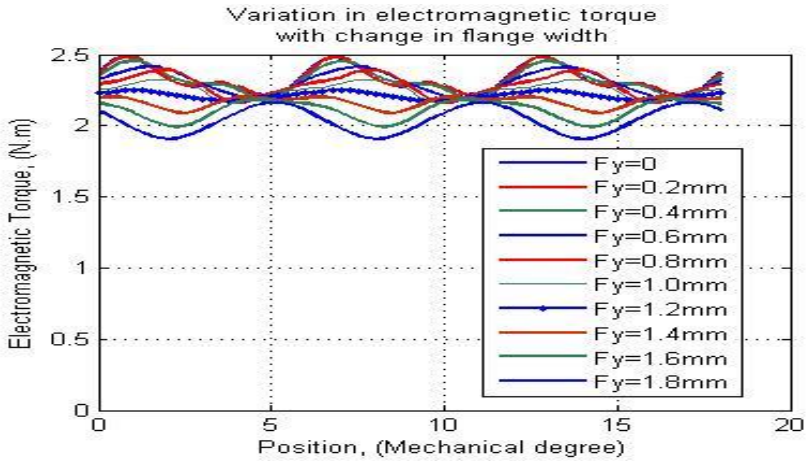

Figure 5.19: Variation in average electromagnetic torque at 400 rpm and J=5A/mm2 with the width of rotor flange.

Table 5.5: Reduction in cogging torque and average electromagnetic torque for various flange widths.

Flange Width (mm)	Peak to peak Torque Ripple (N.m)	Average Electromagnetic Torque (N.m)	Reduction in Torque Ripple (%)	Reduction in Average Electromagnetic Torque (%)
0	0.272	2.34	0	0
0.4	0.28	2.32	-3%	0.85%
0.8	0.24	2.28	11.76%	2.56%
1.2	0.07	2.215	97%	5.34%
1.6	0.26	2.03	4.4%	13.24%

Back-EMF does not reduce significantly with flange height and width variations as shown in Figure 5.18. Figure 5.19 shows that the improvement of cogging torque is achieved by a very small reduction in the average electromagnetic torque. Table 5.5 shows the percentage reduction in cogging torque and average electromagnetic torque. Up to 97% reduction of torque ripple from the original design can be achieved with only 5.34% sacrifice of the average electromagnetic torque.

5.6.1 Torque Separation and Effect on Reluctance Torque

For the 3-phase FSPM operated by vector-control method, the average electromagnetic torque, T_{em} can be expressed in the dq-axis reference frame as

$$\mathrm{T_{em}} = \frac{3}{2} N_r [\varphi_m I_q + (L_d - L_q) i_d i_q] \quad \ldots (5.12)$$

where, N_r is the number of rotor poles, φ_m is the PM flux linkage, i_d, i_q are d- and q-axes currents, respectively, and L_d, L_q are d- and q- axes inductances, respectively. This equation indicates that the torque of FSPM is composed of two components, the PM torque T_{pm}, and the reluctance torque T_r caused by the difference of L_d and L_q. For FSPM motor T_r is negligible compared with the PM torque components since the d- and q-axes inductances are almost the same [54, [70]. The electromagnetic torque can simply be calculated from

$$T_{em} \cong T_{PM} = \frac{3}{2} N_r \varphi_m I_q \quad \ldots (5.13)$$

A frozen permeability analysis have been performed to separate the torque components and verify the effect of the proposed rotor geometry on different torque components.

In order to separate the torque components in Eq. (5.14) using the concept of frozen permeability, a sequence of dedicated processes in one electrical period is performed. First, the magnetic fields in the machine at a given operating condition are solved by time-stepped FE over one electrical period. At each time step or each rotor position, relative permeability of each element in the stator and rotor cores are stored as spatial quantities. Thereafter, the magnetic properties for the stator and rotor cores are updated from the original B-H curves to the spatial quantities at the current time step. Subsequently, the excitation sources are changed according to the descriptions in the second column in Table 5.6. By way of example, to

calculate reluctance torque, FEA is performed by setting the remanence of the magnets to zero while the current excitation is kept as required. After all the components in Table 5.6 are computed, the permeability of stator and rotor cores is updated using the spatial quantities at the next time step. This process continues for one electrical period.

Table 5.6: Separation of Torque components by frozen permeability method

Reluctance torque, T_{rel}	Remove Magnet, Rated Load	T_{rel}
Cogging Torque, T_{cog}	No Load, with Magnet	T_{cog}
Total Electromagnetic Torque	Rated Load, with Magnet	$\mathrm{T_{em}} = T_{mutual} + T_{cog} + T_{rel}$

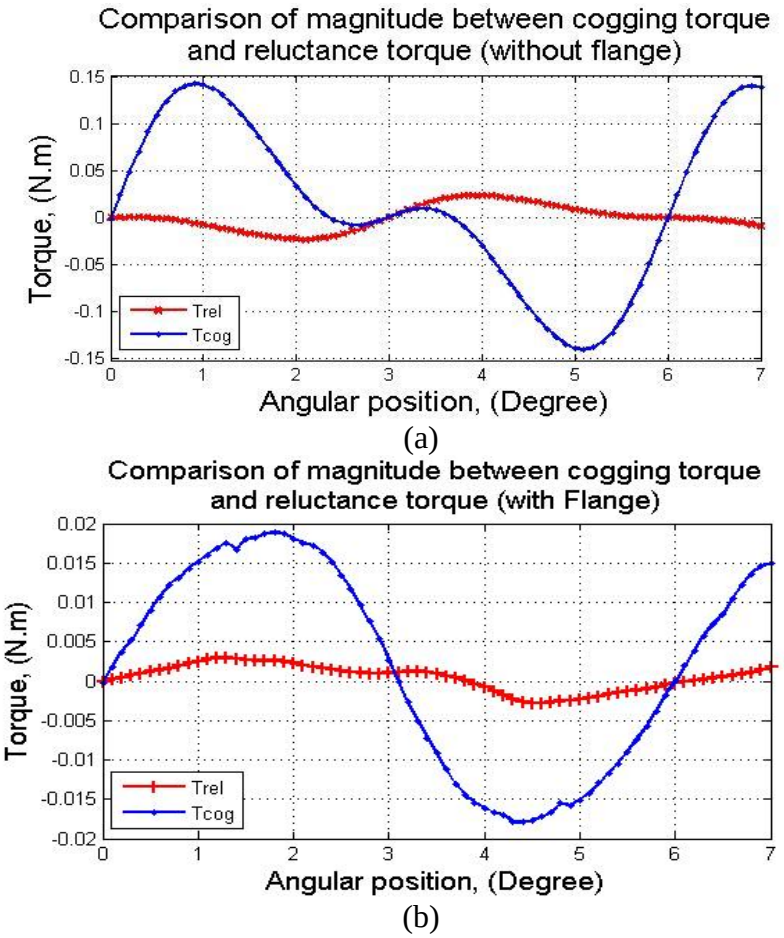

Figure 5.20: Torque separation in 1kW, 12/10 FSPM, (a) without flange, (b) with flange.

Table 5.7: Comparison of magnitudes of torque components

	Cogging torque (T_{cog}) amplitude (p-p), (Nm)	Reluctance torque (T_{rel}) amplitude (p-p), (Nm)	Average electromagnetic torque, T_{avg}	Peak-peak ripple in electromagnetic torque, T_{ripple}
Without Flange	0.283	0.047	2.34	0.273
With Flange	0.037	0.006	2.22	0.071

Figure 5.20 shows a comparison of the separated torque components of the machine, with and without flange. Table 5.7 contains the values of amplitudes of separated torque components. The peak-peak reluctance torque is about 15% of the peak-peak variation of the cogging torque, which remains of the same percentage after applying rotor flange.

5.6.2 Effect of Rotor Eccentricity

An analysis of the effect of rotor eccentricity on FSPM cogging torque and its overall noise and vibration characteristics has been carried out. A range of static eccentricity has been considered from 0 to 0.2 mm, which is 40% eccentricity for a 0.5 mm airgap. The cogging torque simulation with and without eccentricity as well as with and without flange are plotted against mechanical movement as shown in Figure 5.21.

The shape of cogging torque waveform becomes irregular, and both the positive peak and the negative peak increases as the rotor becomes more eccentric. This variation beocmes more significant as the eccentricity becomes more severe.

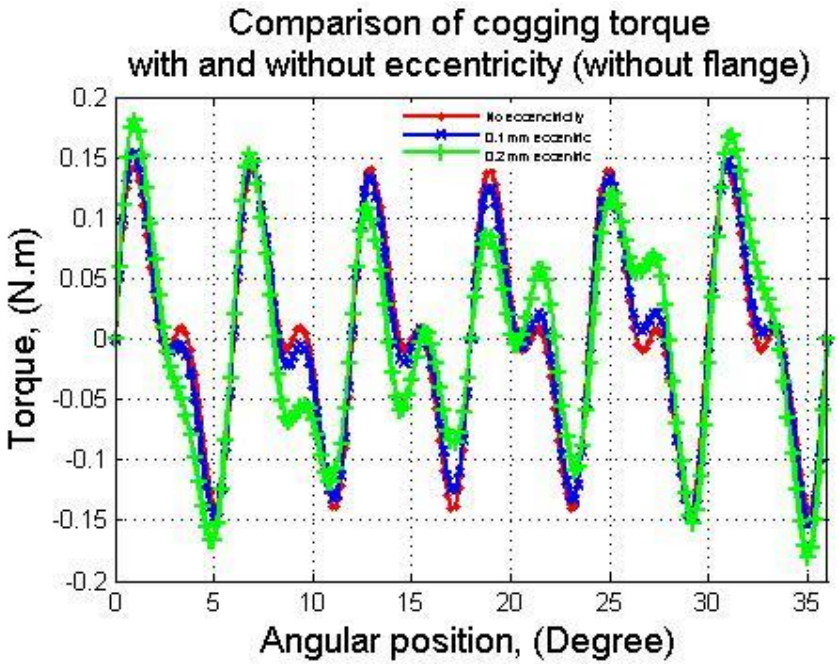

(a)

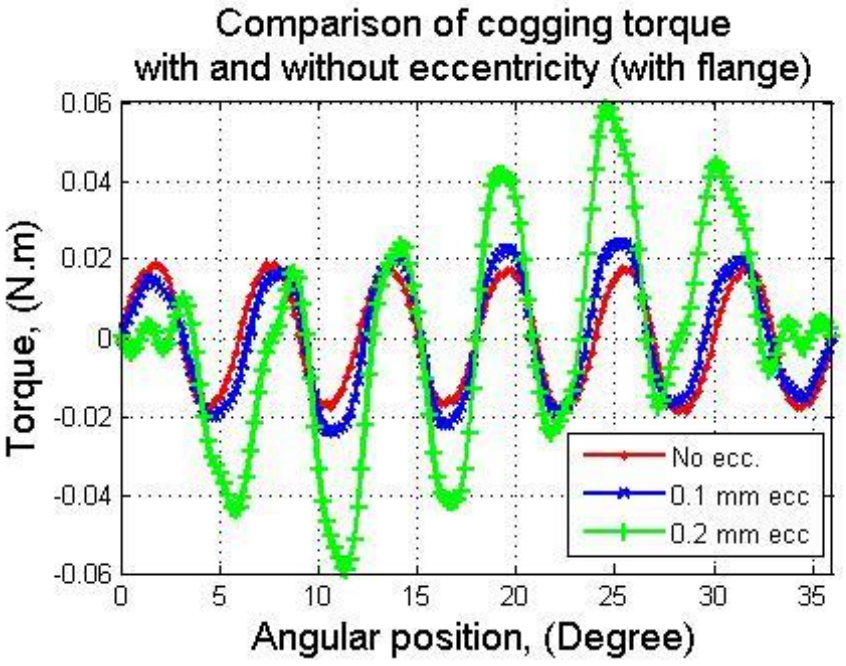

(b)

Figure 5.21: Eccentricity effect on cogging torque (a) without flange, (b) with flange.

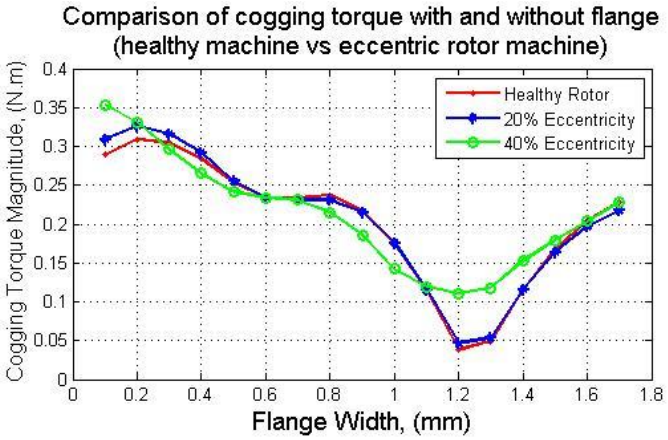

Figure 5.22: Rotor flange in minimizing cogging torque in healthy and eccentric FSPM.

The application of rotor flange in reducing cogging torque magnitude holds true for eccentric machine as well. Figure 5.22 shows the plot and comparison between cogging torque magnitude as flange width is increased among a healthy, a 20% eccentric and a 40% eccentric machine. Table 5.8 gives the amplitude of cogging torque before and after applying flange in healthy and eccentric rotor FSPMs, which shows that the peak to peak cogging torque increases in an eccentric rotor FSPM.

Table 5.8: Comparison of cogging torque amplitude (with and without flange) among healthy and eccentric rotor FSPMs

	Peak-peak T_{cog} (No eccentricity)	Peak-peak T_{cog}, 20% eccentricity	Peak-peak T_{cog}, 40% eccentricity
Without flange	0.28	0.31	0.36
With flange (1.2 mm)	0.037	0.048	0.11

5.7 Rotor Pole Flange in E-Core and C-Core FSPM

The same technique of rotor pole shaping can be applied to other varieties of FSPMs such as the E-core and C-core machines. The advantages of E-core FSPM over conventional FSPMs are reduced magnet usage. An E-Core FSPM was designed in FEA with the same outer diameter and stack length. Similar improvement was observed for cogging torque with varying flange widths as shown in Figure 5.23. Also, similar behavior was observed in C-Core FSPM as shown in Figure 5.24.

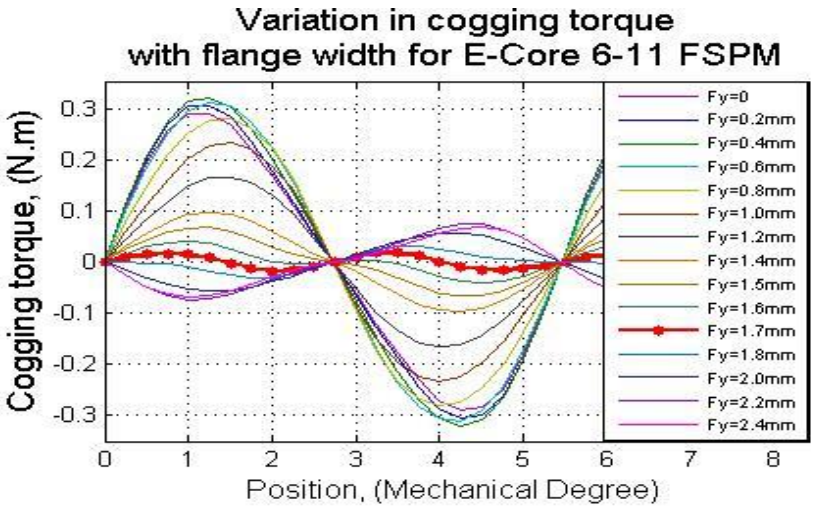

(a)

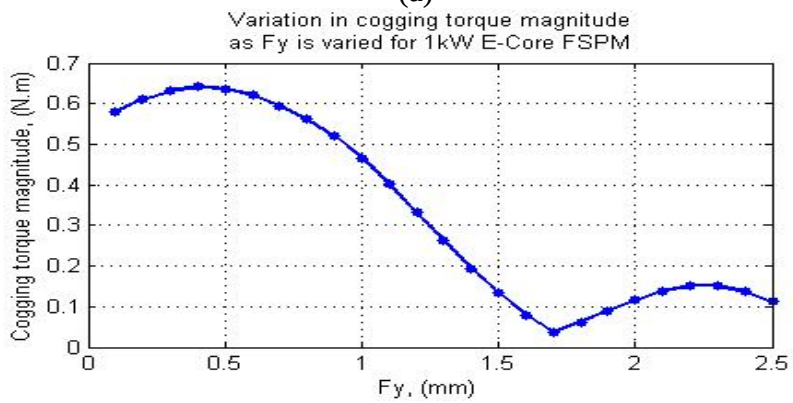

(b)

Figure 5.23: Cogging torque in E-core, 6/11 FSPM (a) Cogging torque as flange width is varied, (b) Variation in cogging torque magnitude with flange width.

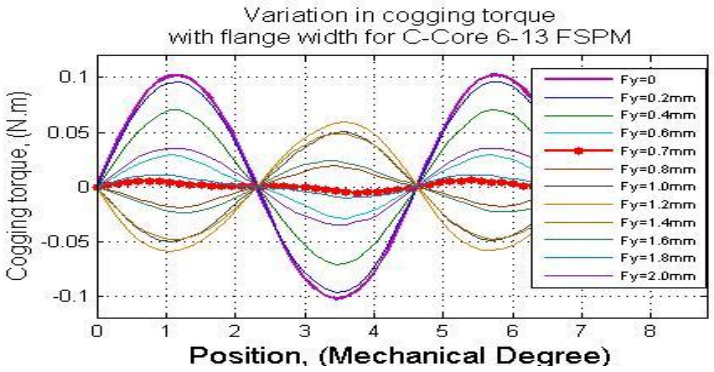

(a)

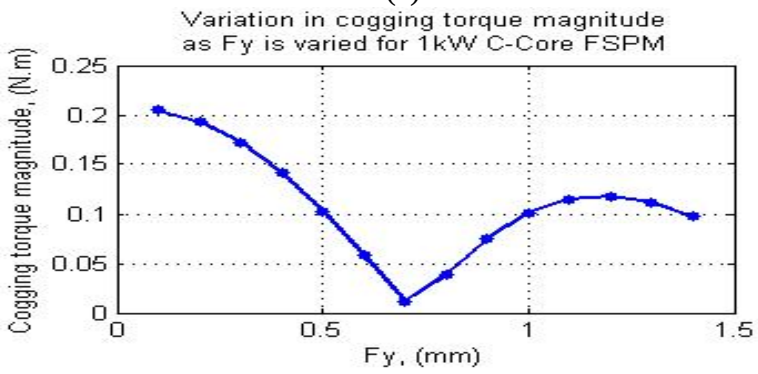

(b)

Figure 5.24: Cogging torque in C-core, 6/13 FSPM (a) Cogging torque as flange width is varied, (b) Variation in cogging torque magnitude with flange width.

Table 5.9: Cogging torque reduction in E-Core and C-Core machine using rotor flange

	E-Core	C-Core
T_{cog} (F_y=0)	0.58 N.m	0.2051 N.m
T_{cog} at optimum	0.037 N.m	0.01165 N.m
Optimum F_y	1.7 mm	0.7 mm
%Reduction	93.6%	94%

Table 5.10: Comparison among important geometrical parameters of the machine and optimum flange width among different topologies of FSPM

FSPM type	Stator tooth width, W_s (mm)	Slot opening, w_{so}, mm	Stator pole pitch, θ_s	Slot opening/pole pitch ratio, $\frac{w_{so}}{\theta_s}$	Optimum F_y	Ratio, F_y/W_s
Regular 12/10	3.237	3.237	$\pi/6$	$19.422/\pi$	1.2	0.37
E-Core, 6/11	4.5	6.573	$\pi/3$	$19.719/\pi$	1.7	0.37
C-Core, 6/13	4.5	15.766	$\pi/3$	$47.3/\pi$	0.7	0.16

Cogging torque magnitude depends largely on slot opening/pole pitch ratio. Since slot opening, pole pitch and stator tooth width are different in different topologies of FSPM, the optimum flange width required to obtain the minimum cogging torque is different in each of them. Figs. 5.23 and 5.24 and Table 5.9 and Table *5.10* illustrates the effect of rotor flange on cogging torque and its magnitude for E-Core and C-Core FSPM machines. From Table 5.10, it can be inferred that, as $\frac{w_{so}}{\theta_s}$ increases, the optimum $\frac{F_y}{W_s}$ ratio decreases for which the minimum cogging torque is obtained. The $\frac{w_{so}}{\theta_s}$ ratio for E-Core FSPM is close to that for 12/10 FSPM but significantly different for C-Core FSPM as can be found in Table 5.10. The optimum $\frac{F_y}{W_s}$ ratio decreases as $\frac{w_{so}}{\theta_s}$ ratio increases. For all the topologies, the value of $\frac{w_{so}}{\theta_s} \times \frac{F_y}{W_s}$ is within a close range to obtain the minimum cogging torque. From inspection, the following design rule is obtained for all the topologies of FSPM:

$$F_y = \frac{C}{\pi} \times W_s \times \frac{\theta_s}{w_{so}} \qquad \ldots(5.14)$$

where *C* is a constant and range in the values of $7.2 \leq C \leq 7.6$.

5.8 Conclusion

In this chapter, a new rotor pole shaping method using rotor pole flanges has been introduced and applied to FSPM machines. The optimum dimension of the flange width was determined both by analytical method and through numerical optimization using FEA. The cogging torque with various flange widths are compared along with instantaneous torque, average electromagnetic torque and torque ripple. The results demonstrate that the presented

pole shaping can simultaneously reduce the cogging torque and torque ripple with a small sacrifice of the average electromagnetic torque. For FSPM machines with slot opening/pole pitch ratio of 0.5, a sizing rule for flange was developed. Current fabrication techniques allow a tolerance of up to 0.05 mm precision, whereas some manufacturers can provide up to 0.01 mm precision. A conservative precision of 0.1mm has been used in determining the flange width. The method simplifies machine construction compared to skewing and can be applied to FSPM machines for high performance applications where torque ripple due to cogging torque can be an issue.

Chapter 6

Design of a Low-Noise FSPM

Noise and vibration in FSPM machines is one of the issues where improvement is needed, especially in topologies that are of segmented stator type. The stator mode frequencies and intensity of acoustic noise generated by magnetic radial force is related to the geometry, configuration and material properties. A method for estimating mode frequencies for segmented stator is proposed in this chapter. A new pole shaping method is proposed to reduce the effect of undesirable mode frequencies on noise and vibration. The mode frequencies have been calculated using analytical models and verified using structural FEA. A low-noise FSPM design technique is proposed based on pole shaping and structural analysis. The effect of the proposed method on electromagnetic performance of the machine has also been investigated. A prototype FSPM is fabricated and tested based on the proposed design.

6.1 Noise and Vibration in FSPM

FSPM provides significant advantages such as high efficiency, high torque density, and high flux weakening capability, and is favorable for simpler thermal management and high speed operation. However, noise and vibration of such a topology has not been addressed extensively in the existing literature and requires more research.

Recent studies have investigated the optimal combination of stator and rotor pole numbers in terms of back electromotive force (EMF) and electromagnetic torque. A general method for winding design and stator-rotor pole selection based on the electromagnetic performance is

available in [74]. Another research showed the effect of the pole counts on noise and vibration [115]. Stress analysis at the air-teeth and at the PM-iron interfaces has been conducted in [116]. This chapter [117] focuses on the normal stress at the airgap, and the resulting noise and vibration due to that since it has the higher contribution compared to the PM-iron interface. Most of the studies on noise and vibration apply to stator made of single lamination pieces such as in conventional PMSM or SRM motors, and very few related to a segmented structure like FSPM. In this chapter, an analytical method for noise and vibration analysis is proposed to account for segmented stator structure.

Stator vibration due to magnetic radial force is the dominant source of acoustic noise in a structure like FSPM. The stator deformation and vibration are related to the circumferential mode shapes and frequencies. Acoustic noise depends on both the mode frequencies and the excitation frequency of the motor operation. Noise is amplified when there is a resonance between any order of harmonics of the excitation frequency and the mode frequency. The magnetic radial force, mode frequencies and generated noise power level are all function of machine geometry, configuration and material properties. Therefore, it is possible to minimize the acoustic noise power level by tuning the appropriate design parameters.

For low-acoustic noise FSPM design, it is desirable to make the dominant circumferential mode frequencies as high as possible. These design guidelines are to be met by compromising reasonably with the machine torque, power, electrical loading and power density. The noise and vibration minimization approach has been combined with previously proposed cogging torque minimization technique [111] and other common techniques found in [98], [100] as a complete design method. The optimization for cogging torque minimization is done entirely on the rotor, whereas improvement for noise and vibration is achieved by stator pole shaping.

A 500 Watt, 3-phase, 12/10, low cogging torque, low noise FSPM prototype is designed and built following the proposed design guidelines. The acoustic performance of the designed low-noise FSPM is examined by structural FEA and compared with that of the regular design that does not consider the noise and vibration issue. The trade-off and sacrifice in electromagnetic behavior to account for low-noise is also discussed.

6.2 Circumferential Mode Shape Due to Stator Vibration

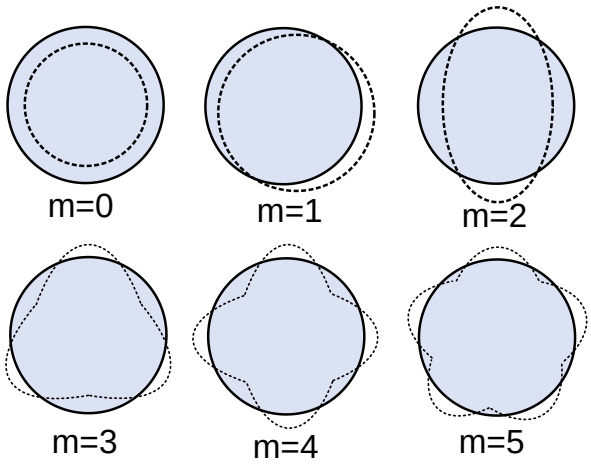

Figure 6.1: Different circumferential mode shapes.

The magnetic radial force acting on the air gap ovalizes the stator yoke of any electrical machine in different circumferential mode shapes having their own natural mode frequencies. Figure 6.1 shows the circumferential mode shapes of the stator vibration for modes *m*=0–5. The most important circumferential modes of vibration for small machines are 0, 2 and 4. In most cases, the second-order cylindrical mode or fundamental mode with m=2 is the predominant one [118].

Researchers have developed several different formulae to estimate the circumferential mode frequencies of the stator following the basic methods [118]–[121]. A formula developed by Jordan, Frohne, and Uner to estimate the circumferential mode frequencies taking into account the effects of shear, rotary inertia, teeth, and windings is used in this research [119]. Accordingly, the mode frequency for the pulsating vibration modes (*m=0, 1, 2* and higher) are

$$f_{m(=0)} = \frac{1}{2\pi R_m}\sqrt{\frac{E_s}{\rho_s \Delta}}\,Hz \qquad \ldots\ldots(6.1)$$

$$f_{m(=1)} = f_{m(=0)}\sqrt{\frac{2}{1+i^2\frac{\Delta_m}{\Delta}}}\,Hz \qquad \ldots\ldots(6.2)$$

$$f_{m(\geq 2)} = \frac{f_{m(=0)}\, im(m^2-1)}{\sqrt{(m^2+1)+i^2(m^2-1)\left(4m^2+m^2\,{}^{\Delta_m}/_{\Delta}+3\right)}}\,Hz \qquad \ldots\ldots(6.3)$$

where

$$i = \frac{1}{2\sqrt{3}}\frac{t_s}{R_m} \qquad R_m = \frac{R_5 + R_4}{2}$$

$$\Delta = 1 + \frac{W_t}{W_y} \qquad W_t = W_p + W_w + W + W_i$$

$$\Delta_m = 1 + \frac{1.91 N_{sp} A_{sp} h_s^3 W_t}{R_m L_{stk} t_s^3 W_p}\left[\frac{1}{3} + \frac{t_s}{2h_s} + \left(\frac{t_s}{2h_s}\right)^2\right]$$

and

m	circumferential mode number	f_m	mode frequency
E_s	modulus of elasticity of stator material	ρ_s	density of stator material
Δ	mass addition factor of displacement	Δ_m	mass addition factor of rotation
W_p	total weight of stator poles	W_y	total weight of stator yoke
W_w	total weight of winding	W_i	total weight of insulation
R_m	mean radius of stator yoke	t_s	back iron thickness of stator yoke
N_s	no of stator poles	h_s	stator pole height
L_{stk}	stator stack length	A_{sp}	cross sectional area of each stator pole

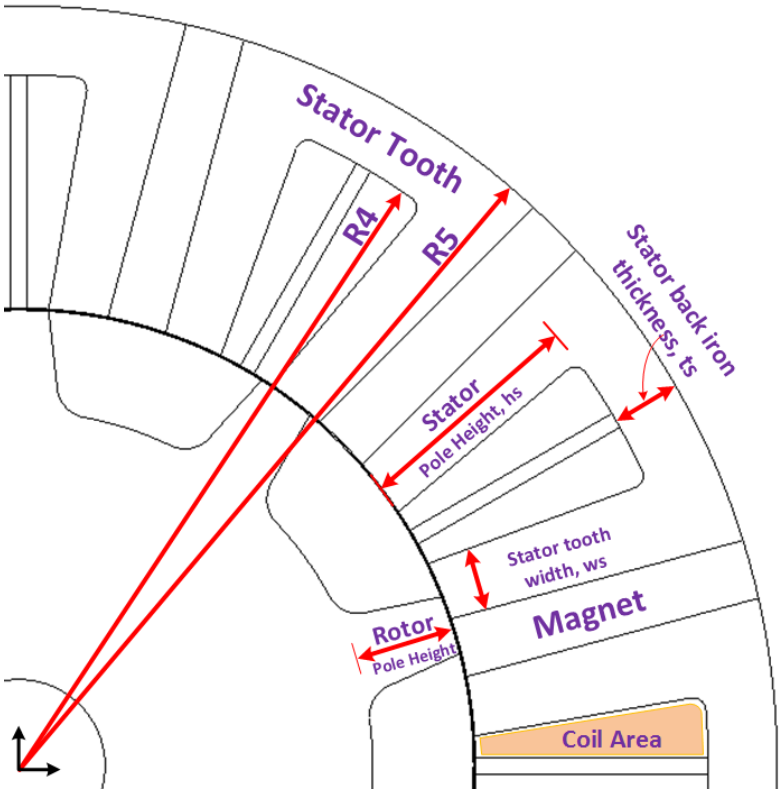

Figure 6.2: Cross-section of a 3-phase, 12/10 FSPM showing parameters that affect the mode frequencies.

The relevant geometric parameters that affect the eigenvalues of circumferential modes frequencies are given with the dimensions shown in Figure 6.2. The dominant stator vibration occur when excitation frequency of radial force harmonics are equal or close to one of the above frequencies. Therefore, it is desirable to push the major mode frequencies as far away as possible to reduce noise and vibration.

6.3 Mode Frequency for Segmented Stator

Eqs. (6.1) to (6.3) can be used for a quick eigenvalue analysis of the stator mode frequencies during the design process. However, these equations are developed assuming a single piece of steel. FSPM has a segmented stator structure containing both PM and U-shaped

steel laminations stacked together. The spoke shaped PM pieces are sandwiched in between the adjacent U-shaped iron laminations. Therefore, directly applying these equations to calculate mode frequencies is not correct. To address this, the following equations are developed to account for multiple materials present in the stator.

$$E_{avg} = \%Steel \times E_{steel} + \%Magnet \times E_{magnet} \quad \ldots\ldots(6.4)$$

$$\rho_{avg} = \%Steel \times \rho_{steel} + \%Magnet \times \rho_{magnet} \quad \ldots\ldots(6.5)$$

After obtaining the average value of Young's modulus of elasticity and mass density, natural mode frequency for the pulsating vibration mode ($m = 0$) and circumferential modes ($m > 0$) can be determined using Eqs. (6.1)-(6.3).

6.4 Sources of Noise and Vibration in Electric Machine

The magnitude of the acoustic noise at any operating condition depends on the extent of circumferential deflection due to magnetic radial force wave F_{rper} (in N/m^2), which is the magnetic radial force per unit area. The expressions of dynamic circumferential deflection D_{cir} and noise power level P_s for modes $m \geq 2$, are [118]

$$D_{cir}(f_{exc}) = \frac{\frac{12F_{rper}(f_{exc})R_m}{m^4 E_{avg}}\left(\frac{R_m}{t_s}\right)^3}{\sqrt{\left\{1-\left(\frac{f_{exc}}{f_m}\right)^2\right\}^2 + \left(\frac{\delta}{\pi}\frac{f_{exc}}{f_m}\right)^2}} \ldots \quad \ldots\ldots(6.6)$$

where, excitation frequency, f_{exc} for FSPM is

$$f_{exc} = \frac{\omega_{rpm} \times N_r}{60}$$

The analysis of sound wave emitted by AC electric machines is facilitated by spherical or cylindrical radiation modes where the modes depend on the geometry of the machine [119], [120]. In order to select an adequate model for sound power analysis, relationship between frequency, wavelength, and radiator dimensions must be considered together with the geometry and dimension of the radiator. Sound radiation factor or relative sound intensity coefficient is a function of the mode number and, thus, of the spatial distribution of the exciting radial force as well. The radiation factor curves of a spherical or cylindrical radiator is a nonlinear function of the wave number. Sound power radiated by an electric machine can be expressed as [118], [119]

$$P_s = 4\sigma_{rel}\rho c\pi^3 f_{exc}^2 D_{cir}^2 R_{out} L_{stk} \quad \ldots\ldots(6.7)$$

where

P_s	sound power radiated	c	travelling speed of sound (m/s) in the medium
σ_{rel}	relative sound intensity=$k^2/(1+k^2)$	ρ	density of air
k	wave number= $2\pi R_{out} f_{exc}/c$	R_{out}	outer radius of stator
		L_{stk}	stack length of stator

Depending on the threshold of human ear sensation, the reference of sound power level, (P_{sRef}) is 10^{-12} Watt. With this consideration, the acoustic noise power level in dB becomes

$$L_w(f_{exc}) = 10\log\left[\frac{2P_s(f_{exc})}{P_{sRef}}\right] dB \quad \ldots\ldots(6.8)$$

It is quite often the case that one or more of the natural mode frequencies of the machine is not far away from the frequencies of the periodic exciting force. Inspection of Eq. (6.6)

indicates that each excitation frequency has a contribution to the dynamic circumferential deflection of the state toward a particular mode shape. The farthest excitation frequency has the lowest contribution, whereas the nearest one has the highest. The contribution reaches the maximum when any one of the excitation frequencies matches with a natural mode frequency.

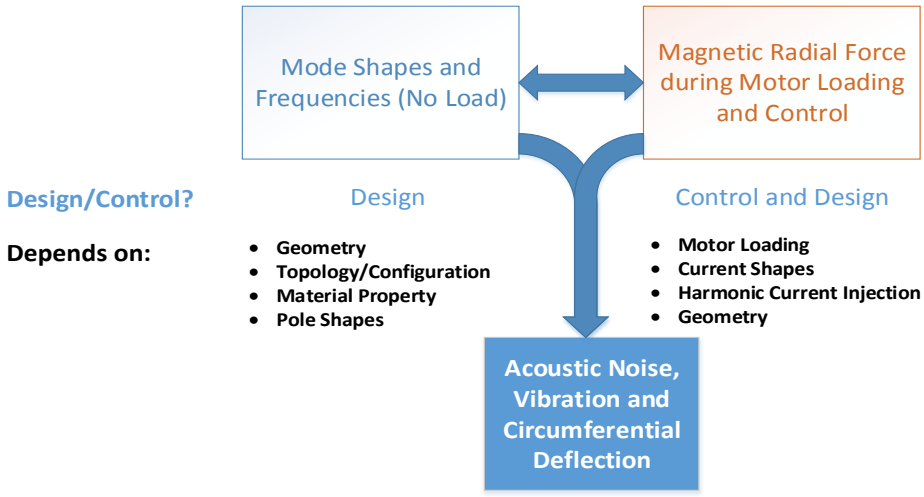

Figure 6.3: Graphical representation of source of noise and vibration in electric motor with preferred mitigation approach.

The sources of predictable and controllable acoustic noise and vibration and their mitigation techniques are summarized in Figure 6.3. The inherent mode shapes and the eigenvalues of the natural mode frequencies depend on the structural properties of the stator and therefore can be improved by manipulating the design, geometry, material properties, machine topology and pole shaping. On the other hand, when the machine is being operated with certain armature current and the rotor is rotating, the generated magnetic radial force on the poles and teeth depends primarily on the current control and current shapes. Therefore magnetic radial force can be manipulated through controls by shaping the armature current. In this chapter, the objective of reducing noise and vibration in FSPM is approached from a design perspective by changing the geometry and pole shapes to reduce the effect of undesired mode

frequencies so that when they resonate with the magnetic radial force on the stator teeth, their combined effect causing the noise and vibration is minimized. Other than these, there are sources of noise and vibration in electric machine that are not predictable or controllable, and more random in nature. These include rotor eccentricity, bearing defect, error during motor assembly, and alignment error. These can only be verified and controlled by an in-process quality control, and therefore, not considered in this research.

6.5 Design Parameters for a Low-noise FSPM

According to Eqs. (6.6) and (6.7), lower mode frequencies f_m and higher radial forces F_{rper} result in higher radial deflection, which increases the noise power level. Increasing the stiffness of any structure will increase the natural mode frequencies. Increasing yoke thickness t_s increases the stiffness of the stator and reduces D_{cir}. However, thicker t_s reduces the power density due to lower utilization of materials. It also decreases the net window area available for windings and increases the thermal diffusion distance for heat transfer. The design objective for lower acoustic noise is to maximize the dominant mode frequencies and minimize the harmonic components of F_{rper} while compromising reasonably with the machine torque, efficiency and power density. A good design objective is to make the dominant circumferential mode frequencies higher than the maximum audible frequency for human (i.e., beyond 20 kHz).

Among various geometric parameters, the ratio of α_s $(= t_s/w_s)$ is identified as the most important parameter contributing directly to the stiffness. The parameters associated with α_s

are given in Figure 6.4 showing how it will affect the structure of the stator. From an electromagnetic point of view, the optimum geometric parameters providing the best electromagnetic outputs have already been identified as design ratios [74], [98], [100] and altering those will have unwanted degradation of electromagnetic performance.

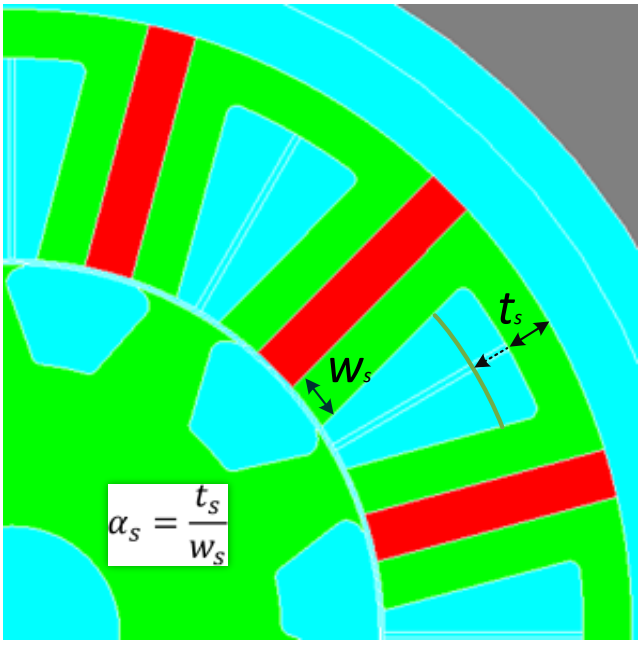

Figure 6.4: Schematic of part of the FSPM showing design parameters affecting mode frequency, noise and vibration.

6.5.1 Selection of α_s

The low-noise FSPM design objective is to maximize the dominant mode frequencies. The design iteration for the 500W FSPM starts with taking the tooth width (w_s) the same as the back iron thickness (t_s) giving $\alpha_s = 1$, which was arrived at considering electromagnetic performance only. As a single objective and single variable function, the ratio α_s is varied from 1 to a higher value within an acceptable range keeping the rest of the parameters constant to obtain a lower noise design of the FSPM.

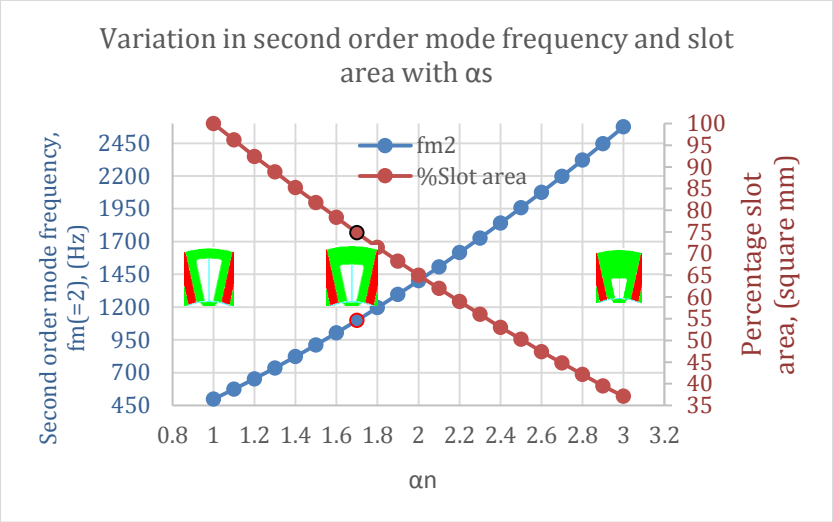

Figure 6.5: Effect of varying α_s on second order mode frequency and available slot area.

Figure 6.5 plots $f_{m(=2)}$ and the corresponding slot area for various α_s while keeping all other geometric parameters of the machine fixed. Only the fundamental mode ($m=2$) is taken into consideration since this is primarily responsible for acoustic noise. The objective of maximizing the second order mode frequency to determine an acceptable range of α_s with a reasonable sacrifice in slot area is applied in this analysis for a low-noise FSPM.

6.6 Final Design and Performance

The dimensions, parameters and ratings of the Low-Noise FSPM machine are given in Table 6.1. The effect of the proposed stator pole shaping on structural, electromagnetic and acoustic performance of the FSPM is compared with the base design for noise performance using structural FEA and presented in this section. The FSPM design that include the rotor pole flange for cogging torque minimization but not the low-noise design modifications is termed as the base design [117]. The prototype low-noise FSPM machine fabricated and its torque ripple performance which is indirectly linked with acoustic noise is also presented in this section.

Table 6.1: Design parameters of the 0.5 kW FSPM

Parameter	**Value**
Stator outer radius, R_5	60 mm
Active stack length	40 mm
Number of stator poles, N_s	12
Number of rotor poles, N_r	10
Airgap length	0.5 mm
Rotor outer diameter	35.5 mm
Split ratio	0.6
Stator tooth width, β_{st}	7.5°
Slot opening, β_{so}	7.5°
Magnet thickness, β_m	7.5°
Stator yoke thickness	7.5°
Rotor pole width, β_{rt}	12°
Stator Tooth Width, t_s	4.7 mm
α_s	1.7
Stator inner radius, R_4	52 mm
Stator Back Iron Thickness, w_s	$\alpha_s \times t_s = 8\,mm$
Rotor Flange Width, $F_y(=F_x)$	1.7 mm
RMS current density, J (A/mm^2)	6 A/mm^2
Rated Speed	1800 RPM
Power	500 W
Number of turns	47
Per phase resistance	0.586 Ohm
Magnet type	Ferrite

6.6.1 Improvement in Noise and Vibration with Structural FEA results

The acoustic noise has been analyzed using the analytical model and verified using structural FEA for both the base design and the low-noise design. Figure 6.6 presents the mode shape for $f_{m(=2)}$ and corresponding mode frequency for both the designs. The radial forces acting on the stator teeth are obtained from magneto-dynamic FE model. The harmonic

components of the radial force wave F_{rper} are evaluated by Fast-Fourier transform of the time domain representation. The circumferential deflection as well as noise power level are then calculated using F_{rper} using Eqs. (6.6) and (6.7). The mode frequencies for the 3-phase, 12/10 FSPM obtained with the base and low-noise design are shown in Table 6.2. In the base design, f_m=2 is close to 600 Hz, which excites mode 2 through its 2nd harmonic at 1800 rpm (f_{exc}=300 Hz). For the low-noise design, all the frequencies are pushed higher in the frequency spectrum.

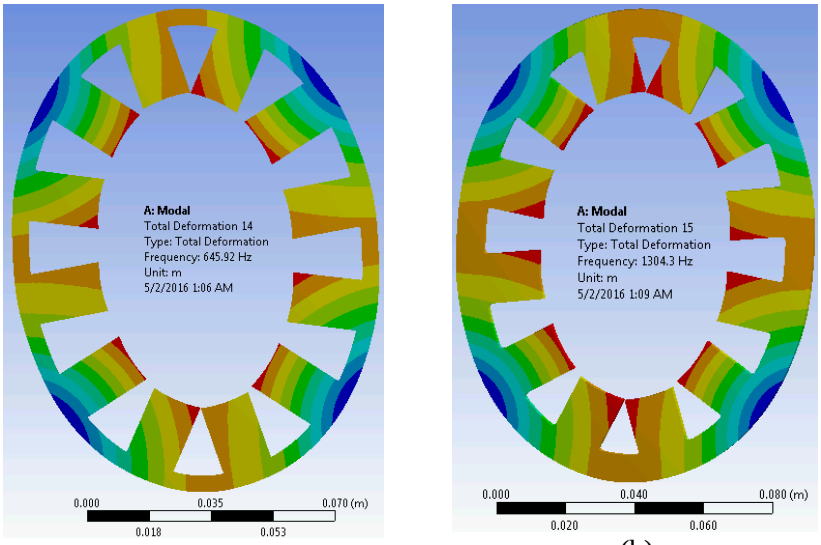

(a) (b)

Figure 6.6: Circumferential Mode Shapes of the stator for (a) *m=2*, base design, (b) *m=2*, Low-Noise FSPM.

Table 6.2: Improvement in mode frequencies with α_s=1.7

	Base design		Low-noise design	
Mode	Analytical (Hz)	Structural FEA (Hz)	Analytical (Hz)	Structural FEA (Hz)
m=2	546	647	1098	1303
m=3	1460	1675	2978	3413
m=4	2625	2880	5411	5922

6.6.2 Circumferential Deflection and Acoustic Noise:

The circumferential deflection and acoustic noise levels for the base design and Low-Noise design FSPMs are plotted against f_{exc} in Figure 6.7. The amount of peak circumferential deflection found from the analytical model developed is also verified with static structural FEA simulation as shown in Figure 6.8. The circumferential deflection in the Low-Noise design (0.3 µm) is less than half of that in the base design (0.8 µm). The values of peak deflection from analytical model and the static structural FEA are in good agreement with each other. A peak acoustic noise at $f_{m(=2)}$ is observed for all the design cases.

Table 6.3 compares the noise levels among the base design and low-noise design at different frequencies for 1800 rpm.

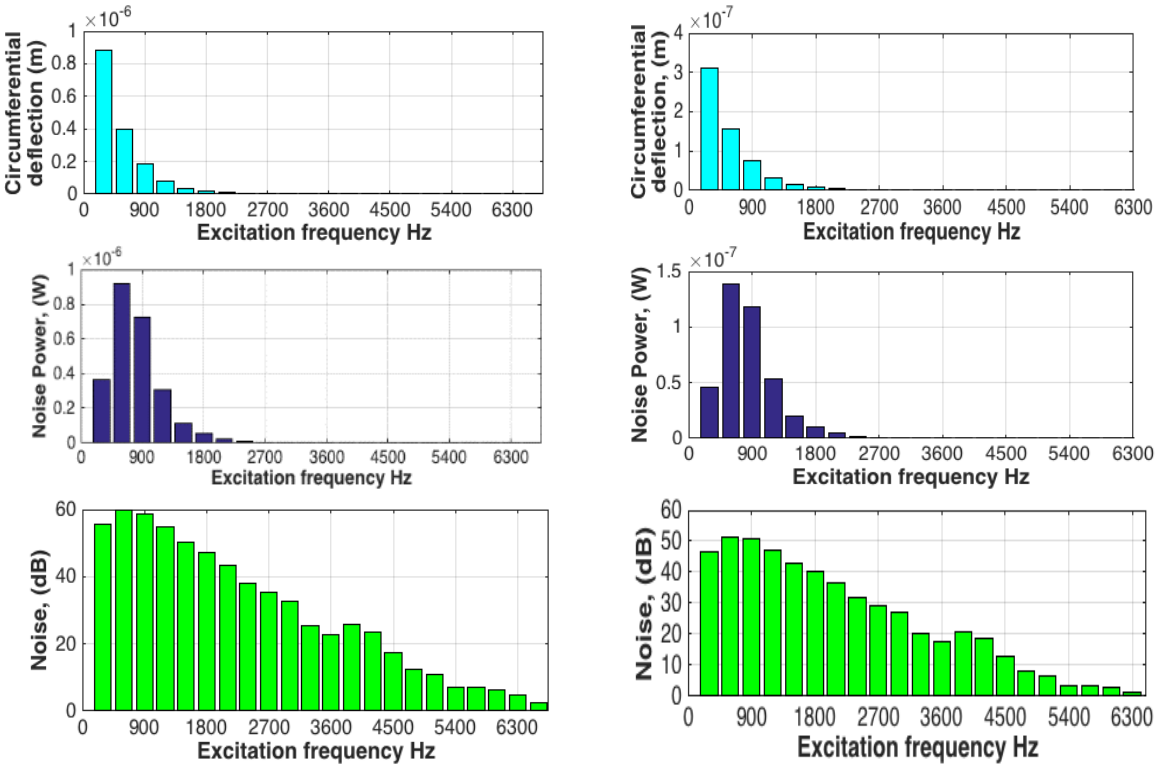

(a) (b)

Figure 6.7: Circumferential deflection and noise levels vs. f_{exc} for (a) base design, and (b) low-noise design at 1800 RPM.

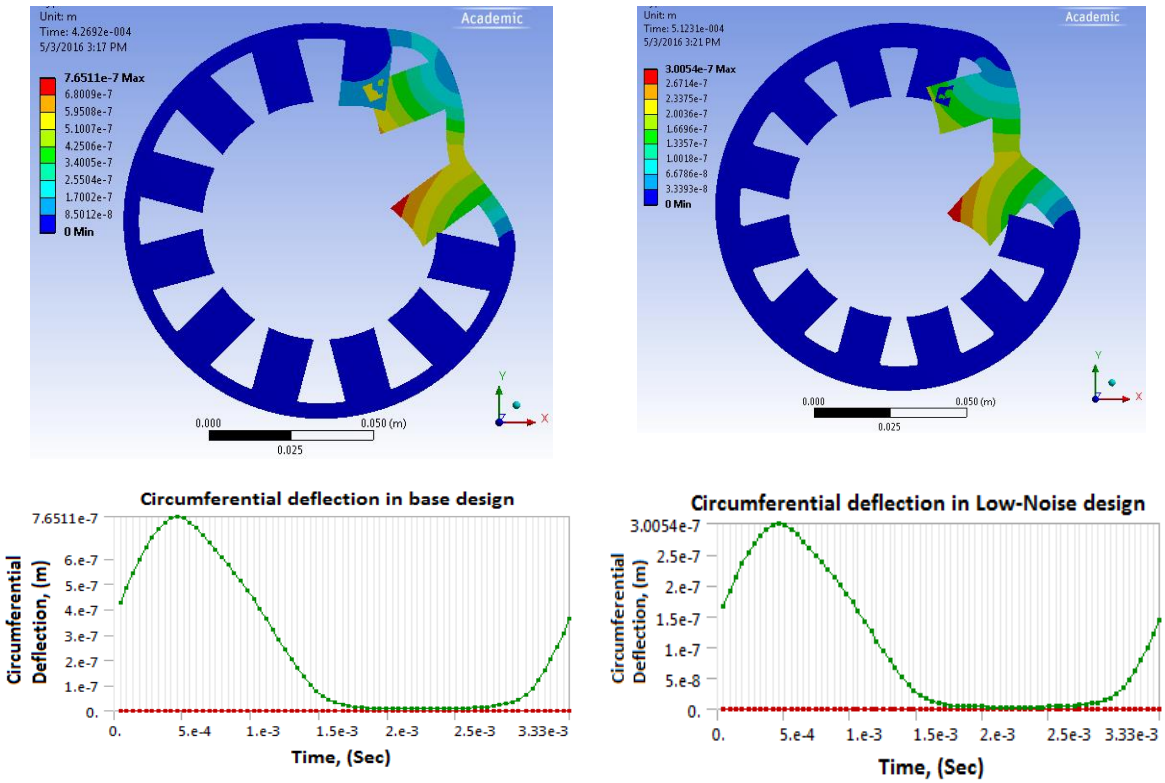

Figure 6.8: Peak circumferential deformation from static structural FEA simulation, (a) base design, (b) Low-Noise design.

Table 6.3: Comparison of noise levels at 1800 RPM

Frequency	Noise Power (dB) (Regular)	Noise Power (dB) (Low Noise)
300	54.6	46.5
600	58.73	51.4
900	57.75	50.7
1200	54.1	47.3
1500	49.7	43.1
1800	46.5	40.2
2100	42.8	36.7

As a result of lower circumferential deflection, a reduction of about 7-8 dB is achieved at all frequencies at the rated speed of at 1800 rpm with the proposed low-noise design. However, the rated operating speed is not the noisiest speed for the machine. It depends on the second

order mode frequency and it is important to analyze the noise power at those speeds as well. For example, $f_{m(=2)}=1098\ Hz$ for the low-noise design. Therefore, the noisiest speeds will be 6588 rpm ($f_{exc}=f_{m(=2)}$), 3294 rpm ($2\times f_{exc}=f_{m(=2)}$), 2196 rpm ($3\times f_{exc}=f_{m(=2)}$), 1647 rpm ($4\times f_{exc}=f_{m(=2)}$) and so on. Similarly, for the base design, the noisiest speeds are 3276 rpm ($f_{exc}=f_{m(=2)}$), 1638 rpm($2\times f_{exc}=f_{m(=2)}$), 1092 rpm ($3\times f_{exc}=f_{m(=2)}$), 819 rpm ($4\times f_{exc}=f_{m(=2)}$) and so on. Noise and vibration performance at these speeds of the corresponding designs are presented in Figure 6.9-Figure *6.11*.

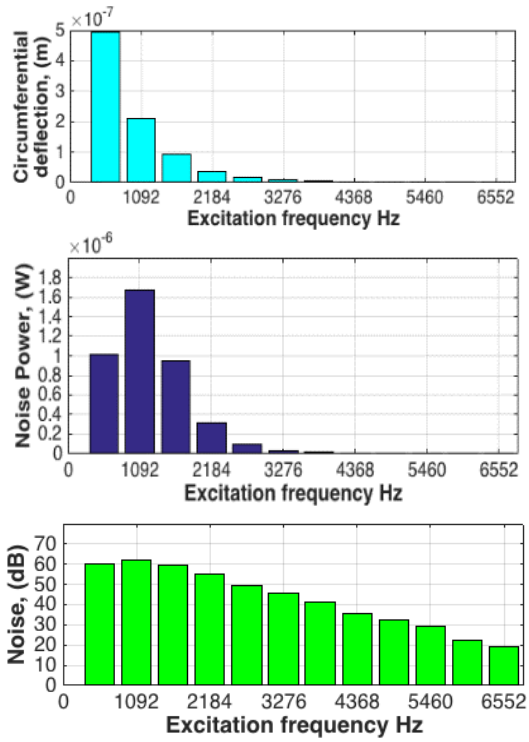

(a) Base design at 3276 rpm ($f_{exc}=f_{m(=2)}$)

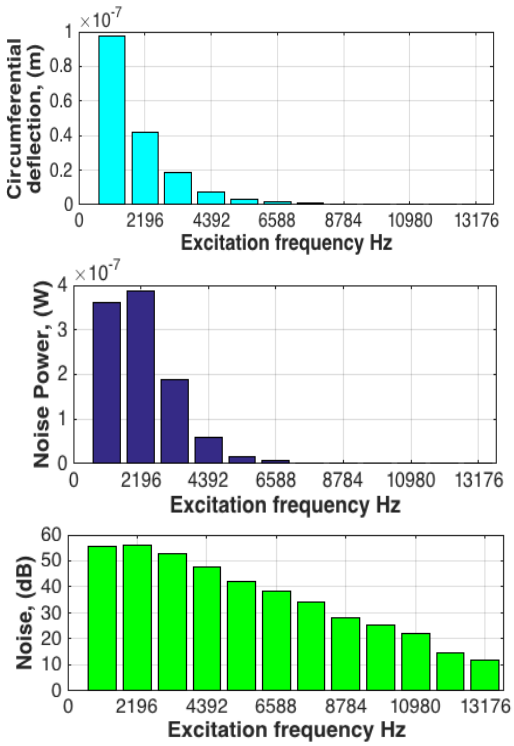

(b) Low-noise design at 6588 rpm ($f_{exc}=f_{m(=2)}$)

Figure 6.9: Circumferential deflection and noise levels vs. f_{exc} for (a) base design at 3276 rpm, and (b) low-noise design at 6588 RPM.

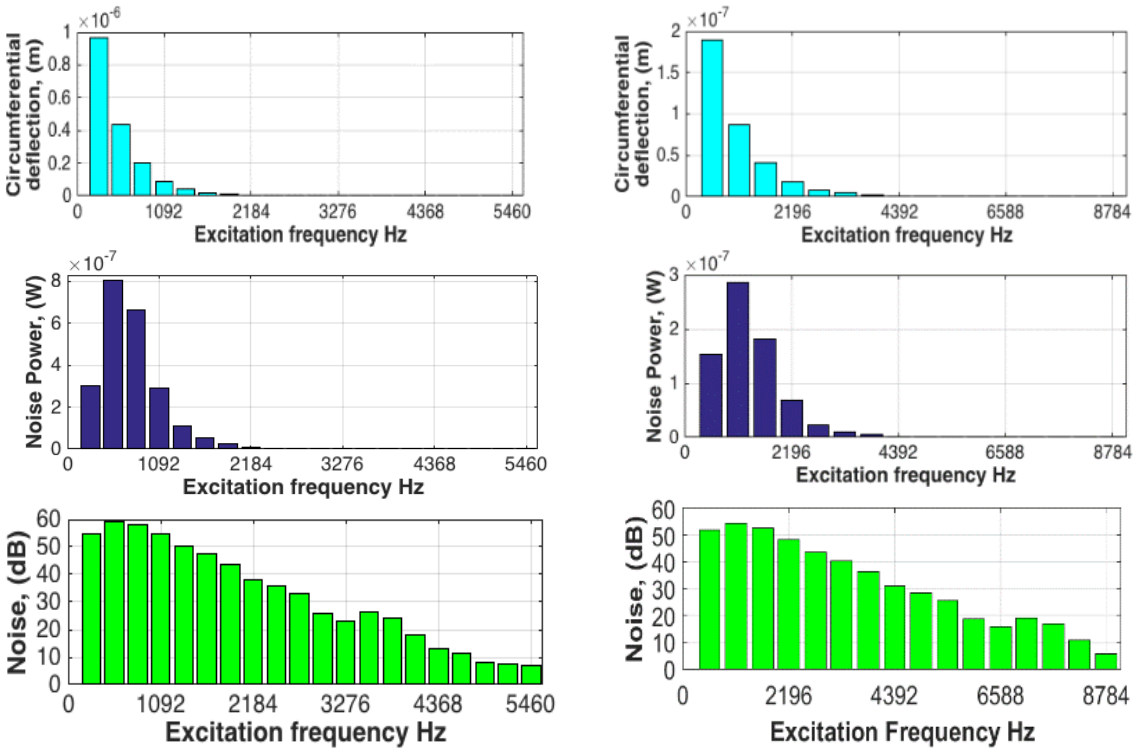

Figure 6.10: Circumferential deflection and noise levels vs. f_{exc} for (a) base design at 1638 rpm, and (b) low-noise design at 3294 RPM.

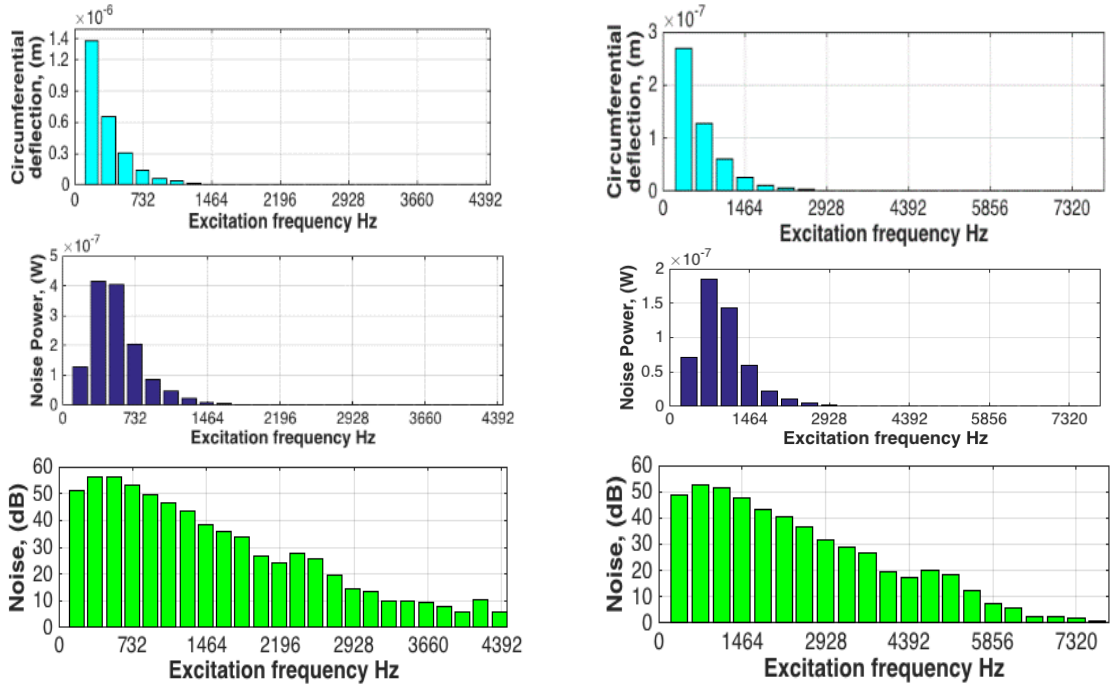

Figure 6.11: Circumferential deflection and noise levels vs. f_{exc} for (a) base design at 1092 rpm, and (b) low-noise design at 2196 RPM.

6.6.3 Effect on electromagnetic performance

A subsequent verification of the key electromagnetic performance parameters were performed by FEA to compare the base design with the low-noise design. Figure 6.12 shows the cogging torque of the regular design with rotor flange as suggested in Chapter 5, and that with increased stiffness with α_s>1. The flux linkage lines through the air gap from rotor to stator does not link the back iron, therefore increasing the back iron thickness does not have any effect on the cogging torque.

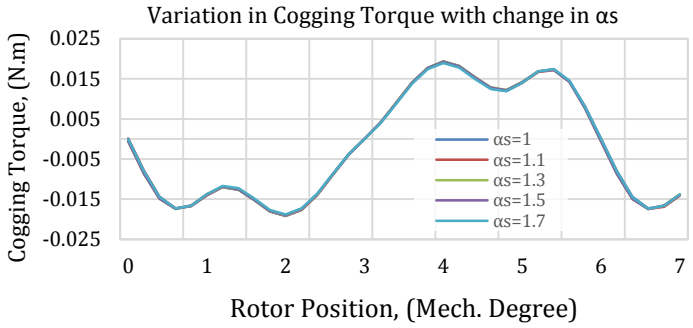

Figure 6.12: Effect of changing back iron thickness on cogging torque.

Phase flux linkage and back-EMF depend on the number of turns only, and are not affected by the increased stator back iron thickness in any way. Due to the decreased coil area, the number of turns, allowable rated RMS current and phase resistance is designed again in an iterative way following the design methods presented as in Chapter 4. The number of turns were kept the same and a smaller wire size was selected to accommodate it. Figure 6.13 shows the rated torque for the base design and low-noise design. Table 6.4 summarizes the differences in key electromagnetic performance parameters.

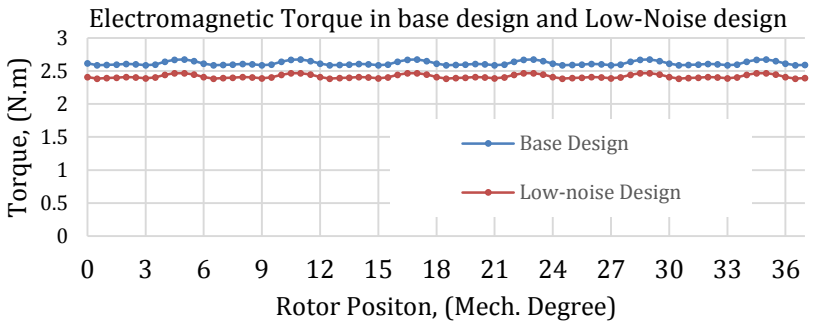

Figure 6.13: Effect of increasing back iron thickness on output torque for the same slot current density.

Table 6.4: Comparison of affected design and performance parameters between the base and Low-Noise design

Parameter	Base Design	Low-noise Design
Number of turns	47	47
Wire size	AWG 18	AWG 19
Phase resistance	0.456 Ohm	0.575 Ohm
Rated RMS phase current	3.8 Amp	3.5 Amp
Rated torque	2.6 N.m	2.4 N.m
Rated mechanical output	475 W	438 W
Copper loss	19.75 W	21 W

A prototype of the 500W, 12/10 low-noise FSPM with ferrite magnets was built and tested to validate the design and performance. The experimentally obtained no-load back-EMF, average electromagnetic torque and torque ripple at different speed and load conditions are in excellent agreement with the FEA simulation results. Detailed experimental test results of the FSPM drive and their comparison with FEA is presented in Chapter 7.

6.7 Stator Deformation from Static Structural FEA Model

The analytical method for predicting circumferential deflection considers only one stator tooth and the force acting on it as a result of applied current and rotor movement. The model calculates the deflection, noise and sound power as the rotor pole passes the stator tooth, based

on the mode frequencies, excitation frequency and the forces. However, it does not consider the boundary condition and the fixed support provided by the casing keeping the stator segments together inside it. A static structural FEA model provides more accurate results for deformation as it considers all the poles and teeth simultaneously, and the forces acting on them. The boundary condition and the mechanical fixed support on the stator also comes into play in such simulation analysis.

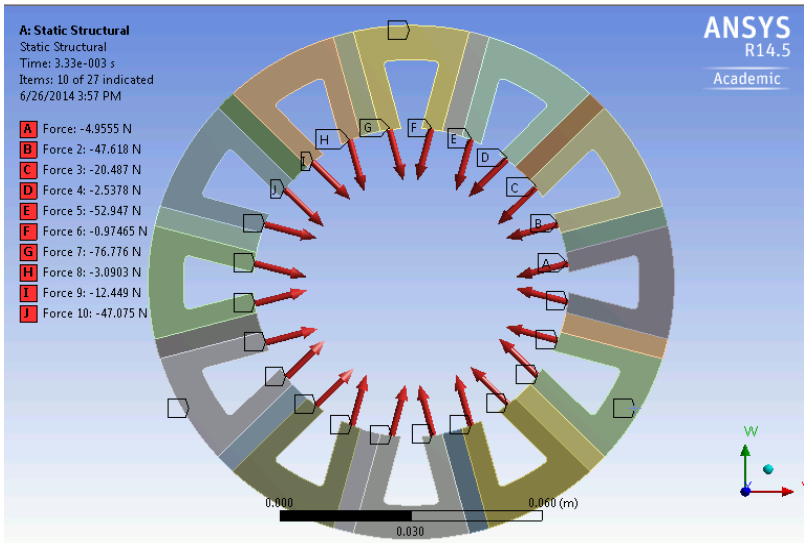

(a)

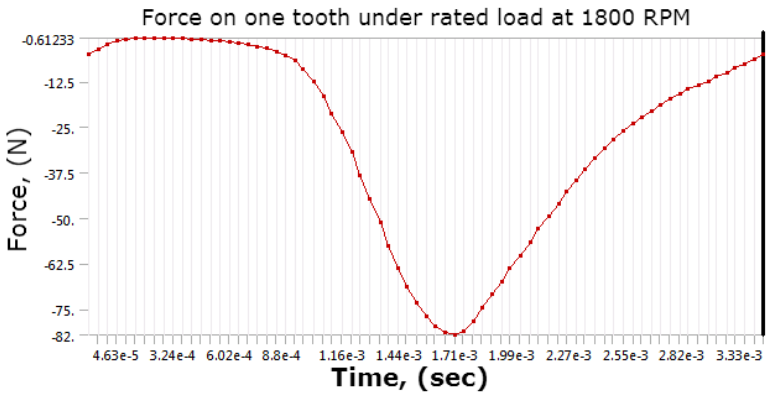

(b)

Figure 6.14: (a) The static structural simulation setup showing forces applied on the 24 stator tooth tips, (b) Force on one stator tooth obtained from electromagnetic FEA.

To get a relative measure of deformation, the force on the stator teeth are measured using electromagnetic FEA model. The force data is taken for a rated torque command of 2.4 N.m. Then these data are imported to Ansys Workbench to perform the deformation analysis. Boundary condition of stator is fixed at the entire outer periphery as applied during the construction of the prototype FSPM. The U-shaped lamination and the PM's of the prototype motor are heat shrink in an internal frame which represents this static structural model. This ensures no displacement of stator on the outer periphery. Figure 6.14 shows the setup for the static structural simulation to perform this analysis.

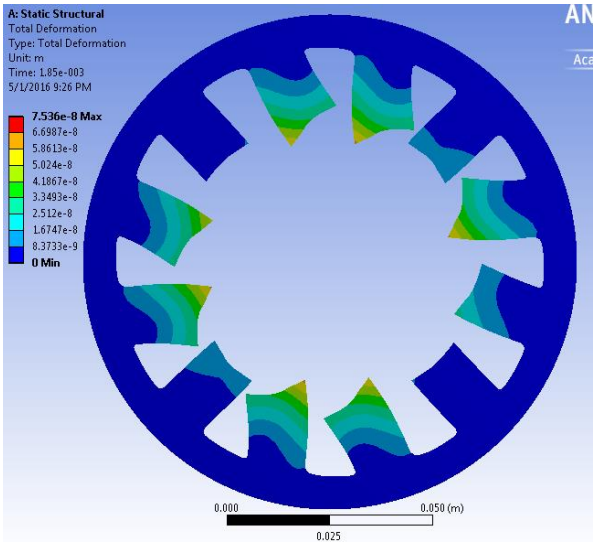

Figure 6.15: Exaggerated stator deformation at one instance within one electric cycle.

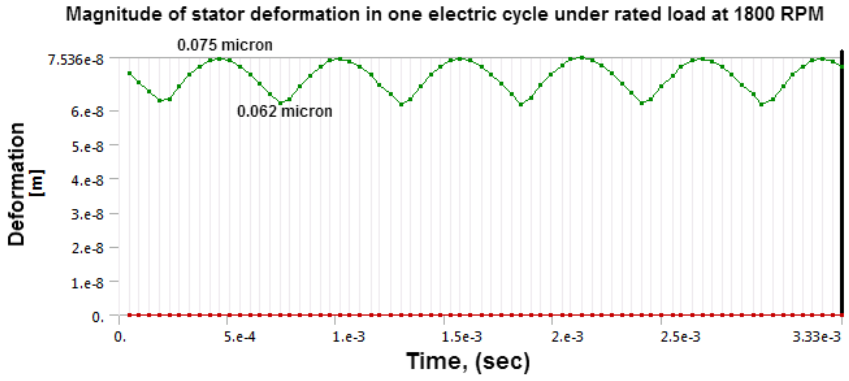

Figure 6.16: Magnitude of stator deformation, showing minimum and maximum.

Figure 6.15 shows one instance of the exaggerated view of the displacement of the stator due to the forces applied on the teeth. It presents the displacement in various parts of the structure as the rotor rotates and forces being applied on stator teeth. At the boundary region, deformation is zero. The stator tooth tips are free to move, and maximum deformation is 0.07 micron on this region. This analysis shows that the deformation of the designed machine is within the limits. Figure 6.16 shows the magnitude of deflection in the static and movable parts of the stator with respect to time for one electric cycle.

6.8 Conclusion

The analytical model presented in this chapter provides a method for predicting radial vibrational mode and acoustic noise of FSPM or any segmented stator at any operating condition. The proposed design methodology enables a low-noise design where the dominant mode frequencies are significantly higher to eliminate the possibility of their resonance with harmonics of excitation frequency. This methodology also maintains a reasonable compromise with the electrical loading and electromagnetic performance of the machine in terms of power, torque and efficiency. A reduction of about 7-8 dB noise level has been achieved at 1800 RPM using modal analysis in structural FEA. Among the other and noisier speeds, the improved design also displays better noise and vibration obtained from the analytical model. The analytical model is able to predict the peak circumferential deflection and acoustic noise due to it considering a simple system of one stator pole and no fixed support. A static structural FEA model considering all the poles and outer fixed support similar to the actual construction of the prototype FSPM machine confirms that the maximum stator tooth deformation is also within acceptable limit.

Chapter 7

Modeling, Control and Performance Testing of FSPM Drive

This chapter [122] presents the control and performance of the Flux Switching Permanent Magnet (FSPM) machine designed and built with non-rare-earth magnets. The design objective has been minimization of volume and cost, and reduction of cogging torque, noise and vibrations. A comprehensive methodology has been adopted for the design of a 12/10 segmented stator structure FSPM. Machine parameters have been identified with a nonlinear model taking mutual coupling and saturation into account. Stator flux oriented vector controller has been implemented using the machine parameters. Experimental results for the designed motor are included for performance validation.

7.1 Challenges and possibilities of FSPM

Flux switching permanent magnet machine (FSPM) is characterized by a doubly salient structure and permanent magnets in the stator. The magnet flux combined with the bipolar change of winding flux result in high flux density and high torque density. FSPM provides significant advantages such as high efficiency, high torque density, and high flux weakening capability and has favorable features for cooling and high speed operation.

Cogging torque and acoustic noise are the few challenges and concerns for FSPM. The cogging torque in FSPM can be high because of its doubly salient structure and high flux density resulting from the flux concentration effects of the circumferentially housed magnets. Prior research have also reported that the torque ripple in FSPM is mainly caused by the

cogging torque [103], [104]. Therefore, cogging torque minimization is important in designing FSPM for high performance requiring applications. The cogging torque minimization technique proposed in [111] by geometric pole shaping of the rotor has been applied for designing the prototype.

There are many sources of noise and vibration in an electric machine. Among those, lower order stator mode frequencies and the normal stress at the airgap originating from electromagnetic excitation are dominant. Pole shaping technique of the stator to reduce the effect of lower order mode frequencies is proposed and applied to the design of the FSPM motor in this chapter. Applying the proposed comprehensive design methodology, the torque ripple is minimized to as low as 5% and the noise reduction at rated speed is about 7-8 dB without significant reduction in electromagnetic torque. This makes the FSPM an attractive alternative for low-torque ripple, high power density applications.

The FSPM behaves the same way similar as any conventional PM AC machine from the control and operation perspective. Therefore, it can be controlled using a stator flux oriented vector control technique. For control of the machine, the motor parameters including the *d*- and *q*-axes inductances have been identified using an advanced model that includes mutual coupling and saturation into account [123], [124]. Finally, the prototype fabricated motor is tested and the experimental are compared with FEA simulation results. A heat run test is also performed to observe the steady state thermal behavior of the machine.

7.2 Final Design of the Prototype FSPM

A comprehensive design methodology has been developed using existing modeling techniques, analytical design rules and finite element analysis (FEA) [74], [98], [100], [111], [125], [126]. The step-by-step procedure is summarized in Chapters 4, 5 and 6. Cogging torque reduction has been achieved by a novel rotor pole shaping technique. Improvement on acoustic noise due to the resonance of excitation frequency with natural mode frequencies have been achieved by stator pole shaping and was verified using structural FEA. Figure 7.1 and Table 7.1 give the geometric design parameters of the machine.

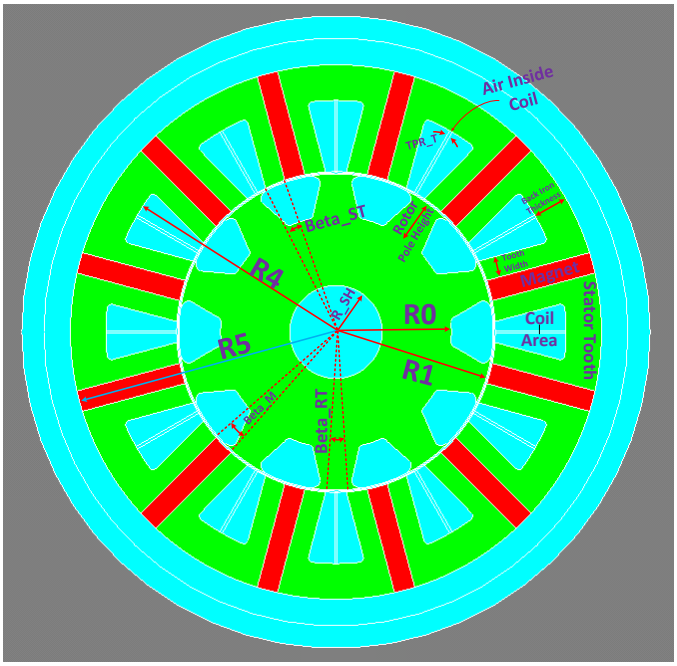

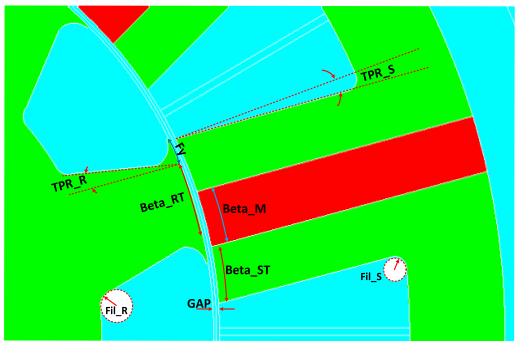

Figure 7.1: FEA Model of the final design of the prototype

Table 7.1: Geometric parameters of the final design

Parameter	Value
Stator outer radius	60 mm
Active stack length	40 mm
Number of stator poles, N_s	12
Number of rotor poles, N_r	10
Airgap length	0.5 mm
Rotor outer diameter	35.5 mm
Split ratio	0.6
Stator tooth width, β_{st}	**7.5**°
Slot opening, β_{so}	**7.5**°
Magnet thickness, β_m	**7.5**°
Stator yoke thickness	**7.5**°
Rotor pole width, β_{rt}	**12**°
Stator Tooth Width	4.7 mm
Stator Back Iron Thickness	8 mm
Rotor Flange Width, Fy(=Fx)	1.7 mm
RMS current density, J (A/mm^2)	6 A/mm^2
Rated Speed	1800 RPM
Power	500 W
Number of turns	47
Per phase resistance	0.586 Ohm
Magnet type	Ferrite

7.3 Modeling of FSPM Including Saturation and Mutual Coupling

Identifying the machine inductances is essential to develop a high performance controller for the FSPM. The *d* and *q*-axes inductance determination starts with the dynamic modeling

and analyzing the cross coupling and saturation effects. The *d* and *q*-axes voltage equation of FSPM can be expressed as:

$$v_d = R_s i_d + \frac{d\varphi_d}{dt} - \omega_e \varphi_q \quad \ldots\ldots(7.1)$$

$$v_q = R_s i_q + \frac{d\varphi_q}{dt} + \omega_e \varphi_d \quad \ldots\ldots(7.2)$$

where

$$\varphi_d = \varphi_m + L_d i_d$$

$$\varphi_q = L_q i_q$$

v_d, i_d, φ_d, L_d: *d*-axis voltage, current, flux linkage and inductance.

v_q, i_q, φ_q, L_q: *q*-axis voltage, current, flux linkage and inductance.

ω_e : Electrical speed (= *No. of rotor poles* × *mechanical speed*)

φ_m: Flux linkage of Permanent Magnet

R_s: Stator winding resistance.

Eqs. (7.1) and (7.2) do not consider saturation and mutual coupling among the phases. To account for this, an empirical model has been developed using the flux linkages for different *d*- and *q*-axes currents and curve fitting technique [123], [124]. The following equations have been used for the flux-linkages to represent their characteristics in an analytical model:

$$\varphi_d(i_d, i_q) = \varphi_m + \frac{K_{Ld}(i_d + I_0)}{1 + K_{Sd}(i_d + I_0) + K_{Sdq} i_q} \quad \ldots\ldots(7.3)$$

$$\varphi_q(i_d, i_q) = \frac{K_{Lq} i_q}{1 + K_{Sqd}(i_d + I_0) + K_{Sq} i_q} \quad \ldots\ldots(7.4)$$

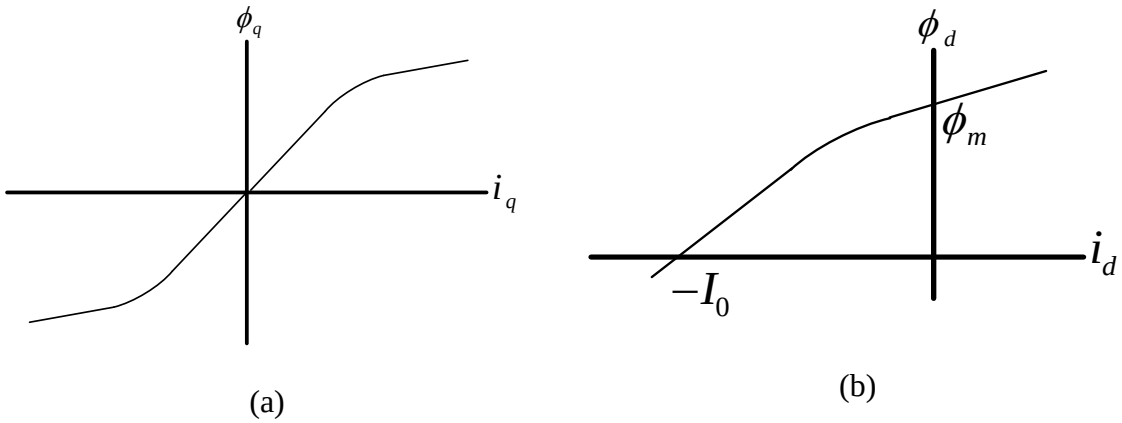

(a) (b)

Figure 7.2: *d*- and *q*-axes flux linkage with corresponding axis currents, with ϕ_m and I_0

Figure 7.2 shows the graphical representation of Eqns. (7.3) and (7.4). In this model, the following assumptions are used:

(i) At $i_d=-I_0$, the magnetic flux linkage caused by i_d and the permanent magnet are balanced in the common flux path of *d*-*q* axes, and

(ii) The cross coupling between i_q and φ_d due to the magnetic saturation of the common flux path did not occur as a result of assumption (i).

Co-efficients K_{Ld} and K_{Sd} governs the shape of the plot containing saturation characteristics, and K_{Sdq} expresses the saturation occurred due the *q*-axis current, i_q. Figure 7.3 shows the vector diagram of FSPM when operated by a non-zero *d*- and *q*-axis current. When $i_d=0$, the resultant *d*-axis flux linkage (φ_d) is simply the magnet flux linkage, φ_m. Co-efficients K_{Lq} and K_{Sq} primarily governs the shape of the flux linkage curve with respect to current, and K_{Sqd} expresses the saturation by *d*-axis current, i_d.

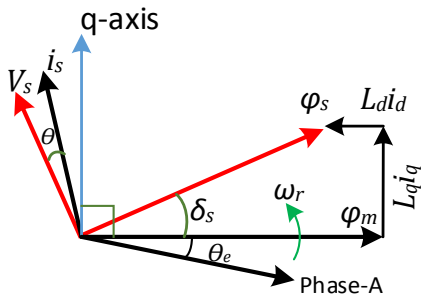

Figure 7.3: Vector diagram of FSPM with non-zero i_q and i_d

The constants and co-efficients can be determined using curve-fitting technique to the actual current-vs flux linkage characteristics of the motor obtained by finite element analysis. Extensive set of data was collected from FEA to obtain *d*- and *q*-axes flux linkages for different *d*- and *q*-axes currents. This was accomplished by sweeping the current angle (γ) and current magnitude. Based on the FEA results and proposed equations, the required co-efficients to account for saturation and mutual coupling was determined using curve-fitting technique. Figure 7.4 shows the flux linkages with respect to current for both the FEA results and the model after applying the co-efficients determined by the model.

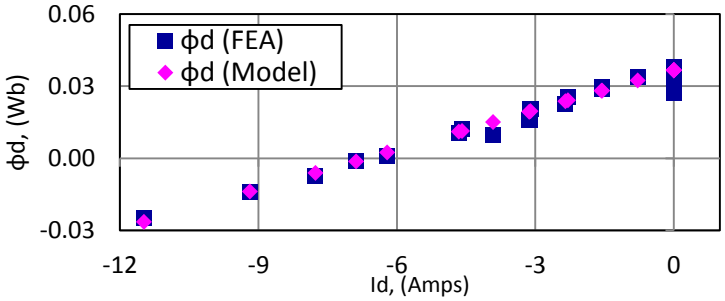

(a) ϕ_d vs. i_d

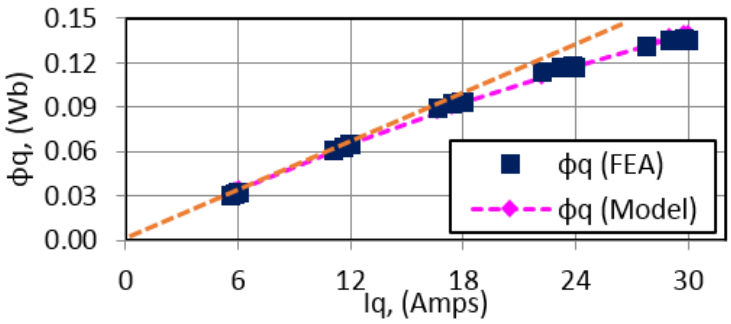

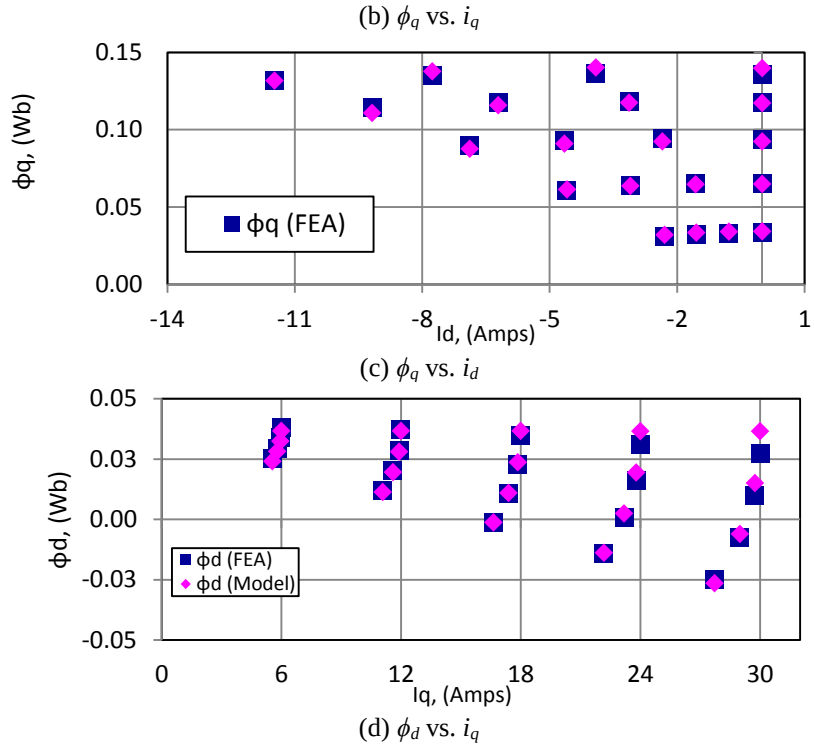

Figure 7.4: Correlation between and current and magnetic flux linkage, from FEA model and using the co-efficients for curve-fitting

Table 7.2: FSPM motor co-efficients obtained using the advanced model

Co-efficient	Value
K_{ld} (L_d)	0.005528
K_{sd}	6.61×10^{-5}
K_{sdq}	0.000208
K_{lq} (L_q)	0.006194
K_{sqd}	0.003196
K_{sq}	0.010312
I_0	6.213062
φ_m	0.036

The parameters in the flux-linkage equations for the designed FSPM are given in Table 7.2. It is important to note that φ_0 represents the flux linkage by PM (φ_m), and can be used to model and predict the torque, torque constant and power for a specific *q*-axis current when $i_d=0$ control is used. The motor will slowly move towards saturation as the *q*-axis current is increased above 12 Amps. This is also verified from experimental results in a later section. The degree of mutual coupling is very low, and therefore *d*- and *q*-axis flux linkages mostly depends

on the corresponding axis currents only. Because of negligible mutual coupling between *d*- and *q*-axes currents and the inductances, K_{Ld} and K_{Lq} can simply be used as a representation of L_d and L_q during normal operation when the machine is not in saturation region,

7.4 Field Oriented Control and Dynamic Co-simulation of FSPM Drive

The mathematical model of FSPM presented in the previous section indicates that the transformation of FSPM into an equivalent separately excited dc motor is possible, and therefore stator field oriented vector control technique can be adopted to control such machines [127]–[129]. According to the vector diagram of Figure 7.3, phase-A is assumed to be the reference. The instantaneous angular position of the rotor with respect to the stator-PM flux linkage is at the angle θ_e from phase-A. The *q*-axis current, i_q is vertical to the stator-PM flux linkage. Consequently, i_d is along the stator-PM flux linkage since in the reference, i_q leads i_d by 90°. A positive i_d results in an increase in the net airgap flux linkage, whereas a negative i_d results in a decrease in net airgap flux linkage, thus facilitating field weakening beyond corner speed which is the speed where the machine enters the constant power region of the torque-speed characteristics. However, applying id has other undesired consequence of deteriorating the overall performance of the machine during normal operation. This is discussed in details in Chapter 4. Therefore, i_d is normally kept zero during rated operation at constant speed.

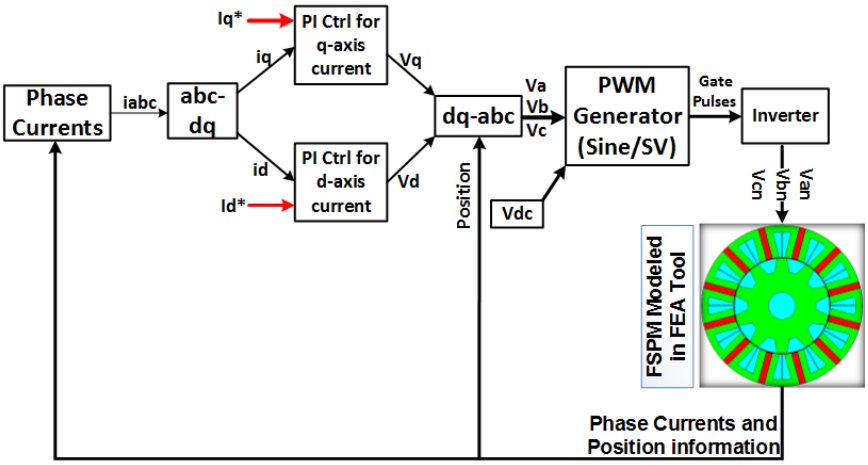

Figure 7.5: Block diagram representation of FSPM drive with stator field oriented control.

To examine the motor performance as well as the controller response, computer simulations are carried out prior to experimental evaluation. In this research, a dynamic co-simulation method is employed to analyze the electromagnetic characteristics of the FSPM machine using FEA model of the machine coupled with mathematical model of the PI-based current controller implemented using Matlab/Simulink. Both solvers exchange the calculated data at each co-simulation time step, and the results achieved by one solver is exported to the other in the next time step. Complex systems that comprise nonlinear dynamic subsystems such as power electronic converter and electrical machines are better modeled using the FEA tools to accurately represent the performance of the system. Such co-simulation model has the ability to directly coupling of multiple simultaneous physical phenomena (popularly known as multyphysics) to provide results that are very close to the actual experimental setup. Figure 7.5 shows the block diagram representation of the transient co-simulation model of the 12/10 FSPM motor drive system. The current controller and the driver circuit is modeled using Matlab/Simulink. The controller generates the required gate signals which is essentially the PWM signals for the commanded current based on the machine output torque and rotor position feedback information.

7.5 FSPM Drive Simulation Results

The electromagnetic performance is investigated using the developed co-simulation model when the machine is operated in constant speed, current control mode. Stator field oriented vector control with $i_d=0$ has been applied to test the controller response. PI controller parameters for *d*- and *q*-axes current have been identified and tuned based on the motor inductances determined in the previous section. Figure 7.6 shows the controller response (i_q, phase currents and electromagnetic torque) from the co-simulation model for a step change in command current to rated, 50% rated and 75% rated current.

The simulation results presented here were obtained at 1800 rpm. A 50 μs time step equivalent to 20kHz has been used in the simulation similar to the real time DSP controller. Space vector modulation scheme has been implemented for generation of PWM. From the simulated waveforms of phase currents and electromagnetic torque, it can be seen that the phase currents have good sinusoid, whereas the electromagnetic torque exhibits some added ripple due to PWM switching as compared to FEA results with ideal sinusoidal phase currents. The controller is designed based on the motor time constant so that it reaches the desired current command within 1 ms. The calculated torque constant of the designed FSPM machine shows good agreement between the predicted torque (from *q*-axes current) and the output electromagnetic torque form the FEA model.

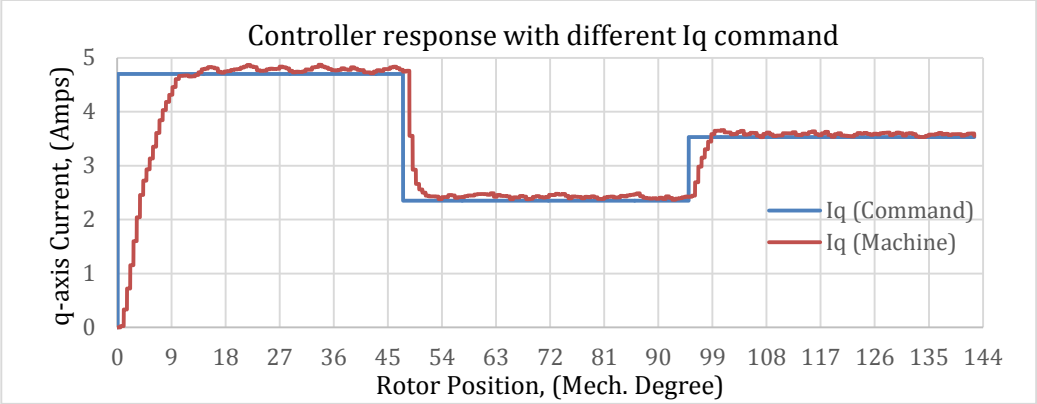

(a)

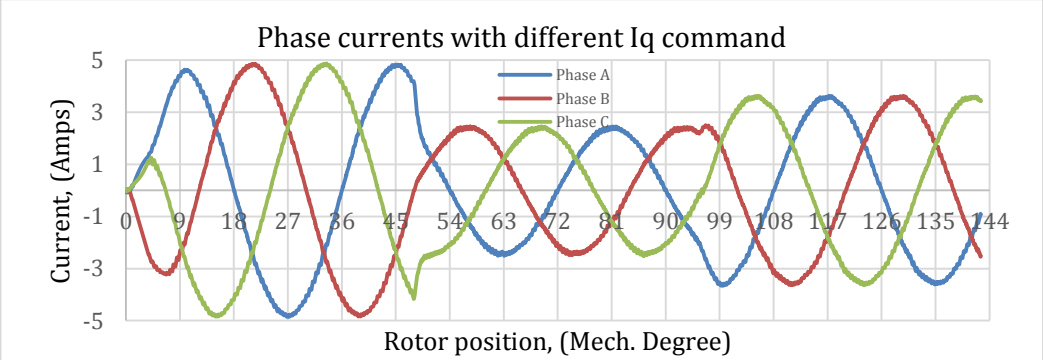

(b)

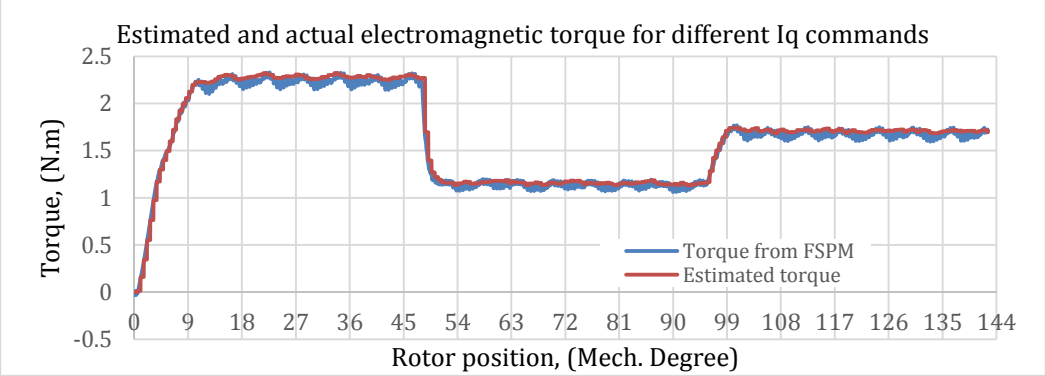

(c)

Figure 7.6: Controller response when the command current changes from 4.7 Amp (rated) to 2.35 Amp (50% rated) to 3.53 Amp (75% rated)

7.5.1 Generation Using FSPM

It is important to note that the early topologies of flux switching or flux reversal family of electric machines emerged as a generator first where both the armature and field excitation are

located in the stator. These machines were popularly referred to as inductor alternator, which is discussed briefly in Chapter 2. Therefore, it is of particular interest to examine the operation of FSPM as a generator. From a control perspective, FSPM works in a similar way as Permanent Magnet Synchronous Machine. Therefore, similar to motoring, the generation operation can also be implemented with proper control and power electronics converter topology.

FSPM generator operation has been implemented in the FEA model and in the dynamic co-simulation model. Generation using FSPM can be implemented by properly timing the excitation and generation of PWM signals as shown in Figure 7.7.

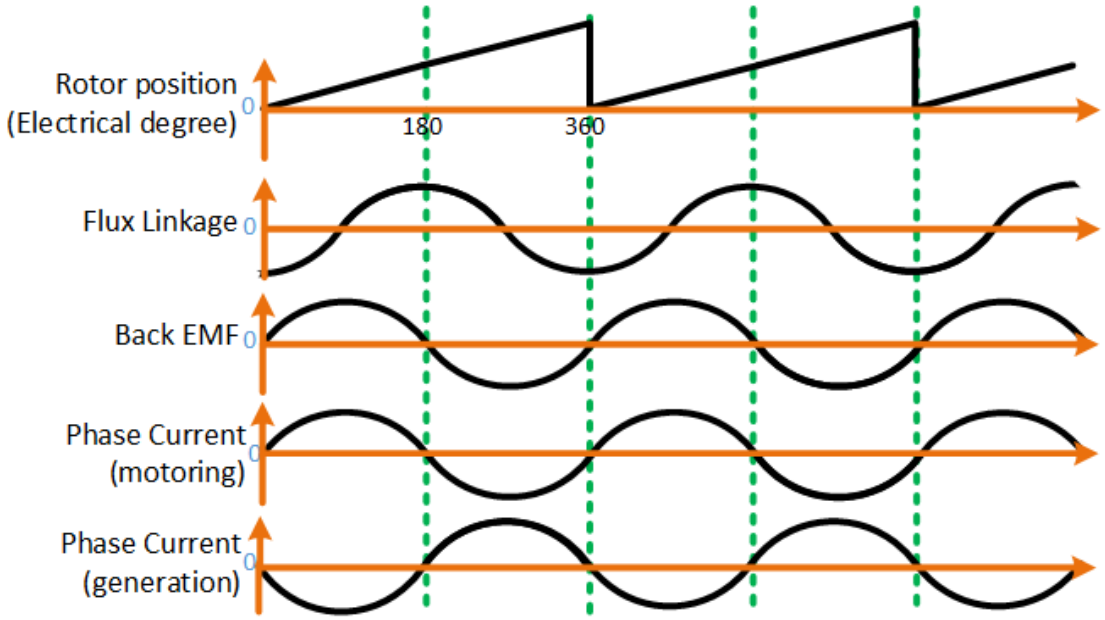

Figure 7.7: Timing of phase current excitation for motor and generator operation using FSPM machine based on rotor angular position.

Figure 7.8 shows the controller response when the FSPM is excited to operate as a generator for a step change in rated, 50% or rated and 75% of rated phase current command. This translates to respective dc-link currents also shown in Figure 7.8 (a). The corresponding

phase currents and torque is shown in Figure 7.8(b) and Figure 7.8(c). Here, the *q*-axis current is of negative magnitude, along with the torque produced.

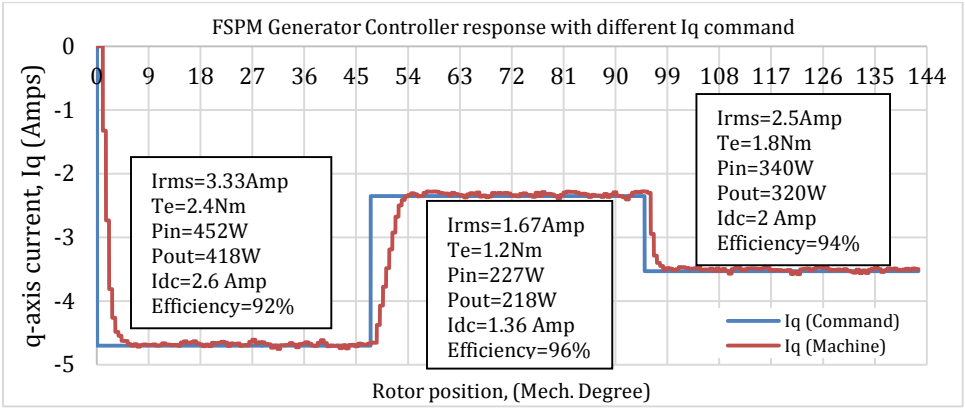

(a)

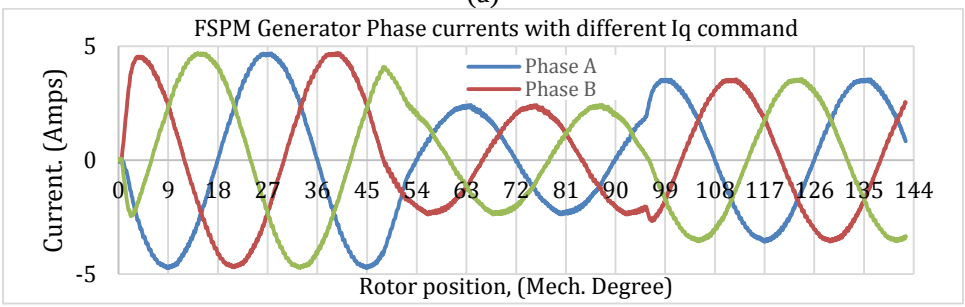

(b)

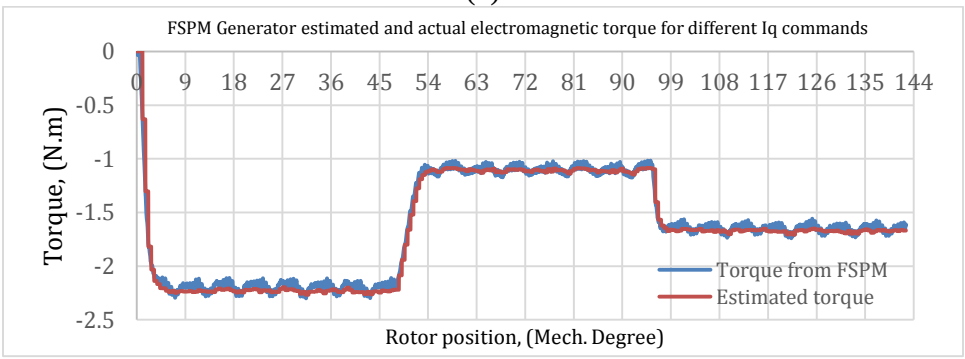

(c)

Figure 7.8: Controller response when the command current changes from -4.7 Amp (rated) to -2.35 Amp (50% rated) to -3.53 Amp (75% rated) in generator mode (a) Iq, (b) Torque, (c) Phase Currents

At rated condition (speed=1800 rpm, i_q=4.7 Amps, i_{rms}=3.3 Amps), the torque is 2.25 N.m to generate dc-link current of 2.61 Amps to a 160V dc-bus. The key performance plots from

the generator operation is shown in Figure 7.9. The generator performance at rated condition (1800 RPM, 3.33 Amps rms phase current) is summarized in Table 7.3.

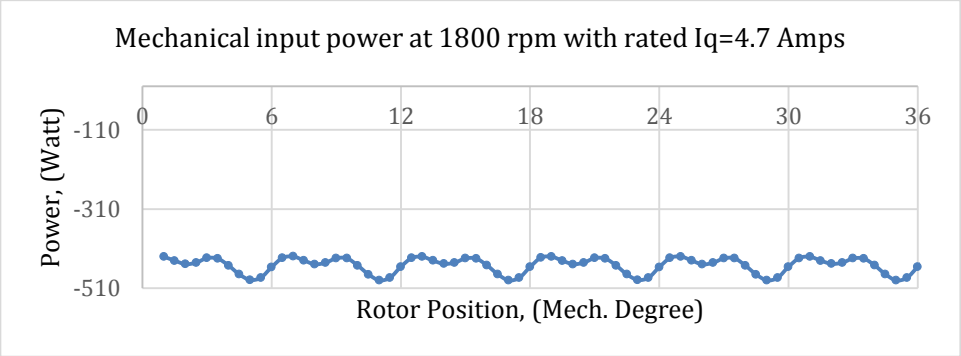

(a)

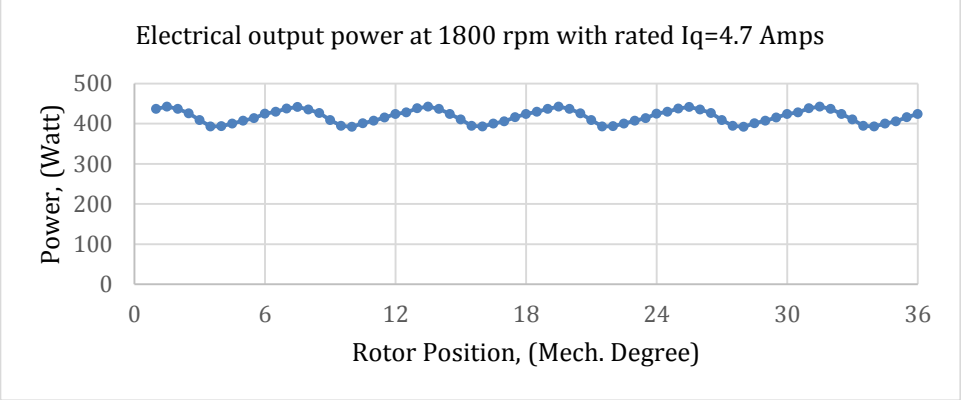

(b)

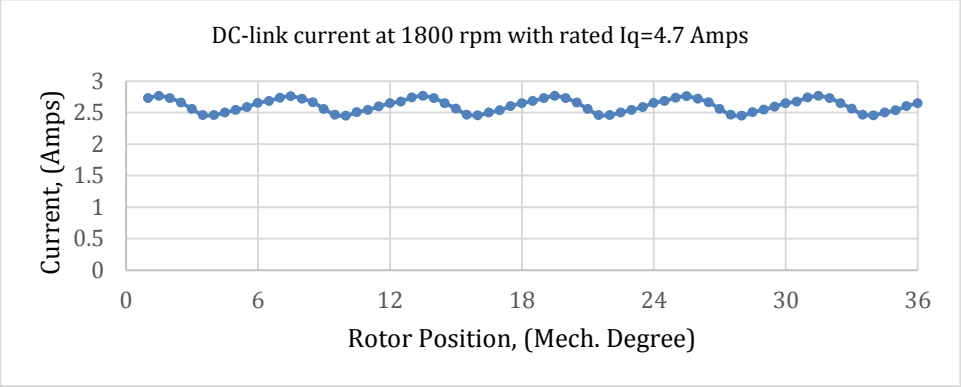

(c)

Figure 7.9: FSPM Generator Performance at 1800 RPM (a) Mechanical Input Power, (b) Electrical Output Power, (c) DC-Link Current Generated

Table 7.3: FSPM Generator Performance at 1800 RPM and Rated Current

Generator Performance Parameter	**Value**
Speed	1800 RPM

RMS Phase Current	3.3 Amps
Rated Torque	2.4 N.m
Mechanical Input Power (W)	452 W
Output Electrical Power (W)	418.1 W
DC Bus	160 V
Generated DC Link current	2.6 Amp
P_{Copper} (W)	20 W
P_{Core} (W)	18 W
Efficiency	89 %
Power Factor	0.76

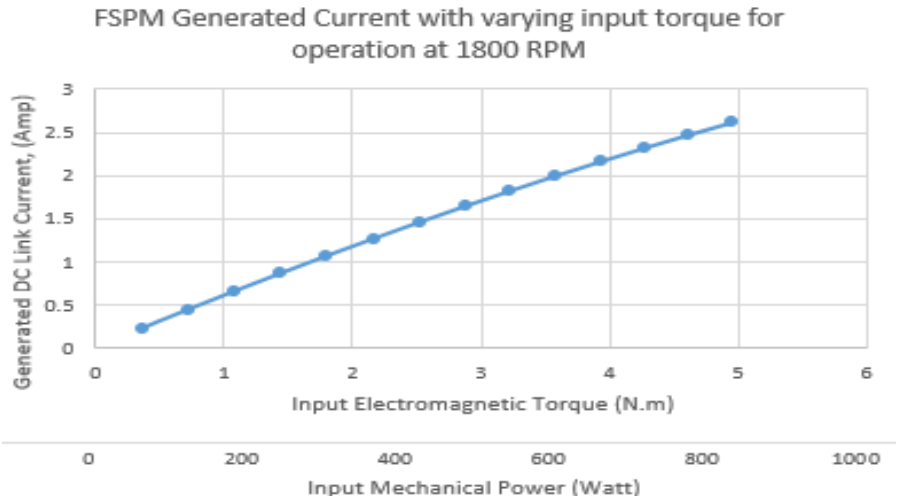

(a)

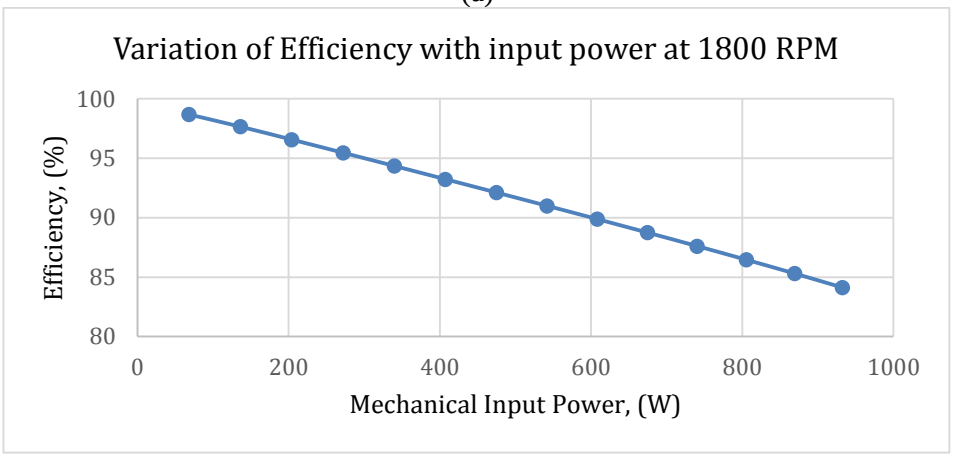

(b)

Figure 7.10: FSPM Generator Performance at 1800 RPM (a) DC-link current variation with input torque and power, (b) Efficiency variation with input power

The FSPM generator performance at rated speed (1800 rpm) for different phase currents, torque or input power are shown in Figure 7.10. At rated current, efficiency is 89% at 1800 rpm. For currents higher than rated, efficiency is decreased mainly because of increased copper

loss which is the dominant loss component. Similar results for other operating speeds are shown in Figure 7.11 (1000 rpm) and Figure 7.12 (500 rpm).

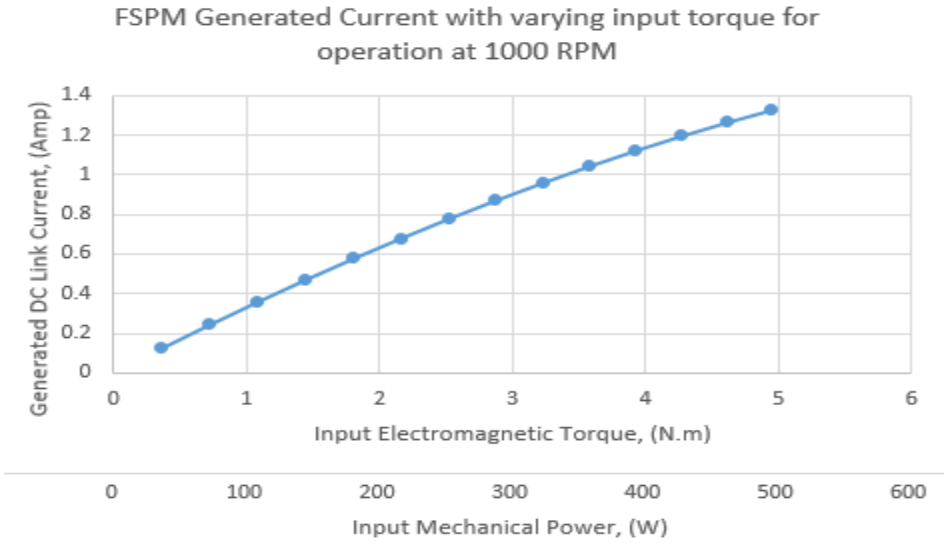

(a)

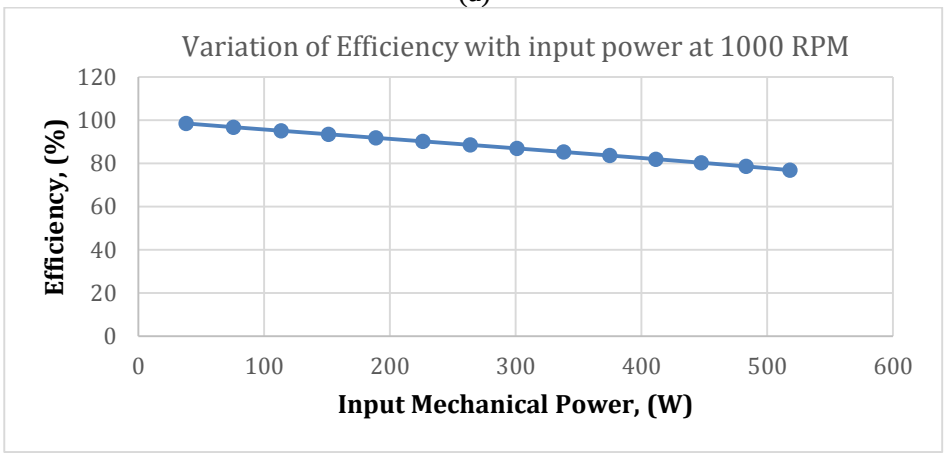

(b)

Figure 7.11: FSPM Generator Performance at 1000 RPM (a) DC-link current variation with input torque and power, (b) Efficiency variation with input power

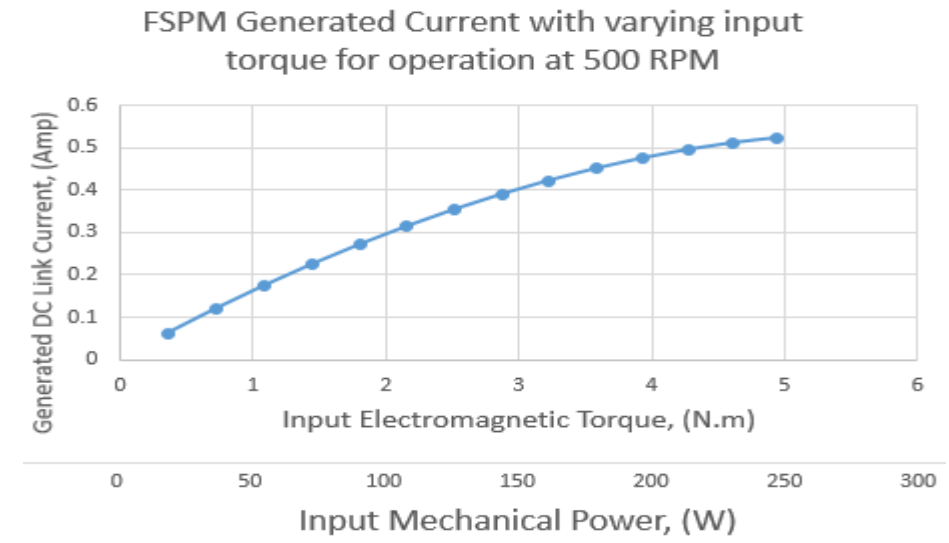

(a)

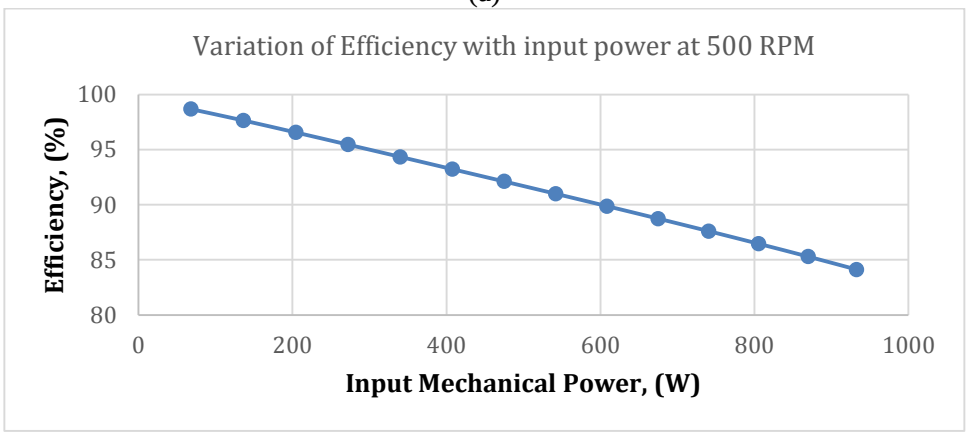

(b)

Figure 7.12: FSPM Generator Performance at 500 RPM (a) DC-link current variation with input torque and power, (b) Efficiency variation with input power

7.6 FSPM Prototype and Test Results

In order to validate the design and performance of the machine, a prototype of the 500W, 12/10 FSPM using ferrite magnets was built and tested. Figure 7.13 shows various parts of the machine as well as the driver circuit board. The U-cores and spoke shaped magnets are glued to each other using epoxy. The entire stator containing the U-core and spoke shaped Ferrite magnets are shrink-fitted onto the inner part of the internal frame to obtain a stator with slots

for coils while eliminating bridges where the PM-flux can be shunted and hence losing performance. The stator is then wound with strands of AWG 19, 47 turns per coil as designed. The salient rotor is similar to any standard SRM rotor as shown in the figure. Texas Instrument's high voltage motor control kit equipped with TMS320F28035 fixed point DSP is used to design and implement drive and controller for the FSPM operation.

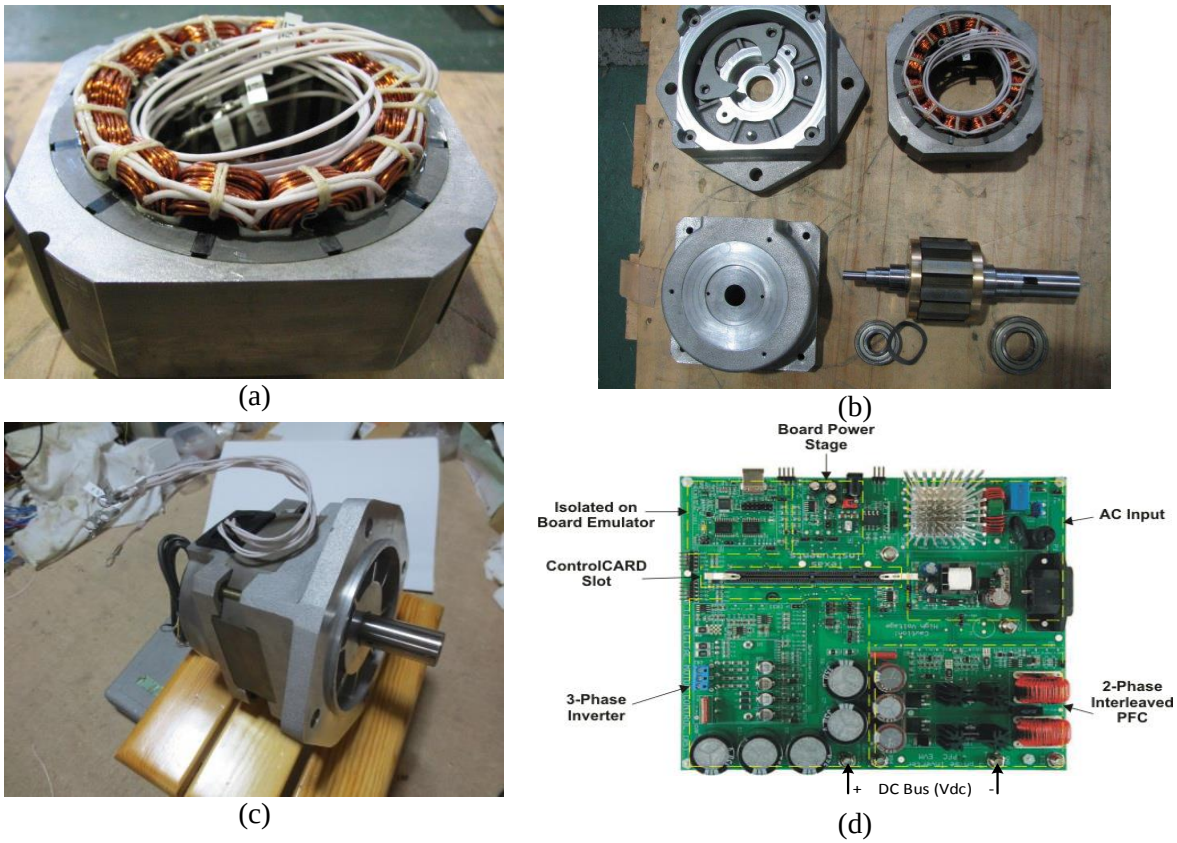

Figure 7.13: Photographs of the prototype built (a) stator with winding, (b) different parts, (c) rotor, (c) complete motor after assembling the stator and rotor into the frame, (e) TI High Voltage Motor Control Kit.

Figure 7.14 shows the prototype mounted on the test stand. A 1kW DC dynamometer is used as a variable load for the test bench. Himmelstein's MCRT 48201V N-Z non-contact type transient torque transducer is mounted between the FSPM and the dynamometer to evaluate torque, speed and mechanical power output from the motor.

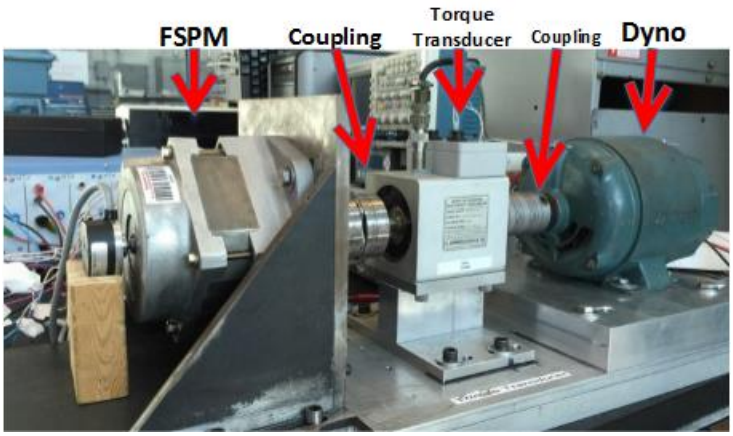

(a)

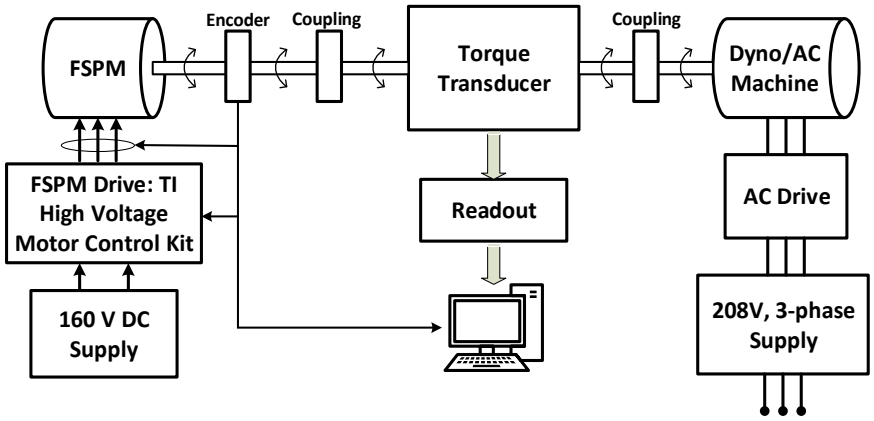

(b)

Figure 7.14: Experimental dyno setup of the FSPM drive system (a) photograph, (b) block diagram.

7.6.1 No-load Test

Figure 7.15 shows the FEA predicted and measured no-load, line to neutral RMS phase voltage against speed. The open circuit back-EMF is in good agreement with the 2D FEA prediction. Figure 7.16 shows the FFT of the back-EMF at different speeds. The measured back-emf values are also in good agreement with the simulation showing close agreement in the magnitude of the fundamental and higher order harmonics. The experimental results support the fact that the designed machine have sinusoidal back EMF, with negligible higher order harmonics according to the design which is one of the many attractive features of FSPM.

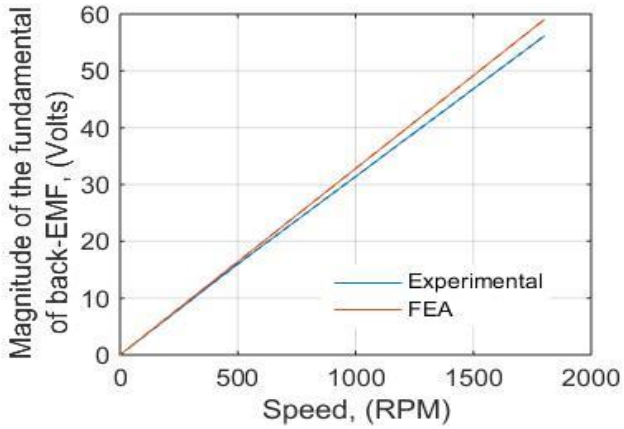

Figure 7.15: Measured and FEA calculated back-EMF magnitude against speed.

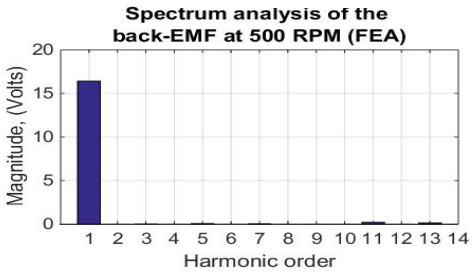

(a) Fundamental=16.42V

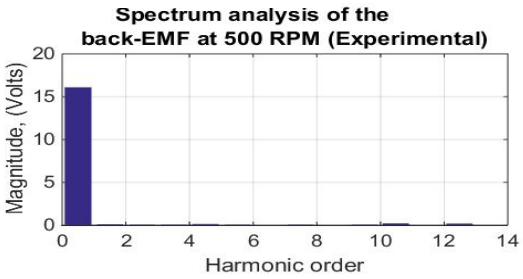

(a) Fundamental=16.04V

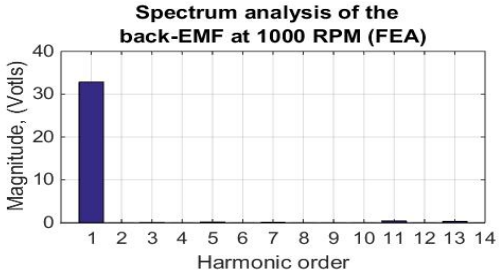

(b) Fundamental=32.83V

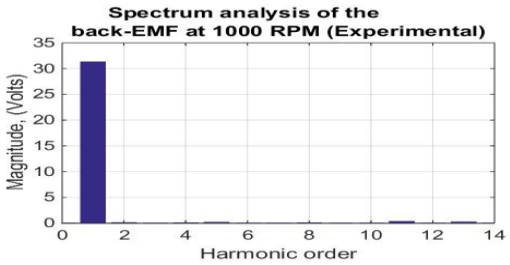

(b) Fundamental=31.33V

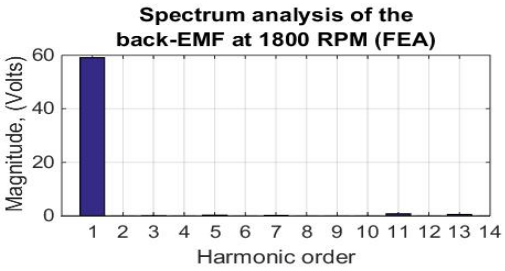

(c) Fundamental = 59 V

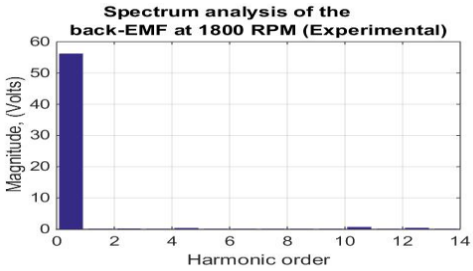

(c) Fundamental = 56.1 V

Figure 7.16: Spectrum analysis of the measured and FEA calculated back-EMF by FFT for different speeds, (a) 500 RPM, (b) 1000 RPM, (c) 1800 RPM.

7.6.2 Steady State Phase Currents, Torque and Torque Ripple

The stator field oriented vector control with $i_d=0$ has been implemented on the 0.5kW prototype FSPM on the TI DSP based controller. Steady state motor performance was tested for different current commands at rated speed and other higher and lower speeds. This section presents the controller response and machine behavior for different commands for the *q*-axis current.

The torque ripple is of particular interest because the machine displays sinusoidal back-EMF, with very negligible harmonics. Also, a novel cogging torque minimization technique has been applied during the design of the machine that helps in minimizing the torque ripple significantly. The results in the figures show excellent regulation in *q*-axis current command, followed by a flat torque with negligible ripple of less than 10%.

Figure 7.17 shows the phase currents and mechanical torque outputs from the machine with three different command current. Table 7.4 presents the torque ripple values and their comparison from simulation and experimental results. The speed is chosen to be 100 RPM because at higher speed, some portion of the ripple is filtered by the system inertia and sensor bandwidth limitation. Therefore, it is critical to observe the ripple performance at lower operating speeds. At 100 RPM, the percentage ripple was found to be less than 10% for all the commanded current.

Table 7.4: Comparison of Torque ripple between simulation and experiment

	Iq = 2 Amps		Iq= 2.5 Amps		Iq= 3.8 Amps	
	Simulation	Experiment	Simulation	Experiment	Simulation	Experiment
T_{avg} (N.m)	0.94	0.82	1.17	1.03	1.79	1.62
T_{ripple} (N.m)	0.08	0.08	0.09	0.098	0.11	0.15
%Ripple	8.5%	9.8%	7.7%	9.6%	6.1%	9.3%

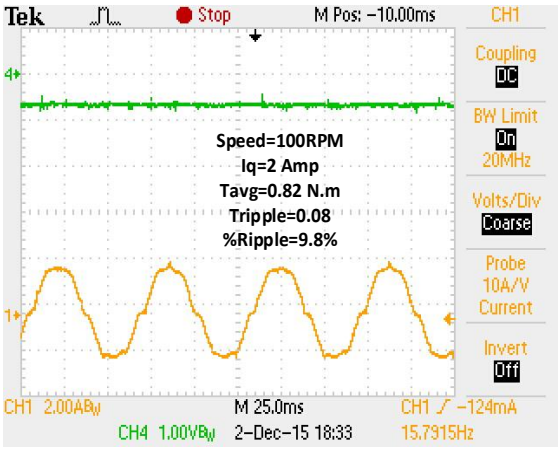

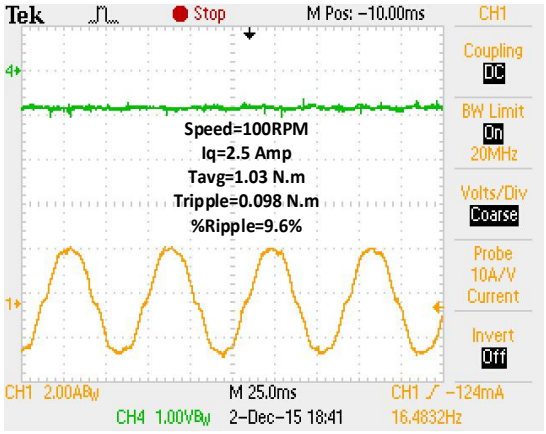

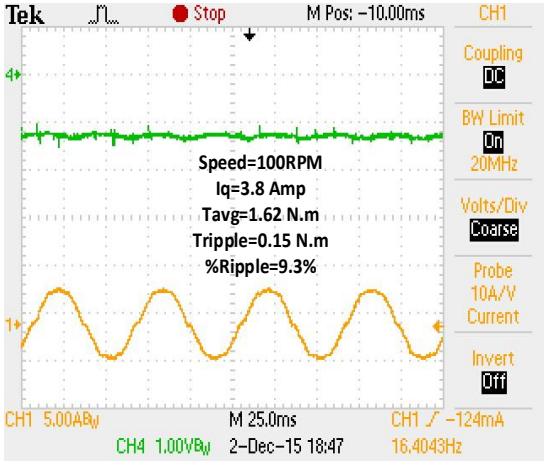

(a)

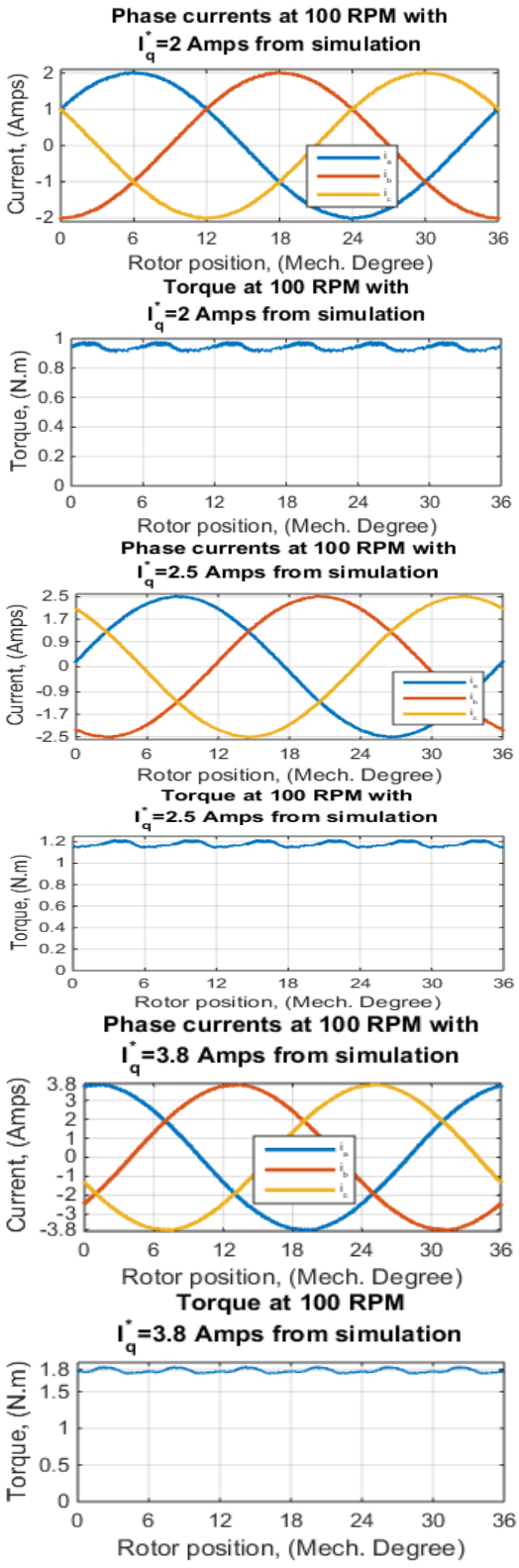

(b)

Figure 7.17: Phase current and torque from (a) experiment, and (b) simulation at 100 RPM for different current commands.

Torque ripple found from experiment was slightly higher than FEA based simulation due to (i) PWM switching, (ii) material characteristics, (iii) eccentricity and (iv) error in mechanical alignment of the machine in the dyno setup. As current command increases, ripple does not amplify as much as the average torque does, thereby showing a reduction in percentage ripple for higher phase current. Ripple due to cogging torque has been addressed in this work during the design of the machine by applying a novel pole shaping method. Torque ripple can be further reduced if required for ripple sensitive applications by applying advanced control techniques and algorithms, such as (i) harmonic current injection and (ii) current profiling. This makes it (FSPM) a very attractive candidate for such applications, one of which can be electric power steering for vehicles.

7.7 FSPM Performance at Different Load Conditions

Stator field oriented control with i_d=0 has been used for torque production at constant speed. The rated *q*-axis current of the machine is 4.7 Amps, and up to 200% of rated load has been applied during the tests. An extensive set of data was collected at three different speeds, and from a current command of zero to up to 200% rated for each speed. Figure 7.18 shows the key machine performances at 1800 RPM with varying current command. Figure 7.19 shows a sample set of steady state data from the power analyzer when the machine is running at 1800 RPM and a *q*-axis current command of 2 Amps (I_{rms}=1.4 Amp).

Figure 7.18 (a) shows the experimental and FEA predicted torque as a function of current. The experimentally measured torque is in good agreement but slightly smaller than simulation at low current. The torque discrepancy increases with the current. The discrepancies in back EMF and torque can be explained by leakage flux. As current increases, the stator lamination

become more saturated and less permeable, leading to more end leakage fluxes and more discrepancy from FEA predicted results.

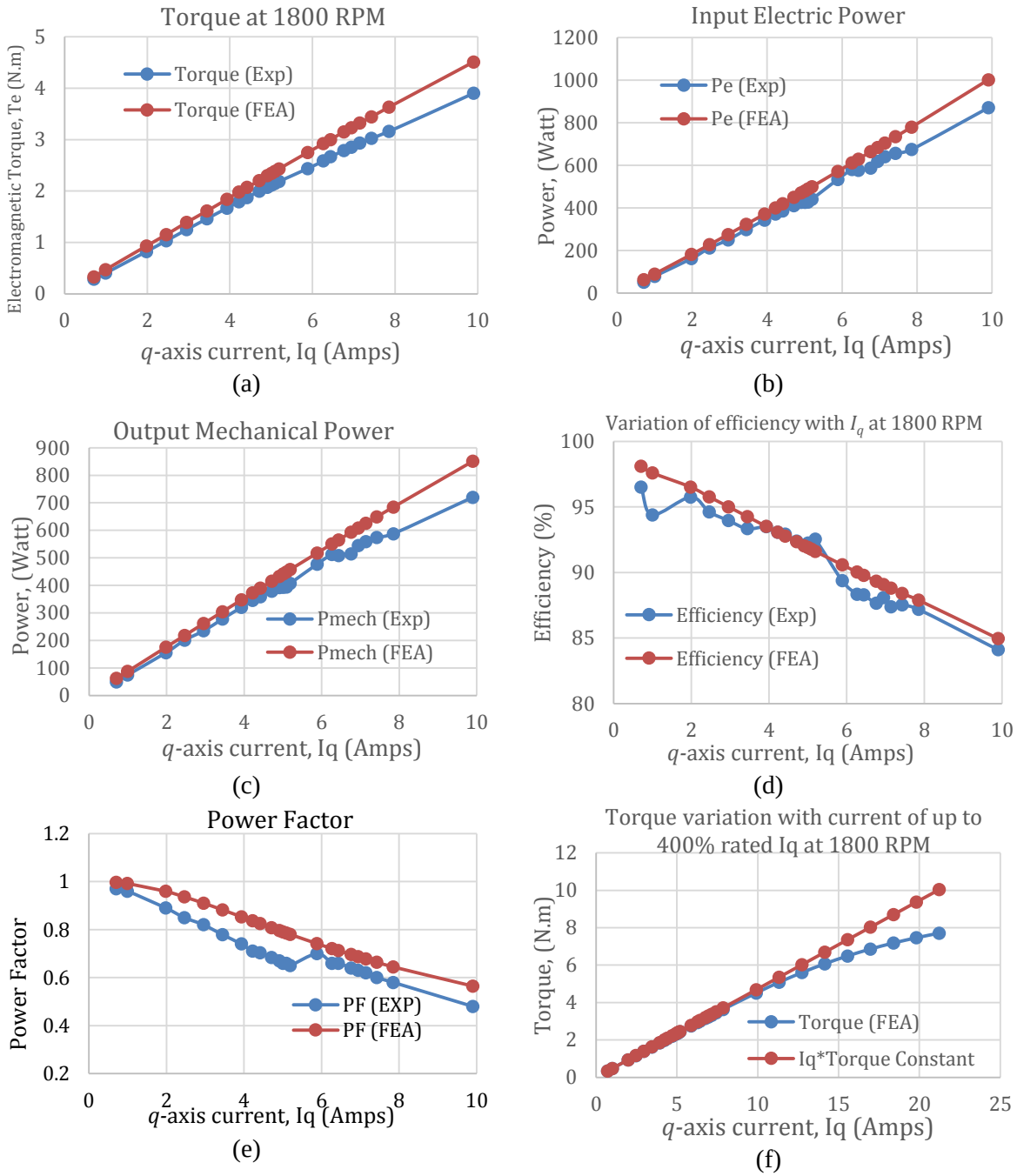

Figure 7.18: Experimental results from the prototype and their comparison with FEA at 1800 RPM (a) Torque vs. i_q, (b) Input power vs. i_q, (c) Output power vs. i_q, (d)Efficiency vs. i_q, and (e) Power factor vs. i_q, (f) Esimated torque and Iq*Torque Constant vs. i_q.

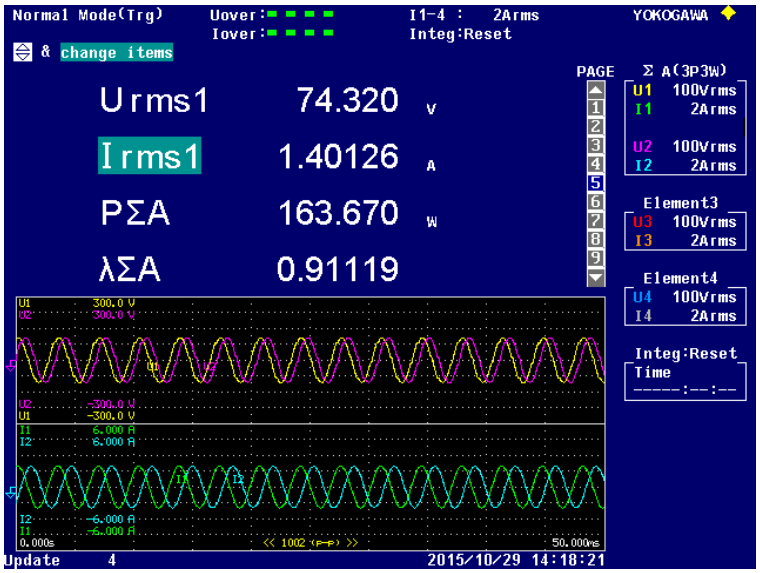

Figure 7.19: Sample data from power analyzer for a command of 1.4 Amps at 1800 RPM.

The measured efficiencies are also reasonably close to the predicted ones. Copper loss is the dominant among losses at a rated speed of 1800 rpm and thereby the main reason behind the reduction in efficiency when higher than rated current is applied. At higher operating speed, core loss will become dominant and end winding and copper loss will have less impact on efficiency.

A subsequent test was performed using FEA to check the saturation level of the motor with increasing *q*-axis current. Figure 7.18(f) shows the unsaturated torque (i_q multiplied by torque constant of the machine in a linear fashion as current increases) and actual output torque obtained from FEA. It is found that the motor slowly move towards saturation as the current increases above 12 Amps. This is also in agreement with the flux linkage vs. *q*-axis current characteristics as seen in Figure 7.4(b).

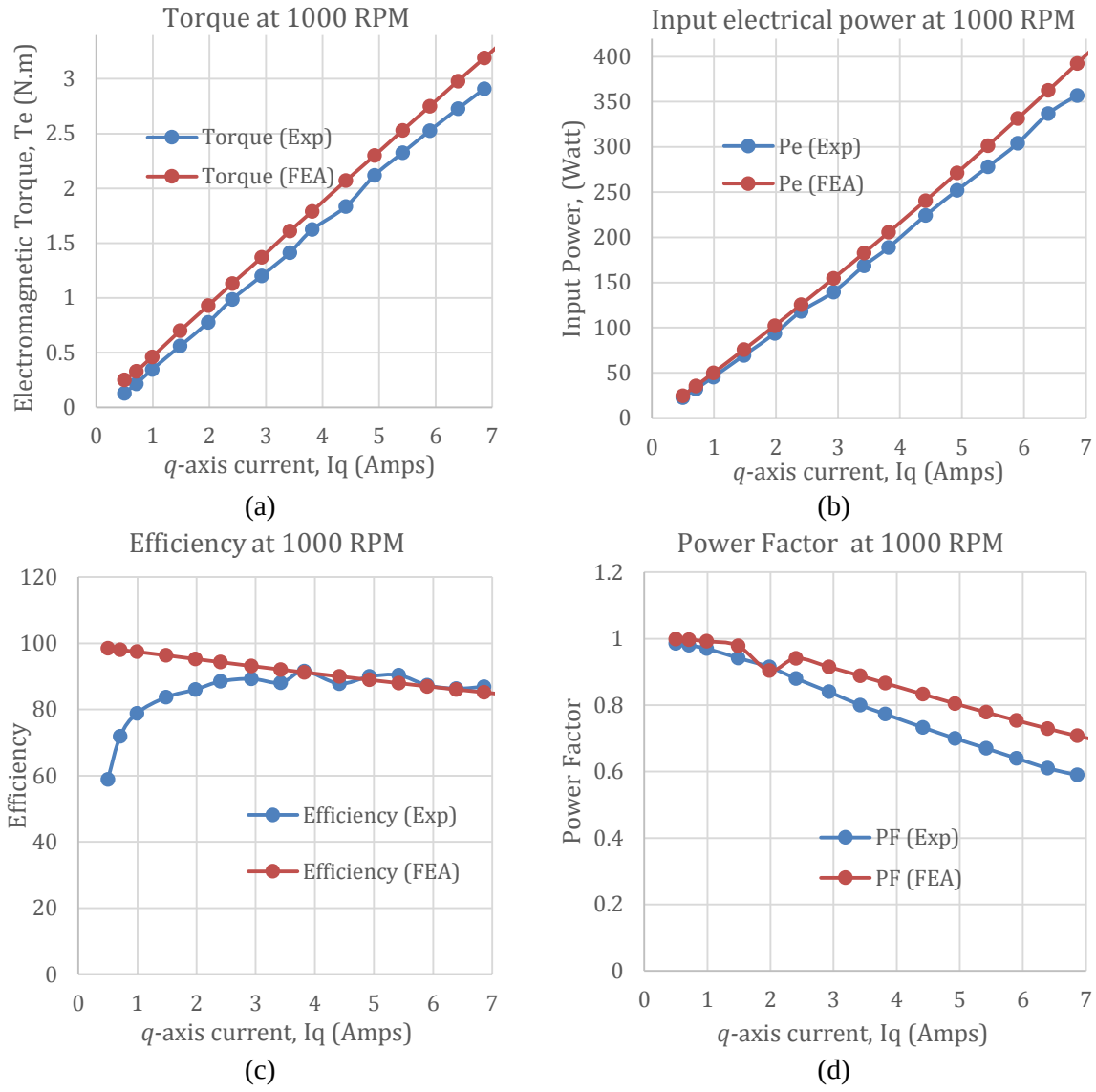

Figure 7.20: Experimental results from the prototype and their comparison with FEA at 1000 RPM (a) Torque vs. i_q, (b) Input power vs. i_q, (c) Efficiency vs. i_q, and (d) Power factor vs. i_q.

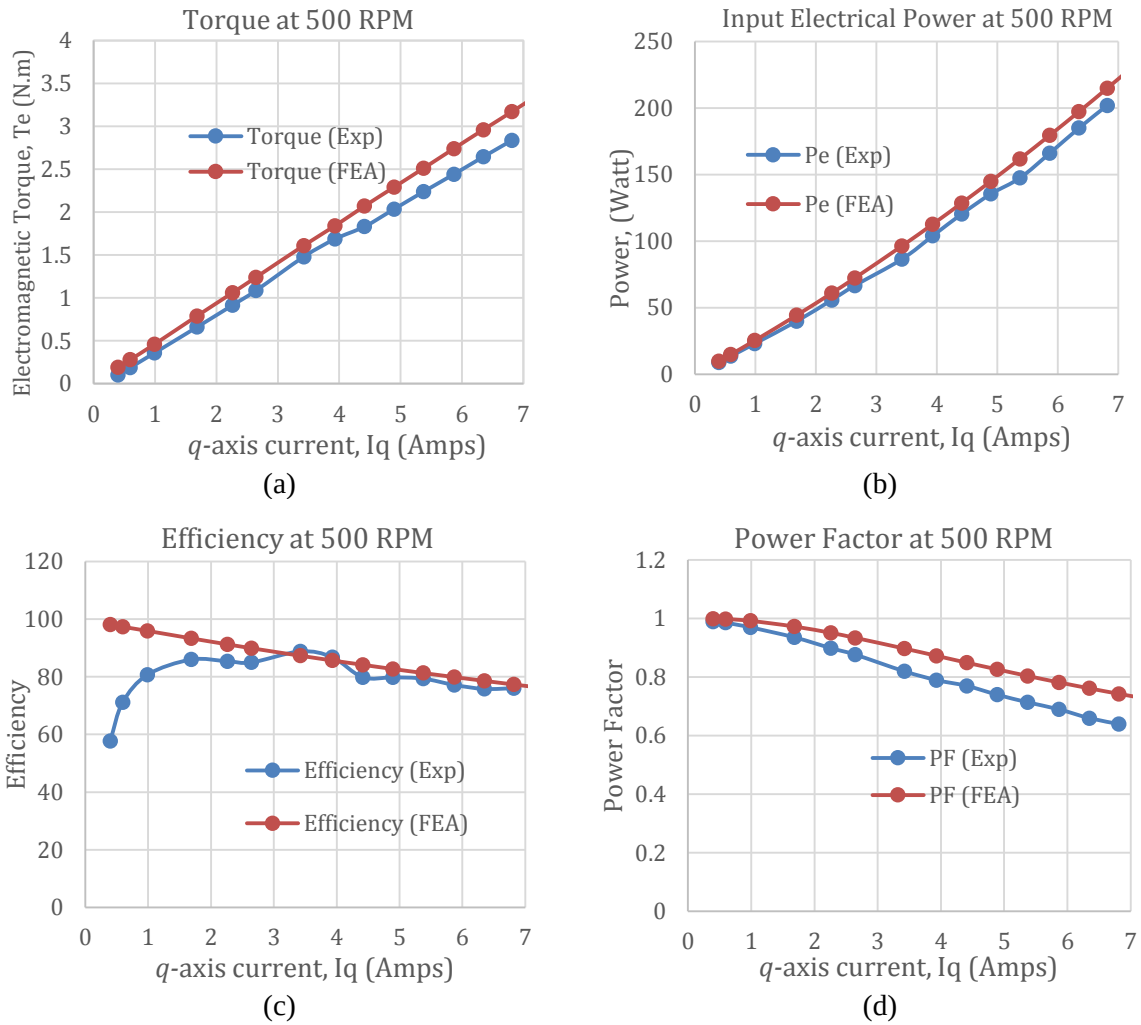

Figure 7.21: Experimental results from the prototype and their comparison with FEA at 500 RPM (a) Torque vs. i_q, (b) Input power vs. i_q, (c) Efficiency vs. i_q, and (d) Power factor vs. i_q.

Figure 7.20 and Figure 7.21 summarize the machine performance measured for up to 200% rated torque operation at other speeds. The machine is able to produce the expected power required by the specification from 500 to 1800 RPM according to the *q*-axis current command. The measured efficiencies are reasonably close to the predicted ones for all the currents at different operating speeds. The lower efficiency measured at lower speed for 200% rated load is due to the domination of copper loss over iron losses. As speed increases, the iron loss will become dominant, and the copper loss will have less impact on efficiency. The

average torque for different current commands, output power, and efficiency from the experimental setup at different operating speeds are in good agreement with FEA results.

7.8 Heat Run Test Results

Figure 7.22 presents the heat run test result at rated operating condition. The prototype FSPM was running under rated i_q command to produce rated torque at the base speed for more than 90 minutes till the temperature reached to steady state in the regions of interest. Then the motor was operated for 30 more minutes to verify that the temperature rise was less than 0.5 degree in every 15 minutes which indicates that it has reached the thermal steady state. Thermocouples were installed to measure temperature at the end winding, permanent magnet and U-core lamination. At 1800 RPM, the copper losses are significant, therefore the hot spot is on the end winding with a temperature rise of 16.1 ºC. Among the remaining stator regions, the next hot spot is on the PM (14 ºC), followed by the iron core lamination (13.5 ºC).

It is expected that at a higher speed, iron losses in the U-cores will become more dominant, and hence, the lamination, and PM temperatures will be higher than that at base speed. If speed is increased even further, the hot spot will gradually shift to the PM because of increased eddy current loss in the magnet, followed by iron core and end winding. The measured temperature rises in the FSPM prototype confirms that the machine can operate safely with the proposed electrical loading and natural cooling scheme as designed.

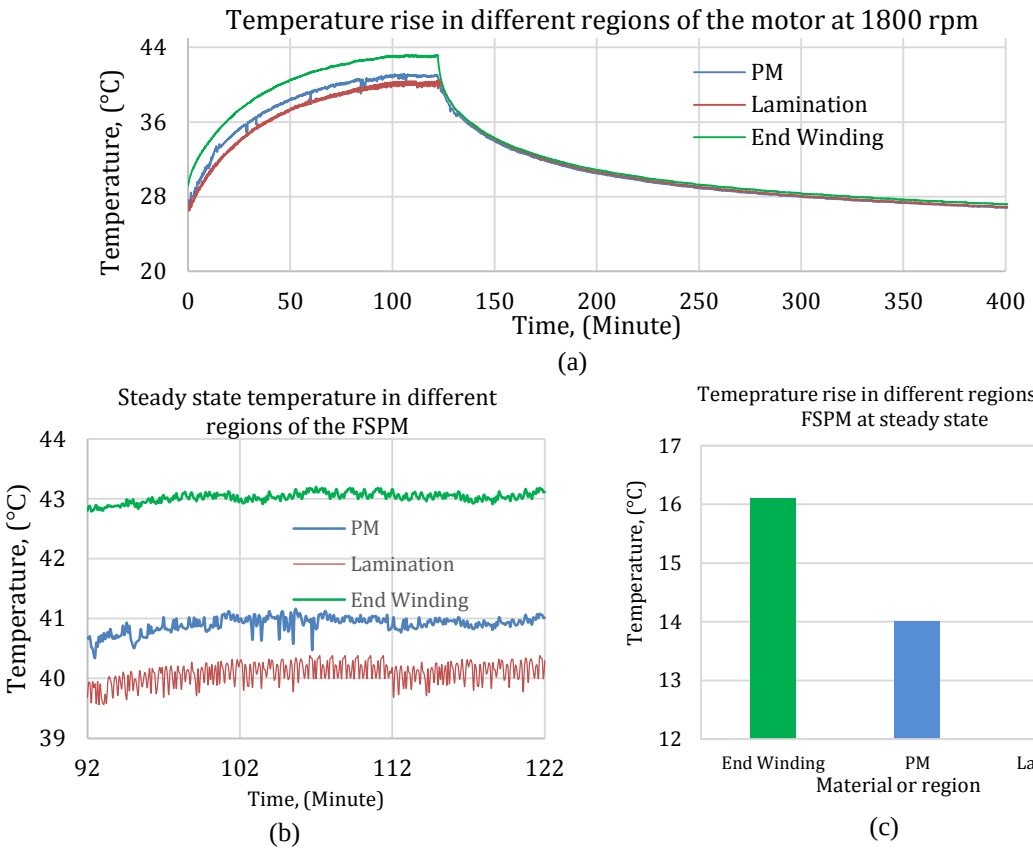

Figure 7.22: Steady state heat run results from the prototype (a) Measured temperatures at three key locations during a heat run under 0.5kW, 1800 RPM continuous operation, (b) Steady state temperature, (c) Comparison of temperature rise in the three regions measured.

It should be noted that for PM and lamination, thermocouples were installed on the surface. Acknowledging the fact that temperature gradients do exist for these materials based on their shape, size and flow of air, the relative average temperature rise (End Winding > PM > Lamination) at rated speed and rated load in different regions of the machine still holds true. Also, an FSPM with ferrite magnet will have negligible magnet eddy loss and thus relatively lower temperature rise in the magnet as compared to FSPM with rare earth magnet because of its low resistivity. A detailed FEA based thermal analysis on the machine would provide more accurate estimation of temperature rise at different regions of the machine at different operating speed and load conditions.

7.9 Conclusions

This chapter investigated the potential for non-rare earth FSPM with improvement in torque ripple, noise and vibration with experimental results. An advanced machine model was developed considering saturation and mutual coupling into account. The machine model is used to implement stator field oriented vector control to run the motor at constant speed and desired current command. A prototype was built based on innovative design techniques addressing electromagnetics and structural features of the machine. The performance parameters from the prototype under continuous operation was in agreement with the simulation results obtained during design. In addition, steady state heat run test was also performed and the prototype was capable of providing the required power with a safe temperature rise of 16 degree for rated operation at 1800 rpm. The design met the specification requirements such as mass, voltage required, current, current density, temperature, and efficiency. Key conclusion from this research is that the topology has a lot of potential to be useful for many applications, like variable speed, servo type or electric power steering. Depending on the requirement, FSPM with rare earth can also be applicable in traction type applications. There are challenges introduced such as torque ripple, noise and vibration due to the structure of the machine that have to be addressed carefully during the design phase.

Chapter 8

Summary and Future Work

This chapter summarizes the advances on Switched Reluctance and Flux Switching machine technologies accomplished through this research along with some suggested future works. The summary section 8.1 gives a brief description of the research presented elaborately in the previous seven chapters. Section 8.2 discusses some of the relevant issues that are proposed as future works.

8.1 Summary

SRM is a very lucrative candidate for applications where both motoring and generating is required at various speed range. Torque ripple and current ripple are the key issues during SRM operations for motoring and generating, respectively. They can be addressed by both manipulating the design or innovative control algorithm and techniques.

This thesis presents a new control technique of SRM as a generator based on geometry based analytical model. The system operation has been verified experimentally using a 1kW SRM drive setup. A detailed analysis has been performed on the DC-link current ripples affecting the overall system performance, efficiency and battery life during generation using SRM. It has also been shown that minimizing current ripple while generating indirectly maximizes the efficiency of the whole SRM drive system.

Efficient and optimum SRG control requires carefully fine-tuned commutation angles. The complexity increases at low speed as compared to high speed operation. At high speed, phase currents go into single pulse mode, therefore, no hysteresis control is required. At low

speed, phase current enters hysteresis region, so that the maximum allowed level also needs to be controlled. Therefore, to achieve ripple minimization or efficiency maximization for operation where various speed range is prerequisite, a two loop controller which controls all the commutation angles along with the reference current is crucial.

A control algorithm has been developed that dynamically varies the commutation angles for the machine operation based on the required and commanded DC-link current level along with continuously monitoring the ripple in DC-link current. The algorithm is implemented and tested at different operating speeds where hysteresis is present for all speeds. This control concept can generally be applied to any SRM for all speed ranges.

Flux-Switching machine topologies can achieve torque and power density very close to that of today's rare earth PM machine topologies with non-rare earth magnets because of their flux focusing structure. Unlike any electric machine technology, there are areas that can be improved in terms of performance and efficiency. FSPMs have naturally low torque ripple and the main source of that is the cogging due to the presence of flux focusing magnets. FSPM can be driven controlled easily using standard *dq* control. Therefore it would be really helpful if the cogging torque can be minimized during the design stage. And among the existing techniques to achieve that, skewing the rotor poses difficulty in manufacturing. In this research, the issue of minimizing torque ripple by reducing cogging torque is addressed from a design perspective. A generalized design rule has been developed and proposed via theoretical analysis using permeance based model. The design rule has been verified using FEA and applied in the design of the target prototype motor. A comparison on the output torque with design of similarly arranged and sized conventional machine have also been performed. A larger, higher power FSPM is also designed to verify the scalability of the design rules.

Because of the structure, the most feasible three-phase topology is 12/10, which poses another challenge of low second order mode frequency which will cause high noise and vibration. The segmented stator structure also needs to be looked into for analytically predicting the mode frequencies, and hence, noise and vibration. Unlike cogging torque, it is possible to minimize the noise and vibration by tweaking the geometrical design of the machine, and verifying it using FE analysis. The issue of noise, vibration and stator deformation is also addressed from a design perspective. Based on the analytical model of natural mode frequencies and stator deformation, another design rule has been proposed to improve the noise and vibration characteristics of the machine. This rule has also been applied in the manufactured prototype. From the result, it has been found that the maximum displacement is 0.075 micrometer which is way less than the acceptable value for most of the noise sensitive applications. Also, the proposed design modification reduces noise by around 7-8 dB at all the operating speeds.

Because of the nature of operation, FSPM can be controlled in a similar technique as done for IPM and Brushless DC machines. However, precise control requires fine modeling of the machine. Existing models do not consider the mutual effects of cross coupling. This research introduces a model including saturation and cross-coupling effect. The model has been used to develop and implement control of the FSPM prototype.

Finally, an experimental prototype of the designed 12/10 FSPM machine was constructed. The predicted and measured machine parameters show good correlation validating the design and analysis of the machine. No-load tests show that the open circuit back EMF is in good agreement with that obtained from FEA simulation. Static measurements of torque and other important performance parameter from the machine when operating as a motor under

load conditions were also performed. The characteristics displayed by FE analysis have been directly tested and verified by measurements. In addition, heat run test was also performed to verify steady state temperature rise and hot spots of the machine. The motoring operation have been implemented using a standard three-phase AC drive with stator field oriented vector control strategy. A steady state heat run test was also performed to confirm that the temperature rise in different parts of the machine are in acceptable range.

8.2 Future Work

The following future research works are suggested further in this topic:

- One of the major contributions of this research is the novel strategy developed for adapting the commutation angles based on the desired DC-link current and ripple in the DC-link current for charging the battery using SRG system. A two loop controller has been developed that produces the required turn on, turn off angle and reference current for efficiency maximization of SRG for a wide speed range. However, the conduction period can be divided into two regions: the excitation period (both switches on, +Vdc applied across the motor terminal), and the switching period in which zero and –Vdc is applied respectively to achieve hysteresis current control. The controller can be even tuned more by appropriately timing this excitation period and switching period. Another loop can be introduced, or a relation can be established to achieve optimum excitation period as well as switching period.
- The bandwidth of the conduction angle controller is higher than that of the turn-off angle controller. Further analysis can be continued on improving the

interaction of the two controllers and a way to find the proper bandwidth of each controller.

- A comprehensive design methodology has been proposed and applied in designing a prototype FSPM. However, motor design is an iterative process and required parameters depend upon a lot of other limiting factors as the design constraints change. A detailed scalability study and analysis can be performed on the design rules for FSPM's of different sizes, power ratings and available cooling methods.
- The design performed in this research is mostly single objective, solving one challenge at a time. The identified issues have been decoupled with one another and a particular method has been proposed for one issue that does not affect another. In applications when the required objectives are more than one (i.e. maximize power, minimize volume, losses), it might be a better idea to perform multi-objective optimization study to achieve the design goals. Multi-objective optimization can be performed on either FEA models, or other magnetic circuit equivalent or mathematical models. The accuracy of the output of such multi-objective optimization study depends on the accuracy of the models. An accurate, magnetic equivalent circuit model of FSPM can be developed, and using that, a multi-objective optimization study and method can be performed to achieve any FSPM design for any desired output.
- Cogging torque, and thus torque ripple has been reduced by geometric pole shaping technique. Experimentally the motor has shown less than 10% torque ripple at 100 RPM and several torque commands. However, for ripple sensitive

applications where a ripple of less than 5% is desired, torque ripple can be reduced more using control techniques such as harmonic current injection. Appropriate design combined with complex control can achieve negligible torque ripple.

- 2D FEA along with analytical model have been used to predict stator deformation, noise and vibration of the designed motor. These can also be verified experimentally, in an anechoic chamber and using an appropriate dyno setup with facilities for noise and vibration measurement. Using 3D FEA will result in more accurate prediction of stator deformation, noise and vibration.
- A detailed thermal analysis can be performed on the motor using analytical model and thermal FEA. In this research, temperature at different parts of the machine is measured experimentally. This results can be verified with thermal FEA if done so. Heat run test is performed for rated speed only. This can also be performed for higher speeds to verify the fact that iron loss and magnet losses dominate at higher speed, and are usually higher than copper loss.
- An accurate machine model has been developed taking saturation and mutual coupling into account. However, the motor was run in unsaturated conditions and therefore, simple PI-based *d*- and *q*-axes controller was developed and implemented. Better controller can be developed using the complex motor parameters determined so that the controller also performs under saturation.
- The machine operation is tested for motoring in experiment. However, FSPM topology can also be used as a generator. FSPM generator operation can be implemented and tested with appropriate bi-directional power converter and

energy storage device. FSPM generator can be used in applications such as wind turbine generator and automotive/traction.

REFERENCES

[1] M. Benhaddadi, G. Olivier, and J. Yelle, "Premium efficiency motors effectiveness," in *SPEEDAM 2010 - International Symposium on Power Electronics, Electrical Drives, Automation and Motion*, 2010, pp. 1607–1612.

[2] D. M. Ionel, "High-efficiency variable-speed electric motor drive technologies for energy savings in the US residential sector," in *Proceedings of the International Conference on Optimisation of Electrical and Electronic Equipment, OPTIM*, 2010, pp. 1403–1414.

[3] M. Benhaddadi, G. Olivier, D. Labrosse, and P. Tetrault, "Premium efficiency motors and energy saving potential," in *2009 IEEE International Electric Machines and Drives Conference, IEMDC '09*, 2009, pp. 1463–1468.

[4] W. R. Finley, B. Veerkamp, D. Gehring, and P. Hanna, "Advantages of using high efficiency motors such as NEMA premium?? around the world," in *Record of Conference Papers - Annual Petroleum and Chemical Industry Conference*, 2007.

[5] W. R. Finley, B. Veerkamp, D. Gehring, and P. Hanna, "Improving motor efficiency levels globally," *IEEE Ind. Appl. Mag.*, vol. 15, no. 1, pp. 39–49, 2009.

[6] R. Boteler and J. Malinowski, "Review of upcoming changes to global motor efficiency regulations," *IEEE Conf. Rec. Annu. Pulp Pap. Ind. Tech. Conf.*, pp. 26–30, 2009.

[7] M. Benhaddadi and G. Olivier, "Barriers and incentives policies to high-efficiency motors and drives market penetration," in *SPEEDAM 2008 - International Symposium on Power Electronics, Electrical Drives, Automation and Motion*, 2008, pp. 1161–1164.

[8] A. T. De Almeida, F. J. T. E. Ferreira, J. A. C. Fong, and C. U. Brunner, "Electric motor standards, ecodesign and global market transformation," in *Conference Record - Industrial and Commercial Power Systems Technical Conference*, 2008.

[9] R. J. Parker, "Survey of Rare Earth Permanent Magnet Applications," *IEEE Trans. Magn.*, vol. M, no. 6, pp. 2985–2987, 1981.

[10] K. G. Knoch, "Rare Earth Permanent Magnet Materials and their Properties," *IEE Colloq. Impact New Mater. Des.*, pp. 8/1–8/5, 1995.

[11] T. Schrefl, J. Fidler, and W. Scholz, "Modeling and limits of advanced HT-magnets," in *IEEE Transactions on Magnetics*, 2000, vol. 36, no. 5 I, pp. 3394–3398.

[12] K. Gallagher, M. Venkatesan, and J. M. D. Coey, "Magnetic properties of mechanically-alloyed Sm-Co nanophase hard magnets," in *IEEE Transactions on Magnetics*, 2001, vol. 37, no. 4 I, pp. 2528–2530.

[13] T. R. T. Renyuan, "Research and development of rare earth permanent magnet machines," *ICEMS'2001. Proc. Fifth Int. Conf. Electr. Mach. Syst. (IEEE Cat. No.01EX501)*, vol. 1, 2001.

[14] M. T. Thompson, "Practical issues in the use of NdFeB permanent magnets in maglev, motors, bearings, and eddy current brakes," *Proc. IEEE*, vol. 97, no. 11, pp. 1758–1767, 2009.

[15] S. Zhang, J. Xu, J. Junak, D. Fiederling, G. Sawczuk, M. Koch, A. Schalja, M. Podack,

and J. Baumgartner, “Permanent magnet technology for electric motors in automotive applications,” *2012 2nd Int. Electr. Drives Prod. Conf. EDPC 2012 - Proc.*, pp. 1–11, 2012.

[16] R. Liu, X. Sun, J. Gong, and S. Guo, “Comparison of Different Arrangement of magnets for the Purpose of Reducing Magnet Usage in Designing an IPM Motor for Electric Vehicles,” pp. 1–5, 2014.

[17] D. Dorrell, L. Parsa, and I. Boldea, “Automotive electric motors, generators, and actuator drive systems with reduced or no permanent magnets and innovative design concepts,” *IEEE Trans. Ind. Electron.*, vol. 61, no. 10, pp. 5693–5695, 2014.

[18] E. Carraro, M. Degano, and N. Bianchi, “Permanent magnet volume minimization in permanent magnet assisted synchronous reluctance motors,” *2013 8th Int. Conf. Exhib. Ecol. Veh. Renew. Energies, EVER 2013*, vol. Mi, pp. 4–7, 2013.

[19] T. M. Jahns and E. L. Owen, “AC adjustable-speed drives at the millennium: How did we get here?,” *IEEE Trans. Power Electron.*, vol. 16, no. 1, pp. 17–25, 2001.

[20] L. Lorenz, “Power semiconductors development trends,” in *Conference Proceedings - IPEMC 2006: CES/IEEE 5th International Power Electronics and Motion Control Conference*, 2007, vol. 1, pp. 39–45.

[21] L. Lorenz, “Key power semiconductor devices and development trends,” *2007 Int. Work. Phys. Semicond. Devices*, 2007.

[22] H. A. Toliyat, *Recent advances and applications of power electronics and Motor Drives - Electric machines and motor drives*, vol. 1. 2005, pp. 34–36.

[23] B. K. Bose, “Power electronics and motor drives recent progress and perspective,” *IEEE Trans. Ind. Electron.*, vol. 56, no. 2, pp. 581–588, 2009.

[24] F. Blaabjerg, A. Consoli, J. A. Ferreira, and J. D. van Wyk, “The future of electronic power processing and conversion,” *IEEE Trans. Ind. Appl.*, vol. 41, no. 1, pp. 3–8, 2005.

[25] L. Lorenz, “Power semiconductors state-of-art and development trends,” in *7th Internatonal Conference on Power Electronics, ICPE’07*, 2008, pp. 683–686.

[26] A. Huang, “Recent advances and applications of power electronics and motor drives - Power semiconductor devices,” *2008 34th Annu. Conf. IEEE Ind. Electron.*, 2008.

[27] G.-A. Capolino, “Recent advances and applications of power electronics and motor drives - Advanced and intelligent control techniques,” *2008 34th Annu. Conf. IEEE Ind. Electron.*, 2008.

[28] L. Alberti, N. Bianchi, and S. Bolognani, “A very rapid prediction of IM performance combining analytical and finite-element analysis,” *IEEE Trans. Ind. Appl.*, vol. 44, no. 5, pp. 1505–1512, 2008.

[29] L. Alberti, N. Bianchi, P. Baldassari, and R. Wang, “Thermal assisted finite element analysis of electrical machines,” in *Electrical Machines, 2008. ICEM 2008. 18th International Conference on*, 2008, pp. 1–4.

[30] W. S. W. Shuhong, L. Q. L. Qingfu, T. M. T. Mingxing, and L. Q. L. Qunfeng, “A new method for design and analysis of a parameterized electrical machine electromagnetic fields finite element package,” *Sixth Int. Conf. Electr. Mach. Syst. 2003. ICEMS 2003.*,

vol. 2, pp. 823–826, 2003.

[31] T. J. E. Miller, *Switched Reluctance Motors and Theirs Control*. Magna Physics Publishing and Claredon Press, Oxford, 1993.

[32] D. G. T. R. S. Wallace, "Three Phase Switched Reluctance Motor Design to Reduce Torque Ripple," in *International Conference on Electrical Machines*, 1990, pp. 783–787.

[33] R. S. Wallace and D. G. Taylor, "Torque Ripple Reduction in Three-Phase Switched Reluctance Motors," *1990 Am. Control Conf.*, 1990.

[34] R. S. Wallace and D. G. Taylor, "Low-torque-ripple switched reluctance motors for direct-drive robotics," *IEEE Trans. Robot. Autom.*, vol. 7, no. 6, pp. 733–742, 1991.

[35] D. E. Cameron, J. H. Lang, and S. D. Umans, "The origin and reduction of acoustic noise in doubly salient variable-reluctance motors," *IEEE Trans. Ind. Appl.*, vol. 28, no. 6, pp. 1250–1255, 1992.

[36] C. Y. Wu and C. Pollock, "Time domain analysis of vibration and acoustic noise in the switched reluctance drive," pp. 558–563, 1993.

[37] R. S. Colby, F. M. Mottier, and T. J. E. Miller, "Vibration modes and acoustic noise in a four-phase switched reluctance motor," *IEEE Trans. Ind. Appl.*, vol. 32, no. 6, pp. 1357–1364, 1996.

[38] K. M. Rahman, B. Fahimi, G. Suresh, A. V. Rajarathnam, and M. Ehsani, "Advantages of switched reluctance motor applications to EV and HEV: design and control issues," *IEEE Trans. Ind. Appl.*, vol. 36, no. 1, pp. 111–121, 2000.

[39] A. V. Radun, "High-power density switched reluctance motor drive for aerospaceapplications," *IEEE Trans. Ind. Appl.*, vol. 28, no. 1, 1992.

[40] E. Richter, "High Temperature, Lightweight, Switched Reluctance Motors and Generators for Future Aircraft Engine Applications," *1988 Am. Control Conf.*, 1988.

[41] T. M. J. T. J. E. Miller, "A Current Controlled Switched Reluctance Drive for FHP Applications," in *Conference on Applied Motion Control (CAMC)*, 1986, pp. 109–117.

[42] T. J. E. Miller, *Brushless Permanent-Magnet and Reluctance Motor Drives*. Claredon Press, Oxford, 1993.

[43] Y. Pang, Z. Q. Zhu, D. Howe, S. Iwasaki, R. Deodhar, and A. Pride, "Comparative study of flux-switching and interior permanent magnet machines," *2007 Int. Conf. Electr. Mach. Syst.*, 2007.

[44] W. Zhao, M. Cheng, W. Hua, and H. Jia, "A redundant flux-switching permanent magnet motor drive for fault-tolerant applications," in *2008 IEEE Vehicle Power and Propulsion Conference, VPPC 2008*, 2008.

[45] I. Husain and S. A. Hossain, "Modeling, Simulation, and control of switched reluctance motor drives," *IEEE Trans. Ind. Electron.*, vol. 52, no. 6, 2005.

[46] A. Y. Yang, B. Y. Zhang, and C. S. Wang, "Four-quadrant control of dsp-based switched reluctance drives for EV," in *ICIEA 2007: 2007 Second IEEE Conference on Industrial Electronics and Applications*, 2007, pp. 2162–2167.

[47] D. A. Torrey, "Switched reluctance generators and their control," *IEEE Trans. Ind. Electron.*, vol. 49, no. 1, pp. 3–14, 2002.

[48] X. D. Xue, K. W. E. Cheng, J. K. Lin, Z. Zhang, K. F. Luk, T. W. Ng, and N. C. Cheung, "Optimal control method of motoring operation for SRM drives in electric vehicles," *IEEE Trans. Veh. Technol.*, vol. 59, no. 3, pp. 1191–1204, 2010.

[49] E. Mese, Y. Sozer, J. M. Kokernak, and D. A. Torrey, "Optimal excitation of a high speed switched reluctance generator," *APEC 2000. Fifteenth Annu. IEEE Appl. Power Electron. Conf. Expo. (Cat. No.00CH37058)*, vol. 1, 2000.

[50] P. J. Lawrenson, D. Sc, I. E. E. E. Fel, C. Eng, and J. M. Stephenson, "Variable-speed switched reluctance motors," *Electr. Power Appl. IEE Proc. -*, vol. 127, no. 4, pp. 253–265, 1980.

[51] S. E. Rauch and L. J. Johnson, "Design Principles of Flux-Switch Alternators," *Trans. Am. Inst. Electr. Eng. Part III Power Appar. Syst.*, vol. 74, no. December, pp. 1261–1268, 1955.

[52] E. Hoang, H. Ahmed, and J. Lucidarme, "Switching flux permanent magnet polyphased synchronous machines," *Epe 97*, 1997.

[53] R. P. Deodhar, S. Andersson, I. Boldea, and T. J. E. Miller, "The flux-reversal machine: A new brushless doubly-salient permanent-magnet machine," *IEEE Trans. Ind. Appl.*, vol. 33, no. 4, pp. 925–934, 1997.

[54] Z. Q. Zhu, Y. Pang, D. Howe, S. Iwasaki, R. Deodhar, and a. Pride, "Analysis of electromagnetic performance of flux-switching permanent-magnet machines by nonlinear adaptive lumped parameter magnetic circuit model," *IEEE Trans. Magn.*, vol. 41, no. 11, pp. 4277–4287, 2005.

[55] Y. Zhao, Z. Zhang, W. Qiao, and L. Wu, "An extended flux model-based rotor position estimator for sensorless control of interior permanent magnet synchronous machines," *2013 IEEE Energy Convers. Congr. Expo.*, pp. 3799–3806, 2013.

[56] J. Zhang, M. Cheng, and Y. Zhang, "Single phase doubly salient permanent magnet generator with full-pitched winding," *2009 IEEE Int. Electr. Mach. Drives Conf. IEMDC '09*, pp. 311–316, 2009.

[57] B. J. H. Walker and A. Member, "The theory of the inductor alternator*," pp. 227–241, 1941.

[58] J.D. Herbst, A. L. Gattozzi, and R. E. Hebner, "A Megawatt Power Module for Ship Service Supplement," vol. 1, no. Program Technical Report, 2007.

[59] K. Sivasubramaniam, E. T. Laskaris, M. R. Shah, J. W. Bray, and N. R. Garrigan, "High-temperature superconducting homopolar inductor alternator for marine applications," *IEEE Trans. Appl. Supercond.*, vol. 18, no. 1, pp. 1–6, 2008.

[60] C. Pollock and M. Wallace, "The flux switching motor, a DC motor without magnets or brushes," *Conf. Rec. 1999 IEEE Ind. Appl. Conf. Thirty-Forth IAS Annu. Meet. (Cat. No.99CH36370)*, vol. 3, 1999.

[61] D. A. Phillips, "Switched Reluctance Drives: New Aspects," pp. 579–584, 1989.

[62] F. Liang and T. a. Lipo, "New variable reluctance motor utilizing an auxiliary

commutation winding," *IEEE Trans. Ind. Appl.*, vol. 30, no. 2, pp. 423–432, 1994.

[63] Y. Liao, F. Liang, and T. A. Lipo, "Novel permanent magnet motor with doubly salient structure," *IEEE Trans. Ind. Appl.*, vol. 31, no. 5, pp. 1069–1078, 1995.

[64] C. Wang, S. A. Nasar, and I. Boldea, "Three-phase flux reversal machine (FRM)," *IEE Proceedings - Electric Power Applications*, vol. 146, no. 2. p. 139, 1999.

[65] C. X. Wang, I. Boldea, and S. A. Nasar, "Charactenzation of three phase flux reversal machine as an automotive generator," *IEEE Trans. Energy Convers.*, vol. 16, no. 1, pp. 74–80, 2001.

[66] Y. Chen, S. Chen, Z. Q. Zhu, D. Howe, and Y. Y. Ye, "Starting torque of single-phase flux-switching permanent magnet motors," *IEEE Trans. Magn.*, vol. 42, no. 10, pp. 3416–3418, 2006.

[67] Y. Cheng, C. Pollock, and H. Pollock, "A permanent magnet flux switching motor for low energy axial fans," in *Conference Record - IAS Annual Meeting (IEEE Industry Applications Society)*, 2005, vol. 3, pp. 2168–2175.

[68] Y. Pang, Z. Zhu, D. Howe, S. Iwasaki, R. Deodhar, and A. Pride, "Eddy current loss in the frame of a flux-switching permanent magnet motor," in *INTERMAG 2006 - IEEE International Magnetics Conference*, 2006, p. 188.

[69] W. Hua, Z. Q. Zhu, M. Cheng, Y. Pang, and D. Howe, "Comparison of flux-switching and doubly-salient permanent magnet brushless machines," *2005 Int. Conf. Electr. Mach. Syst.*, vol. 1, pp. 165–170, 2005.

[70] W. Hua, M. Cheng, H. Jia, and X. Fu, "Comparative study of flux-switching and doubly-salient PM machines particularly on torque capability," in *Conference Record - IAS Annual Meeting (IEEE Industry Applications Society)*, 2008.

[71] R. L. Owen, Z. Q. Zhu, A. S. Thomas, G. W. Jewell, and D. Howe, "Fault-tolerant flux-switching permanent magnet brushless AC machines," in *Conference Record - IAS Annual Meeting (IEEE Industry Applications Society)*, 2008.

[72] A. S. Thomas, Z. Q. Zhu, R. L. Owen, G. W. Jewell, and D. Howe, "Multi-phase flux-switching permanent magnet brushless machine for aerospace application," in *Conference Record - IAS Annual Meeting (IEEE Industry Applications Society)*, 2008.

[73] J. T. Chen, Z. Q. Zhu, and D. Howe, "Stator and rotor pole combinations for multi-tooth flux-switching permanent-magnet brushless AC machines," *IEEE Trans. Magn.*, vol. 44, no. 12, pp. 4659–4667, 2008.

[74] J. T. Chen and Z. Q. Zhu, "Winding configurations and optimal stator and rotor pole combination of flux-switching PM brushless AC machines," *IEEE Trans. Energy Convers.*, vol. 25, no. 2, pp. 293–302, 2010.

[75] L. Hao, M. Lin, X. Zhao, and H. Luo, "Analysis and optimization of EMF waveform of a novel axial field flux-switching permanent magnet machine," in *2011 International Conference on Electrical Machines and Systems, ICEMS 2011*, 2011.

[76] J. T. Chen, Z. Q. Zhu, and D. Howe, "Optimization of multi-tooth flux-switching PM brushless AC machines," *Proc. 2008 Int. Conf. Electr. Mach. ICEM'08*, 2008.

[77] J. T. Chen, Z. Q. Zhu, S. Iwasaki, and R. P. Deodhar, "Comparison of losses and

efficiency in alternate flux-switching permanent magnet machines," *19th Int. Conf. Electr. Mach. ICEM 2010*, 2010.

[78] J. T. Chen, Z. Q. Zhu, S. Iwasaki, and R. P. Deodhar, "A novel E-core switched-flux PM brushless AC machine," *IEEE Trans. Ind. Appl.*, vol. 47, no. 3, pp. 1273–1282, 2011.

[79] H. Pollock, C. Pollock, R. T. Walter, and B. V. Gorti, "Low cost, high power density, flux switching machines and drives for power tools," *38th IAS Annu. Meet. Conf. Rec. Ind. Appl. Conf. 2003.*, vol. 3, 2003.

[80] C. Pollock, H. Pollock, and M. Brackley, "Electronically Controlled Flux Switching Motors: A Comparison with an Induction Motor Driving an Axial Fan," in *IECON Proceedings (Industrial Electronics Conference)*, 2003, vol. 3, pp. 2465–2470.

[81] E. Hoang, M. Lecrivain, and M. Gabsi, "A new structure of a switching flux synchronous polyphased machine with hybrid excitation," in *2007 European Conference on Power Electronics and Applications, EPE*, 2007.

[82] E. Hoang, S. Hlioui, M. Lecrivain, and M. Gabsi, "Experimental comparaison of lamination material (M330-50 & NO20) case switching flux synchronous machine with hybrid excitation," *EPE J. (European Power Electron. Drives Journal)*, vol. 20, no. 3, pp. 28–33, 2010.

[83] R. L. Owen, Z. Q. Zhu, and G. W. Jewell, "Hybrid-excited flux-switching permanent-magnet machines with iron flux bridges," in *IEEE Transactions on Magnetics*, 2010, vol. 46, no. 6, pp. 1726–1729.

[84] Y. Sozer, D. A. Torrey, and E. Mese, "Automatic control of excitation parameters for switched-reluctance motor drives," *IEEE Trans. Power Electron.*, vol. 18, no. 2, pp. 594–603, 2003.

[85] Y. Sozer and D. A. Torrey, "Closed loop control of excitation parameters for high speed switched-reluctance generators," *IEEE Trans. Power Electron.*, vol. 19, no. 2, pp. 355–362, 2004.

[86] I. Kioskeridis and C. Mademlis, "Optimal efficiency control of switched reluctance generators," *IEEE Trans. Power Electron.*, vol. 21, no. 4, pp. 1062–1072, 2006.

[87] a. Radun, "Generating with the switched reluctance motor," *Proc. 1994 IEEE Appl. Power Electron. Conf. Expo. - ASPEC'94*, pp. 41–47, 1994.

[88] J. Kim and R. Krishnan, "High Efficiency Single-Pulse Controlled Switched Reluctance Motor Drive for High Speed (48k RPM) Application: Analysis, Design, and Experimental Verification," in *2008 IEEE Industry Applications Society Annual Meeting*, 2008, pp. 1–8.

[89] Y. Sozer and D. A. Torrey, "Optimal turn-off angle control in the face of automatic turn-on angle control for switched-reluctance motors," *IET Electric Power Applications*, vol. 1, no. 3. p. 395, 2007.

[90] S. Narla, Y. Sozer, and I. Husain, "Switched reluctance generator controls for optimal power generation and battery charging," *2011 IEEE Energy Convers. Congr. Expo.*, pp. 3575–3581, 2011.

[91] A. M. Omekanda, “A new technique for multi-dimensional performance optimization of switched reluctance motors for vehicle propulsion,” *Conf. Rec. 2002 IEEE Ind. Appl. Conf. 37th IAS Annu. Meet. (Cat. No.02CH37344)*, vol. 1, 2002.

[92] C. Sikder, I. Husain, and Y. Sozer, “Switched reluctance generator control for optimal power generation with current regulation,” *IEEE Trans. Ind. Appl.*, vol. 50, no. 1, pp. 307–316, 2014.

[93] A. Radun, “Analytically computing the flux linked by a switched reluctance motor phase when the stator and rotor poles overlap,” *IEEE Trans. Magn.*, vol. 36, no. 4, pp. 1996–2003, 2000.

[94] A. Radun, “Analytical calculation of the switched reluctance motor’s unaligned inductance,” *IEEE Trans. Magn.*, vol. 35, no. 6, pp. 4473–4481, 1999.

[95] J. Faiz and R. Fazai, “Optimal excitation angles of a high speed switched reluctance generator by efficiency maximization,” *EPE-PEMC 2006 12th Int. Power Electron. Motion Control Conf. Proc.*, pp. 287–291, 2007.

[96] J. W. Kolar and S. D. Round, “Analytical calculation of the RMS current stress on the DC-link capacitor of voltage-PWM converter systems,” *IEE Proc. - Electr. Power Appl.*, vol. 153, no. 468, p. 535, 2006.

[97] J.-T. Chen and Z.-Q. Zhu, “Coil connections and winding factors in flux-switching PM brushless AC machines,” *COMPEL Int. J. Comput. Math. Electr. Electron. Eng.*, vol. 30, pp. 84–97, 2011.

[98] W. Hua, M. Cheng, Z. Q. Zhu, and D. Howe, “Analysis and optimization of back-EMF waveform of a novel flux-switching permanent magnet motor,” *Proc. IEEE Int. Electr. Mach. Drives Conf. IEMDC 2007*, vol. 2, pp. 1025–1030, 2007.

[99] Z. Q. Zhu and J. T. Chen, “Advanced flux-switching permanent magnet brushless machines,” *IEEE Trans. Magn.*, vol. 46, no. 6, pp. 1447–1453, 2010.

[100] Z. Q. Zhu, Y. Pang, J. T. Chen, Z. P. Xia, and D. Howe, “Influence of design parameters on output torque of flux-switching permanent magnet machines,” *2008 IEEE Veh. Power Propuls. Conf. VPPC 2008*, pp. 1–6, 2008.

[101] T. J. E. M. Jr, J. R. Hendershot, *Design of Brushless Permanent-Magnet Motors*. Oxford: Magna Physiscs Publishing and Claredon Press, 1994.

[102] H. Zijlstra, “Permanent magnets,” *Phys. Technol.*, vol. 7, no. April, pp. 98–107, 1976.

[103] M.-J. Jin, Y. Wang, J.-X. Shen, P. C.-K. Luk, W.-Z. Fei, and C.-F. Wang, “Cogging torque suppression in a permanent-magnet flux-switching integrated-starter-generator,” vol. 4, no. December 2009, pp. 647–656, 2010.

[104] Y. H. Yeh, M. F. Hsieh, and D. G. Dorrell, “Different arrangements for dual-rotor dual-output radial-flux motors,” in *IEEE Transactions on Industry Applications*, 2012, vol. 48, no. 2, pp. 612–622.

[105] H. Jia, M. Cheng, W. Hua, W. Zhao, and W. Li, “Torque ripple suppression in flux-switching PM motor by harmonic current injection based on voltage space-vector modulation,” in *IEEE Transactions on Magnetics*, 2010, vol. 46, no. 6, pp. 1527–1530.

[106] D. Wang, X. Wang, D. Qiao, Y. Pei, and S. Y. Jung, “Reducing cogging torque in

surface-mounted permanent-magnet motors by nonuniformly distributed teeth method," *IEEE Trans. Magn.*, vol. 47, no. 9, pp. 2231–2239, 2011.

[107] M. F. Hsieh, D. G. Dorrell, Y. H. Yeh, and S. Ekram, "Cogging torque reduction in axial flux machines for small wind turbines," in *IECON Proceedings (Industrial Electronics Conference)*, 2009, pp. 4435–4439.

[108] Y. Wang, M. J. Jin, W. Z. Fei, and J. X. Shen, "Cogging torque reduction in permanent magnet flux-switching machines by rotor teeth axial pairing," *IET Electric Power Applications*, vol. 4, no. 7. p. 500, 2010.

[109] W. H. W. Hua and M. C. M. Cheng, "Cogging torque reduction of flux-switching permanent magnet machines without skewing," *2008 Int. Conf. Electr. Mach. Syst.*, 2008.

[110] D. Wang, X. Wang, and S. Y. Jung, "Reduction on cogging torque in flux-switching permanent magnet machine by teeth notching schemes," *IEEE Trans. Magn.*, vol. 48, no. 11, pp. 4228–4231, 2012.

[111] C. Sikder, I. Husain, and W. Ouyang, "Cogging Torque Reduction in Flux-Switching Permanent-Magnet Machines by Rotor Pole Shaping," *IEEE Trans. Ind. Appl.*, vol. 51, no. 5, pp. 3609–3619, 2015.

[112] N. Bianchi and S. Bolognani, "Design techniques for reducing the cogging torque in surface-mounted PM motors," *IEEE Trans. Ind. Appl.*, vol. 38, no. 5, pp. 1259–1265, 2002.

[113] T. Raminosoa, C. Gerada, and M. Galea, "Design considerations for a fault-tolerant flux-switching permanent-magnet machine," *IEEE Trans. Ind. Electron.*, vol. 58, no. 7, pp. 2818–2825, 2011.

[114] X. Xue, W. Zhao, J. Zhu, G. Liu, X. Zhu, and M. Cheng, "Design of Five-Phase Modular Flux-Switching Permanent-Magnet Machines for High Reliability Applications," vol. 49, no. 7, pp. 3941–3944, 2013.

[115] G. Verez, G. Barakat, Y. Amara, O. Bennouna, and G. Hoblos, "Impact of pole and slot combination on noise and vibrations of flux-switching PM machines," *Proc. - 2014 Int. Conf. Electr. Mach. ICEM 2014*, pp. 182–188, 2014.

[116] J. Boisson, F. Louf, J. Ojeda, X. Mininger, and M. Gabsi, "Magnetic forces and vibrational behavior analysis for flux switching permanent magnet machines," *Proc. - 2012 20th Int. Conf. Electr. Mach. ICEM 2012*, pp. 2988–2993, 2012.

[117] C. Sikder and I. Husain, "Stator Vibration and Acoustic Noise Analysis of FSPM for a Low-Noise Design," in *2016 IEEE Energy Conversion Congress and Exposition, ECCE 2016*, 2016.

[118] S. J. Yang, *Low-Noise Electrical Motors*. Oxford, U.K.: Claredon Press, Oxford, 1981.

[119] P. L. Timar, *Noise and Vibration of Electric Machines*. Oxford, U.K.: Elsevier, 1989.

[120] E. C. Sewall, J.L. and Naumann, "An experimental and analytical vibration study of thin cylindrical shells with and without longitudinal stiffness." NASA, Houston, TX, 1968.

[121] R. S. Girgis and S. P. Verma, "Method for Accurate Determination of Resonant Frequencies and Vibration Behaviour of Stators of Electrical Machines," *Electr. Power*

Appl. IEE Proc. B, vol. 128, no. 1, pp. 1–11, 1981.

[122] C. Sikder, W. Ouyang, and I. Husain, "Design, Control and Implementation of a Non-Rare-Earth Flux Switching Permanent Magnet Machine," in *2016 IEEE Energy Conversion Congress and Exposition, ECCE 2016*, 2016.

[123] J. Nakatsugawa, N. Iwasaki, H. Nagura, and Y. Iwaji, "Proposal of Mathematical Models Taking into Consideration Magnetic Saturation and Cross-Coupling Effects in Permanent Magnet Synchronous Motors," *IEEJ Trans. Ind. Appl.*, vol. 130, pp. 1212–1220, 2010.

[124] H. Nagura, Y. Iwaji, J. Nakatsugawa, and N. Iwasaki, "New vector controller for PM motors which modeled the cross-coupling magnetic flux saturation," *2010 Int. Power Electron. Conf. - ECCE Asia -, IPEC 2010*, no. 1, pp. 1064–1070, 2010.

[125] J. T. Chen, Z. Q. Zhu, S. Iwasaki, and R. P. Deodhar, "Influence of slot opening on optimal stator and rotor pole combination and electromagnetic performance of switched-flux PM brushless AC machines," *IEEE Trans. Ind. Appl.*, vol. 47, no. 4, pp. 1681–1691, 2011.

[126] R. L. Owen, Z. Q. Zhu, A. S. Thomas, G. W. Jewell, and D. Howe, "Alternate poles wound flux-switching permanent-magnet brushless AC machines," *IEEE Trans. Ind. Appl.*, vol. 46, no. 2, pp. 790–797, 2010.

[127] I. Takahashi and T. Noguchi, "A New Quick-Response and High-Efficiency Control Strategy of an Induction Motor," *Ind. Appl. IEEE Trans.*, vol. IA-22, no. 5, pp. 820–827, 1986.

[128] P. Pillay and R. Krishnan, "Modeling, simulation, and analysis of permanent-magnet motor drives. I. The permanent-magnet synchronous motor drive," *Ind. Appl. IEEE Trans.*, vol. 25, no. 2, pp. 265–273, 1989.

[129] T. M. Jahns, "Flux-weakening regime operation of an interior permanent-magnet synchronous motor drive," *IEEE Trans. Ind. Appl.*, vol. IA-23, no. 4, pp. 681–689, 1987.